Analytical and Experimental Studies of Vehicle Pollution Dispersion

by David Michael Hargreaves, BSc, MSc

Thesis submitted to the University of Nottingham for the degree of Doctor of Philosophy, October 1997

Abstract

Using a dual approach of wind tunnel experimentation and the development of an analytical model, the dispersion of pollutants from road vehicles has been investigated.

A series of novel tests were conducted in an environmental wind tunnel which looked at the dispersion of propane in the wake of a $1/50^{\text{th}}$ scale model of a lorry which was fired across the wind tunnel using a special rig. Time histories of concentration and air flow were taken as the lorry sped across the tunnel.

Two experimental scenarios were investigated. The first, a simulation of a typical rural boundary layer, confirmed the existence of a wake behind the moving lorry. Concentration measurements revealed that the dispersion was largely Gaussian in nature and that at low cross wind speeds the vehicle-induced turbulence was the dominant mixing effect.

Measurements were taken as the lorry passed along a model of an idealized urban street canyon. Time histories for individual firings exhibited two peaks as the propane was swept around the canyon in the resident vortex. Ensemble averages of several firings allowed a quantitative assessment of the rate of dispersal from the canyon to be made.

A computer model has been developed which predicts the dispersion of vehicular pollutants in both the rural and the urban street canyon environments. The model, based around the Gaussian Puff Method, extends the range of applicability of earlier models in several areas. It is a transient model which enables the investigation of traffic congestion and non-steady above canyon wind fields. It is also the first model to include individual vehicles as sources of both pollutant and turbulence. A detailed sensitivity study is presented, followed by an application of the model which attempts to predict probability distributions of pollutant in a street canyon.

Finally, a comparison between the analytical model and the experimental program is presented which demonstrates that the model is capable of modelling a real situation to a good degree of accuracy but also demonstrates that further validation is required.

Contents

1 Introduction **1**

2 Background **4**
2.1 Introduction 4
2.2 Basic Meteorology 4
2.2.1 The Atmospheric Boundary Layer and Stability 5
2.2.2 Analytical Description of the ABL 6
2.3 Vehicle Aerodynamics and Emission Rates 11
2.3.1 Vehicle Aerodynamics 11
2.3.2 Vehicle Emissions 16
2.3.3 Traffic Models 18
2.4 Dispersion of Vehicular Pollutants 20
2.4.1 General Dispersion 20
2.4.2 Dispersion - The Rural Case 21
2.4.3 Pollution Dispersion - The Urban Case 24
2.5 Puff Models 38
2.5.1 Relevant Puff Models 39
2.5.2 The Efficiency of Puff Models 40
2.6 Summary 41

3 Experimental Investigation **42**
3.1 Introduction 42
3.2 Experimental Equipment and Techniques 42
3.2.1 The Wind Tunnel 42
3.2.2 The Moving Model Rig 43
3.2.3 The Lorry Model and Trolley Configuration 45
3.2.4 Gas Supply System 47
3.2.5 Anemometry 49
3.2.6 Gas Measurements 51
3.2.7 Data Acquisition 52
3.2.8 Flow Visualization 54
3.2.9 Wind Tunnel Scaling Requirements 54
3.2.10 Presentation of Results 56
3.3 Results and Discussion - The Rural Case 58
3.3.1 Empty Tunnel Case 58

3.3.2 Characteristics of the Rural Boundary Layer 58
3.3.3 Effects of a Passing Vehicle in a Cross-wind 64
3.4 Results and Discussion - The Urban Case 72
3.4.1 Characteristics of the Urban Boundary Layer 72
3.4.2 Vortex Flow in the Street Canyon 76
3.4.3 Flow Visualization 76
3.4.4 Effects of a Passing Vehicle in a Street Canyon 79
3.5 Conclusions 89

4 Analytical Investigation **90**
4.1 Introduction 90
4.2 Theory 91
4.2.1 The Domain 91
4.2.2 Traffic Simulation Sub-model 91
4.2.3 Gaussian Puff Theory 96
4.2.4 Transport of the Puffs 97
4.2.5 Dispersion Parameters 100
4.2.6 Roof Level Puff Entrainment 102
4.2.7 End Entrainment and Cyclical Boundaries 104
4.3 Implementation on Computer 105
4.4 Sensitivity Study 106
4.4.1 The Urban Base Case 106
4.4.2 Urban Sensitivity Study 108
4.4.3 Rural Base Case 120
4.4.4 Rural Sensitivity Study 120
4.5 Inter-model Comparison 128
4.5.1 PUFFER versus STREET 128
4.5.2 PUFFER versus CPB3 129
4.6 Statistical Application of the Model 131
4.7 Conclusions 137

5 Reconciling the Investigations **140**
5.1 Introduction 140
5.2 The Rural Case 141
5.2.1 Constructing the PUFFER input data 141
5.2.2 Variation of Concentration with Distance Downstream 143
5.2.3 Variation of Concentration with Wind Speed 143
5.3 The Urban Case 146
5.3.1 Constructing the PUFFER input data 146
5.3.2 Variation of Concentration with Height on the Leeward Wall . . 146
5.3.3 Variation of Concentration with Wind Speed 147
5.4 Conclusions 150

6 Conclusions and Suggested Future Work **151**
6.1 Introduction 151

6.2 Conclusions . . . 151
6.3 Suggestions for Future Work . . . 154

A Installing the Moving Model Rig **164**
A.1 Introduction . . . 164
A.2 Design of the New Sub-structure . . . 165
A.2.1 Design of the Main Section . . . 167
A.2.2 Design of the Launch Section . . . 167
A.2.3 Design of the End Section . . . 167
A.2.4 Configuration of the Support Plates . . . 168
A.2.5 Configuration of the Beam Splices . . . 168
A.3 Alterations to the Wind Tunnel . . . 168
A.3.1 Working Section . . . 168
A.3.2 Control Room . . . 169
A.3.3 Far/Laser Side . . . 170
A.4 Further Work . . . 170

B Documentation of PUFFER **181**
B.1 PUFFER Data Files . . . 181
B.1.1 Main Input File, `puffer.dat` . . . 182
B.1.2 Receptor Position File, `puffer.rcp` . . . 184
B.1.3 Restart Input File, `puffer.rsi` . . . 185
B.1.4 Main Output File, `puffer.out` . . . 185
B.1.5 Tracking File, `puffer.xyz` . . . 185
B.1.6 Restart Output file, `puffer.rso` . . . 185
B.1.7 Vehicle Position File, `puffer.veh` . . . 185
B.1.8 Echo File on Standard Output . . . 185
B.2 Running the PUFFER program . . . 186
B.3 Description of the Source Code . . . 188
B.3.1 File `pdefines.h`, version 1.8 . . . 188
B.3.2 File `ptypes.h`, version 1.8 . . . 193
B.3.3 File `puffer.c`, version 1.7 . . . 197
B.3.4 File `puffs.c`, version 1.10 . . . 200
B.3.5 File `read_data.c`, version 1.7 . . . 203
B.3.6 File `receptors.c`, version 1.6 . . . 204
B.3.7 File `vehicles.c`, version 1.8 . . . 206
B.3.8 File `write_track.c`, version 1.3 . . . 209
B.3.9 File `restart.c`, version 1.4 . . . 211
B.3.10 File `arma0.f`, version 1.5 . . . 212
B.3.11 File `arma1.f`, version 1.2 . . . 213
B.3.12 File `post.c`, version 1.2 . . . 213
B.3.13 File `write_ucd.c`, version 1.5 . . . 214

C Miscellaneous **216**
C.1 Simulation of time series of gusty winds . . . 216

C.1.1 Characteristics of the von Karman Spectra 216
C.1.2 Simulation 217
C.1.3 An ARMA-generated time series 219
C.2 Calculation of Spectra 219
C.3 Method for the Determining ${}^{x}L_{u}$ 220
C.4 Calibration of a Hot-wire Anemometer 221
C.5 Calibration of Cross-wire Anemometers 222
C.6 Calibration of the FID 223

List of Figures

2.1 Typical von Kàrmàn spectrum (after Cook [20]). 9
2.2 Flow separation around a circular prism (after Chadwick and Morfett [16]). 12
2.3 Schematic of the situation modelled by Eskridge and Hunt [30]. 14
2.4 Velocity vectors for a vehicle moving in a cross wind. 14
2.5 Nitrous oxides from petrol cars as a function of speed and acceleration (after Hickman [44]). 18
2.6 Plume patterns in different atmospheric stability situations. 22
2.7 Representation of an typical street canyon. 25
2.8 Types of flows within street canyons (after Oke [69]). 26
2.9 A typical transverse vortex in a street canyon. 27
2.10 Concentration contours across a symmetric canyon generated by the SCALAR model (after Johnson and Hunter [56]). 32
2.11 Simulated wind flow and concentration for various two-dimensional configurations (after Moriguchi and Uehara [66]). 33
2.12 Wind field obtained with the Hotchkiss-Harlow model for a mean wind field of 5 ms^{-1} in a unit aspect ratio canyon. 34
2.13 Modelling region used in the INPUFF model of Rao *et al* [74]. 40

3.1 Schematic of the British Gas Environmental Wind Tunnel at Fauld, Staffordshire. 44
3.2 The Moving Model Rig, transverse tunnel section (after Baker [4].) . . . 46
3.3 The Moving Model Rig track (after Baker [4].) 46
3.4 The Moving Model Rig, carriages and model train (after Baker [4].) . . 46
3.5 The 1/50th scale lorry model used in testing 48
3.6 Configuration of the MMR trolley (plan and side views). 49
3.7 Photograph of the model lorry mounted on the MMR trolley. 50
3.8 Photograph of the trolley showing the toggle valve and regulator in detail. 50
3.9 Mean velocity profiles in the empty tunnel. 59
3.10 Turbulence intensity profiles in the empty tunnel. 59
3.11 Roughness elements used in the simulation of the rural boundary layer. . 60
3.12 Mean velocity profiles for the rural boundary layer. 61
3.13 Turbulence intensity profiles for the rural boundary layer. 61
3.14 Mean u-component of wind speed along the line $x = 0$ m, $z = 0.2$ m. . . 62
3.15 Spectral power, $S_{uu}(n)$, against frequency, n, for the rural boundary layer. 63

3.16 Spectral density, $nS_{uu}(n)/\sigma_u^2$, versus frequency, ${}^xL_u n/\overline{u}$ for the rural boundary layer. 63
3.17 Variation of pollutant concentration with exhaust flow rate. 65
3.18 Six plots showing the variation of both the *u*- and *v*-components in the wake of vehicle with both wind speed (a, b and c) and distance downstream (a, d, e, and f). 68
3.19 Twenty individual concentration time series for $u_{\text{ref}}/U = 0.54$ at $(l_v/2, 0, h_v/2)$. 69
3.20 Variation of scaled concentration with reference wind speed. 71
3.21 Variation of scaled concentration with distance downwind. 71
3.22 Roughness elements used in the simulation of the urban boundary layer. 72
3.23 Mean velocity profile for the urban boundary layer. 74
3.24 Mean turbulence profile for the urban boundary layer. 74
3.25 Spectral power, $S_{uu}(n)$, against frequency, *n*, for the urban boundary layer. 75
3.26 Spectral density, $nS_{uu}(n)/\sigma_u^2$, against frequency, ${}^xL_u n/\overline{u}$ for the urban boundary layer. 75
3.27 *u*-component of flow along the vertical centreline of the last canyon. . . 77
3.28 *w*-component of flow along the horizontal centreline of the last canyon. 77
3.29 Video capture of a strong vortex in a 1:1 aspect ratio street canyon. . . . 78
3.30 Video capture of a intermittent vortex in a 2:1 aspect ratio street canyon. 78
3.31 Street canyon configuration in the wind tunnel. 80
3.32 Sixteen individual concentration time series for $u_{\text{ref}}/U = 1.0$ at $z = H/8$ on the leeward wall of a 1:1 aspect ratio canyon. 82
3.33 Variation of concentration with height on the leeward face of a 1:1 aspect ratio canyon. 85
3.34 Variation of concentration with height on the leeward face of a 2:1 aspect ratio canyon. 85
3.35 Variation of concentration with height on the windward face of a 1:1 aspect ratio canyon. 86
3.36 Variation of concentration with height on the windward face of a 1.5:1 aspect ratio canyon. 86
3.37 Variation of concentration with aspect ratio on the leeward face. 87
3.38 Variation of concentration with reference wind speed on the leeward face of a 1:1 aspect ratio canyon. 87
3.39 Variation of concentration with reference wind speed on the windward face of a 1:1 aspect ratio canyon. 88
3.40 The effect of wind speed on the time constants for both the leeward and windward walls of a 1:1 aspect ratio canyon. 88

4.1 A section of the street canyon showing the origin of the coordinate system. 91
4.2 Schematic of several important features of the traffic model. 94
4.3 An example of emission rate variation that can be constructed using the emission sub-model. 96
4.4 Wake coordinate system. 98

4.5 Schematic of the entrainment process for a single puff being sheared by the velocity differential at roof level. 103
4.6 Displacement of the Gaussian distribution in the across canyon direction due to the velocity differential. 104
4.7 Characteristics of the urban base case scenario. 109
4.8 Variation of concentration with wind speed in a street canyon. 114
4.9 Variation of concentration with vehicle speed in a street canyon. 115
4.10 Response of the model to increases in the puff removal limit. 116
4.11 Response of the model to changes in the dispersion parameter, α_1. . . . 117
4.12 Variation of concentration with wind direction in a street canyon. 118
4.13 Response of the model to decreases in the puff reduction factor. 119
4.14 Variation of concentration with distance downstream of the roadway. . . 123
4.15 Variation of concentration with height at a distance l downstream of the roadway. 123
4.16 Variation of concentration with height at a distance $4l$ downstream of the roadway. 124
4.17 Vertical concentration profiles a distance $4l$ downstream of the roadway. 124
4.18 Variation of concentration with wind speed at a distance $2l$ downstream of the roadway. 125
4.19 Variation of concentration with vehicle speed at a distance $2l$ downstream of the roadway. 125
4.20 Variation of concentration with time step size. 126
4.21 Variation of concentration with dispersion parameter, α_1. 126
4.22 Variation of concentration with emission rate, q_0. 127
4.23 Comparison of results from the PUFFER and STREET models. 130
4.24 Comparison of results from the PUFFER and CPB3 models. 130
4.25 Full scale experiments of Reynolds and Bell [10]. 132
4.26 Concentration time series for base case with simulated wind speed fluctuations. 134
4.27 Concentration probability distribution for base case with simulated wind speed fluctuations. 134
4.28 Concentration time series for base case with traffic signal control. . . . 135
4.29 Concentration probability distribution for base case with traffic signal control. 135
4.30 Concentration time series for base case with two vehicles types. 136
4.31 Concentration probability distribution for base case with two vehicle types. 136
4.32 Concentration time series for base case with all effects combined. . . . 138
4.33 Concentration probability distribution for base case with all effects combined. 138
4.34 Concentration probability distribution for daily traffic simulation. 139

5.1 Individual breakthrough curves obtained using PUFFER with an ARMA-generated wind speed in rural mode. 142
5.2 Comparison between experimental and analytical predictions for the variation of concentration with distance downstream, rural case. 144

5.3 Comparison between experimental and analytical predictions for the variation of concentration with wind speed, rural case. 145
5.4 Individual breakthrough curves obtained using PUFFER with an ARMA-generated wind speed in urban mode. 147
5.5 Comparison between experimental and analytical predictions for the variation of concentration with height on the leeward wall. 148
5.6 Comparison between experimental and analytical predictions for the variation of concentration with wind speed on the leeward wall. 149

A.1 Schematic plan view of the British Gas Environmental Wind Tunnel at Fauld, Staffordshire, showing the proposed position of the Moving Model Rig. 166
A.2 Schematic side elevation of the British Gas Environmental Wind Tunnel at Fauld, Staffordshire, showing the proposed position of the Moving Model Rig. 166
A.3 Reproduction of Drawing MMR/001. 172
A.4 Reproduction of Drawing MMR/002. 173
A.5 Reproduction of Drawing MMR/003. 174
A.6 Reproduction of Drawing MMR/004. 175
A.7 Reproduction of Drawing MMR/005. 176
A.8 Reproduction of Drawing MMR/007. 177
A.9 Reproduction of Drawing MMR/008. 178
A.10 Reproduction of Drawing MMR/010. 179
A.11 Reproduction of Drawing MMR/011. 180

B.1 Diagram of the input and output files for the PUFFER program. 181
B.2 Initialization phase of the PUFFER program. 189
B.3 Time stepping loop of the PUFFER program. 190

C.1 Circuit diagram for a constant-temperature anemometer. 222
C.2 Schematic of cross-wire configuration and geometry. 224
C.3 Behaviour of the mixer at various inlet pressures. 226
C.4 FID response values for various mixer inlet pressures 227

List of Tables

2.1 Typical values of terrain parameters z_0 and d, after ESDU 85020 [28]. . 7

3.1 Summary of the characteristics of the boundary layers used in the testing. 60

4.1 Values of parameters used in the urban base case. 107

Notation

A	cross-sectional area of vehicle in wake theory of Eskridge and Hunt [30]
B	width of street canyon
C	constant in wake theory of Eskridge and Hunt [30]
C_1	velocity control parameter
C_2	headway control parameter
C^*	normalised concentration in Hoydysh and Dabberdt [49]
D	density of traffic of a stream of traffic **or** the headway between two vehicles in a lane of traffic
D_j	jam density of a stream of traffic
H	height of street canyon
H_{up}	height of upwind building in Hoydysh and Dabberdt [49]
I_i	i^{th} component of turbulence intensity
$K_{1/3}$, $K_{2/3}$	modified Bessel functions of the second kind of order $1/3$ and $2/3$ respectively
L	length of street canyon
${}^xL_i$	length scales of turbulence in the x direction relating to components $i = u, v,$ or w
N	traffic flow in STREET model
N_l	number of lanes of traffic in the domain
N_p	number of puffs in the domain
N_r	number of receptors in the domain
N_{vi}	number of vehicles per lane
Q	flow rate of a stream of traffic **or** emission rate of pollutant
Re, R_e	Reynolds Number
S	mean speed of a stream of traffic
S_{ii}	i^{th} component of spectral density for isotropic turbulence
U	speed of vehicle (in the positive x direction)
U_H	above canyon wind speed in STREET model
$(V_H)_k$	reference wind speed at roof level in ARMA process
V_r	resultant wind speed acting on a vehicle at the yaw angle
$\underline{V_v}$	ventilation velocity in DePaul and Sheih [26]
$\underline{V_f}$	free flow space mean speed for a stream of traffic
$\underline{V_s}$	space mean speed for a stream of traffic
$\underline{V_z}$	mean hourly wind speed at height z

$a_i(p)$	autoregressive parameters in an ARMA model of order (p,q)
a_r	regression coefficient in Hoydysh and Dabberdt [49]
b	width of vehicle(s)
b_e	effective width of vehicle in Baker [6]
$b_j(q)$	moving average paramters in an ARMA model of order (p,q)
b_r	regression coefficient in Hoydysh and Dabberdt [49]
b_w	width of the wake
c	general concentration
c_e	concentration of pollutant in the exhaust gas
c_i, c_s, c_a	idling, speed- and acceleration-dependent coefficients for pollutant concentrations
c_r	concentration at receptor
d	zero-plane displacement height
d_e	diameter of exhaust pipe
e_k	terms in a white noise series with zero mean
h	height of vehicle(s)
h_w	height of the wake
$k = \pi/B$	variable in canyon vortex equations
l, l_v	length of vehicle
m	wind direction dependent exponent in Baker [6]
n	wind direction dependent exponent in Baker [6] **or** frequency in spectral analysis
n_u	non-dimensional frequencies used in spectral analysis for components $i = u, v,$ or w
$_p$	subscript which identifies variables with puffs
q_e	flow rate of pollutant from the exhaust pipe
q_i, q_s, q_a	idling exhaust flow rate, and speed- and acceleration-dependent coefficients for exhaust flow rates
$_r$	subscript which identifies variables with receptors
(s,t,z)	local wake coordinates
u	x component of air velocity
u_H	along canyon component of above canyon wind
u_{ref}	reference wind speed
u_w	velocity deficit in wake
$(u_w)_{\max}$	maximum velocity deficit in wake
$\overline{u}$	mean component of wind speed
u'	turbulent component of wind speed
$u_\star$	friction velocity

v	subscript which identifies variables with vehicles
v	y component of air velocity
v_H	cross canyon component of above canyon wind
w	z component of air velocity
$x_n^l, \dot{x}_n^l, \ddot{x}_n^l$	position, speed and acceleration of the n^{th} vehicle in a lane of traffic at the l^{th} time step
(x_p, y_p, z_p)	global coordinates of puff centre
(x_r, y_r, z_r)	global coordinates of receptor
(x_v, y_v, z_v)	global coordinates of vehicle
y_{li}	offset of the i^{th} lane of traffic
$z' = z - H$	translated z coordinate in canyon vortex equations
z_0	surface roughness
z_g	gradient height
α	minimum headway distance
α_1, α_2	turbulence intensity and anisotropy parameters
ΔC_L	concentration on the leeward wall in STREET model
ΔC_W	concentration on the windward wall in STREET model
ΔM	reduction in mass of puff over a time step
Δl	length of slug of pollutant which is emitted by a vehicle over a time step
Δt	length of time step
β	variable in canyon vortex equations **or** headway calculation parameter
γ	variable in canyon vortex equations
γ_w	parameter in wake theory of Eskridge and Hunt [30]
λ_f	puff reduction factor
λ_l	puff removal limit
θ	angle between the wind and the axis of the lanes of traffic
ϕ	yaw angle
ρ_i	normalised vehicle-type density
ρ_{ii}	i^{th} component of the autocorrelation functions for isotropic turbulence
$\sigma_u, \sigma_v, \sigma_w$	components of the standard deviation of turbulence
$\sigma_x, \sigma_y, \sigma_z$	dispersion lengths
τ	lag in autocorrelation functions **or** driver reaction time **or** canyon decay time constant of Lee and Park [61]
$\tilde{\tau}_i$	non-dimensionalized time lags in autocorrelation function
(ξ, η, ζ)	non-dimensionalized wake coordinates

Acknowledgements

Without the following people, this thesis would have been a lot shorter and I thank them all profoundly...

Rev. Prof. Chris Baker provided the inspiration, the funding and the experience to make this thesis what it is. I am indebted to him greatly.

Dr. Wayne Pearce who spent hours toiling at the wind tunnel with me. His ability to get up early and drive a car when absolutely knackered were an inspiration. He actually likes spending time at the wind tunnel. Thanks Wayne.

Dr. Sam Dalley was there at the start of the testing at the wind tunnel. Her experience, insight and cheerfulness were priceless when the temperature was down below zero.

Mike Langford provided the muscle and technical expertise when we were building the moving model rig. For doing the jobs of two men and not complaining, thanks Mike.

Faculty Workshop who fabricated much of the steelwork needed for the MMR and delivered on time, every time.

Bob Collins a legend.

Roger Brown of British Gas who was instrumental in setting up the wind tunnel deal. A manager with the common touch and a real scientific interest in what we were doing. Rare.

And to my friends, my wife Alice, oh, and me - you were all great.

Chapter 1

Introduction

The major cause of pollution in the urban environment is no longer heavy industry but one of its products - the motor car. Initially the car was seen as a great liberator, a sign of a bright, new technological era in which standards of living were to rise greatly. However, while the majority of the population in the developed world still ascribe to this ideal, there is an increasing realization that the motor car has undesirable costs, both economic and environmental. According to official UK government figures [46], the number of vehicles on our roads is set to increase by at least 50% by the year 2025 with the obvious associated degradation of the environment. Pictures of the traffic-induced smog over Los Angeles only serve to bring home the effect of the pollution caused by the over-reliance on this form of transport.

This thesis will concentrate on the environmental cost and will, in many respects, take the pessimistic view that the current levels of traffic will remain with us for the foreseeable future and will, in all probability, get worse. Assuming these levels, one conceivable method of alleviation would be to redesign the urban environment so that the effects of pollution could be reduced as much as possible. While not for one moment advocating the wholesale rebuilding of our cities, it would be negligent not to adopt new building geometries or street layouts if they had been proved beneficial to the mitigation of pollution.

The recurrent theme of this thesis, however, is the effect of the wind on the dispersal of the pollution. Smoggy days in Los Angeles do not generally occur in strong winds, but rather on hot, still days. On days such as these there is very little achieved by building environmentally friendly street grids. On days where there is wind, though, there may be a way of lessening the effect of the pollution. And, because many of the effects of the chemicals which are emitted by vehicles are cumulative over periods of years, taking advantage of even the weakest wind to clear the pollution would be desirable.

Current methods of predicting pollution dispersal have been developed for free moving traffic conditions in relatively open country. They have failed to take into account varia-

tions in traffic conditions or the complex topology of the urban environment. This thesis aims to address these shortcomings in two ways. Firstly, a mathematical model will be developed which includes both a complex traffic sub-model and sufficient numerical complexity to be able to cope with the problems associated with the urban situation. Secondly an investigation of vehicle pollution from scale models of vehicles in an environmental wind tunnel will be presented. The novelty of this wind tunnel study is the ability to fire models across the direction of flow in the tunnel, thus simulating the the complicating effect of the cross-wind.

While at first seeming like two separate studies, it is hoped to show that the two are inextricably linked - with the wind tunnel study providing vital information for the calibration and validation of the mathematical model.

It was not possible to investigate the urban problem without first considering the rural situation. In this context, rural can be taken to mean the simplified situation with no buildings or other urban detritus present. Familiarity with the behaviour of vehicular pollution in this situation is of paramount importance if one is to attempt to predict its dispersion in the urban environment. Thus, in addition to the symmetry provided by the two-pronged (theoretical and experimental) analyses, this thesis also considers both the rural and urban situations.

Chapter 2 provides an extensive background to the key areas of this topic. These include basic meteorology, traffic modelling and pollution dispersion. Then, with the reader familiarized with some of the more important concepts, a comprehensive literature review is presented. The review first covers the rural case, focusing in particular on the nature of the vehicle wake. The urban environment is then discussed, with brief coverage afforded to the more general aspects of the problem before concentrating on the urban street canyon. Briefly, the urban street canyon can be envisaged as a road with buildings of roughly uniform height running down each side. For both the rural and urban cases, full-scale tests, wind tunnel tests and analytical models are discussed in order to provide the best possible coverage.

The experimental investigation is described in Chapter 3. The scene is set by a description of the two major pieces of equipment used in the study: the wind tunnel and the moving model rig. The unfamiliarity of the wind tunnel and the prolonged installation of the moving model rig dictate that this is a lengthy description. The rest of the apparatus is then described before the chapter considers the rural and urban scenarios. For both, an atmospheric boundary layer is produced within the wind tunnel using standard techniques which has the same (scaled) properties as the full-scale situation it attempts to model. With the boundary layers successfully generated, a scale model of a lorry which emits propane is fired across the tunnel. Using appropriate anemometry and hydrocarbon sensors, the transient flow and concentration fields behind the moving model are presented.

Chapter 4 then describes the new analytical model of vehicular pollution which has been

developed in parallel with the wind tunnel tests. The structure of the chapter follows a standard pattern for mathematical models: a theoretical background; a description of the computer implementation of the model; and an extensive verification procedure. In addition, an extra section deals with the potential statistical applications of the model and how these relate to 'real world' situations.

The next chapter attempts to bring together the two sides of the study. While Chapters 3 and 4 draw very few conclusions and merely present observations, Chapter 5 compares the experimental results with the predictions of the analytic model.

Finally, Chapter 6 summarizes the findings of this study, criticizes the work and suggests areas of improvement and further study.

Chapter 2

Background

2.1 Introduction

This Chapter, in essence, combines a general introduction into basic meteorology, traffic theory and dispersion modelling with a detailed review of pertinent research. To this end, Section 2.2 introduces the subject of meteorology in a manner not unlike a text-book on the subject would do. However, only those aspects of this wide topic which are relevant to the present study are presented. Section 2.3 then goes on to discuss the aerodynamics of vehicles and their (extreme) capacity to produce pollution. When describing the vehicle-air interaction, this section concentrates on the effects on the air, rather than on the vehicle. The next section, 2.4, is a detailed review of the various full-scale, wind tunnel and analytical studies of vehicle pollution in both the urban and rural environments. The urban street canyon scenario is reviewed in depth, with evidence provided to support the hypothesis that the existing models are lacking in their generality. Then, somewhat pre-empting Chapter 4, a review of the relevant Gaussian puff models is presented. Finally, general conclusions are drawn in Section 2.6.

2.2 Basic Meteorology

As may already be clear, one of the recurrent themes of this thesis is the major effect that the wind has on the movement and dispersion of vehicular pollutant. While there exist excellent treatises on the vast subject of the nature and effects of the wind (for example, Cook [20] and Oke [69]), it is worth covering in some detail those facets of study of the wind which are of relevance to the present study.

2.2.1 The Atmospheric Boundary Layer and Stability

Wind, as we perceive it, can be crudely regarded as the manifestation of a fluid, the air, moving across a rough surface, the earth. The movement is almost exclusively caused by the non-uniform heating of the atmosphere by solar radiation which drives convective flows of air above the surface of the earth. The Atmospheric Boundary Layer (ABL) is the term commonly used to describe the region of the atmosphere in which movement of the air is retarded by the surface. Inside the ABL, the wind speed increases with height up to the free atmosphere speed at an elevation usually referred to as the gradient height, z_g.

The urban ABL, in particular, can be further divided into a number of sub-layers which are described in some detail in Oke [69, pp37-42]. Here we discuss only two of these sub-layers which are relevant to the present study.

Roughness Layer which lies adjacent to the surface and extends from the surface up to a height which is governed by the height of the roughness elements such as buildings, trees and the general topology of the land but may well extend some distance above these. The top of this layer is often refered to as the zero displacement height. In this layer, the mean flow is zero.

Turbulent Surface Layer extends from the top of the roughness layer up to a height of 10% of the atmospheric boundary layer. Here small scale turbulence dominates the transfer of momentum in the vertical direction.

One of the major factors affecting atmospheric dispersion is the level of turbulence in the atmospheric boundary layer. Such are the Reynolds numbers associated with the ABL, that it could be expected to be highly turbulent at all times. However, thermal effects can enhance or diminish the turbulence. Consider a parcel of air as it rises, due to mechanical turbulence caused by the surface roughness. It will experience a steadily decreasing pressure and, if it is moving adiabatically, the parcel will tend to expand and thus cool. The rate at which the temperature of such a parcel would drop is known as the Adiabatic Lapse Rate (ALR) and has a constant value of $-9.8 \times 10^{-3}\,\mathrm{Km}^{-1}$.

This ideal is rarely encountered in the atmosphere. The Environmental Lapse Rate (ELR) which is the gradient of the temperature profile is actually what occurs. It is the relative magnitudes of the ALR and ELR which determine the type of atmosphere at any place or time. There are three possible cases in the relationship between the ALR and the ELR:

Stable Conditions are often encountered over land during clear nights with weak winds. If the ELR is less negative than the ALR, then stable conditions will prevail. In the case where the ELR is positive (*ie* the temperature increases with height), we

say we have an *inversion*. Under these conditions a mechanically displaced air packet will find itself relatively either colder, if displaced upwards, or warmer, if displaced downwards, and will thus tend to move back towards its initial position. Thus, a stable atmosphere is less prone to mechanical turbulence which is effectively damped out by the thermal effects.

Neutral Conditions occur when the ALR and ELR are equal and are symptomatic of the day-night, night-day transitions or heavily overcast skies. In these cases the heating effects of the sun are absent and the insulating effect of the cloud cover tends to damp any temperature stratification. An air parcel under these conditions will move with any turbulent mixing but will not oppose or supplement the motion due to imbalances in buoyancy forces.

Unstable Conditions occur when the ELR is more negative than the ALR. Such a condition is called a strong lapse rate and leads to an unstable boundary layer. Consider a parcel of air displaced vertically by the effects of mechanical turbulence. It will find itself warmer than the surrounding air and so will tend to accelerated upwards. Thus, the turbulence is augmented by the existence of the strong lapse rate. Unstable conditions occur typically during still, hot summer days where the surface is heated by the sun which then emits radiation which heats the air above it and induces the strong lapse rate.

Thus, depending on the conditions a range of stabilities are typically encountered and associated with the differing levels of turbulence. And, as we have seen, these levels of turbulence can also vary considerably with height.

2.2.2 Analytical Description of the ABL

Thus far the overall qualitative nature of the wind environment has been discussed. For the purposes of the present and most other work, a more quantitative description of the wind is required.

Velocity Profile

As with all boundary flows, the speed of the wind in the turbulent surface layer obeys a logarithmic law,

$$\bar{V}_z = \frac{u_\star}{\kappa} \ln \frac{z-d}{z_0} \tag{2.1}$$

where $\bar{V}_z$ is the mean hourly wind speed at a height, z, $u_\star$ is the friction velocity, κ is von Kàrmàn's constant ($= 0.4$), d is the displacement height, and z_0 is the roughness length of the surface. Equation 2.1 is only valid up to a height of, typically, 100 m but the present study stays well below this height. The displacement height, d, is more important

Terrain Description	z_0 (m)	d (m)
City centres Forests	0.7	15 to 25
Small towns Suburbs of large towns and cities Wooded country (many trees)	0.3	5 to 10
Outskirts of small towns Villages Countryside with many hedges, some trees and some buildings	0.1	0 to 2
Open level country with few trees and hedges and isolated buildings; typical farmland	0.03	0
Fairly level grass plains with isolated trees	0.01	0
Very rough sea in extreme storms (once in 50 yr extreme) Flat areas with short grass and no obstructions Runway area of airports	0.003	0
Rough sea in annual extreme storms Snow covered farmland Flat desert or arid areas Inland lakes in extreme storms	0.001	0

Table 2.1: Typical values of terrain parameters z_0 and d, after ESDU 85020 [28].

in the urban situation and corresponds roughly to the top of the roughness layer, although more exact expressions have been suggested, for instance, $0.8\times$mean building height. For very rough surfaces (e.g. city centres), Equation 2.1 will not hold below d where complex flows typically exist. Table 2.1 is copied from ESDU 85020 [28] and shows the variation of z_0 and d over a whole range of terrains. This Table is used in Chapter 3 when deciding on the characteristics of the two boundary layers which are to be generated in the wind tunnel. There are more sophisticated versions of Equation 2.1 such as that of Deaves and Harris [24] which allow the model to be used in the outer reaches of the Ekman layer where the flow is no longer able to be described by a logarithmic law,

$$\bar{V}_z = \frac{u_\star}{\kappa} \ln \frac{z-d}{z_0} + 5.75z' - 1.88z'^2 - 1.33z'^3 + 0.25z'^4$$

where $z' = z - d/z_g$ with z_g again being the gradient height. For our the present investigation which is restricted to the lower reaches of the atmosphere, Equation 2.1 is sufficient.

Turbulence Profile

The reduction in the kinetic energy of the wind in the surface layer manifests itself as turbulence. Cook [20] presents a good description of turbulence as it relates to the wind. In a turbulent flow, each component of the wind velocity is split into a mean or 'steady' component and a turbulent part. For example, the *u*-, or along wind, component of the flow can be written as,

$$u = \bar{u} + u'$$

where the mean value, $\bar{u}$, may well vary over time scales which are large compared to the time scales associated with the variation of the turbulent part, u'. By definition, the turbulent part is unsteady and has a mean of zero. So, in order to gain some measure of the strength of the turbulence, the root-mean-square (rms) value is often used. To add information about the relative strength of the turbulence, it is conventional to divide by the mean hourly wind speed at the measurement height to give the components of *turbulence intensity*, I_i,

$$I_i = \frac{\sigma_i}{V_z}$$

where σ_i is the standard deviation of the components of the wind speed and which is identical to the rms of the turbulence. The work of Deaves and Harris model was developed to give an expression for the *u*-component of turbulence intensity at any height over a uniform flat terrain,

$$I_u(z) = \frac{3\left[1-(z-d)/z_g\right]\left\langle 0.538+0.090\ln\left[(z-d)/z_0\right]\right\rangle^{\left[1-(z-d)/z_g\right]^{16}}}{\ln\left[(z-d)/z_0\right]\left[1+0.156\ln(6z_g/z_0)\right]} \tag{2.2}$$

which describes a general decrease in turbulence with height. Expressions for the *v*- and *w*-components are available (see Cook [20, pp153]) but are not reproduced here.

Turbulence Spectra

Spectral analysis is another commonly used method of gaining an insight into the nature of this complicated turbulence phenomenon. Box and Jenkins [13] is one of the seminal texts on the subject of time series analysis and covers spectral analysis in considerable depth. Basically, spectral analysis of a time series like wind speed, transforms from the time domain to the frequency domain and produces an indication of how much power is associated with each frequency. Figure 2.1 shows a typical turbulence spectrum, plotted in a form often used by wind engineers.

A conceptual model often used to aid understanding of the turbulence and its spectra is the eddy model. This model assumes that a large number of variously sized and oriented circular eddies exist in the mean flow. A low frequency fluctuation implies the passing of a large, slowly rotating eddy, while a high frequency fluctuation is typical of a small eddy passing.

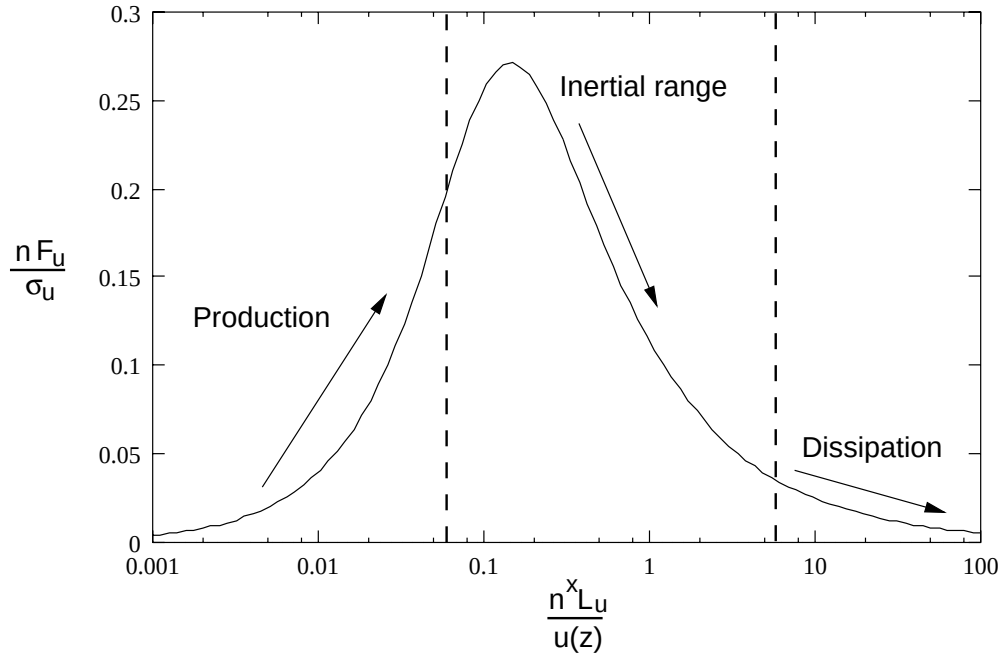


Figure 2.1: Typical von Kàrmàn spectrum (after Cook [20]).

In the production range in Figure 2.1, large eddies are generated from instabilities in the main flow. These large eddies then transfer their energy to smaller eddies as they break up since the eddy is a highly unstable flow structure. These smaller eddies break into even smaller ones and so on, all the time transferring their energy in a cascade known as the inertial range. It is called the inertial range because it is the inertial terms in the equations of motion of turbulent flow that dominate in this process.

Finally in the high frequency dissipation range, the eddies become so small and the viscous stresses so large that the the kinetic energy of the eddies is lost on the molecular scale (as heat).

There exists a great body of experimental data for wind spectra at different heights over a whole range of terrain types. The von Kàrmàn spectral equations (Equations 2.3 and 2.4) are generally regarded as the best description of isotropic turbulence and are here reproduced from ESDU 85020 (1985). Notice that although there are three components of the wind spectra, there are only two equations since the *v* and *w* components have been found to be identical.

$$\frac{nS_{uu}}{\sigma_u^2} = \frac{4n_u}{(1+70.8n_u^2)^{5/6}} \tag{2.3}$$

$$\frac{nS_{ii}}{\sigma_i^2} = \frac{4n_i(1+755.2n_i^2)}{(1+283.2n_i^2)^{11/6}} \tag{2.4}$$

with,

$$n_u = \frac{n^x L_u}{\bar{V}_z} \qquad \text{and} \qquad n_i = \frac{n^x L_i}{\bar{V}_z}$$

where, $i = v$ or w, n is the frequency (in Hz), S_{uu} and S_{ii} are the spectral densities for the three components, ${}^xL_u$ and ${}^xL_i$ are the characteristic[1] length scales of the spectra, and σ_u^2 and σ_i^2 are the variances of the velocity time series. The curve in Figure 2.1 is the von Kàrmàn spectrum for the u-component of the wind velocity.

The characteristic length scale is a rough representation of the size of the eddy which contains the peak power of the spectrum and is a critical parameter when describing a particular wind. Typical values for ${}^xL_u$ fall in a wide range which covers several order of magnitude from 10 m to 1000 m. The values depend largely on the mean wind speed and the height at which the readings are taken. As the measurement height is increased it is found that the length scales increase in a non-trivial manner as the eddies get stretched in the deeper boundary layer.

Autocorrelation Functions

The autocorrelation functions, ρ_{ii}, for gust components at a point can be derived from Equations 2.3 and 2.4 using an appropriate Fourier transform to give,

$$\rho_{uu}(\tau) = 0.5925\,(\tilde{\tau}_u)^{1/3}\,K_{1/3}(\tilde{\tau}_u) \tag{2.5}$$

$$\rho_{ii}(\tau) = 0.5925\,\left[(\tilde{\tau}_i)^{1/3}\,K_{1/3} - 1/2\,(\tilde{\tau}_i)^{4/3}\,K_{2/3}(\tilde{\tau}_i)\right] \tag{2.6}$$

with,

$$\tilde{\tau}_u = 0.747\,\frac{\tau\bar{V}_z}{{}^xL_u} \qquad \text{and} \qquad \tilde{\tau}_i = 0.3735\,\frac{\tau\bar{V}_z}{{}^xL_i}$$

where $K_{1/3}(\tilde{\tau}_i)$ and $K_{2/3}(\tilde{\tau}_i)$ are modified Bessel functions of the second kind, of order $1/3$ and $2/3$ respectively.

These functions, which are closely associated with the spectral equations are used both in the generation of spectra from time series and in the generation of time series from given spectra. Later in this thesis both procedures will need to be followed which explains the inclusion of the autocorrelation functions here.

[1] Also commonly referred to as the integral length scales.

2.3 Vehicle Aerodynamics and Emission Rates

2.3.1 Vehicle Aerodynamics

Aerodynamics is defined as the study of the interaction between a body and the atmosphere through which it moves. Much of the research into road vehicle aerodynamics has concentrated on reducing drag and increasing fuel efficiency. This is understandable because much of the work has been driven by the motor industry who want fast, efficient and safe cars. There are a number of books covering the subject from this standpoint, for example, Scibor-Rylski [81]. The present study, however, is concerned with the pollution from vehicles and must, therefore, look at the aerodynamics of vehicles from the point of view of the air and, in particular, its capacity to mix the exhaust fumes.

The Vehicle Wake in the Absence of Wind

As it travels, a vehicle imparts some of its momentum to the surrounding air. This air forms a turbulent wake behind the vehicle which can often been seen on the street when dry leaves are suddenly picked up behind a passing vehicle and dragged along, often in spiral patterns.

To understand exactly how this wake forms, it is necessary to look at a simplified situation. On a bluff body such as a circular prism, the air-stream will gradually slow down as the body slopes away from the flow. In this case, an adverse pressure gradient will form which will assist the frictional forces in the boundary layer and which will cause the air inside the boundary layer to slow down and eventually move in the opposite direction to the air-stream.

Figure 2.2 from Chadwick and Morfett [16] clearly shows this effect. A boundary layer is still present. However, it is no longer in contact with the cylinder, instead its lower boundary is defined by a line of stationary air (the dashed line in Figure 2.2). In these circumstances, the flow is said to have separated. Since the air is moving in opposite directions either side of the dashed line, there is a local rotation of the air which causes the formation of vortices which will then move away from the cylinder in the general direction of the flow. Thus, at or near the separation point, vortices will be shed in a very haphazard way resulting in the familiar turbulent wake behind the body. It must be emphasized that the formation of the wake is an unpredictable process and, at best, Figure 2.2 shows a snapshot of the phenomenon.

In the discussion above, separation is caused by the velocity variation over a “smooth” bluff body. However, separation often occurs at sharp corners of vehicles: the cabs of lorries are a good example of the type of shape which would induce separation and wake formation. Even features such as wing mirrors and roof gutters can induce separation at

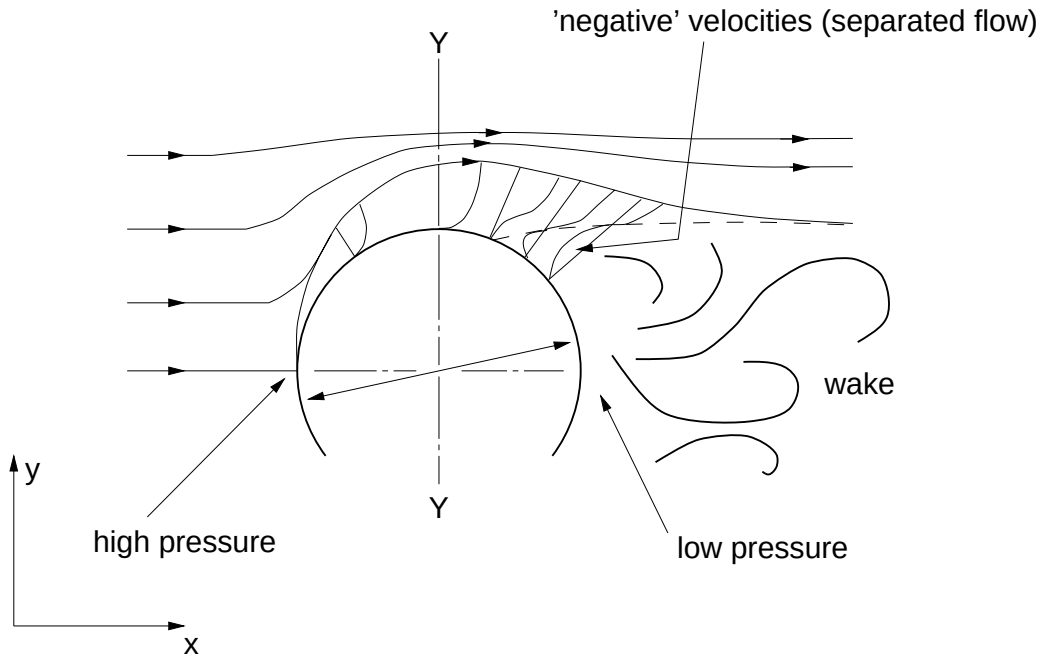


Figure 2.2: Flow separation around a circular prism (after Chadwick and Morfett [16]).

a point nearer to the front of the vehicle.

The point at which the flow moves from being laminar to turbulent is poorly defined and depends largely on the fluid velocity and the geometry of the problem in question. The Reynolds Number, Re, is defined as,

$$\mathrm{Re} = \frac{ul}{\nu}$$

where u is the fluid velocity, ν is the kinematic viscosity and l is a typical length scale associated with the flow. Generally speaking, the onset of turbulent occurs above some critical range of values. For example, for commercial pipelines, the flow is almost certain to be turbulent when $\mathrm{Re} > 4000$.

The nature of the wake of a vehicle is therefore a very complex matter and one of the first attempts to investigate it was that of Hunt [52] who was looking, from a strictly theoretical standpoint, at the wake of a surface mounted 2D body in a laminar boundary layer. He found that the velocity deficit in the object's wake was related to the couple on the object and not to the drag as had been found previously for similar bodies in uniform approach flow. Counihan *et al* [21] took Hunt's work one step further, moving from the laminar to the turbulent case. Again this work was concerned with surface mounted objects - no mention was made at this stage by Counihan or his co-workers, one of whom was Hunt, about the application to vehicles.

The obvious extension to vehicle wakes was made several years later. Building on Hunt's

previous work, Eskridge and Hunt [30] developed a theory for the velocity deficit in the wake of a vehicle in still air using a variation on the perturbation analysis which Hunt had used previously. The following observations can be drawn from the paper. With reference to Figure 2.3, the height of the wake, h_w, and the maximum velocity deficit therein, $(u_w)_{\max}$, are given by the expressions,

$$h_w = \gamma_w A h \left(\frac{s}{h}\right)^{\frac{1}{4}} \qquad (u_w)_{\max} = UA\left(\frac{s}{h}\right)^{-\frac{3}{4}} \tag{2.7}$$

where s is the distance behind the vehicle, U is the vehicle's speed, h is the height of the vehicle, γ_w is a constant and A is the cross-sectional area of the front of the vehicle. Qualitatively it can be seen that the maximum wake velocity decreases with distance downstream of the vehicle, while the wake height increases - both observations which appear to be intuitively correct. Eskridge and Hunt were able to further expand on the expression for the velocity deficit using similarity theory to produce the following expression for the velocity at any point in the wake,

$$u_w = CU\left(\frac{s}{h}\right)^{-\frac{3}{4}} \zeta \exp\left\{-\frac{(\zeta^2+\eta^2)}{8}\right\} \tag{2.8}$$

where C is some constant introduced for clarity, $\eta = y/h_w(s)$ and $\zeta = z/h_w(s)$. Similar expressions were derived for the components of the turbulence in the wake.

It should be emphasized that the above arguments hold only in the far wake region, some 15 vehicle heights downwind of the vehicle. The turbulent structure of the near wake is ignored in the analysis of Eskridge and Hunt. Complex effects such as the maintenance of "horseshoe" vortices and separation bubbles are beyond the scope of the above theory. In addition, the shape of vehicle plays an important rôle in the formation of the wake, both in the near and far wake regions. For example, Ahmed *et al* [2] conducted extensive wind tunnel studies of the wake of a saloon-shaped vehicle with various rear ends. By varying the angle of slant of the rear end they were able to show that this had a significant effect on the structure of the wake in the near field. The front of the vehicle they used was rounded to delay separation so as to reduce the effects of the front of the vehicle on the wake structure. The sharp angled fronts to lorries and trucks result in early separation and create different wakes to the streamlined models of Ahmed *et al*.

The Influence of the Wind

In the previous Section the movement of the vehicle was entirely responsible for any interaction between itself and the surroundings. It would be nice to believe that conceptually a vehicle moving at 20 ms^{-1} into a headwind of 10 ms^{-1} is the same as a vehicle traveling through still air at 30 ms^{-1}.

However, when considering real situations it is necessary to include the effects of the wind on the wake. Hider [45] has recently looked at the case of a vehicle moving into

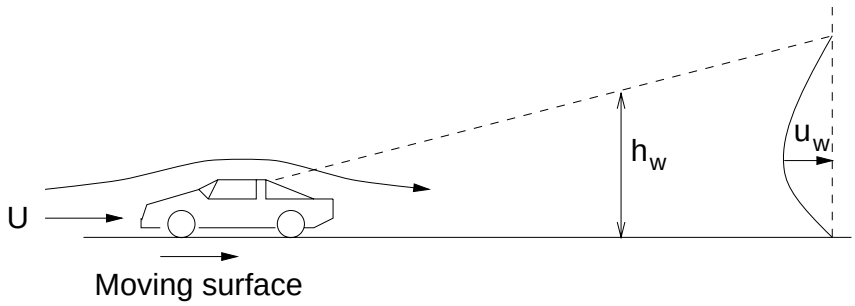


Figure 2.3: Schematic of the situation modelled by Eskridge and Hunt [30].

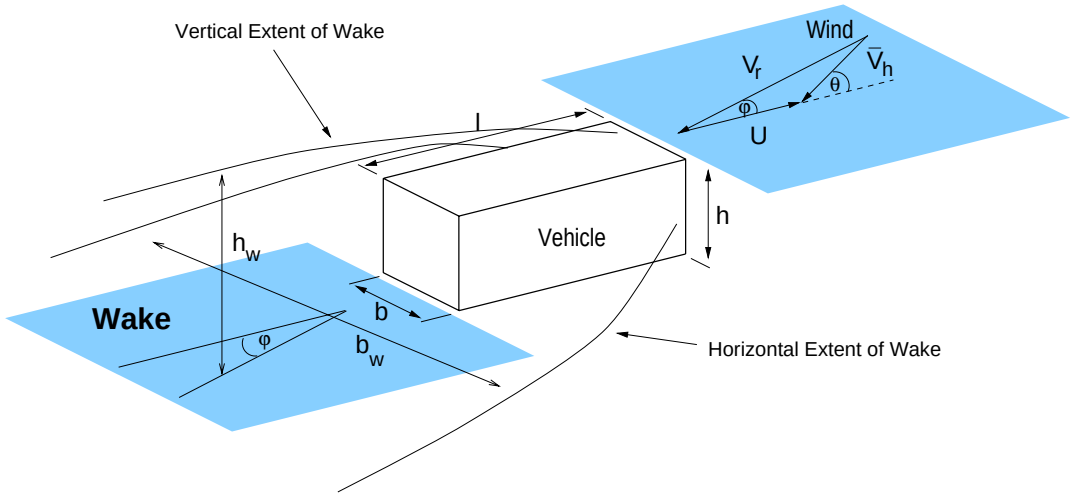


Figure 2.4: Velocity vectors for a vehicle moving in a cross wind.

a shear layer with a power law profile of the form $1/z^2$. While by no means a realistic boundary layer profile, by working the profile into the original Eskridge and Hunt theory, she found that Equation 2.8 needs to be modified by adding extra terms in ζ. The extra terms serve to 'flatten' the wake by concentrating the velocity deficit in a region closer to the ground.

The wind becomes of even greater importance when not aligned along the vehicle's line of travel. Side winds can cause vehicles to overturn or swerve dramatically - see, for example, Baker [5]. Side winds also skew the wake behind the vehicle and thus effect the path of any exhaust fumes emitted.

In order to put what follows into context, Figure 2.4 shows the various velocity vectors for a vehicle moving at speed U into a cross wind whose speed, $\overline{V}_h$, is given at the height of the vehicle, h. The angle between the wind and the direction of travel is θ. The resultant wind velocity, V_r, acts along a line which makes an angle, ϕ, the yaw angle, with the direction of travel.

In a recent conference paper, Baker [7] outlines a method of dealing with side winds which is at the same time both a simplification and extension of the work done by Eskridge and Hunt. In the paper, Baker took the experimental and theoretical evidence presented in Eskridge and Thompson [32] and distilled the following. In shear-free flow, as we have seen above, the velocity deficit in the wake decays as $s^{-3/4}$ whereas in sheared flow, this is found to be more like $s^{-3/2}$. These two extreme cases can be readily equated to the cases where $U \gg \bar{V}_h$ and $U = 0$, respectively. Similarly, the height of the wake varies with $s^{1/4}$ and $s^{1/2}$ in the two cases.

From this data and the frame of reference setup in Figure 2.4, Baker was able to describe the wake in the following terms,

$$\frac{u_w}{V_r} = \left(\frac{s}{h}\right)^m \tag{2.9}$$

$$\frac{h_w}{h} = \left(\frac{s}{h}\right)^n \tag{2.10}$$

$$\frac{b_w}{b_e} = \left(\frac{s}{h}\right)^n \tag{2.11}$$

where u_w, h_w and b_w are the velocity deficit, height and width of the wake respectively. The effective width of the vehicle, b_e, is given by the following expression,

$$b_e = l\sin\phi + b\cos\phi$$

where l is the length of the vehicle. Based on the data gleaned from Eskridge and Thompson, the following expressions for m and n are obtained,

$$m = -\frac{3}{4}\left(1+\frac{2\phi}{\pi}\right) \tag{2.12}$$

$$n = \frac{1}{4}\left(1+\frac{2\phi}{\pi}\right) \tag{2.13}$$

which assumes a linear variation between the two extremes of, on the one hand, a stationary vehicle and, on the other, a very fast one. Although Equation 2.9 does not describe the variation of the velocity deficit across the wake, as Equation 2.8 does, the above equations are consistent with the Eskridge and Hunt formulation.

Hider [45] uses a similar approach in the derivation of a modified form of the full Eskridge and Hunt equations in the presence of a cross-wind. By transforming into a coordinate system based on the centreline of the wake, she was able to again modify the Eskridge and Hunt equations for the wake velocity deficit. In broad terms, the wake is found to rotate about the vehicle but in a more complex way than that described by Baker's equations above.

One of the obvious extensions to the work of Eskridge and Hunt for the single vehicle case was to extend the model to look at multiple vehicles traveling in a train. This they did in the same paper of 1979 (Eskridge and Hunt [30]). They assumed that the wakes

of individual vehicles were independent of the other wakes and that the total effect of a number of vehicles passing a point is equal to the sum of the effects of all the vehicle wakes. It should be noted that these assumptions are for a slight side wind, in which case the wakes will be skewed behind the vehicle in any case. In the absence of wind it is difficult to see the effect of the wake from the vehicle in front being anything other than a second order effect at a point in the trailing vehicle's wake.

2.3.2 Vehicle Emissions

In order to emphasize the magnitude of the problems associated with vehicular emissions, there follows a brief description of some of the more potent chemicals contained in the mix of gases and particles which are emitted by the typical vehicle exhaust. Much of this information is taken from Read [77] which a summary of a symposium held on the effects of vehicle pollution on health.

Carbon Monoxide is formed from the incomplete combustion of hydrocarbons. Ninety percent of all CO in the UK is produced by vehicles. Emissions of CO are highest at low speeds and decrease to a minimum at about 75 km hr^{-1} and then start to increase again. From the pathological point of view, relatively high levels ($\approx$ 0.3% by volume) cause death in half an hour while lower levels effect the mental abilities of driver and pedestrians alike.

Oxides of Nitrogen include NO and NO_2, the former being produced in far more abundance by vehicles than the former. However, NO rapidly oxidizes to NO_2 which destroys lung tissue with the obvious negative implications for asthmatics. Rates of emission remain level at low vehicle speeds and rise significantly as the vehicle speeds up.

Ozone is formed on hot sunny days from nitrogen oxides and volatile organic compounds. Ozone irritates the eyes and air passages which can trigger asthma attacks. Surprisingly, high levels tends to occur over rural rather than urban areas because of the complex processes which govern its production and annihilation.

Volatile organic compounds (VOCs) of many types are present in vehicle exhaust gases - although they tend to manifest themselves on filling station forecourts. Benzene, a known carcinogen, is perhaps the best known of these VOCs.

Lead is becoming less of a problem with the introduction of lead-free petrol[2] but is still present in significant quantities. Perhaps the reason lead-free petrol became so popular in the last five years is because lead impairs the normal intellectual development of children.

[2]There is evidence that lead-free petrol is not necessarily 'greener' and produces other of the harmful chemicals in higher concentrations than leaded petrol.

Particulates have emerged in recent years as a public health issue because of their adverse effects on the respiratory system and the heart. Monitoring points in London have shown that concentrations of particulate matter are 2 to 3 times higher at roadside that at urban background sites. However, since this investigation is concerned mainly with conservative tracer pollutants, particulates are mentioned only in passing.

Notice that in the above list, some emphasis was placed on the relationship between the rate of emission of the various pollutants and the speed of the vehicle. Most of the observations made in the above list were qualitative in nature. Many national motoring research bodies have conducted research into the relationship between emissions, speed and acceleration. It seems that each national body has its own so-called driving cycle - a series of manoeuvres designed to mimic typical urban or out-of-town driving conditions. In Japan, for instance, there are eight categories of vehicle type. In each categories there are further subdivisions depending on engine and fuel types. Karim and Matsui [58] reproduced several polynomials relating NO_X emission to vehicle speed for the eight vehicle types. For example, a passenger car with an engine capacity of less than 660 cc outputs pollutants at a rate of,

$$r = 0.1851 - 0.00143v + 4.47 \times 10^{-5}v^2 + 1.12 \times 10^{-10}v^3$$

gm km^{-1}vehicle^{-1} where v is the vehicle speed. This demonstrates the size of the problem. Data does exist which links the fuel consumption to engine speed and torque for a number of engines such as the Ford 2.5 litre DI Diesel engine (Stone [85, page 193]). However, once the engine is put inside vehicles with different aerodynamic characteristics, gear ratios and drivers, this data is no longer useful. Thus, it is very difficult to relate vehicle emissions to the speed of the vehicle.

Recently, Hickman [44] has published the results of emission tests from 150 cars which drove collectively more than 70 000 km in six cities. From this data he was able to ascertain that not only was there strong link between emissions and speed but also that the acceleration of the vehicle was of similar importance. Figure 2.5 shows this relationship - the plot was constructed from a graph of Hickman's data which was thought not to demonstrate the link quite as clearly[3]. Note that Hickman looked only at the oxides of Nitrogen in his study - the other chemicals in the above list will have different speed/acceleration footprints.

Having dealt with the emissions from vehicles in terms of their content and production rate, discussion of how they disperse in the environment will be held back until Sections 2.4.2 and 2.4.3.

[3]There is some uncertainty about the units of acceleration which were not made clear in Hickman's article. However, the numbers generated by his data suggest ms^{-2}.

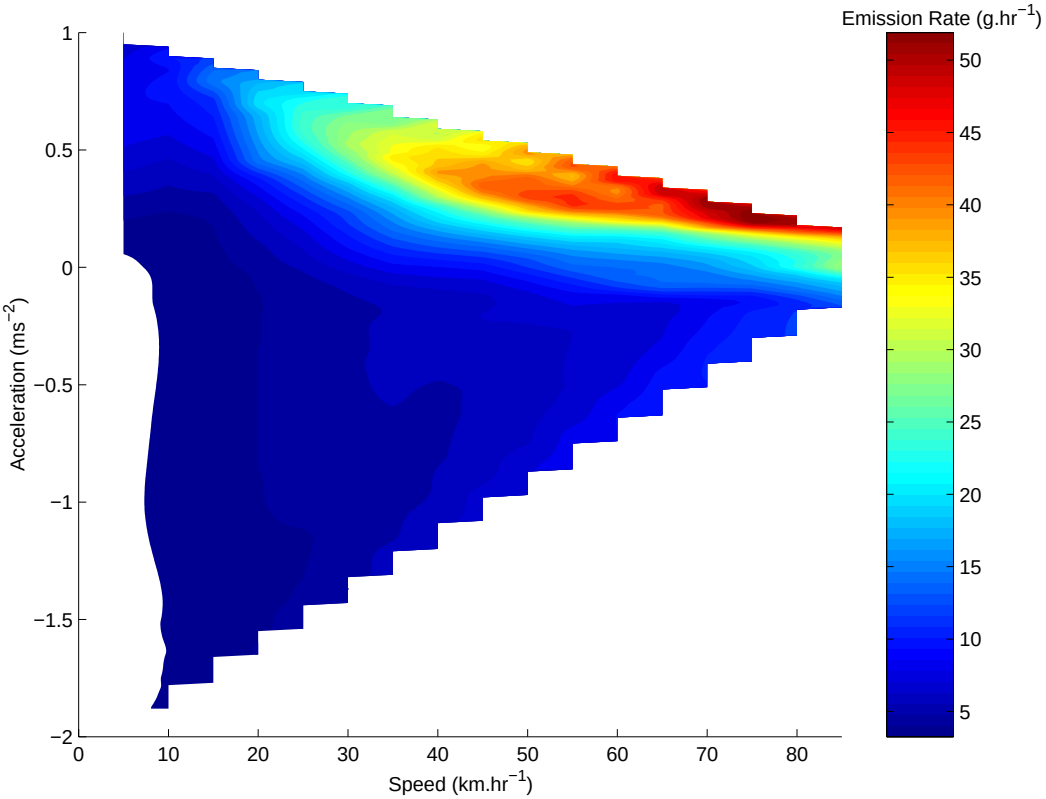


Figure 2.5: Nitrous oxides from petrol cars as a function of speed and acceleration (after Hickman [44]).

2.3.3 Traffic Models

Traffic models can, for our purposes, be broken into two types: statistical and deterministic. The former deals with the gross properties of the traffic such as density, average speed and flow rates. For a full treatment of this particular approach, see Salter [79]. There follows a brief synopsis of the more important concepts of the statistical approach.

As just mentioned, the three characteristics of traffic flow of concern are speed, defined as the space mean speed; the density, defined as the number of vehicles per unit length of highway; and the flow, defined as the number of vehicles passing a given point on the highway per unit time. Consider a short section of highway of length L in which N vehicles pass a point in the section during a time interval T, with all the vehicles traveling in the same direction. It can be shown that,

$$\begin{array}{lll} \text{The flow rate,} & Q & = N/T \\ \text{The density,} & D & = N/L \\ \text{The mean speed,} & S & = \text{flow/density} \end{array} \tag{2.14}$$

For instance, one of the earliest researchers in the field, Greenshields [35], found a linear relationship between speed and density on the rural roads of Ohio,

$$\bar{V_s} = \bar{V_f} - \left(\frac{\bar{V_f}}{D_j}\right) D \tag{2.15}$$

where $\bar{V_s}$ is the space mean speed, $\bar{V_f}$ is the space mean speed for free flow conditions and D_j is the jam density (*ie* the density of traffic in a stationary traffic jam). So there is a range of velocities from the highest when the cars are far enough apart not to affect each other, the free flow condition, to the other extreme of stationary vehicles in a jam.

In addition to these three main descriptors of a particular traffic pattern, there are two further parameters which are useful: the time headway, defined as the time interval between the passage of two successive vehicles; and the space headway, similarly defined as the distance between two successive vehicles.

The other type of approach is the deterministic approach. Here, the individual vehicles are modelled explicitly, each one following its own set of guidelines. Over the years these models have become very sophisticated - even modelling the psychological behaviour of the drivers. One of the earliest was a simple 'follow-the-leader' model by Helly [39] which was used to simulate bottlenecks in single lanes of traffic. Basically in a 'follow-the-leader' model, the speed and acceleration of a vehicle depend on its distance from, and relative speed to, the vehicle in front. For a more detailed description of Helly's work see Section 4.2.2.

2.4 Dispersion of Vehicular Pollutants

2.4.1 General Dispersion

Before going on to discuss the two specific scenarios of relevance to this study, it is worth discussing the basics of pollution dispersal. Much of the theory presented here concerns an elevated point source (*ie* a chimney). The most popular technique in this case is the Gaussian Plume Method which assumes that the pollutant spreads in such a manner that the pollutant maintains a Gaussian distribution across the plume. Mathematically, this can be expressed as follows for an instantaneous release of pollutant at a point $(0,0,H)$ in a wind with mean velocity, u, directed along the x-axis,

$$\begin{aligned} c(x,y,z,t) &= \frac{Qt}{(2\pi)^{\frac{3}{2}}\sigma_x\sigma_y\sigma_z}\cdot\exp\left\{-\frac{(x-ut)^2}{2\sigma_x^2}\right\}\cdot\exp\left\{-\frac{y^2}{2\sigma_y^2}\right\} \\ &\quad \cdot\exp\left\{-\frac{(z-H)^2}{2\sigma_z^2}\right\}\cdot\exp\left\{-\frac{(z+H)^2}{2\sigma_z^2}\right\} \end{aligned} \tag{2.16}$$

where c is the concentration, Q is the emission rate, and σ_x, σ_y and σ_z are the rms dispersions (or dispersion parameters) and are functions of time and are generally not equal in turbulent diffusion. At distances close to the source, σ_i vary according to,

$$\begin{aligned} \sigma_x &= \sigma_u t \\ \sigma_y &= \sigma_v t \\ \sigma_z &= \sigma_w t \end{aligned} \tag{2.17}$$

where σ_u, etc. are the standard deviations of the turbulent components of the wind. Notice that in Equation 2.16 there are two terms in z. The first term corresponds to the direct "line of sight" contribution from the stack, the second is from the so-called image source which takes into account the reflection of the plume in the ground. This is equivalent to there being a second source at a height $-H$ underground.

Csanady goes on to show that under the above conditions (Equations 2.17), Equation 2.16 can be written as,

$$c(x,y,z) = \frac{Q}{2\pi\sigma_y\sigma_z u}\cdot\exp\left\{-\frac{y^2}{2\sigma_y^2}\right\}\cdot\exp\left\{-\frac{(z-H)^2}{2\sigma_z^2}\right\}\cdot\exp\left\{-\frac{(z+H)^2}{2\sigma_z^2}\right\} \tag{2.18}$$

where Q is the release rate. The major challenge when creating a Gaussian model of atmospheric dispersion is to correctly define the dispersion parameters. Notice, also, that a major failing of the Gaussian Plume Method occurs in instances of zero wind - the denominator of Equation 2.18 tends to zero. To overcome this and other problems, the Gaussian Puff Method was developed - see Section 2.5.

Further complications arise in real winds because of the various stability conditions which can occur. These were discussed previously in Section 2.2.1 and fall into three

categories: stable, neutral and unstable. Figure 2.6 shows a variety of different plume configurations which can result from various atmospheric stability types. We will briefly discuss each in turn:

Looping occurs in conditions of strong instability. The large eddy structures advect the plume rather than dispersing it. Consequently the plume follows the eddies while at the same time moving on average with the mean wind speed.

Coning occurs in near neutral conditions often characterized by strong winds. In these conditions, the plume is advected by the mean wind speed and the actions of the mechanical turbulence on a relatively small scale tend to disperse the plume in the classic Gaussian manner.

Fanning occurs in very stable atmospheres. Turbulent mixing is suppressed and the plume is given very little opportunity to disperse vertically but does spread significantly in the horizontal plane.

2.4.2 Dispersion - The Rural Case

The terminology “rural” is introduced at this stage because of the need to differentiate between the two scenarios under investigation. In what follows we will assume the absence of obstacles such as buildings or trees. This review of a large field of research will be limited and will concentrate mainly on the work of Eskridge, Rao and their respective co-workers.

Full Scale Studies

In late 1975, General Motors conducted a notable full-scale investigation of pollution dispersion and wind fields near an actual roadway. Although extensive descriptions of the experiment can be found in Eskridge and Hunt [30] and Eskridge *et al* [29], the most useful paper is by Chock [17], one the members of the experimental team.

In summary, a fleet of automobiles, numbering in excess of 350, were driven up and down a 10 km highway on the mornings of 17 days. The site was described as “rather flat” in the vicinity of the highway and was covered by medium length grass - a good approximation to open countryside. A series of towers either side of the road were equipped with anemometers, thermometers and syringe samplers at various positions along their length. The syringe samplers were used to collect samples of air which were polluted not only by the automotive emissions but also by a tracer gas, SF_6, which was released by trucks positioned near the centre of each passing convoy. Thus, a whole range of local flow and pollution data was made available from this experiment.

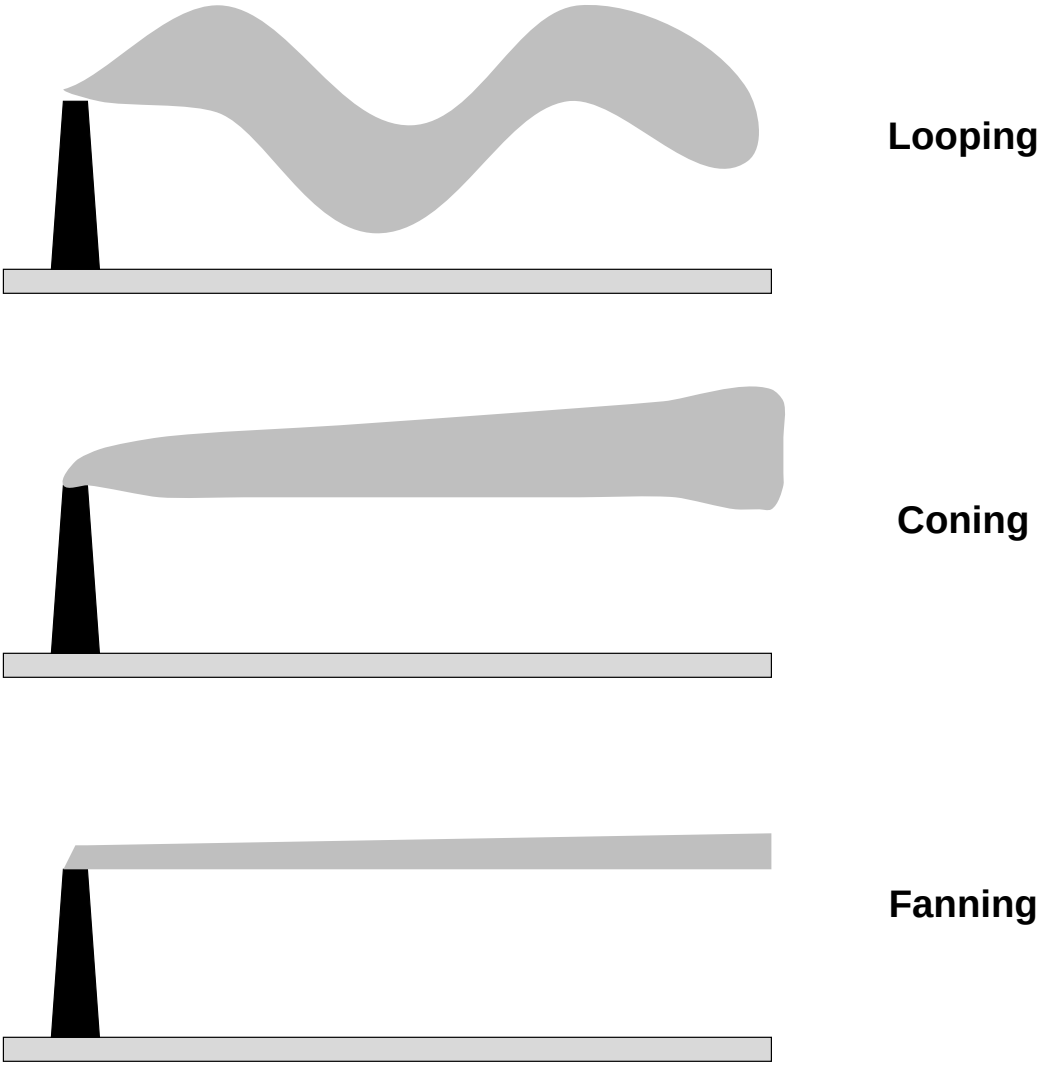


Figure 2.6: Plume patterns in different atmospheric stability situations.

In general, Chock and his co-workers found that the highest concentrations were observed at the foot of the nearest tower to the roadway. As the plume expanded downwind, concentrations at the higher levels increased while those at lower levels decreased - the plume was expanding upwards due to the buoyancy of the heated exhaust gases. For low wind speeds it was found that the plume was not expanding as predicted by the Gaussian theory. The traffic-induced turbulence close to the road was thought to be forcing the pollutant away from the road at a greater rate than expected and it was suggested that some kind of wind speed correction factor was required to account for this effect. Indeed, at distances up to 100 m from the road, the traffic-induced turbulence dominated the stability-induced mixing. This has certain implications in urban canyon which are generally of much smaller dimension than this.

While the GM experiment was somewhat of an idealized situation, another study, that carried out next to the Long Island Expressway in suburban New York (Rao *et al* [76]), was set in a real context. A heavily trafficked section of the Expressway was chosen with the minimum of surrounding buildings. The aim of the experiment was to glean as much information as possible about the turbulence structure close to the highway. In addition, temperature and concentration readings were taken at a number of positions on the towers that were erected either side of the road.

In summary, they found that the turbulent kinetic energy in the vicinity of the road was increased dramatically by the presence of the vehicles. The dominant frequency for the turbulence was in the range 0.1-1.0 Hz, corresponding to an eddy size of several metres. The effect of the slipstream of the passing vehicles was significant as far as 37 m from the road. This was characterized by an acceleration in wind speed in the lowest 8 m in cases were the wind direction was nearly parallel to the road.

Wind Tunnel Studies

The wake theory developed by Hunt and carried forward by Eskridge required some experimental validation. To this end, Eskridge and Thompson [32] performed a rather complicated wind tunnel experiment in which a scale block-shaped obstacle (representing a vehicle) was suspended just above the moving floor of the wind tunnel. The idea behind the conveyor belt floor was to generate a shear-free approach flow resulting in a situation exactly equivalent to a vehicle moving into still air. Velocity measurements were made in the wake of the obstacle using X-configured hot-film anemometers at frequencies up to 100 Hz. The velocity deficit in the wake exhibited a strong shear layer near the moving surface, while the wake itself did not have the self-preserving form assumed by much of the theory of Eskridge and Hunt.

This same experimental set up was used later to determine turbulence mixing parameters by releasing ethylene into the wind tunnel. Eskridge and Rao [31] describe how a Flame Ionisation Detector (FID) was used to measure the concentration of gas. Lateral profiles of tracer concentrations were taken at various distances downstream of the vehi-

cle (all the distances were greater than 30 vehicle heights). The extent to which the gas had dispersed gave the investigators an idea of the level of turbulence in the wake. By conducting a sensitivity study on both the wind tunnel data and the ROADWAY model (to be described in the next section), they were able to test the importance of various length scales on the dispersion process. As a result they were able to modify the original ROADWAY model in light of this new data.

Analytical Models

A Gaussian Plume model of the dispersion of vehicular pollution from a roadway was developed in the early 1970s by the Environmental Protection Agency in USA. The model, variously called EPA-HIWAY or HIWAY, is first referred to in Zimmerman and Thompson [91], a report which the present author has not been able to obtain. However, a later paper (Rao and Keenan [75]) which suggests improvements to the original model contains much of the relevant details. The original HIWAY model was found to have several drawbacks including the lack of a decent description of the near wake dispersion due to the turbulence caused by the passing vehicles. Rao and Keenan's paper includes a regression analysis of the GM data which is then used to justify their modifications to the model.

Eskridge *et al* [29] developed a pollution dispersion model (which was subsequently to be named ROADWAY) based around the wake theory developed in Eskridge and Hunt [30]. Using a modification of the original wake theory in which the wake coordinate system was rotated due to the cross wind to generate the flow field, it was possible for them to model the dispersion of pollutant from a lane of traffic. A finite difference solution of the conservation of mass equation for a tracer was solved using finite differences. Chief among the uncertainties in this approach was the specification of the dispersion parameters and they attempted to gain some insight into their values by comparing with the GM Motors experimental data. The model performed better in the comparison than the EPA-HIWAY model.

The one fact that recurs in the above brief review is that the turbulence from the movement of the vehicles is by far the dominant process for mixing close to the lanes of traffic. It follows that in the enclosed case of the urban street canyon, which will be discussed next, the vehicle induced mixing is bound to play an important rôle.

2.4.3 Pollution Dispersion - The Urban Case

The geometry of the typical urban environment is complex, confusing and unpredictable. It follows that airflow patterns in such assemblies of roads and buildings will be dependent on the local infrastructure and meteorology. Indeed, many of the full scale and wind tunnel studies which are now to be discussed have concentrated on specific lo-

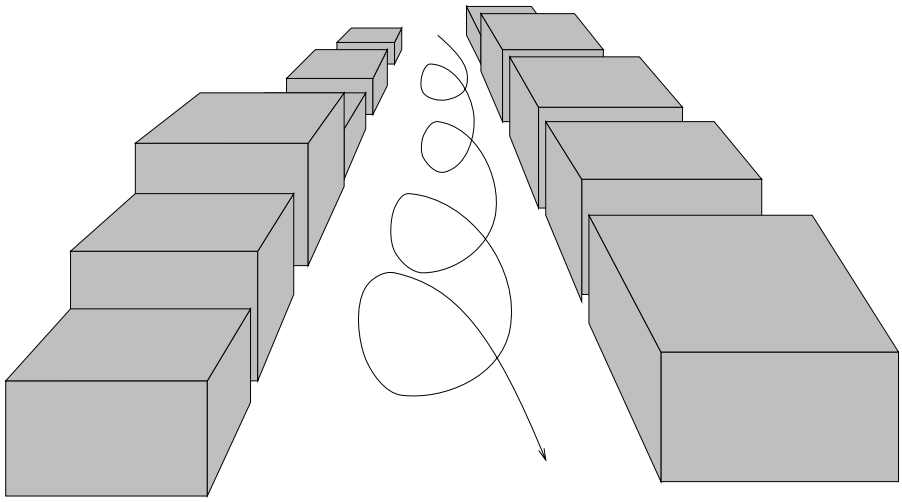


Figure 2.7: Representation of an typical street canyon.

cations, often situated in the locale of the institute involved in the research. However, the areas for the studies tend to have one thing in common - they have within them an urban street canyon such as that shown in Figure 2.7. Simply stated, this is a reasonably straight stretch of urban road, on each side of which are two rows of buildings which form the canyon. Depending on the angle the wind makes with the road, complex vortex patterns may exist inside the canyon with obvious consequences for the mixing of the pollutant released from the vehicles on the road. From the point of view of pedestrian health (if not comfort), it would be preferable if the noxious gases could be flushed from the canyon by the resident airflow.

Before embarking on the literature review, it is useful to introduce some terminology associated with the various flow regimes in street canyons. With the wind perpendicular to the axis of the canyon, Oke [69] used the following terms to describe the flows found in canyons of increasing aspect ratios:

Skimming flow occurs in very tall, thin canyons with aspect ratios $H/W > 1.0$. The above roof flow is hardly diverted into the canyon at all but nonetheless a vortex is induced in the canyon. This type of flow is often encountered in city centres.

Wake Interference flow occurs for slightly wider canyons in the range $0.25 < H/W < 1.0$. Here flow is highly oscillatory in nature with the flow alternating between a vortex and a flow in which the upstream building wake is affected by the downstream building.

Isolated Roughness flow occurs when the spacing between the buildings is large, $H/W < 0.25$. In this case, the wind profile will partly re-establish itself after the upstream building and will then induce a flow against the above roof wind near the windward wall of the downstream building. The flow patterns downstream of the first

Figure 2.8: Types of flows within street canyons (after Oke [69]).

building are not too dissimilar from those seen with an isolated building, hence the terminology.

All three flow regimes can be seen in Figure 2.8 which was taken from Oke's book and shows (a) isolated roughness flow, (b) wake interference flow and (c) skimming flow.

Full Scale Studies

Such is the complex nature of the street canyon dispersion problem that it has been driven largely by experiment, with theoretical models being fit to the available data. Some of the earliest field studies were performed in Frankfurt am Main by Georgii, Busch and Weber [34] and by Dabberdt *et al* [23] in San Jose and St. Louis. Also reported around that time are results from a further study in San Jose at an intersection (Johnson *et al* [57]). They found that the wind direction at the roof level determined the Carbon Monoxide concentrations in the canyon more than any other factor (time of day, etc.). Further, they reported the expected inverse relationship between the wind speed and the concentration. The concentration was also found to decrease with height in the

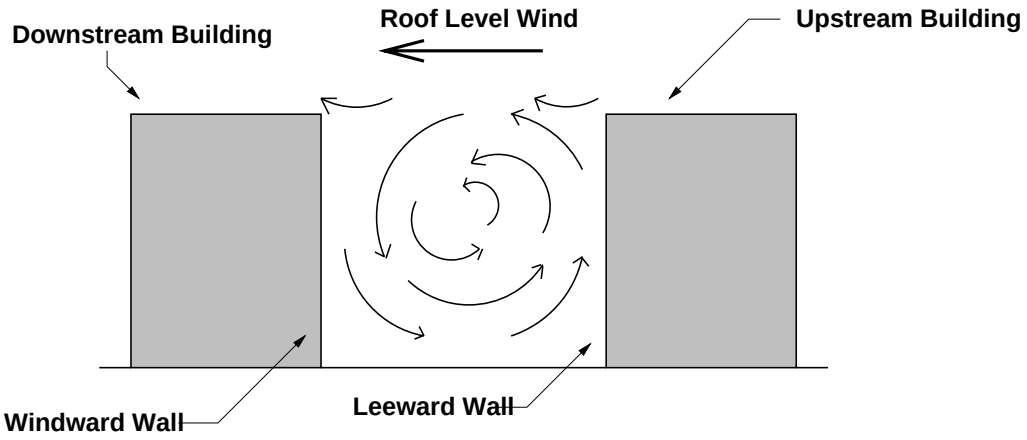


Figure 2.9: A typical transverse vortex in a street canyon.

canyon. This decrease was more pronounced on the leeward wall[4] of the canyon with a more uniform, but on average lower, concentration profile found on the windward wall. This was evidence, they suggested, for the existence of a vortex of the kind shown in Figure 2.9 in the canyon.

More recent studies have included De Paul and Sheih [25, 26] in which both the flow field and pollutant retention times were studied in some detail. The flow field in a street canyon in Chicago was visualized by releasing counter-weighted helium balloons into the street and following their paths using photographic techniques. There was strong evidence to show that a vortex existed in the canyon for ambient normal wind velocities above the range 1.5 to 2.0 ms^{-1}. They found that a large downdraft existed on the downwind (windward) face and that a uniform updraft was present on the upwind face. De Paul and Sheih went on to describe a tracer experiment in the same street canyon in which they looked at the typical retention times of pollutant in the canyon. They were able to characterize the canyon by means of a vertical ventilation velocity, V_v, which was responsible for the entrainment of the pollutant from the top of the canyon. Typical values for V_v were found to be 0.15 to 0.8 ms^{-1} for wind speeds ranging from 1.7 to 4.5 ms^{-1}.

One of the most comprehensive studies of the turbulence and air speed in an urban street canyon was conducted by Rotach [78]. Using a complex array of sonic and cup anemometers, wind vanes and thermometers, he was able to gather large amounts of data in a typical Zürich street. Although he was concentrating mainly on the region above roof level, there is evidence to suggest that the turbulence increased towards the lower part of the canyon. However, such was his experimental set-up, which consisted of a bridge across the road onto which anemometers were mounted, he was unable to take measurements below about 5m - well above the traffic. As such, Rotach's results

[4]With reference to Figure 2.9, the leeward wall is the wall of the upstream building, while the windward wall is the wall of the downstream building and faces towards the flow.

provide limited help to the present study.

As an interesting aside, a small scale urban canyon was built on the roof of the National Building Research Institute at Technion, Israel. Swaid [86] used this scale model of a street canyon to look primarily at heating effects in the canyon. She was able to glean certain information about the flow patterns in the model canyon which agreed qualitatively with much of the work described above. Indeed, a comprehensive discussion of the effects of varying canyon aspect ratios is presented in her paper.

Wind Tunnel Studies

One of the earliest relevant studies was conducted by Hoydysh *et al* [51] in a wind tunnel at New York University. Chief amongst their concerns were the degree to which the extent of the model and the wind speed have on the wind field and pollutant distribution in several idealized urban configurations. The second of their configurations was a two-dimensional experiment which involved a number of bars which spanned the width of the tunnel and which were intended to mimic a series of street canyons. In the course of these experiments they observed all the classic street canyon characteristics, including the higher leeward wall concentrations. Perhaps the most significant result, though, and one on which subsequent studies would rely, was that the minimum wind speed criterion was described by, $R_e > 3400$ where, R_e is the Reynold's number based on the canyon height, H, and the free stream velocity, u_{ref}. This result was based on the concentration profiles collapsing down as the wind speed was gradually increased.

Hoydysh and Dabberdt [49] conducted a series of experiments in an atmospheric boundary layer wind tunnel. In particular they looked at the effect on tracer dispersion of varying the heights of the leeward and windward buildings. Street level concentrations on the leeward side were found to be about twice those on the opposite side (for the canyon with equal sized buildings on both sides). For the leeward face, it was found that the concentration profile could be represented by the equation,

$$C^* = a_r \exp\left\{\frac{b_r z}{H_{\text{up}}}\right\} \tag{2.19}$$

where C^* is the normalized concentration; a_r and b_r are regression coefficients which depend in a very complex way on θ, the angle between the wind direction and the axis of the street; and H_{up} is the height of the upwind building. The existence of a vortex in the street was confirmed by studying the trajectories of small bubbles which were released into the the canyon. Most bubbles were seen to exit via the top of the canyon on, at most, the third rotation in the vortex.

Later, Dabberdt and Hoydysh [22] performed further investigations in an atmospheric boundary layer wind tunnel on a scale model of an idealized urban environment consisting of an orthogonal street/avenue configuration typical of many American cities. While both rectangular and square blocks were used in the experiment, it is only the former

which is of interest here since the present study concentrates on isolated street canyons. For flows perpendicular to the canyon, they confirmed the presence of the higher concentrations on the leeward side of the street with the associated greater rate of decrease with height than on the windward side. When the wind direction was parallel to the street, the concentration contours on both sides of the canyon were found to be parallel to the ground. They also showed that a significant contribution to the total concentration in a canyon in such an environment is due to leakage from adjacent canyons; a point they discuss further in [50] which looks at concentration distributions around intersections. Importantly, though, they reported that from time to time, the entire contents of the canyon were purged by strong gusts of wind.

Yamartino and Wiegand [89] describe an atmospheric boundary layer wind tunnel study of Bonner Strasse in Cologne which was conducted by Builtjes [14]. This produced several notable results:

- A vortex is present in the canyon for winds ranging from perpendicular to the canyon right down to angle of about 10° from the parallel.
- The axial component of the flow exhibited a simple $U\cos\theta$ relationship, where U is the above roof wind speed and θ is the angle between the wind direction and the street.
- They identify a breakdown in the vortex pattern from time to time which may be similar to the purging effect described later by Dabberdt and Hoydysh [22] (see below).

Moriguchi and Uehara [66] looked at a whole range of road and building configurations in an atmospheric boundary layer wind tunnel at the National Institute for Environmental Studies, Ibaraki, Japan. They used ethane (C_2H_6) as a tracer and used a hydrocarbon analyzer to continuously monitor concentrations. An urban canyon was included in the configurations studied which also included a roadway in open country, an open cut roadway and various elevated roadway situations. They found that apart from the obvious fact that the elevated roadway dispersed pollutant most effectively, the concentrations inside the street canyons displayed the distinctive low concentrations on the downwind (luv) building face and high values on the upwind (lee) building face.

In the early 1970s, Kennedy and Kent [59] looked at a scale model of Sydney in an atmospheric boundary layer wind tunnel. They used the novel approach of using a couple of heated nichrome wires to simulate the roadways rather than a source of pollutant. Their reasoning was that the governing equations of heat and pollutant transport are so similar that the analogy could be used. Using a heat source rather than a tracer gas makes the experimental procedure somewhat simpler - thermocouples rather than expensive (and intrusive) gas sampling devices can be used.

An interesting result from their research was the reduction of predicted pedestrian level pollution in the wake of a couple of tower blocks which were introduced into the local

topology. It was suggested that high velocity flows around the tall buildings at street level, with the associated high turbulence, facilitated the dispersion of pollutant.

In those studies which looked at the dispersion of pollutant, the source was invariably modelled as a line or point - no-one attempted to model an actual train of vehicles. Indeed, even the single vehicle case, which the present research hopes to use, was not considered by any of the above workers in their wind tunnels. Some recent work by Pearce and Baker [71] at Nottingham University went some way to address this omission. Using a conventional line source of pollutant lying along a street canyon, they were able to perturb the wind-induced flow field by firing a train of vehicles along the street. In this way they were able to introduce some of the mixing effects of passing vehicles without actual having a moving source. As the vehicles passed, they did observe some perturbation (an increase, in fact) of the resident concentration field which almost indicated that the vehicle wakes somehow concentrated the pollutant, temporarily giving pedestrians a 'blast' of noxious chemicals. Their results, however, were inconclusive. The piece of equipment they used to fire the vehicles across the wind tunnel and down the street canyon is called a Moving Model Rig (MMR) and will be discussed in Chapter 3 when it is put to use in the present research.

In a recent paper, Meroney *et al* [65] continued the trend of using a line source of pollutant to model the vehicles in much the same way as Pearce and Baker. Two different configurations were used: an isolated street canyon in the midst of typical rural boundary layer; and a large number of canyons (20 in fact) upstream of the test canyon.

In the former case, one of the more interesting effects they observed was that the flow in the canyon appeared independent of Reynolds number inasmuch as the concentration distribution was largely unaffected by changes in the free stream wind speed. They also observed significant concentrations on the roof of the upstream building. This, it was postulated, was due to a recirculated bubble on the upstream roof which was sucking concentration out of the canyon before allowing it to move into the free stream aloft of the two rows of buildings.

For the second case, in which the 20 upstream canyons would ensure a stabilised boundary layer, well outside the transition zone, none of these recirculation effects were observed. Indeed, they went on to remark that the vortices in the 'urban' case were far more stable than in the isolated 'rural' canyon. Indeed, this is further evidence of the two quite separate zones, one above the roof height which can be described as a boundary layer flow over large roughness elements and a lower zone inside the urban canopy.

Computational Fluid Dynamics Models

Before embarking on a discussion of CFD models of the street canyon environment, a few brief sentences describing the basic methodology used in CFD modelling are necessary. These models derive their physical basis from the solution of the partial differential

equations which govern fluid flow - for instance, the Navier-Stokes and continuity equations. To do this the domain of interest must be sub-divided into small areas or volumes (2 or 3D models) in which the equations are linearized. These linear equations are then recombined to form a large system of equations which describe the whole domain and which are then solved giving the required flow and pressure fields. That, in brief, is the idea - the reality is far more complex because of the highly non-linear nature of the governing equations and the inability of present models to describe turbulence mathematically. CFD, however, is a powerful tool which can provide its proponents with valuable insights into the flow fields around geometries which otherwise could not be visualized. It should be stressed that CFD modelling is still a comparatively young method but recent advances in the field are very encouraging. For a more in depth discussion of CFD see, for example, Abbott and Basco [1].

In what follows, the work of several groups of investigators will be described in which the problem of air flow and pollution dispersion in the urban street canyon will be addressed.

Lee and Park [61] used a 2D finite area model to simulate the flow and dispersion of pollutant in a single street canyon. The model revealed the presence of a single vortex in canyons with an aspect ratio close to 1.0. As the ratio rose to values above about 2.1, they showed that a second, much weaker, vortex appeared below the first. In both the single and double vortex cases, the maximum concentration occurred at the centre of the (upper) vortex, and the indications were that higher concentrations are observed on the leeward side of the canyon. This is perhaps a little misleading in the present context because they assumed that the canyon was initially uniformly full of pollutant - significantly different from the actual situation of a ground level source of pollution being emitted from the traffic. The chief aim of their work, however, was to parameterize the process of pollutant leaving the canyon at roof level. To facilitate this, they introduced a time constant, τ, which was defined as the time required for the average pollution concentration in the canyon to be reduced by a factor of *e*. They found that the values of τ varied over a range of approximately 20 s to 2500 s as they altered the above canyon wind speed, the canyon aspect ratio and the diffusion coefficients for the tracer gas.

Ca *et al* [15] used a large eddy simulation which included the effects of heat flow to model the flow fields in a canyon. They also reported the existence of a second, and sometimes third, vortex near the foot of canyons with large aspect ratios. The existence of the third vortex may be due to the inclusion of the heat-induced turbulence which explains the perceived difference between these results and those of Lee and Park above.

Berkowicz *et al* [11] described a 3D incompressible Navier-Stokes solver which they recently used to model similar street canyon problems. Their results agree well with the work of Hotchkiss and Harlow (see next Section) and the single vortex model of Lee and Park. For non-parallel winds, they observed a weak spiral such as that shown schematically in Figure 2.7.

Figure 2.10: Concentration contours across a symmetric canyon generated by the SCALAR model (after Johnson and Hunter [56]).

As an interesting addition, Hunter *et al* [53] conducted a 3D numerical study of street canyons, this time looking at the various types of flow that occur for different aspect ratios. For very thin canyons, they observed a "skimming" effect in which the roof level flow is hardly diverted into the canyon at all. For wider canyons, the familiar vortex flow was seen to develop. Hunter *et al*, in line with the terminology of Oke, referred to this particular type of flow as "wake interference". Finally, "isolated roughness flow" occurred when the aspect ratio was very small and in which the shear layer separates around the top of the leeward face and a sustained vortex does not have the opportunity to develop.

Building on this research, Johnson and Hunter [56] describe a new body of work they performed using the SCALAR code which this time included the dispersion of pollutant within the canyon. For instance, with the characteristic vortex present in the canyon, they found the maximum concentrations occur in the lower, leeward corner of the canyon as shown in Figure 2.10 which is reproduced from their paper.

Moriguchi and Uehara [66], in addition to their wind tunnel work mentioned in the previous section, described a numerical study of the same large range of roadway configurations. A Finite Difference scheme was used to solve the Navier-Stokes equations and the contaminant transport equation. Although a two-dimensional solution can never fully model reality, the results from their 2D simulations are shown reproduced in Figure 2.11. The top and bottom plots in the Figure are the interesting ones as far as this work is concerned - the top is helpful for the open country case while the bottom one displays the, by now familiar, high concentrations on the upwind building face and low concentrations on the downwind face.

Figure 2.11: Simulated wind flow and concentration for various two-dimensional configurations (after Moriguchi and Uehara [66]).

In a recent conference preprint (Leitl and Meroney [62]), an attempt was made to reproduce the wind tunnel results of Rafailidis at Hamburg University using the CFD code FLUENT. Firstly, they used a 2D model of several canyons and were able to to reproduce the leeward building concentrations observed in the canyon. Indeed, their work stands out from the other reviewed here in that they introduced a conservative tracer into the canyon in order to study the dispersion characteristics. The windward building faces were not so good, however, and prompted the authors to move onto more realistic 3D simulations. It is worth to mention in passing that Leitl and Meroney also investigated the flow and flushing regimes associated with gable-ended buildings. While not strictly relevant to the present study, the predictions from the CFD model of these roof configurations were less representative of the wind tunnel observations.

A very comprehensive study of the urban canyon system can be found in a paper by Sini *et al* [84]. Using an in-house code, CHENSI, they looked into the development of the canyon vortices for a number of aspect ratios and found patterns roughly in line with the findings of Lee and Park and Hunter *et al* - specifically the tower of vortices in very narrow canyons and the recirculation region in the wake interference regime. They also looked into the effects of pollutants in the canyon. Their method, however, is perhaps not entirely relevant to the present study because they released the tracer so as to simulate a cloud of tracer passing above the canyon. In this way they were able to study the degree to which the pollutant penetrated the canyon but could not give any

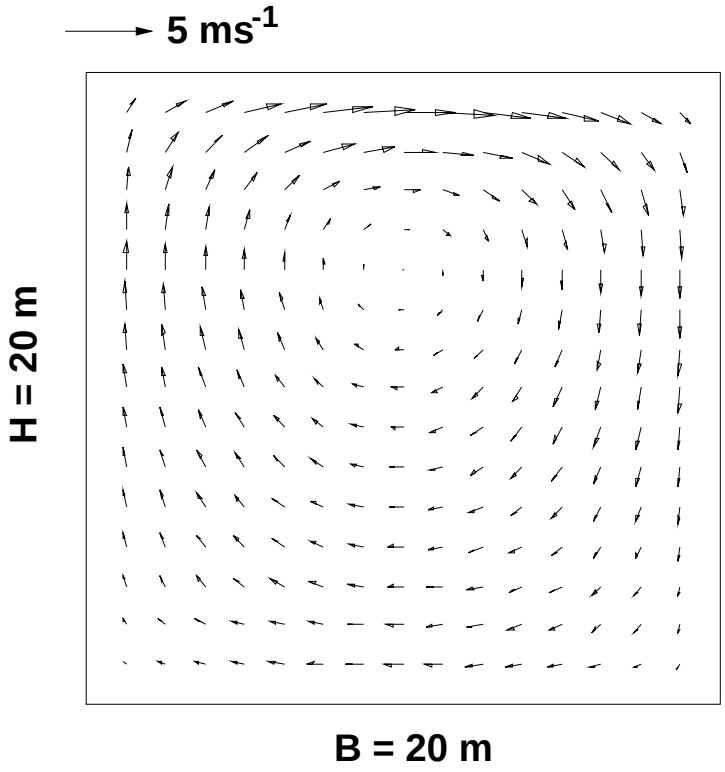


Figure 2.12: Wind field obtained with the Hotchkiss-Harlow model for a mean wind field of 5 ms^{-1} in a unit aspect ratio canyon.

indication as to the effects of pollutant produce within the canyon. This is not to say that this particular aspect of their research is not useful when looking at the effects of vehicular pollutants in the urban environment - far from it, in fact. Such studies may well prove useful in determining the so-called 'background' pollution levels in the canyon environment which arise from vehicles in other part of the town or perhaps from local industrial plants.

A further aspect of their research which requires a mention is their investigation into the effects of heating the walls of the canyon. This is one area where CFD has distinct advantages. For example, by heating the windward wall in a typical skimming flow regime, they found that the buoyancy of the air was sufficient to oppose to usual downward flow on the windward face and thus two contra-rotating flow cells appeared in the canyon.

It is interesting to note that the vast majority of these CFD investigations were performed with new computer models which were invariably written and developed by the authors of the papers. From this authors perspective, this introduces firstly a lot of extra work for the researchers and secondly a whole series of questions about the validity of these 'in-house' codes.

Analytical Models

In was recognized at an early stage in this field of research that the vortex in the street canyon was an important feature of the dispersion process. Hotchkiss and Harlow [47] looked at the effect of an above canyon wind perpendicular to the axis of the canyon on the velocities in the canyon. They derived an analytical expression (from the linearized Navier-Stokes equation for an incompressible fluid) for the velocities which can be written in the following form,

$$\begin{aligned} v &= \frac{v_H}{1-\beta}\left[\gamma(1+kz') - \beta(1-kz')/\gamma\right]\sin ky \\ w &= -\frac{v_H kz'}{1-\beta}\left[\gamma - \beta/\gamma\right]\cos ky \end{aligned}$$

where $k = \pi/B$, $\gamma = \exp(kz')$, $\beta = \exp(-2kH)$, $z' = z - H$ and v_H is the cross canyon wind speed at roof level. These equations describe a vortex, the strength of which decreases towards the bottom of the canyon and the centre of which is skewed towards the top of the canyon as shown in Figure 2.12.

The so-called STREET model was developed in the early 1970s as a sub-model of a general urban diffusion model and is described in Johnson *et al* [57]. The need for a street canyon sub-model arose partly because many of the important effects of vehicle pollutants on pedestrians could not be described adequately by a large scale urban dispersion model and partly because most of the data available to the researchers at that time was taken in city centre streets in San Jose. Indeed, there was additional evidence available from workers such as Georgii *et al* [34] that leeward concentrations far exceeded those on the opposite wall of the canyon.

STREET is a simple box model which predicts the above ambient concentration on the leeward face to be of the form,

$$\Delta C_L = \frac{0.07N}{(v_H + 0.5)\left[(x^2+z^2)^{1/2} + 2.0\right]} \tag{2.20}$$

where N is the traffic flow (vehicles hr^{-1}), v_H is the mean above canyon wind speed, and x and z are the horizontal distances from the lane of traffic to the receptor. The numerical values which appear in Equation 2.20 were determined specifically for the San Jose scenario: 0.5 is a minimal dilution velocity; 2.0 is an initial mixing length (notably roughly the height of a typical vehicle); and 0.07 is an empirically determined parameter, presumably related to the emission strength of the roadway. For the windward side of the canyon, the following expression holds,

$$\Delta C_W = \frac{0.07N}{B(v_H + 0.5)} \tag{2.21}$$

where B is the width of the street. Johnson and his co-workers admitted at the time, however, that Equation 2.21 should have exhibited a slight vertical gradient. It should be

noted that Equations 2.20 and 2.21 are only applicable for predominantly cross canyon wind directions. For the parallel wind case (taken to be when the wind direction and street axis are aligned to within 30°), an intermediate concentration is defined as the arithmetic mean of Equations 2.20 and 2.21.

The Canyon Plume-Box Model (CPB) of Yamartino and Wiegand [89] arose from a major investigation into the impacts of urban automotive emissions. It was an attempt to supersede the STREET model and provide a more general model with a greater range of applicability. To do this, Yamartino and Wiegand looked at the problem in terms of the flow, turbulence and concentration distribution within the canyon.

They separated the air flow in the canyon into two components: an along canyon flow model and a transverse flow model. The latter was based on the solution provided by Hotchkiss and Harlow [47] as described above while u was approximated by a simple logarithmic profile,

$$u(z) = u_H \log[(z+z_0)/z_0] / \log[(H+z_0)/z_0]$$

where u_H is the above canyon, along canyon wind speed and z_0 is a surface roughness. They found that for the model to accurately describe observed wind profiles, z_0 had to be a function of the above canyon wind direction, θ. It is important to note that z_0 in this context is not the same as that used in wind speed profiles.

The much more difficult problem of estimating the turbulence within the canyon was addressed by Yamartino and Wiegand in the following way. They developed an empirical relationship between the turbulence components, σ_i, and those variables thought to have a significant bearing on the observed turbulence levels. Without going into too much detail, they produced an expression which had contributions due to ambient wind, heating from the sun and vehicles and some default night-time turbulence.

Using this basic framework, Yarmatino and Wiegand went on to describe an integrated Gaussian plume model which has both a vortex and non-vortex capability. The latter situation occurred when turbulence across the canyon dominated proceedings and the tell-tale vortex pattern broke down - probably due to high traffic densities.

By now it will have become clear that the CPB contains a large number of parameters, the values of which are not readily available. Thus, the major problem with mathematical model in this area of modelling becomes clear - without field data, whether it be full-scale or obtained in a wind tunnel, the models are useless for anything other than for drawing simple conclusions. And often these conclusions were the basis for the model in the first place. For the CPB and others, specific field data is essential if confidence is to be placed in the model. For the case of the CPB, Yamartino and Wiegand extensively used field data obtained in Bonner Strasse in Cologne.

Hertel and Berkowicz [42, 41, 43] and Hertel *et al* [40] describe the development of the Operational Street Pollution Model (OSPM). The basic model is formulated in the first of these papers. It is a well constructed model with the concentration at a receptor due to

both a direct component from the line source of vehicles and a recirculated component due to the resident vortex. A Gaussian plume model is used in the calculation of the direct component with dispersion parameters dependent on the turbulence which is due to both the traffic and the above canyon wind. A simple box model (*c.f.* the STREET model) is used for the recirculating component. One of the later papers (Hertel and Berkowicz [43]) introduces a much more rigorous treatment of traffic-induced turbulence, although it should be noted that they shunned the idea of superimposing wakes in the way suggested by Eskridge and Hunt [30].

Lanzani and Tamponi [60] recently took the CPB model one step further by using the flow and turbulence fields in the canyon as the basis on which to build a Lagrangian particle tracking model. As with STREET, CPB and OSPM the presence of vehicles only manifested itself in the form of a line source and an extra term in the expression for turbulence. The explicit presence of the vehicles as distinct, turbulence-producing entities was not assumed. Lanzani and Tamponi described a sensitivity study in which they showed the effects of changing certain model parameters on the predicted concentrations. Interestingly, a comparison between their model, named GEM, and CPB and another code, CANYON[5], was conducted. Because of the vastly differing mathematical and conceptual bases for the three models they found what, at best, can be described as qualitative agreement. However, the disciplines of submitting a new model to both a sensitivity analysis and inter-model comparison are both good habits which the present study will adopt in due course (see Chapter 4).

[5]It appears, in fact, that CANYON was a subroutine in the APRAC3 code (Simmon *et al* [83]) and that the subroutine was simply an implementation of the STREET model.

2.5 Puff Models

Gaussian Puff Models have already been mentioned in passing: firstly there was Baker's [7] far field treatment of dispersion behind a single vehicle in a cross wind; and there is a rather vague reference in Dabberdt and Hoydysh's [22] paper to a puff model. Since Chapter 4 details the author's development of a Gaussian Puff model for dispersion modelling in both the street canyon and open country cases, it is worth reviewing relevant work.

Although the present application is to a street canyon, puff[6] models arose chiefly from attempts to better describe pollution from elevated sources such as chimney stacks. Section 2.4.1 looked at the immediate precursors to puff models - Gaussian plume models. Under reasonably constant wind and source release conditions, plume models have proved to be quite successful in predicting concentrations in the "shadow" of chimneys. However, if the wind speed and direction are varying quite significantly over time periods of the order of the observation time, then an alternative approach is required - puff models.

A puff model differs from a plume model in that a series of clouds or puffs of pollutant are released from the source(s) over a period of time. Each puff maintains the basic Gaussian distribution of mass but moves and disperses independently of all the other puffs. It is the flow conditions at the centre of the puff that define the subsequent movement and dispersal.

This approach is similar in many ways to particle tracking: both methods follow individual "packets" of pollution as they move in a variable flow pattern. The very nature of the puff method lends itself to simulation by computer. A puff can be released at each time step and transported according to simple differencing schemes. It becomes clear that the concentration of pollutant at a receptor in a puff model is determined by the sum of contributions from all the available puffs. Indeed, if the physical boundaries of the domain are sufficiently distant, then the concentration at a receptor at coordinates (x_r, y_r, z_r) is given by,

$$c_r(x_r, y_r, z_r) = \sum_{p=1}^{N_p} c_p(x_p, y_p, z_p) \tag{2.22}$$

where the contribution from an individual puff is,

$$\begin{aligned} c_p(x_p, y_p, z_p) &= \frac{Q\Delta t}{(2\pi)^{\frac{3}{2}}\sigma_{x_p}\sigma_{y_p}\sigma_{z_p}} \\ &\times \exp\left\{-\frac{(x_r - x_p)^2}{2\sigma_{x_p}^2}\right\} \cdot \exp\left\{-\frac{(y_r - y_p)^2}{2\sigma_{y_p}^2}\right\} \cdot \exp\left\{-\frac{(z_r - z_p)^2}{2\sigma_{x_p}^2}\right\} \end{aligned} \tag{2.23}$$

where (x_p, y_p, z_p) are the coordinates of the centre of puff p and σ_{x_p}, etc. are the dispersion parameters of that puff. The dispersion parameters for a puff do not differ concep-

[6] We drop the word Gaussian for clarity.

tually from those associated with a Gaussian plume - they define the extent to which the puff has expanded due to local mixing.

2.5.1 Relevant Puff Models

Using this basic formulation, puff models have been applied to various physical situations and have been refined to increase the efficiency and reduce the storage requirements of the computer implementations. In Chapter 4 an application of the puff method to the problem of traffic pollution modelling is presented which is a broad amalgam of some of the work which follows here.

Perhaps the most relevant is the work of Nishi and Cermak [67]. They looked at the problem of air pollution in the locale of airports, specifically the only recently completed Osaka Bay airport in Tokyo. Traditionally the approach had been to use plume models, often representing the runway as a line source of pollutant. However, it was found that this was a flawed approach because of the relatively long period between successive aircraft departures or arrivals.

This was a situation ideally suited to the application of a puff model with a number of moving sources and this is precisely the approach adopted by Nishi and Cermak. Indeed they took the model further, the movement of each aircraft was divided into four phases: taxiing; takeoff; climb-out and approach. In each phase, puffs of pollutant could be released according to the different meteorological conditions in each region. As is often the case with puff models it is the determination of the dispersion parameters which presents most problems. Instead of developing some kind of theoretical approach, they simply fit the model to the observed data. The observed data was obtained by sending out a helicopter along the expected flight paths of the aircraft. The helicopter released SF_6 gas which could be collected at a number of sampling points.

The quality of the results produced by the calibrated model suggest that the moving source puff model was a definite improvement on the line source plume models which preceded it. And, although Nishi and Cermak themselves said that motor vehicles could be represented by a stationary line source, it was this success which persuaded the author to adopt a similar scheme in the urban canyon model of Chapter 4.

Also of direct relevance to the urban canyon model is a model developed in conjunction with a major field experiment in the Brush Creek Valley in Colorado. Rao *et al* [74] described a computer program called INPUFF which they developed to help understand the nocturnal drainage of pollutant from the valley. Figure 2.13 shows their basic configuration. The valley walls are quite clearly marked as are the source, S, a puff, P, and a receptor, R. In an attempt to place some physical limit on the lateral spread of the puffs in the valley, two image sources, I_1 and I_2 are introduced into the model. These are analogous to the last term in Equation 2.16 which accounts for the reflection of the Gaussian plume in the ground.

Figure 2.13: Modelling region used in the INPUFF model of Rao *et al* [74].

Although Rao *et al* realized that the box approach was somewhat of a simplification of their problem (a real valley with all its irregularities), it is a very good approximation for a street canyon and as such their work is very useful to the present research. They did suggest that a continuous distribution of image sources would be needed is a bowl-shaped valley cross-section were to be adopted. This, they said, was an area of current research but a later paper (Tangirala *et al* [87]) showed no evidence of any progress being made on this front.

2.5.2 The Efficiency of Puff Models

Although they are a marked improvement on plume models, puff models do tend to require much longer run times on computers, partly because of the need to track thousands of puffs and partly because the summation of Equation 2.22 must be performed for each receptor. It is not, therefore, surprising that numerous attempts have been made virtually from the time puff models were introduced to decrease their voracious appetite for computer resources.

Ludwig *et al* [63], writing at a time when computer resources were at much more of a premium than nowadays, discussed a number of ways of reducing run times and storage requirements for puff models. The most important aspect of their work was the notion of purging puffs. Any puff which was too weak or diffuse was removed from their model and since CPU time is directly related to the number of puffs this was an obvious time-saving device. Merging puffs which became separated by small distances was another method of reducing the number of puffs. They suggested that two puffs could be combined into one whose properties were the average values of the two parent puffs. However, their suggestion of centering the new puff equidistant between the centres of its parents seems an oversimplification, especially when merging two puffs of quite different sizes. Also mentioned was the work of Ruff *et al* [33] who used a lookup table

to replace the standard $\exp(-x)$ function.

Later Zannetti [90] employed the puff merging scheme in model called AVACTA. Zannetti used a slightly different approach by using both puffs and segments of Gaussian plumes in his model, again in attempt to reduce the computational overhead. Verver and de Leeuw [88] used the exact opposite of this - in regions of rapidly varying wind speed, they split large puffs into several smaller ones. They did, however, use puff merging techniques in regions of uniform wind speed. The trade-off between the accuracy of having more puffs and the efficiency of having fewer is thus demonstrated.

More recently, Hurley [54] split the problem into two parts: a puff model in the horizontal direction and a particle solution in the vertical. He did this, not to slow down a puff model, but to speed up a particle tracking model.

2.6 Summary

If only one conclusion were to be drawn from this chapter then it would be that there is a need for a model of the urban street canyon that combines a more sophisticated description of dispersion and traffic flow with a set of parameters defined, not just as best guesses, but by empirical evidence. It it hoped that the remainder of this thesis, with its dual empirical/analytical approach, can go some way towards meeting this need.

However, it is also clear that the proposed wind tunnel study of the behaviour of pollution in the wake of a vehicle moving through a cross-wind has not been attempted before (to the best of the author's current knowledge). As will become clear in the next chapter, the unique facilities at the author's disposal in the wind tunnel are ideally suited to a study of this nature.

Chapter 3

Experimental Investigation

3.1 Introduction

The aim of this chapter is to cover in as much detail as possible, the experimental work in the environmental wind tunnel. An extensive discussion of the apparatus and methods opens the Chapter. In that section, the wind tunnel and the moving model rig (MMR), are the focus, they being the major pieces of equipment used. Then, anemometry, gas measurement and scaling issues are dealt with.

Two quite distinct sections then follow which deal with first the rural/open country scenario and second, the urban canyon case. Both sections follow the same pattern, however, with a description of the generation of and properties of a correctly scaled boundary layer and then a detailed presentation and discussion of the moving model results.

Finally, some specific and then more general conclusions are drawn. What is not attempted at this stage, however, is to try and compare these results with the predictions of the analytical model of Chapter 4.

3.2 Experimental Equipment and Techniques

3.2.1 The Wind Tunnel

The environmental wind tunnel used throughout these studies is situated at Fauld in Staffordshire, and is owned by British Gas plc. The tunnel was designed to be able to cope with the high concentrations of natural gas used in some of British Gas' more explosive experiments. For this reason the tunnel is of the single-pass type - recirculation of potentially explosive gases being an unwanted hazard - and is fabricated completely

from steel. The motor housing and fan are continuously purged by a separate fan to flush out any lingering flammable gas.

The single pass design has implications for both the simulation of scale boundary layer, the spectra of which may have low frequency peaks due to slowly (relative to those intentionally generated) moving gusts outside, but also the measurement of gas concentrations. At times during these experiments, a herd of cows with their inherent flatulence, would graze in the field near the wind tunnel intake with severe implications for the background hydrocarbon levels.

Figure 3.1 shows clearly the design of the tunnel (note that the diagram has been distorted by a factor of two in the cross-tunnel dimensions). Starting at the inlet, there is a series of louvres, removable filters and a flow straightener in the form of a honeycomb. With the filters in place the effects of external wind variations can be reduced at low speeds - indeed, the filters cannot be used at tunnel wind speeds greater than about 3 ms^{-1} without damaging them. There is then a contraction which reduces the cross-sectional area by a factor of 3, down to 4 $\times$ 2 m (width$\times$height). This cross-section is maintained throughout the 17 m long fetch and the 6 m long working section, except for a very slight tapering of the roof to reduce the upper boundary layer. Viewing windows are situated between the working section and the control room and a roof work area. British Gas workers tend to refer to the near side of the tunnel as the control room with the far side being called the “laser room” side. We shall use this convention later in the chapter.

The fan is capable of producing wind speeds in the tunnel of up to 20 ms^{-1} and is controlled manually by means of a solenoid. As a result, in all but the calmest of external wind conditions, the wind speed is prone to vary with time. There is no feedback circuit built into the control of the fan to account for these external influences.

3.2.2 The Moving Model Rig

During 1996 the wind tunnel was modified to accommodate the Moving Model Rig (MMR), which was previously housed in the The University of Nottingham Environmental Wind Tunnel on the main campus in Nottingham. The MMR had, in fact, been built at Cranfield Institute of Technology from where it was moved to Nottingham. Whilst installed at the University, the MMR was used during several notable studies of the effects of cross-winds on road vehicles and trains (Baker [4] and Coleman and Baker [19]).

The early stages of installation of the MMR including the design of the supporting superstructure and the breaching of the tunnel walls and floor was supervised by the author. Details of this work can be found in Appendix A. In particular, the fact that the tunnel floor was breached meant that, unless remedial action of some form were taken, air would be sucked into the tunnel which would completely disrupt the flow therein. To

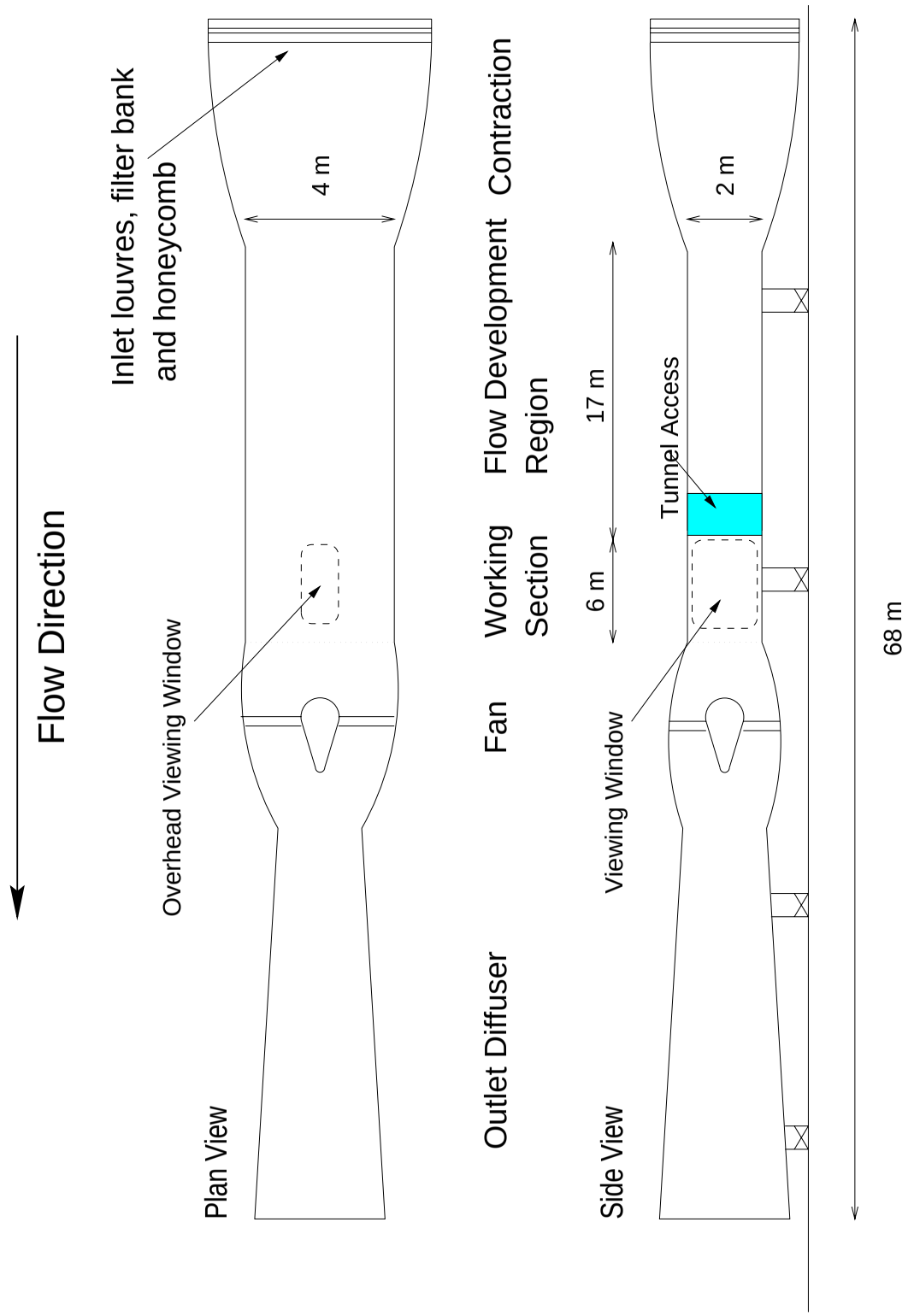


Figure 3.1: Schematic of the British Gas Environmental Wind Tunnel at Fauld, Staffordshire.

alleviate this problem it was decided to build an air-tight room around the whole of the MMR. By doing this, it was hoped that the pressure inside the room and the tunnel would equalize when the fan was in operation and air flow between the two cavities would be effectively zero. Smoke tests were conducted to verify this fact and it was indeed shown to be the case.

The general arrangement of the MMR as it originally stood in the wind tunnel at Cranfield is shown in Figures 3.2 to 3.4 which are taken from Baker [4]. The model sits on a trolley (or carriage) which rides on a Hepco guide-way which in turn is attached to a leveled I-beam, itself mounted on a series of concrete blocks. The model carriage is initially connected to a firing carriage which gains its momentum from a number of stretched bungees. The firing and model carriages part company before the working section of the tunnel is reached by which time the model carriage is traveling at a near constant speed. Having traversed the working section, the carriage is brought to rest by a braking mechanism. In the years since 1986, a mechanism for automatically returning the model carriage to its firing position has been constructed and added to the MMR. A heavy duty electrical motor is used to drive a chain continuously at both sides of the guide-way. On the chain there are hooks which attach themselves to the model carriage and drag it back to its firing position.

3.2.3 The Lorry Model and Trolley Configuration

Despite much of the previous wind tunnel research and modelling work having been conducted using simple, block-shaped objects as vehicles, it was decided that during this research a lorry would be used. The reasoning behind this is that the model lorry was used in a previous set of experiments which looked at the forces on the lorry (Coleman [18]). So, there was already a large bank of knowledge concerning the lorry at Nottingham University and the lorry was an approximation to a block-shape. The exact dimensions of the lorry are presented in Figure 3.5 (which has been reduced to 75% of the original 1/2 scale to fit on the page). The lorry is fabricated out of balsa wood and is largely hollow because it was previously used to house a force balance.

The lorry was mounted as shown in Figure 3.6, some 100 mm above the trolley. Such are the space limitations between the floor of the wind tunnel and the trolley that the lorry had to be mounted with part of the regulator knob inside it - see the photograph in Figure 3.7. This was unavoidable but was thought not to disrupt the aerodynamics too much because the knob was effectively behind the cab of the lorry. Two rigid screw threads hold the lorry in position.

In order to sense the passage of the trolley, while at the same time recording its speed, an LED sensor device was mounted at the side of the Hepco guide-way. The sensor consisted of a LED and a light-sensitive diode (LSD) facing each other across a small gap. Built into the device was an electronic circuit which allows an output voltage of

Figure 3.2: The Moving Model Rig, transverse tunnel section (after Baker [4].)

Figure 3.3: The Moving Model Rig track (after Baker [4].)

Figure 3.4: The Moving Model Rig, carriages and model train (after Baker [4].)

about 5 volts when there is no obstruction between the LED and LSD, which then drops to 0 volts when there is an obstruction. Two metal prongs were then attached to the underside of the trolley. A distance of exactly 1 m separated the centrelines of the prongs which were both 1 cm wide - this width was just enough for the prongs to be sensed, given the sampling rates and trolley speeds used. The prong nearer the front of the trolley was 10 cm forward of the front of the model lorry. The speed of the trolley could then be calculated simply by finding the difference in time between the two occurrences of a reading of 0 volts on the LED channel (*ie* when a prong passes between the LED and LSD). Section 3.2.7 below describes the exact implementation of this trigger system when acquiring data.

3.2.4 Gas Supply System

Such was the nature of these experiments that there was no alternative but to mount the gas supply system on the trolley which would then be fired across the tunnel. While firing high pressure gas cylinders at high speeds towards a brick wall is not usually recommended, significant thought was put into safety considerations, especially the braking mechanism at the far side of the tunnel. Indeed a comprehensive Safety Assessment (Hargreaves [36]) was prepared in line with British Gas' requirements and was duly passed. Part of this assessment required that the gas cylinder and its attendant pipes were securely mounted on the trolley with no possibility for lateral or vertical movement.

The source of gas was a "lecture" bottle which contained a calibration mix of 1.1% propane in air mixture[1]. These bottles were supplied by Argo International Limited - a specialist firm in this area. When full, these bottles are at a pressure somewhat in excess of 100 Bar. Again because of space limitations, it was necessary to mount the regulator (again supplied by from Argo International limited) some distance from the bottle. A high pressure pipe/hose system was constructed for the experiment by another specialist firm, G.I.S., to connect the lecture bottle and regulator together in the configuration shown in Figure 3.6.

Since the piping on the other arm of the regulator was at much lower pressures (approx. 1 Bar), less robust equipment was required here. The red, nylon piping which forms a loop below the model lorry in Figures 3.7 and 3.8 was used in this part of the gas delivery system. Such was the expense of the gas that great care was taken to minimize leaks in this section of the piping. There was no risk from explosion from leaks because the 1.1% concentration is below the lower explosive limit for propane in any case.

From the regulator (which is seen below the lorry in Figure 3.8), the gas is taken through a toggle valve (which is below and to the left of the lorry in Figure 3.8). This valve was used to switch on the gas supply to the trolley just before the trolley was launched and

[1] A mix of 1.1% corresponds to a concentration of propane in air of 2.16×10^{-2}kg m^{-3}.

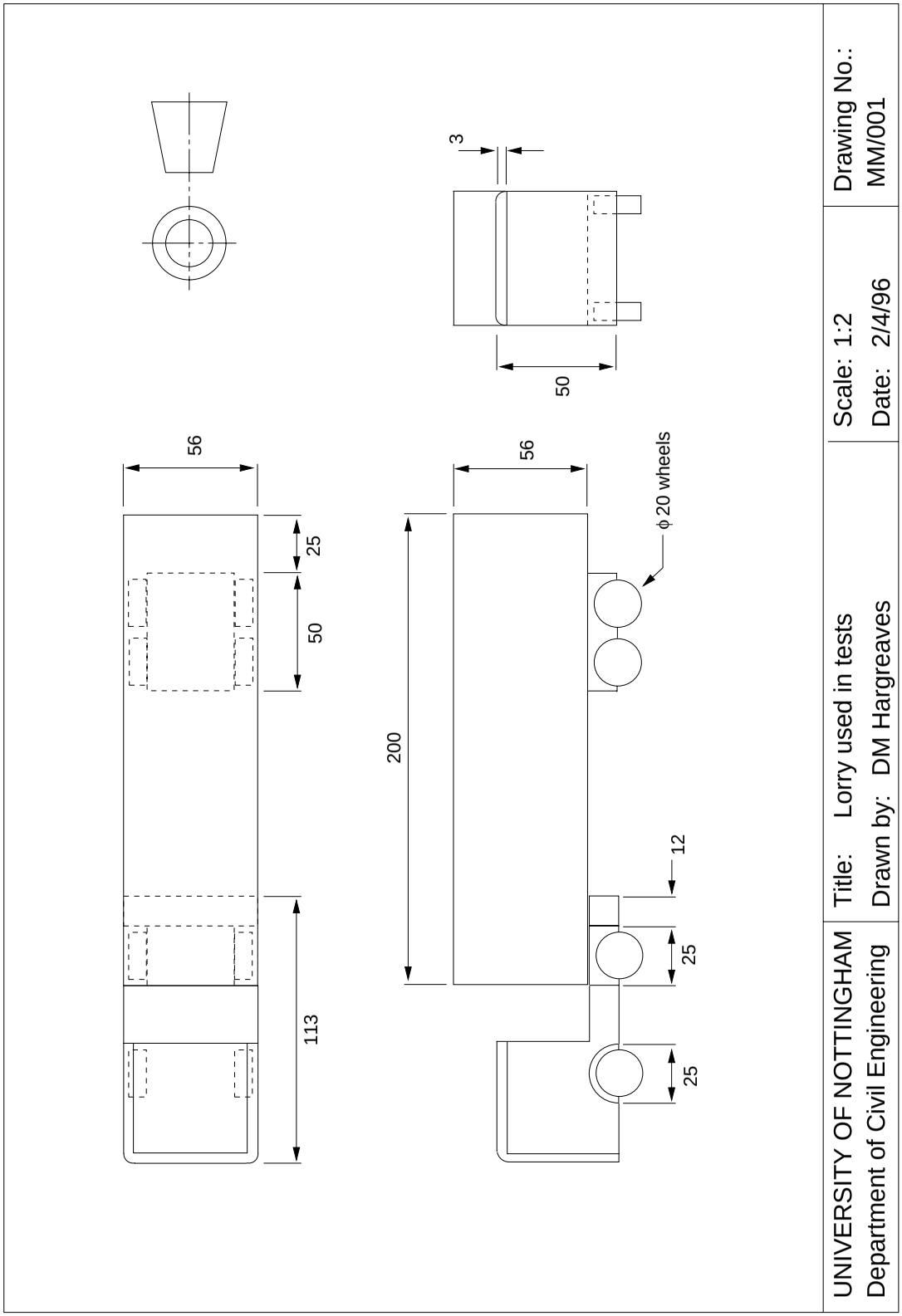


Figure 3.5: The 1/50th scale lorry model used in testing

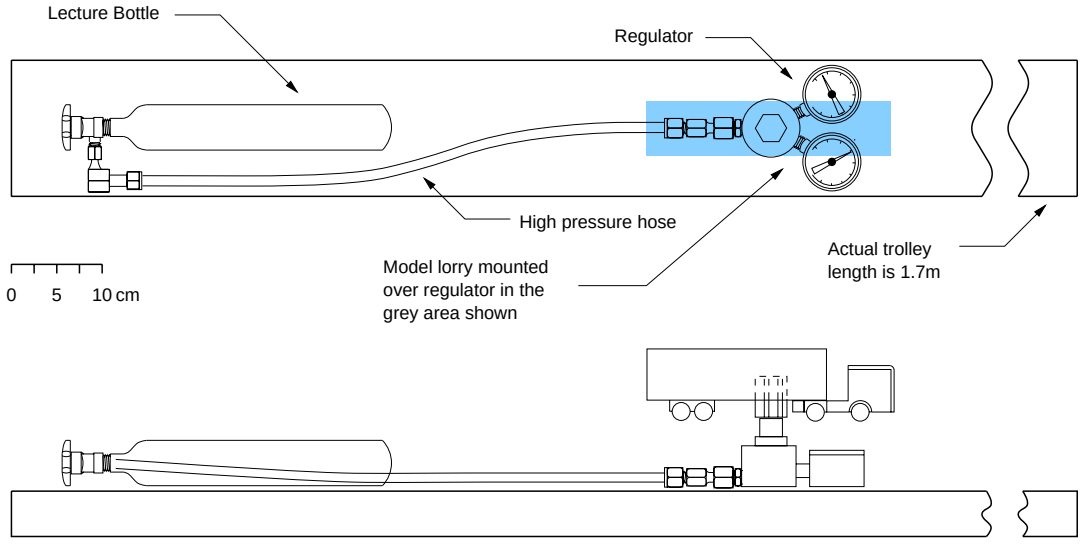


Figure 3.6: Configuration of the MMR trolley (plan and side views).

then switch off the gas at the far side of the tunnel. There were two reasons for doing this. Firstly, to minimize the amount of gas lost during each cycle of the firing/retrieval procedure and secondly, to ensure that the gas had sufficient time to disperse completely between firings.

From the toggle valve, the gas was finally fed to the exhaust pipe which was mounted at the rear of the lorry, skewed towards the downwind side. The exhaust pipe was simply a metal tube with inside diameter 1.5 mm.

3.2.5 Anemometry

The wind velocity was recorded variously using a pitot-static tube and hot-wires. The pitot-static tube was mounted at a height of 1.6 m above the wind tunnel floor, well out of both the floor boundary layer and the smaller roof boundary layer. The pitot-static tube was connected to a pressure transducer which had a constant sensitivity of 19.39 mm of water per volt. The frequency response of the pitot-static was such that it was only used for mean measurements throughout the tests.

Both single and cross-wire hot-films were used in these experiments. Capable of frequency responses far in excess of anything that would be required here, these devices were the obvious choice for measuring wind velocities. Thermal System Inc. (TSI) hot-films, connected to a constant temperature anemometer, TSI Model 1054-B, coupled to a TSI Model 1056 Bridge unit were used.

Figure 3.7: Photograph of the model lorry mounted on the MMR trolley.

Figure 3.8: Photograph of the trolley showing the toggle valve and regulator in detail.

The calibration of the hot-wires is dealt with in detail in Appendix C.4.

3.2.6 Gas Measurements

A BMT Hydrocarbon Gas Detector was used to measure the concentration of propane in the wind tunnel. The propane, although at a maximum in-air concentration of 1.1%, was present at levels well within the range of the equipment used. For a detailed description of the gas detector, see [12].

In brief, however, the detectors employ Flame Ionisation Detectors (FIDs) to measure the concentration of any hydrocarbon at the point of measurement. The FID operates by burning a hydrogen jet in air in a chamber across which a high voltage is applied. Any molecule of hydrocarbon passing through this chamber is immediately ionized. If the molecules are present in sufficiently high numbers, a current proportional to the rate of passage of carbon atoms is generated. The current is then converted to a voltage to give outputs in the range 1V/ppm to 10mV/ppm.

The FID chamber itself is quite a bulky device, measuring approximately $100 \times 100 \times 40$ mm in size. Also, the frequency response of the FID decreases with the length of the sampling tube attached to it. Ideally, it would be better if the FID chamber were as far as possible from the measurement position because its very presence disturbs the flow some distance upstream of it. However, if a longer tube is used to facilitate this, then the frequency response suffers. Thus, a compromise has to be reached. It should be noted that this is only of importance when looking at the rural measurements - in the urban case, the chamber can be mounted inside one of the buildings which form the street canyon. In the User Manual, it is stated that for a 100 mm sampling tube of 0.5 mm diameter and a sampling rate of 70 cc/min, tests have shown a -3 dB point at a frequency of 80 Hz.

A couple of useful equations are supplied by BMT for calculating the maximum frequency response. Firstly, the time constant, τ, of the FID is given as,

$$\tau = 18d^2(L/V)^{\frac{1}{2}}$$

where d is the diameter of the sample tube (in mm), L is the length of the sample tube (in mm) and V is the volume flow rate in the sample tube (in cc/min). From this, it is possible to calculate the maximum frequency response thus,

$$f_c = \frac{460}{\tau}$$

where the figure of 460 was obtained by BMT from a series of sensitivity studies.

Calibration of the FID

In theory, the calibration of the FID should have simply been a matter of playing the gas issuing from the exhaust pipe of the lorry over the FID measuring tube and noting the FID output voltage. This single reading, in addition to the zero value, should then have been sufficient to determine the FID response, assuming the FID does, in fact, have a linear response over that range. Unfortunately the 1.1% propane in air mixture in the lecture bottle was too concentrated and subsequently caused the electronics associated with the FID to saturate.

Thus, a consistent method was required to reduce the concentration of the gas reaching the FID during calibration. A Signal Series 850 Gas Blender was used to this end. In brief, the exhaust gas from the lorry and a compressed air line were fed at equal inlet pressures into the mixer which then combined to varying degrees which could easily be controlled by the user. The mixing was achieved using a thermal choke inside the mixer.

Unfortunately, the exhaust gases were fed into the mixer at lower pressures than recommended by the manufacturer and thus the calibration was not as reliable as hoped. Appendix C.6 details the problems encountered with the calibration. In short, however, the absolute values of concentration obtained from the FID cannot be relied on. This is a major mishap - a point which cannot be stressed too strongly. To minimize this problem, a final (and correct) calibration was performed using the Gas Blender at the correct inlet pressures. The calibration constant from this calibration was applied to all the results presented in this chapter, based on the assumption that any changes in the day-to-day FID setup were smaller than the errors associated with the incorrect FID calibration. Even so, reliance on the validity of the absolute values of concentration is by no means guaranteed. What can be guaranteed to some extent, though, are the relative values between FID readings taken on the same day which have the same calibration.

In addition to the calibration problems, the FID suffered from drift in the zero readings over periods of time greater than the typical sampling time of 5 or 10 seconds. To overcome this problem, it was first assumed that the sensitivity of the FID did not change appreciably during the testing. Then to account for the drift in the zero reading, the average concentration for the first 0.5 seconds of the trace would be subtracted from the rest of the trace. This initial 0.5 seconds represents a period during which the vehicle and hence the propane had not yet reached the FID to any appreciable degree.

3.2.7 Data Acquisition

The signals from the various measurement devices (FID, hot-wires, Pitot-static and LED trigger) were fed into an Amplicon PC-74A analogue-to-digital conversion board. The board is now somewhat outdated but is still more than adequate for these tests. Up to eight channels are available, offering sampling rates up to several Megahertz with a 12-

bit sensitivity (*ie* 4096 discrete amplitudes can be output). The board was slotted into a IBM-compatible 386 computer with a large hard disc with more than enough capacity for the amounts of data envisaged.

In the mode of operation used here, the conversion from the integer number generated by the board to a voltage is achieved by using the following expression,

$$E = 5.0 \times \left(\frac{i - 2048}{2048} \right) \tag{3.1}$$

where E is the voltage, i is the integer from the board, 5.0 corresponds to the voltage range (-5 V to +5 V) and 2048 is half of the 4096 integer range.

For the determination of the characteristics of the rural and urban boundary layers, the software which accompanies the PC-74A card was used since this involved simply sampling data for a given period of time - see Section 3.3.2. However, due to the complex nature of the MMR tests, especially the need for the sampling to be triggered as the trolley passed, a sampling program was written in FORTRAN which accessed the board directly. In brief, the program was based on the following algorithm:

1. Initialize the A/D board.
2. Take wind-off readings for the channels attached to the pitot-static and hot-wires.
3. Enter a loop which is repeated for n trolley firings:
   (a) Wait for the trolley to fire - this event is determined by the first prong on the trolley passing the FID.
   (b) Start sampling as this first spike on the trigger channel is observed.
   (c) End sampling after the specified period (5 or 10s in all the tests described herein).
   (d) Write the sampled data to disk, after converting from integer levels to voltages, using Equation 3.1 above.
   (e) Try to find the second spike in the stored data.
      - If found, calculate the trolley speed and display.
      - If not found, end the program cleanly.
   (f) Ask the user if they wish to proceed. This option was introduced to give the user some time in which to remedy intermittent problems with the firing mechanism of the MMR during a series of firings.
   (g) Wait for the trolley to return - this event is signaled by two further spikes being detected on the trigger channel.
4. Repeat step 3.

In order to operate correctly, the program has to be started with the trolley in a position just prior to firing.

The sampling rate throughout was 200 Hz, which applied to all five channels used. The two channels for the the cross-wire were routed through a 100 Hz filter.

3.2.8 Flow Visualization

Some rudimentary flow visualization experiments were performed using a smoke generator to seed the air flow. The smoke was then illuminated using bright spotlights. The resultant flow patterns were videotaped and then captured on a Silicon Graphics Indy Workstation. The still colour images thus obtained were then converted to grey-scale images. These were then manipulated so that the brightest regions were coloured red and the darkest blue. In effect, this means that in any such images presented here, the densest areas of smoke are red. This of course is a very rudimentary form of flow visualization but does provide some insight into some of the gross flow features encountered during these investigations - especially in the street canyon.

3.2.9 Wind Tunnel Scaling Requirements

When attempting to model the behaviour of a physical system in a wind tunnel using scale model simulations, it is necessary to be acquainted with the various problems associated with moving to the smaller scale.

Boundary Layer Simulation

When attempting to model an atmospheric boundary layer in a wind tunnel, Baker [8] states that the following dimensionless groups should have the same values at full and model scale:

- Reynolds number, $V(h)H/\nu$, where $V(h)$ is the mean wind speed at height h, H is a typical length of the building or vehicle in question, and ν is the kinematic viscosity of air.
- Gravity number, $gH/V(h)^2$, which indicates the relative sizes of the inertial and gravitational forces.
- Geometric scaling, H/h, as before is perhaps the easiest to obtain in practice.
- Jensen number, z_0/h, where z_0 is the surface roughness, which is needed to ensure the correct velocity profile in the boundary layer.

- Velocity profile, $V(z)/V(h)$, which should follow from the previous point.
- Turbulence intensity profile, $\sigma(z)/V(z)$.
- Length scale profile, ${}^{x}L_u(z)/{}^{x}L_u(h)$.

In practice, it is difficult to fulfill the Reynolds number similarity criteria in the wind tunnel for the following reason. As the geometric scale is reduced by, typically, a factor of 100, the air speed must increase by the same factor in order to maintain the Reynolds number. Quite clearly this is impossible to achieve in practice with near supersonic flows required in the wind tunnel.

Pearce [70] notes that wind tunnel models of full-scale flows become qualitatively similar to the full-scale when the Reynolds number of the flow surpasses some critical value. Mean value functions become largely independent of Reynolds number above these values and it is only effects of small-scale turbulence which are not matched. This has important implications for the present study because of the inherently transient nature of the tests.

The problem of defining the Reynolds number for a general urban area has proved elusive to workers in the area (Hoydysh and Chui [48], Hoydysh *et al* [51] and Bachlin *et al* [3]). For such calculations, some typical length scale needs to be defined and this seems to be the area of most concern and fabrication. There is, however, general agreement that the critical value for the Reynolds number lies somewhere between 1.0×10^3 and 1.0×10^4. However, for some of the tests discussed in Pearce [70] refer to the independence of building pressures on Reynolds number and not pollution concentrations which is of primary concern here.

Moving Vehicle Scaling Requirements

The use of a moving vehicle emitting a stream of gas as it moves introduces a further layer of complexity to the problem of scaling. In order to fully describe the situation, the following variables need to be specified:

- dimensions of the canyon: length, L; height, H; and width, B.
- width of the buildings, W.
- dimensions of the vehicle: length, l; height, h; and width, b.
- speed of the vehicle, U.
- emission rate from the vehicle, q_0, in $\mathrm{m^3 s^{-1}}$.
- concentration of the emitted gas, c_0, in $\mathrm{kgm^{-3}}$.

- mean wind speed at some reference height, u_{ref}.
- air density and dynamic viscosity, ρ and ν.
- elapsed time.

The measured concentration in the canyon is therefore a function of,

$$c = f(H, L, W, B, l, h, b, U, q_0, c_0, g, u_{\text{ref}}, \rho, \mu, t) \tag{3.2}$$

A consistent non-dimensionalized form of the concentration is required. Taking our lead from Meroney *et al* [65], it is proposed to use the following non-dimensionalized form,

$$\frac{cl^2 u_{\text{ref}}}{c_0 q_0} = f\left(\frac{H}{l}, \frac{L}{l}, \frac{W}{l}, \frac{B}{l}, \frac{h}{l}, \frac{b}{l}, \frac{u_{\text{ref}}}{U}, \frac{u_{\text{ref}} l}{\nu}, \frac{q_0}{l^2 u_{\text{ref}}}, \frac{u_{\text{ref}}}{\sqrt{gl}}, \frac{\rho}{\rho_{\text{air}}}\right) \tag{3.3}$$

All geometric scaling is again trivial and only amounts to building the models accurately. Maintaining the ratio u_{ref}/U is also easy - the problems arise with groups such $u_{\text{ref}}/\sqrt{gl}$, a Froude number. For example, with the $1/50^{\text{th}}$ geometric scaling we propose to adopt here, this means that an approximately seven-fold reduction in velocities is required.

Taking the Reynolds number $u_{\text{ref}} l/\nu$, a value of 1.8×10^4 is obtained for a typical speed of 1 ms^{-1} which is somewhat lower, than the ideal, although it is above the values for critical Reynolds numbers discussed in the previous section.

The final group, ρ/ρ_{air}, can, to all intents and purposes, be ignored because this ratio is held constant between full and model scale.

3.2.10 Presentation of Results

Over the course of the next two sections, certain terminology and conventions will used which should be clarified at this stage.

- A right-handed coordinate system is adopted such that,
  - x increases towards the fan, with $x = 0$ lying on the centreline of the slot in the floor through which the model is fired.
  - y increases towards the laser room, with $y = 0$ lying halfway between the control and laser room walls.
  - z increases towards the roof, with $z = 0$ lying on the floor of the tunnel.

  It should be noted that this is not the same coordinate system as that adopted in the analytic model of Chapter 4.
- A *firing* refers to a single pass of the model across the tunnel.

- A *run* refers to a series of firings at the same position, reference wind speed, aspect ratio, etc.
- When presenting the moving model time series data, the results will often be in the form of ensemble averages of a number of individual firings of the model (*ie* the average for a single run).
- The term *breakthrough curve* will be use to mean plots of the variation of concentration at the FID with time.
- The reference wind speed, u_{ref}, is measured using the pitot-static tube, well outside the floor and roof boundary layers.
- A non-dimensionalized time scale, $\tau = Ut/l_v$: where, U, is the vehicle speed; and l_v is the vehicle length is used on the x-axis of the moving model times series plots. The subscript $_v$ is appended to the l because on many of the plots which follow, the use of Helvetica font leads to an ambiguous l which looks like the digit 1.
- The origin on the scaled time axis of the moving model plots coincides with the moment at which the y-coordinate of front of the lorry and the the measuring device coincide. This provides a standard reference point across all the experimental configuration in which the y-coordinates of the FIDs and hot-wires are moved for various reasons.

3.3 Results and Discussion - The Rural Case

3.3.1 Empty Tunnel Case

The proposed investigation called for the generation of both a rural and an urban boundary layer. The latter also had to accommodate several urban canyons. Both boundary layers were originally generated before the installation of the Moving Model Rig.

Before either of the 'simulated' boundary layers were created, several mean along-tunnel velocity and turbulence profiles were taken in the empty tunnel. This was done in a attempt to identify any gross anomalies in the tunnel's flow regime.

Figure 3.9 shows velocity profiles on the centreline of the tunnel ($y = 0$ m) and ± 0.5 and ± 1.0 m either side of the centreline, while Figure 3.10 shows the turbulence intensity profiles at those same positions. From these plots, it is possible to see that the vertical extent of the boundary layer is approximately 400 mm from the floor, which at full-scale equates to about 20 m.

3.3.2 Characteristics of the Rural Boundary Layer

The Rural Boundary Layer was based on a 1:40 scale simulation described in a British Gas Report [82]. Although, the present study requires a 1:50 scale boundary layer, this was thought to be a sufficiently similar simulation. In order to generate this boundary layer a 0.35 m high fence was placed on the tunnel floor at the point where the cross-section of the tunnel became uniform, just downstream of the contraction. This was followed by a fetch of length 19.5 m which was covered in roughness elements consisting of small wooden cubes of side 25 mm, spaced as per Figure 3.11, nailed to large wooden boards.

Three vertical traverses were made, level, in each case, with the rear of the last of the roughness elements (*ie* at $x = 0$). Figures 3.12 and 3.13 show the mean velocity and turbulence profiles along these traverses. The growth of the boundary layer with height in this case was more rapid than in the empty tunnel, as is to be expected with the roughness elements in place.

Values of z_0, the surface roughness, and d, the zero-plane displacement height, were obtained using linear regression on plots of u versus $\log(z-d)$. The values obtained, 0.08 m and 0.5 m respectively, are typical of a rural boundary layer and are shown in summary in Table 3.1. Notice that these values are the full-scale values corresponding to the 1/50th scale we have adopted for these tests.

In addition, a lateral traverse was made from $y = -1.5$ m to $y = +1.5$ m along the line

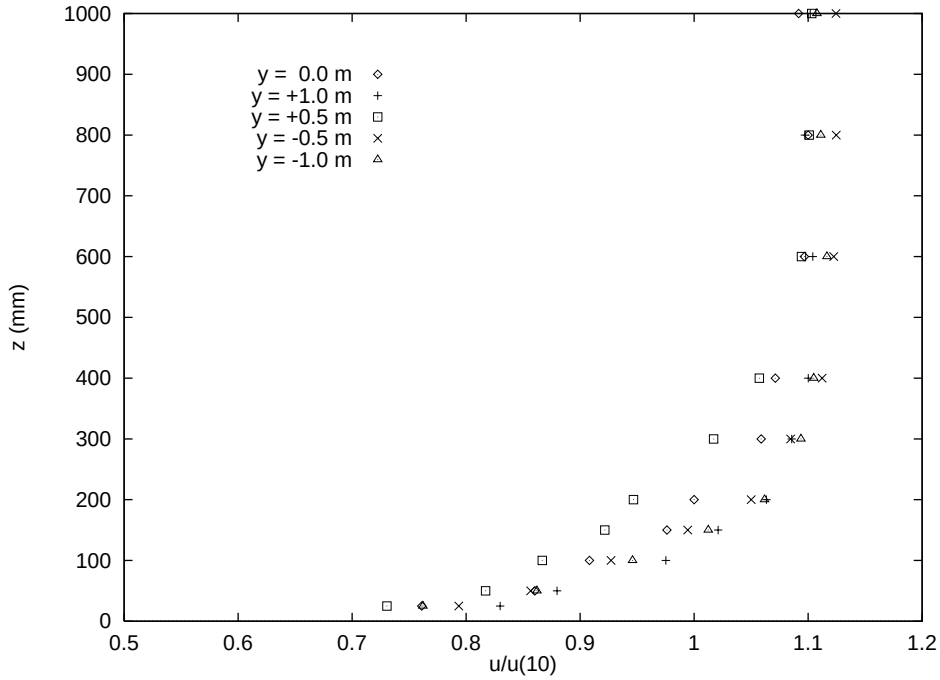


Figure 3.9: Mean velocity profiles in the empty tunnel.

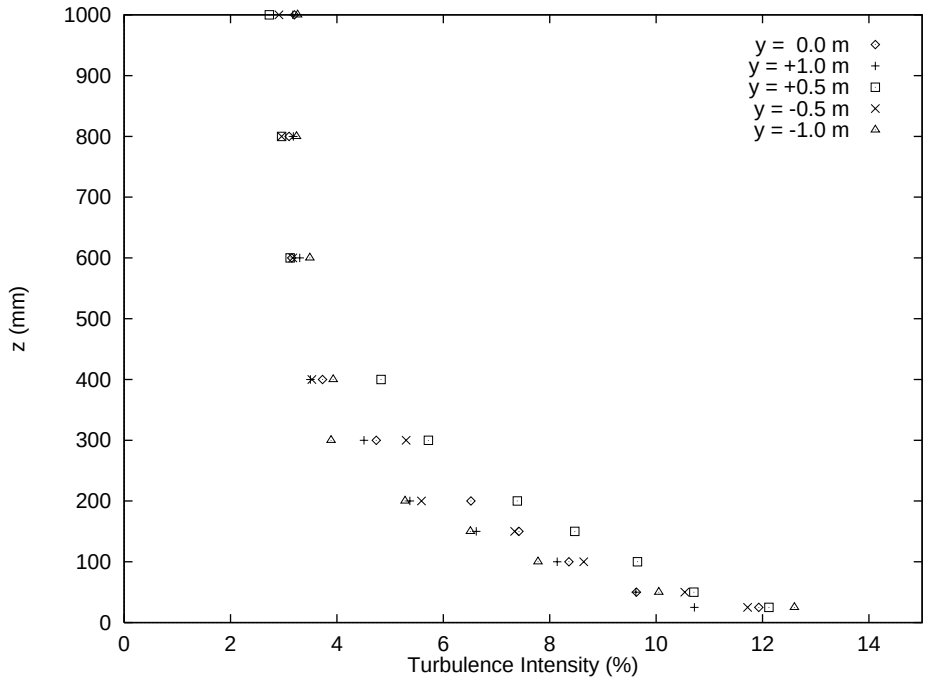


Figure 3.10: Turbulence intensity profiles in the empty tunnel.

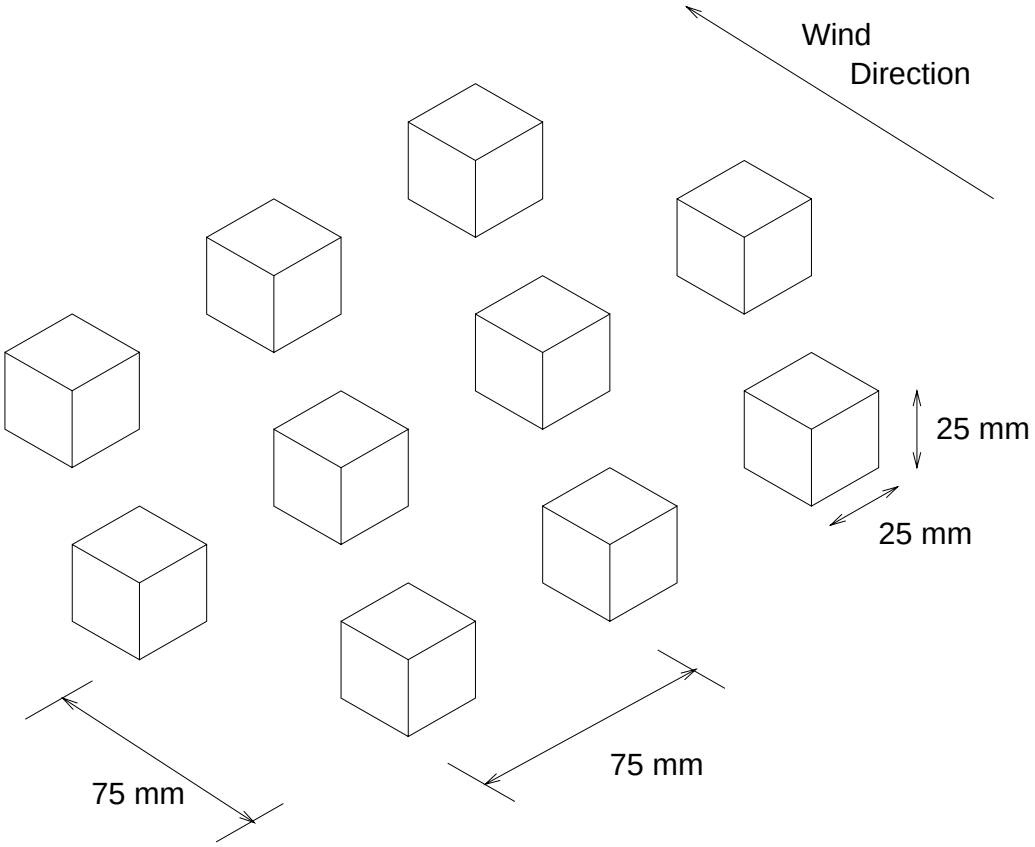


Figure 3.11: Roughness elements used in the simulation of the rural boundary layer.

Configuration	z_0 (m)	d (m)	${}^{x}L_{u(z=10)}$ (m)	**Notes**
Empty Tunnel	0.0015	–	–	No time series are available for analysis due to lack of A/D card at the time.
Rural Boundary Layer #1	0.08	0.5	24.0	Zero-plane displacement height measured from floor of tunnel and not top of the roughness board base.
Urban Boundary Layer #1	0.30	8.0	34.0	

Table 3.1: Summary of the characteristics of the boundary layers used in the testing.

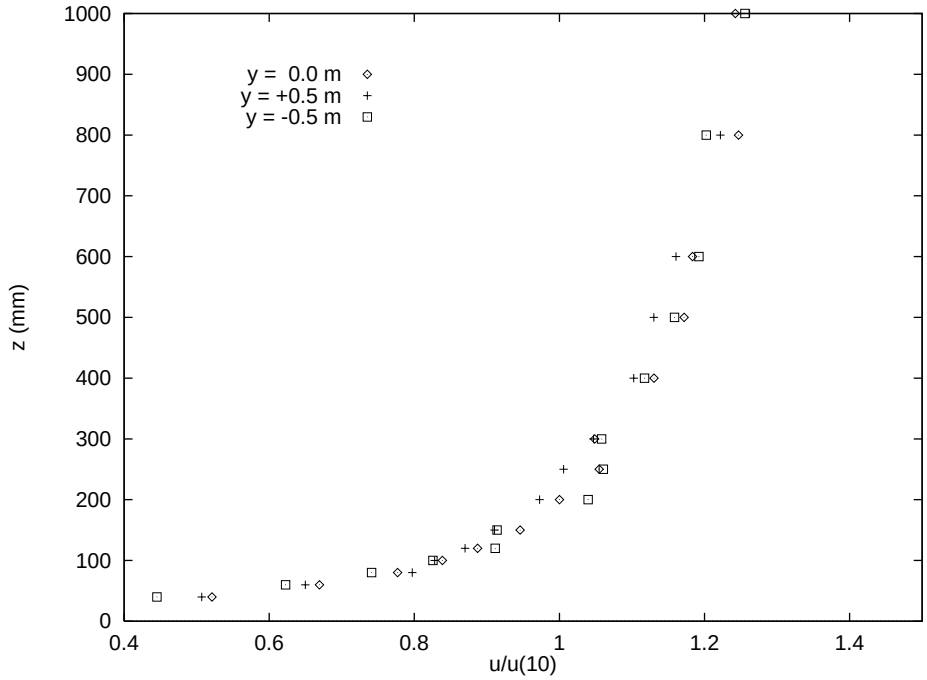


Figure 3.12: Mean velocity profiles for the rural boundary layer.

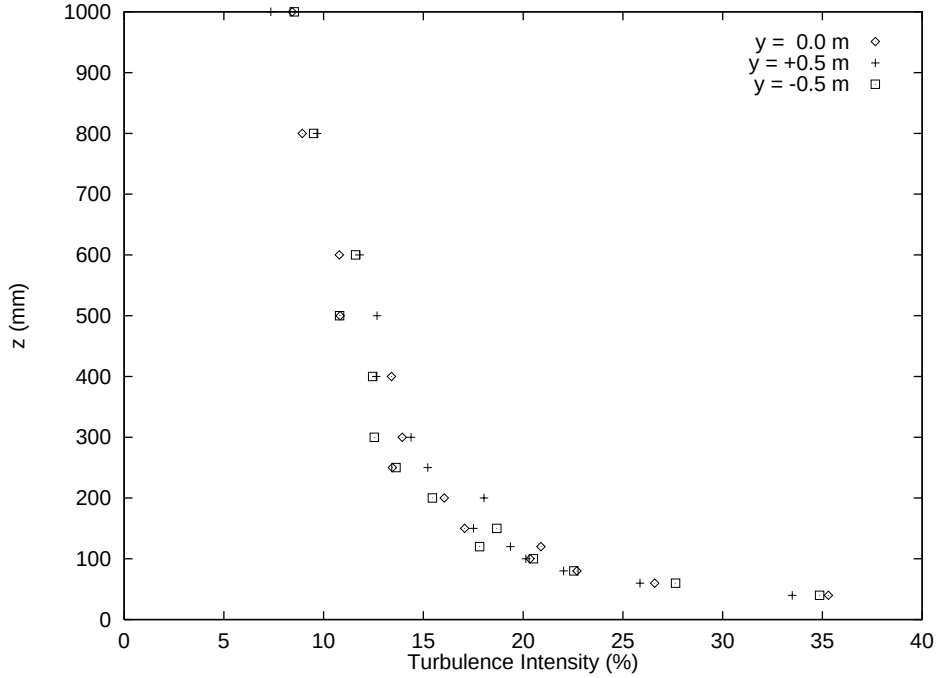


Figure 3.13: Turbulence intensity profiles for the rural boundary layer.

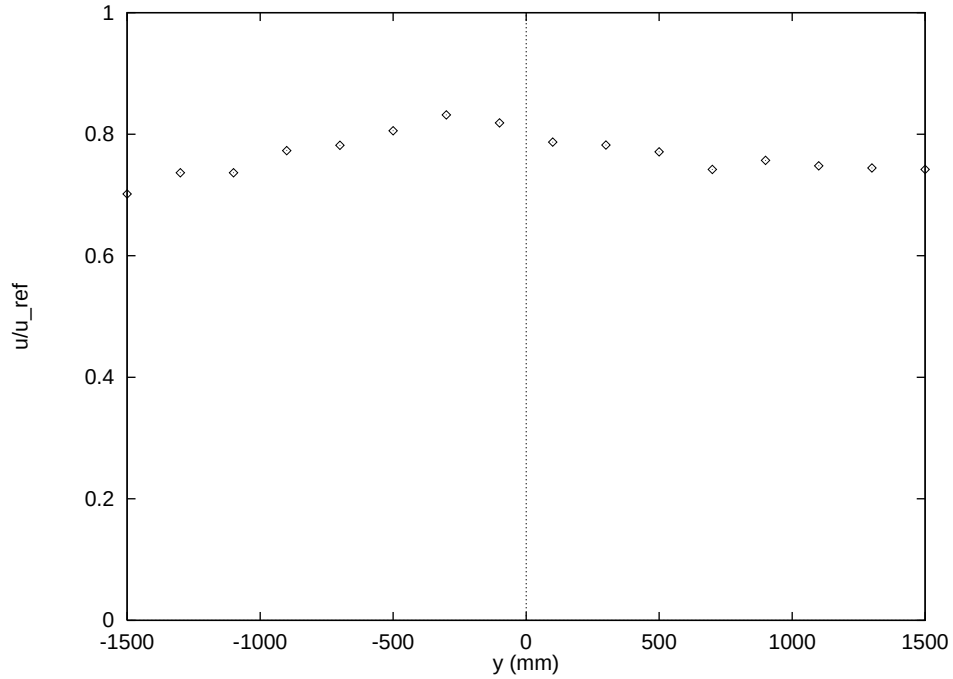


Figure 3.14: Mean u-component of wind speed along the line $x = 0$ m, $z = 0.2$ m.

($x = 0$ m, $z = 0.2$ m), the results of which are shown in Figure 3.14. As can be seen from the Figure, the u-component of wind velocity is lower towards the sides of the tunnel where boundary layer effects come into play. There was a significant increase in velocity, centred around $y = -250$ mm which was thought to be due to a flaw in the flow-straightening honeycomb in the inlet of the tunnel. Figure 3.9 displays similar behaviour: the greatest velocities are observed in the region of $y = -500$ mm. The turbulence intensity along this same lateral traverse was roughly constant, varying by only $\pm 10\%$, with the expected decrease in regions which saw an associated increase in velocity.

Several time histories were recorded at the point $(0, 0, 200)$ mm (*ie* at a height of 10 m full-scale). For each recording period, 4096 samples were taken at a frequency of 250 Hz. The signal from the hot-film was filtered with a low-pass filter whose cut-off was set at 100 Hz. Figures 3.15 and 3.16 show different properties of the spectra obtained from this data. Appendix C.2 discusses the details of the spectral calculations. In both cases, the experimental curve was obtained by averaging the spectra of five time series which were smoothed using a Parzen lag window of size 512 (*c.f.* the total sample size of 4096).

The first is a log-log plot of $S_{uu}(n)$, the power, versus n, the frequency. Also, shown on this plot is the theoretical high frequency slope of $n^{-\frac{5}{3}}$, here slightly displaced for ease of comparison. In Figure 3.16, the non-dimensionalized spectral density, $nS_{uu}(n)/\sigma_u^2$ versus the log of the non-dimensionalized frequency, ${}^{x}L_u n/\overline{u}$ is shown, where $\overline{u}$ is the

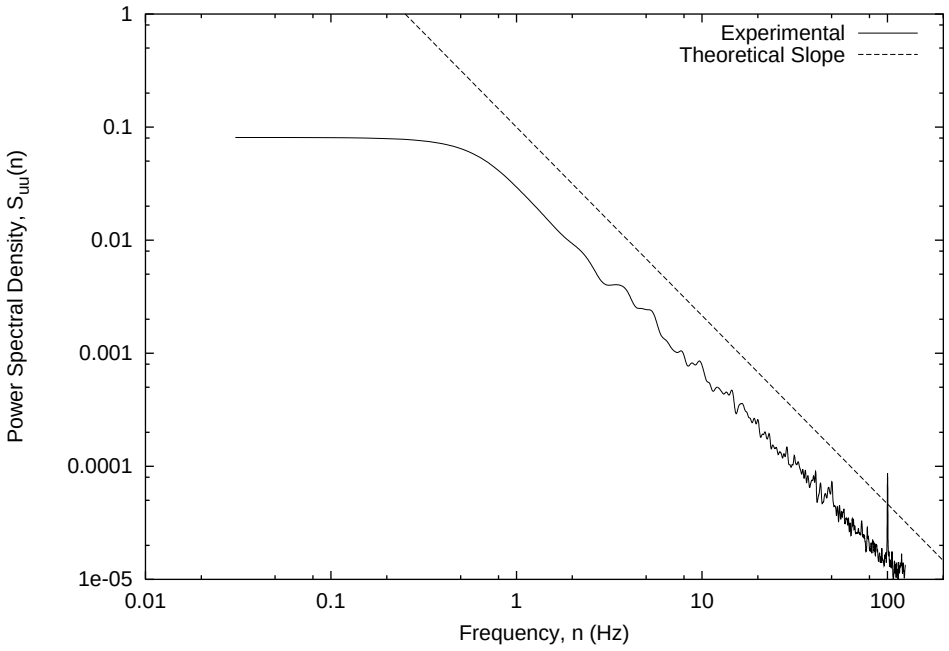


Figure 3.15: Spectral power, $S_{uu}(n)$, against frequency, n, for the rural boundary layer.

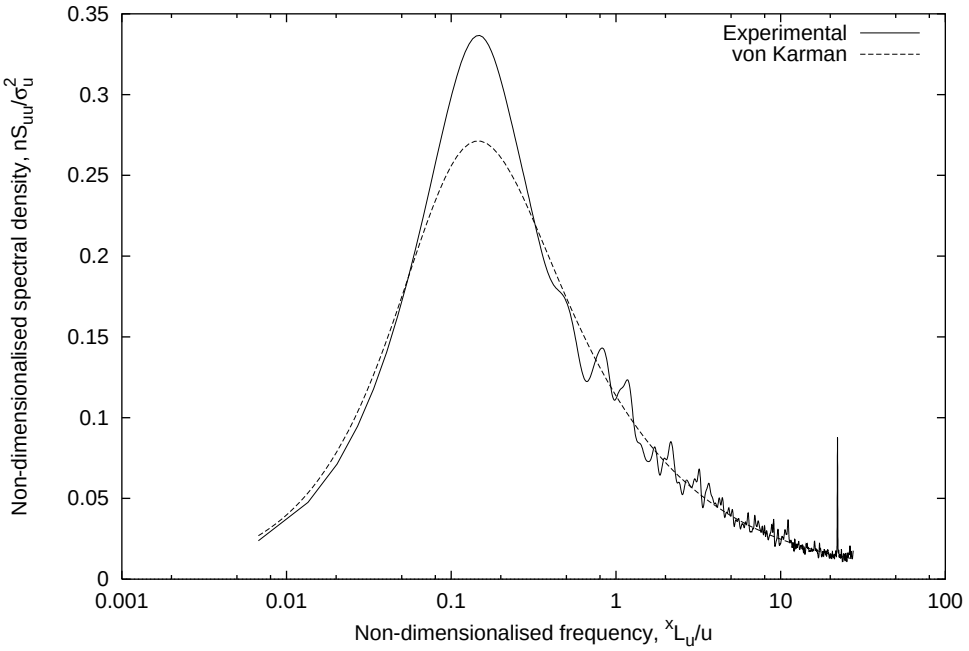


Figure 3.16: Spectral density, $nS_{uu}(n)/\sigma_u^2$, versus frequency, $^xL_u n/\bar{u}$ for the rural boundary layer.

mean value of the along-tunnel component of the wind speed and σ_u^2 is the variance. On this plot both the von Karman and the experimental curves are plotted. The method of determining ${}^xL_u$ is described in detail in Appendix C.3.

The full-scale value of ${}^xL_u$ obtained in this case was 24.0 m at a full-scale height of 10 m. This compares with a value of approximately 80 m for a roughness length of 0.08 m taken from ESDU 85020 [28]. This inequality is often found when trying to reproduce the spectral properties of atmospheric boundary layers in wind tunnels.

On both plots, there is a spike at approximately 100 Hz - the cut-off value for the low-pass filter used when taking the measurements. This is of concern and may be due to a faulty filter.

3.3.3 Effects of a Passing Vehicle in a Cross-wind

With the MMR now in place, it was possible to carry out some novel tests involving the measurement of the wake and the dispersion of pollutant therein behind a vehicle moving in a cross-wind. The rural boundary layer described in the previous section was again simulated. The roughness boards were shifted slightly downstream so that the last of them would butt up to the slot in the tunnel floor. An additional roughness board was placed downstream of the slot in order to preserve the boundary layer in the region of interest. It was not intended to take any measurements upstream of the passing vehicle, mainly for experimental reasons - the FID and hot-wires would, almost inevitably, impede the passage of the vehicle. A gap of about 60 mm was left between the upstream and downstream roughness boards. Any potential loss of propane to the sealed cavity below the tunnel was reduced further by the use of brush-type draught excluders across the gap.

Variation of Concentration with Exhaust Flow Rate

In what was essentially a preliminary study, a single FID and the cross-wire were fixed to the traverse in close proximity to each other, separated by 40 mm in the cross-tunnel direction. Throughout the following, the two measuring devices sat either side of the centre-line of the tunnel. The cross-wire was oriented such that it would give positive readings of the *u*-component of flow along the the tunnel, towards the fan. The *v*-component would be positive in the cross-tunnel direction (*ie* in the direction of travel of the vehicle). Although there was expected to be some variation in the *w*-component of the flow in the wake, it was thought that this would be the least revealing aspect of the flow and so the decision was made to ignore it for the present study.

With the FID calibrated and in-situ, a short study was conducted to investigate the effect of varying the exhaust flow rate from the lorry. It should be noted that little or no effect

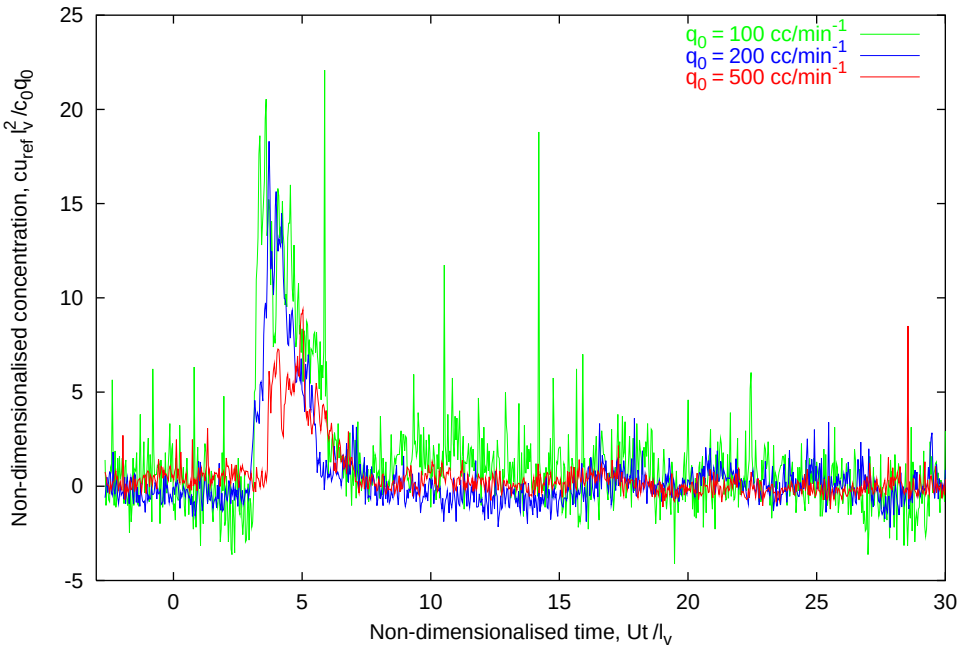


Figure 3.17: Variation of pollutant concentration with exhaust flow rate.

was measured by the FID for a flow rate of 50 cm^3min^{-1}. The response of the FID for the three flow rates of 100, 200 and 500 cm^3min^{-1} is shown in Figure 3.17. The probes were positioned close to the passing lorry at $(l, 0, h/2)$. The reference wind speed in the tunnel was set to about 2 ms^{-1} and the vehicle speed was also about 2 ms^{-1}. There were slight variations in both speeds during the runs but these are included in any results presented.

Figure 3.17 suggests, by the fact that the three curves have not collapsed onto each other, that the flow rate and concentration are not directly related. This is, however, difficult to believe inasmuch as it goes against all the theoretical models. It may well be that the higher ejection speed (4.7 ms^{-1}) of the exhaust gas at 500 cm^3min^{-1} is causing more mixing than the lower ejection speeds.

Due to a breakdown in the mechanical switch used to turn the exhaust gas on and off, only these three runs were possible in the initial study. Obviously, three runs are not sufficient to gain much insight into the process of diffusion in the wake of a vehicle. What they did show at this stage, however, is that the methodology was sound and the shapes of the breakthrough curves were qualitatively, at least, in line with expectations.

With the experience gained from the preliminary study, a further series of tests were conducted with very much the same setup as before with one or two exceptions. For instance, the launching mechanism on the MMR was re-designed and made more reliable and the small gas switch on the trolley was replaced with a much more robust one which

subsequently proved to be very durable.

Variation of Vehicle Wake with Wind Speed

Before any discussion of the dispersion of the exhaust gas from the moving vehicle, it is revealing to look first at the effects on the air flow near the vehicle. Using the cross-wires in close proximity to the vehicle it was possible to observe the disturbance quite clearly.

Figures 3.18(a) to (c) show the variation of both the u and v-components of the flow at the cross-wire as the mean wind speed in the tunnel is varied. The components of flow are normalized with respect to the reference wind speed, u_{ref}. The hot-wire was positioned at $(l/2, 0, h/2)$ for these measurements. Throughout the following the vehicle speed, U, is approximately 3 ms^{-1}.

It can be seen from the Figure that for all wind speeds, there is a sudden increase in u-component as the air speeds up in front of the lorry, followed by the expected dip as the lorry blocks the cross-wind. There is not such a discernible increase as the rear of the vehicle passes. Notice also that the initial peak occurs sooner at the higher tunnel speed than for the lower speed - due to the faster propagation of the disturbance at the higher speed.

In the absence of the vehicle wake, the v-component of the wind is, on average, zero. However, when the lorry passes there can be observed an initial dip as the bow wave of the vehicle passes - possibly due to a small separation region in the lee of the vehicle. Following the dip, the wake of the vehicle is seen as the air behind the vehicle is dragged along and we see a peak in the positive y-direction. The duration of the peak is longer at the lower wind speed, but the effect is much smaller in absolute terms. This can be explained by the fact that the turbulent mixing process has more time to disperse the wake before it reaches the cross-wires than at the higher wind speed.

Variation of Vehicle Wake with Distance Downstream

The variation of the components of flow in the wake with varying distance downstream is now discussed. Figures 3.18(a) and then (d), (e) and (f) show ensemble averages of both components at four positions downstream of the vehicle. In this case, the u-components tell us very little, but there is a distinct peak in the v-component at all four positions. Again, this is a very clear representation of the air being pulled behind the vehicle in the wake. In order to investigate this effect further, a Gaussian of the form,

$$f(x) = ae^{-b(x-c)^2} + d$$

where a, b, c and d are constants, was fitted to each peak using the GNUPLOT[2] plotting package. The position downstream was then plotted against the constants, c, which correspond to the position of the peak, obtained in each case. From the gradient of this line, it was possible to calculate a speed of propagation for the wake effect which was found to be $\approx 0.6u_{\text{ref}}$ which is the wind speed at a height of $z = h/2$ - a fact which can be confirmed by looking at the u-components of the wind speed in all these plots. Thus, it may be said that the wake effect is transported downstream of the vehicle at the speed of the local wind field close to the floor.

An interesting rider to this observation is that the intercept of the straight line did not pass through the origin. This is due to the fact that the peak of the disturbance was used as a measure of the position of the wake and not the first indication of its arrival, the position of which was more difficult to determine accurately.

Concentration Time Series for Individual Firings

Before moving on to discuss the general behaviour of the gas in the wake of the moving vehicle, it is instructive to look at the behaviour of the FID over the 20 firings in each individual run. Figure 3.19 shows the traces for 20 such firings of the MMR with $u_{\text{ref}}/U = 0.54$ at a distance $l_v/2$ downstream of the model. The important thing to notice about these plots is not the values on the scales but rather the distinct lack of consistency between firings. Some firings have a single, sharp peak, others two or more peaks. The magnitude of the traces also varies considerably - almost by an order of magnitude in some cases. This behaviour is characteristic of a turbulent, chaotic system such as the wind - here with the added complication of a moving bluff body.

It is usual practice to take averages of such effects in wind engineering to gain an insight into the general effect such as the mean wind loading on a building. The process being studied here is not stationary and so the idea of taking averages is open to question. The averaging process tends to obscure very real effects such as those seen in Firings 17, 18 and 19 in Figure 3.19 in which three consecutive firings reveal a definite double peak. This could be mere coincidence or could be evidence of a large eddy behind the vehicle which delays the movement of about half the pollutant.

It is nevertheless useful to present ensemble averages of the runs in order to see general effects, even though these interesting 'snapshots' become obscured. From time to time, when it is thought relevant, such individual plots will be presented to demonstrate real effects which the ensemble plots do not.

[2]GNUPLOT is a free plotting package available on most UNIX systems. It has extensive curve fitting abilities. Most of the plots in this thesis were produced using it.

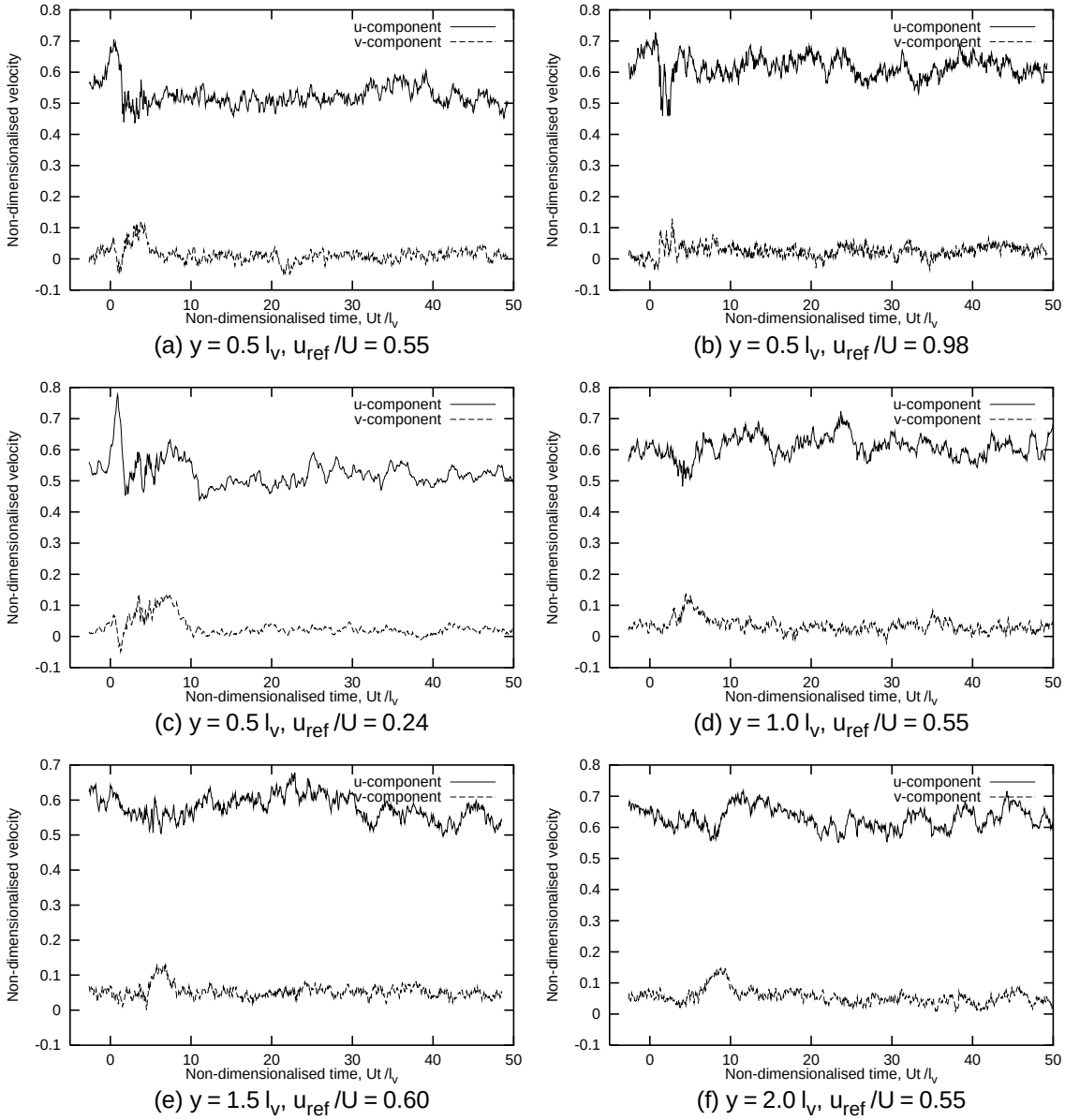


Figure 3.18: Six plots showing the variation of both the *u*- and *v*-components in the wake of vehicle with both wind speed (a, b and c) and distance downstream (a, d, e, and f).

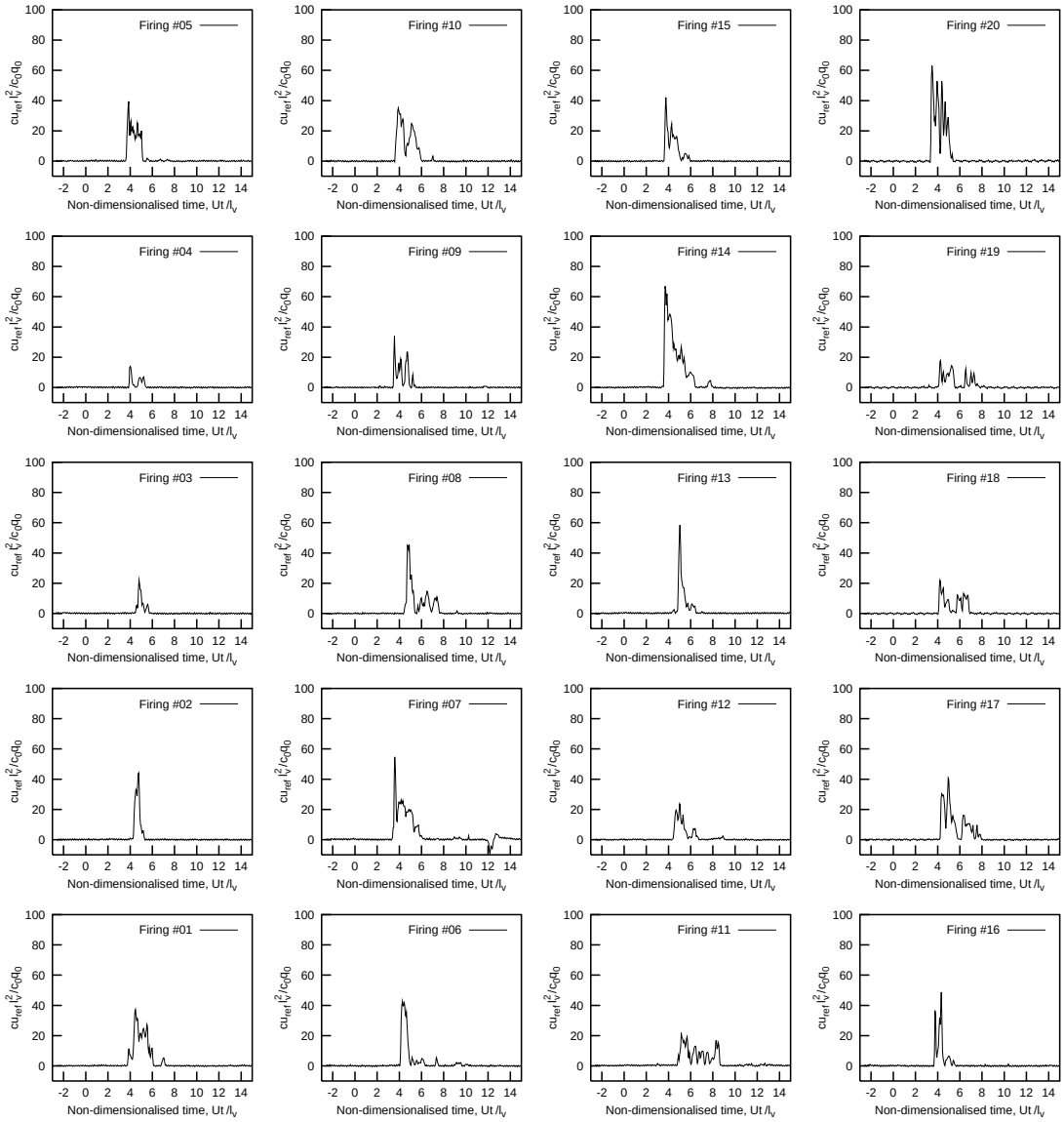


Figure 3.19: Twenty individual concentration time series for $u_{\mathrm{ref}}/U = 0.54$ at $(l_v/2, 0, h_v/2)$.

Variation of Concentration with Wind Speed

Figure 3.20 shows the effect on the scaled concentration of varying the reference wind speed. Notice that the normalized concentration this time used the vehicle speed, U, as the velocity scaling. This was done so that the general trend would not be obscured by scaling effects. It can be seen from the plot that the lower the wind speed, the longer the pollutant takes to reach the receptor which was positioned at $(l_v/2, 0, h_v/2)$. Equally important is the increased spread at the lower wind speed. This is due to the longer period of mixing in the wind which would thus appear to be the dominant cause of mixing at these speeds. The wake of the vehicle could be said to be a secondary source of mixing.

The unexpected aspect of this plot, however, is the magnitude of the breakthrough curves. In relative terms, these results are reliable because they were all taken on the same day in quick succession and hence the FID was calibrated the same for each run. These results suggest that there is the maximum peak value is observed around values of $u_{\text{ref}}/U = 0.5$ which falls off as the wind speed diverges from this value. These three results, unfortunately, are insufficient to make such observations with any degree of confidence.

Variation of Concentration with Distance Downstream

Figure 3.21 shows the expected variation of scaled concentration with distance downstream of the MMR for single wind speed, $u_{\text{ref}}/U = 0.5$. It can be clearly seen that the classic spread of pollutant downwind of the source is being followed in this case. The increasing time at which breakthrough occurs, the diminishing peak value and the increased spread of the trace are all indicative of a Gaussian-like pollutant spread.

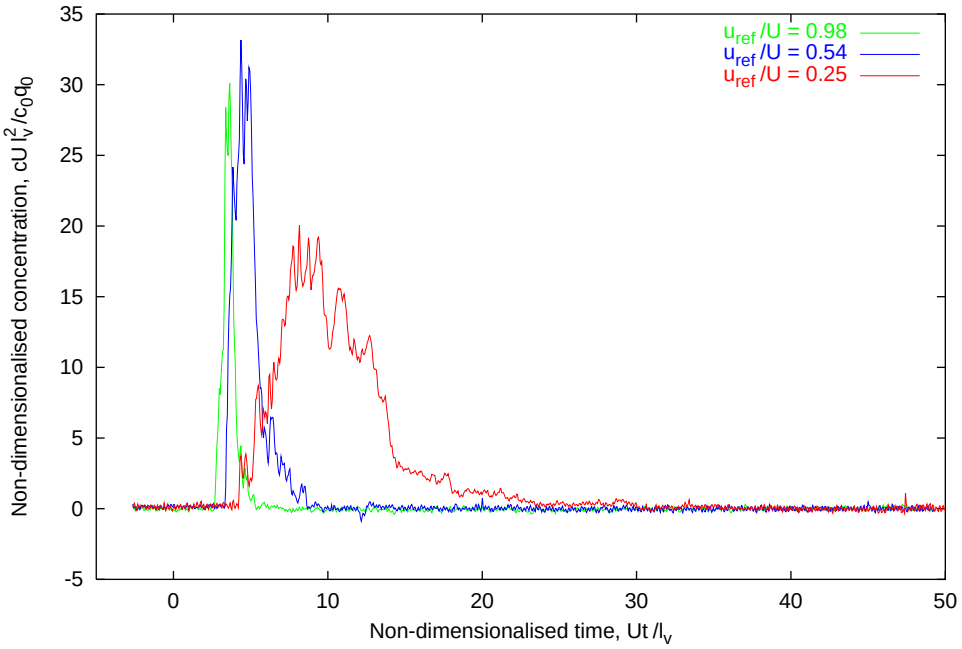


Figure 3.20: Variation of scaled concentration with reference wind speed.

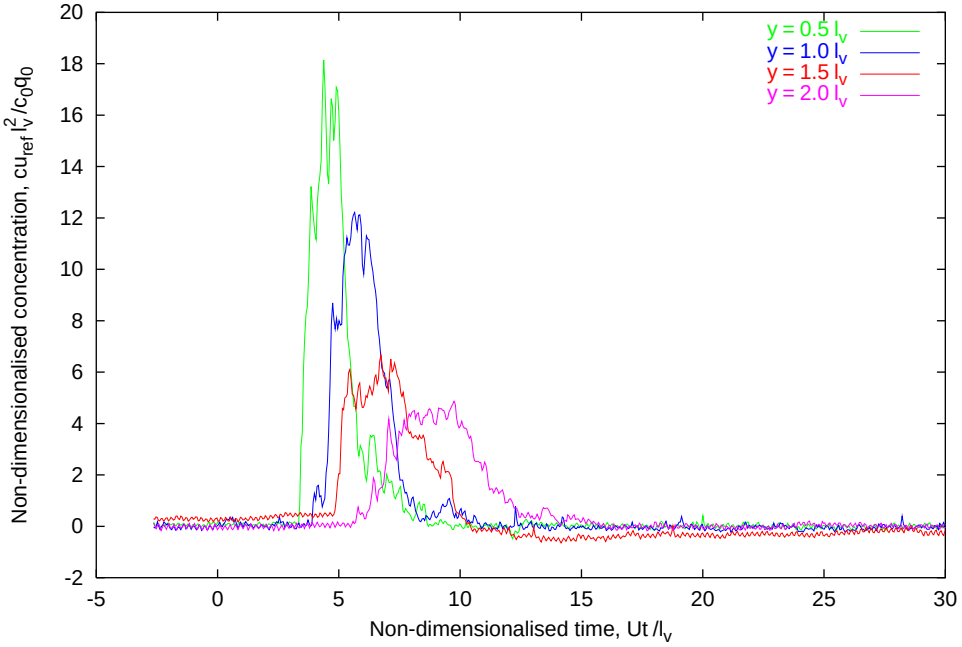


Figure 3.21: Variation of scaled concentration with distance downwind.

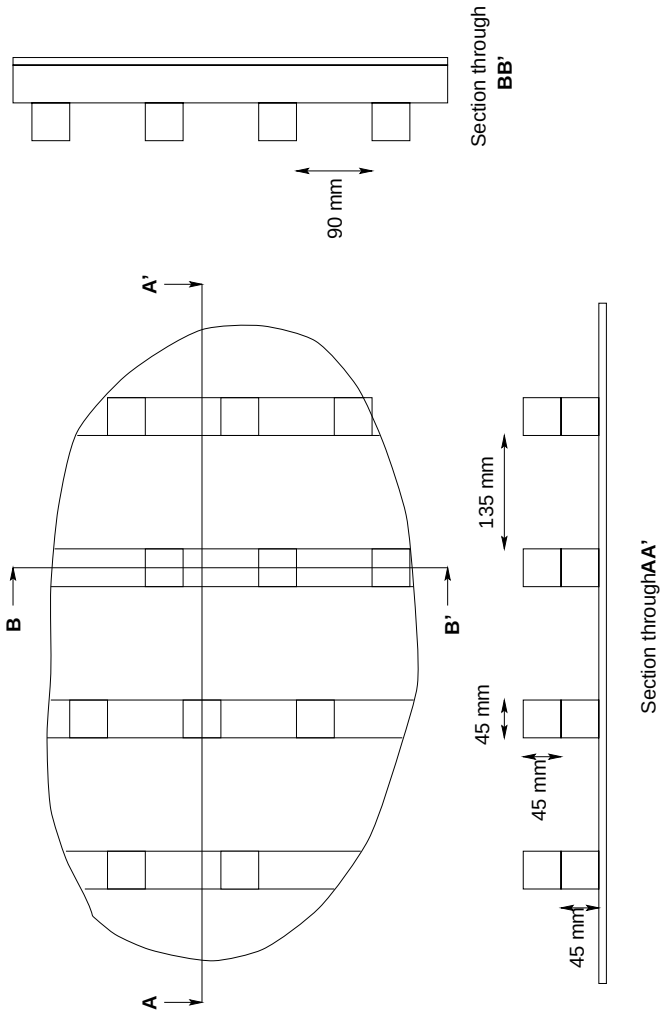


Figure 3.22: Roughness elements used in the simulation of the urban boundary layer.

3.4 Results and Discussion - The Urban Case

3.4.1 Characteristics of the Urban Boundary Layer

A second boundary layer was constructed. This time the aim was to simulate a typical sub-urban approach to an idealized group of urban street canyons. Thus, a sufficiently turbulent boundary layer with a zero-plane displacement height somewhere near the height of the street canyons, some 10 m full-scale, was required. To achieve this, the same fence as for the rural simulation was used but this time was followed by 15 m of large roughness boards[3], the layout of which is shown in Figure 3.22.

[3]It should be noted that the first 8.5 m of roughness boards were too short to span the tunnel and so had to be staggered to prevent any serious flow funneling from taking place.

Downstream of the roughness boards, a series of large roughness elements (190 mm cubes), were placed in one half row and two complete rows across the wind tunnel. The rows were offset from each other by the width of a block in order to create optimal mixing conditions. The purpose of these blocks was to raise the zero-plane displacement height prior to the street canyons.

Finally, the street canyons, consisting of 5 rows of buildings, were placed across the wind tunnel, the rear face of the last building lying at $x = 0$ m. For the initial generation of the boundary layer, the canyons were given an aspect ratio of 1:1, or a width of 200 mm. These five rows of buildings, along with the large blocks just upstream, were thought to be sufficient to ensure that the downstream canyon would not lie in the transition zone between the roughness boards and the simulated urban region. Hoydysh *et al* [51] indicate that "several rows of buildings are necessary..." in order that this criterion be satisfied.

It should be noted that the rows of buildings spanned the full width of the tunnel. Each row consisted of two 2 m lengths with cross-sections of 0.2×0.2 m. Because of the slight bowing of the tunnel and the model buildings, the last two rows of buildings were taped in place both in an attempt to seal any gaps and to hold them in place more securely.

Figure 3.23 shows the variation of the u-component of wind speed with height for the urban canyon case. The readings were taken above the centreline of the last canyon. The growth of the roof boundary layer can be seen clearly here.

Again, linear regression analysis was used to calculate the values of z_0 and d for this boundary layer. The values obtained, respectively 0.30 m and 8.0 m (from Table 3.1), are in good agreement with those of a typical urban boundary layer. Table 2.1 in Chapter 2 lists the properties of typical boundary layers over a whole range of surfaces.

A good deal more data was gathered for the urban boundary layer, including numerous time series at various heights above the canyon (sampling rates and durations were the same as for the rural boundary layer). Figures 3.25 and 3.26 show similar spectra to those presented earlier for the rural boundary layer. The first is a log-log plot of $S_{uu}(n)$ versus n, with the displaced theoretical slope again present for comparison. The second is a non-dimensionalized plot which is overlayed with the von Karman spectra.

The full-scale value of ${}^{x}L_u$ obtained from this analysis was found to be 34.0 m (Table 3.1). Again comparison with the ESDU 85020 tables reveals that this compares unfavourably with the actual value of 65 m. Such discrepancy in the characteristic length scale scaling is a fundamental flaw in the modelling of atmospheric boundary layers in wind tunnels. Indeed, it should be noted that the value for the urban boundary layer is better than for the rural case.

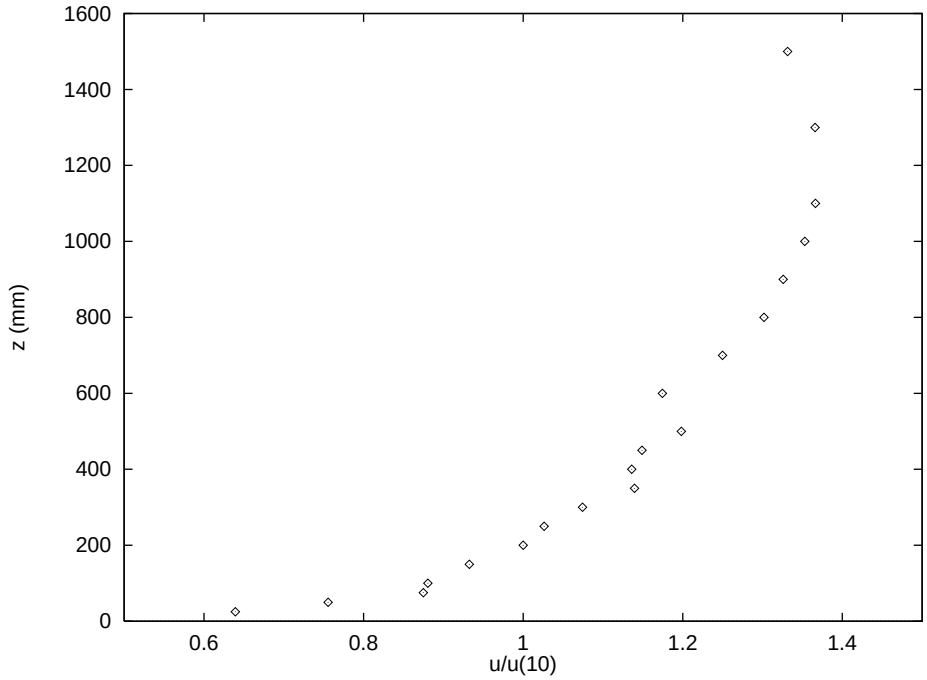


Figure 3.23: Mean velocity profile for the urban boundary layer.

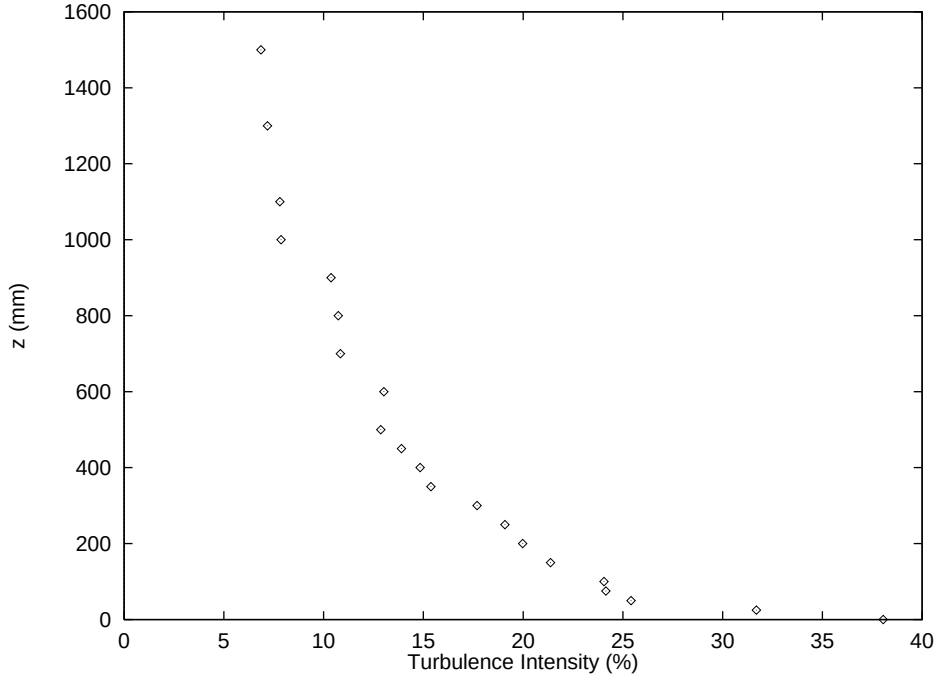


Figure 3.24: Mean turbulence profile for the urban boundary layer.

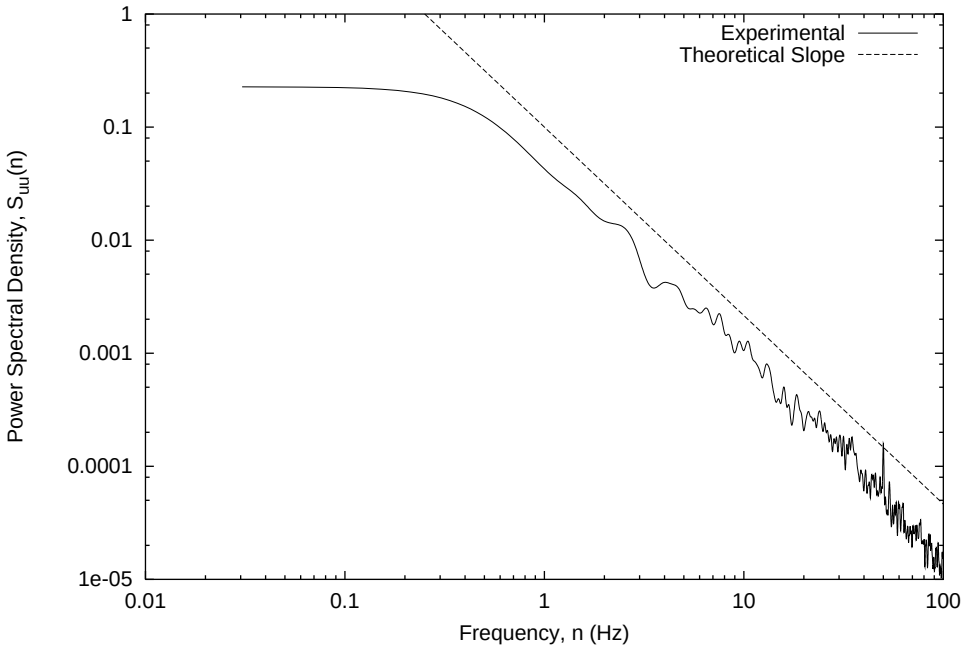


Figure 3.25: Spectral power, $S_{uu}(n)$, against frequency, n, for the urban boundary layer.

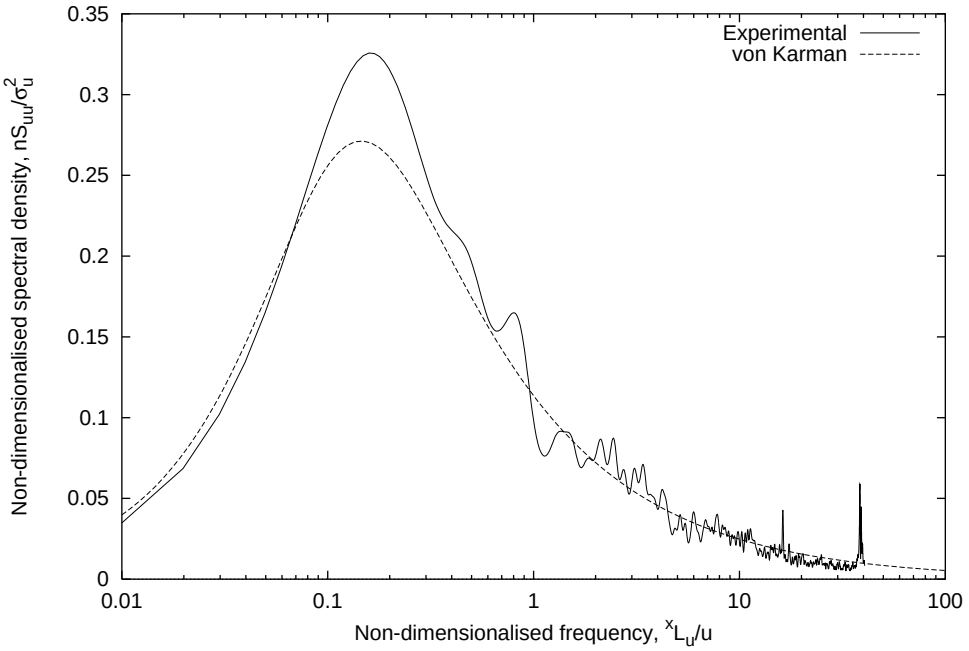


Figure 3.26: Spectral density, $nS_{uu}(n)/\sigma_u^2$, against frequency, $^xL_u n/\bar{u}$ for the urban boundary layer.

3.4.2 Vortex Flow in the Street Canyon

Two hot-wire traverses were made in the last (furthest downstream) street canyon. One traverse measured the variation of the *u*-component of flow along the vertical centreline of the canyon, while the other measured the variation of the *w*-component along the horizontal centreline. Figures 3.27 and 3.28 show the results more clearly. Notice the scaling of the flow components with respect to the reference wind speed, u_{ref}. Also, the error bars represent the turbulence measured at these positions, the size of the bars being relative to the mean value measured.

This is a good example of the limitations of using hot-wires in such directional, turbulent flow[4]. Not being able to discern the direction of the flow with a single hot-wire, flows that on average have a mean velocity around zero are seen to have artificially high turbulence levels. A further consequence is that the flow reversal one would expect in the the canyon vortex is not seen, in absolute terms at least.

These two plots do give an indication of the rate of rotation of the vortex in the canyon. If it assumed that the speed of rotation is directly related to the reference wind speed (for which there is some evidence - Yamartino and Wiegand [89]), then it can be seen, at least in broad terms, that the rotation component of the flow is about $0.3u_{\text{ref}}$ towards the walls and floor of the canyon.

3.4.3 Flow Visualization

To reinforce the view that vortices were indeed present in the canyons in this configuration, some flow visualization tests were performed using smoke illuminated by spotlights. Figure 3.29 shows a typical stable vortex in a 1:1 aspect ratio canyon with $u_{\text{ref}} \approx 1.5\,\text{ms}^{-1}$, while Figure 3.30 shows the less stable situation for the wider 2:1 aspect ratio canyon at the same wind speed. Both these Figures have been altered so that the regions of highest intensity red correspond to those areas of densest smoke. Also, the images have been annotated using a drawing package to make the various features, such as the canyon walls and the smoke nozzle, more obvious.

The first of the two figures clearly shows the stable vortex that can exist in canyons in the skimming flow regime. Notice that the concentrations are distinctly higher on the leeward wall in this case. This may well be largely due to the direction in which the smoke is being ejected from the nozzle (from left to right on the picture), but this effect was seen on other stills taken from the video. The second Figure shows an instant when the vortex in the wider canyon had broken down.

[4] An attempt was made to use Laser Doppler Anemometry at this point but the equipment loaned to us by British Gas was somewhat faulty and it was not possible to resolve the flow to any satisfactory degree.

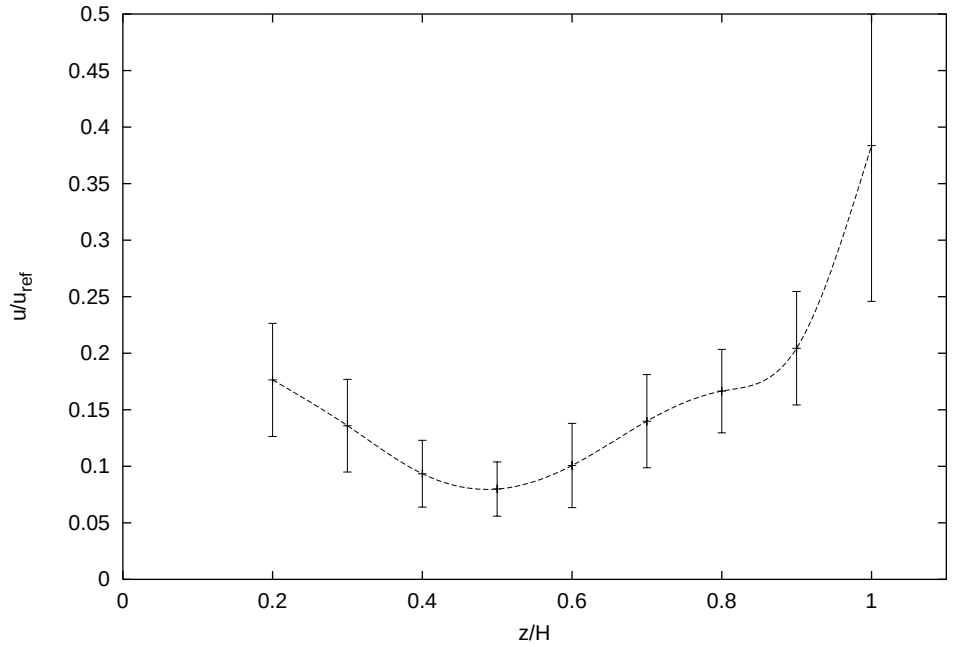


Figure 3.27: *u*-component of flow along the vertical centreline of the last canyon.

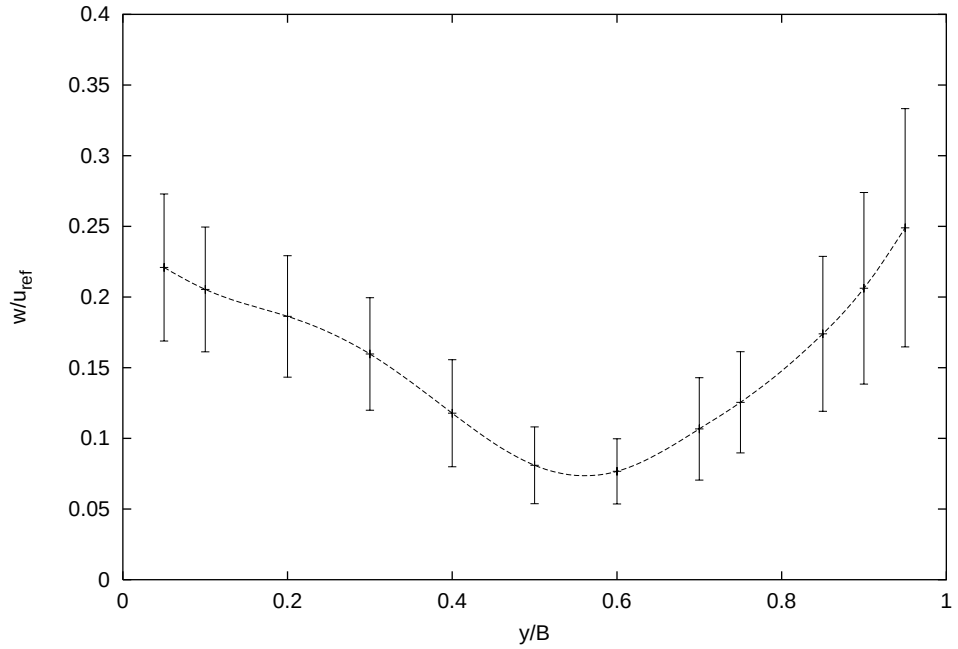


Figure 3.28: *w*-component of flow along the horizontal centreline of the last canyon.

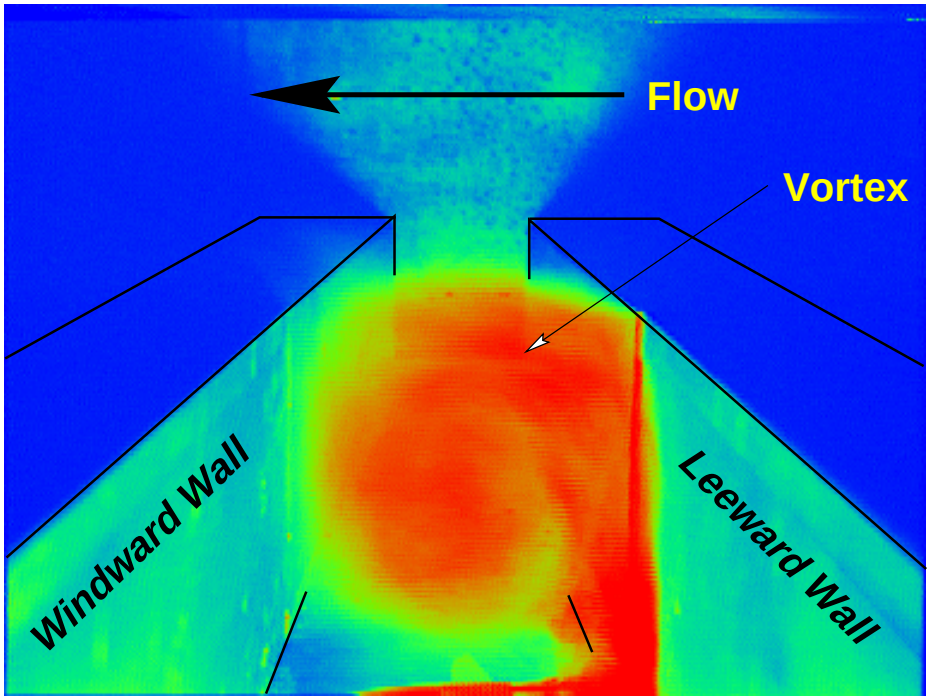


Figure 3.29: Video capture of a strong vortex in a 1:1 aspect ratio street canyon.

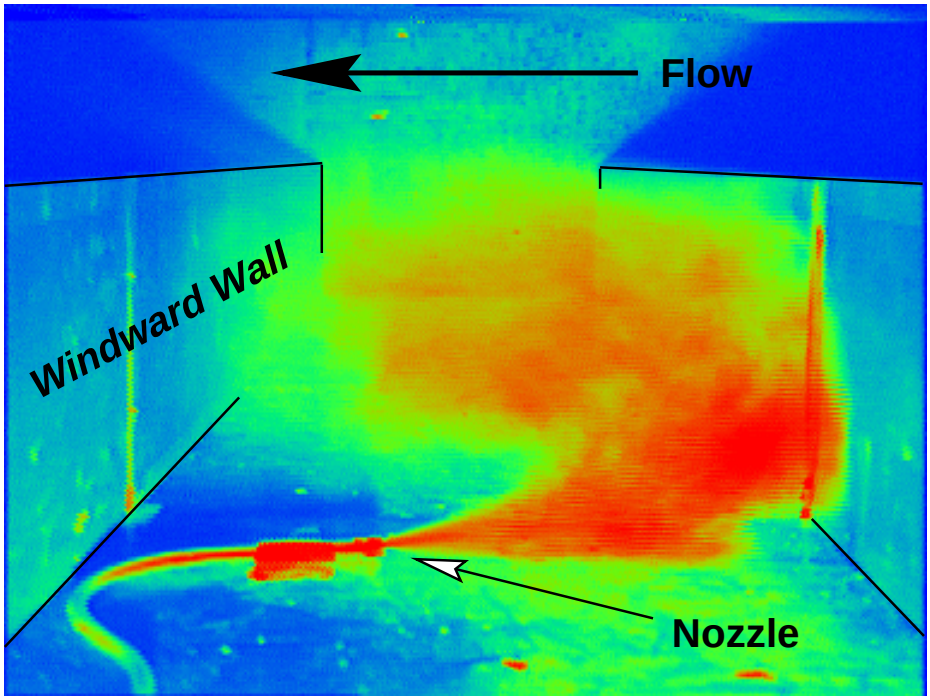


Figure 3.30: Video capture of a intermittent vortex in a 2:1 aspect ratio street canyon.

3.4.4 Effects of a Passing Vehicle in a Street Canyon

The following results were taken well after this initial investigation has been completed and the MMR had been installed. The roughness elements and canyons were re-introduced into the tunnel in exactly the same configuration as before. The centreline of the slot in the tunnel floor coincided with the centreline of the last street canyon which initially had an aspect ratio of 1:1.

For this set of experiments, the FID was mounted inside one of the half-rows of buildings - see Figure 3.31(a). The sampling tube of the FID was then connected to any one of the seven syringe tubes which protruded into the canyon through the wall of the building. The positions of the tubes were as follows: $7H/8$, $3H/4$, $5H/8$, $H/2$, $3H/8$, $H/4$ and $H/8$. For measurements on the leeward wall, the half-row was positioned upstream of the MMR slot: for windward wall measurements it was rotated through 180 degrees and was swapped with the half-row downstream of the slot on the laser room side of the tunnel, hence the appearance of two arrays of probes in Figure 3.31(b) either side of the tunnel centreline. Thus it was necessary only to fabricate one half-row which could hold the FID and all its requisite gas supply and exhaust tubes.

Concentration Time Series for Individual Firings

As with the rural case, it is first useful to look at the range of time series obtained for all the firings of a single run of the model. The first such group of time series (Figure 3.32) show the time series obtained at the foot of the leeward wall ($z = H/8$), with $u_{\mathrm{ref}}/U = 1$ for a 1:1 aspect ratio canyon.

With reference back to the previous plot of this type in the rural case which displayed very little consistency between individual firings, this series of firings does display some noticeable features. For instance, on many of the plots there is an initial peak followed by a quick drop and then a more prolonged second peak. Firing 5 is a good example of this type of trace. There are other traces in which this double peak is smeared into one. This is to be expected due to the highly turbulent nature of the flow in the canyon.

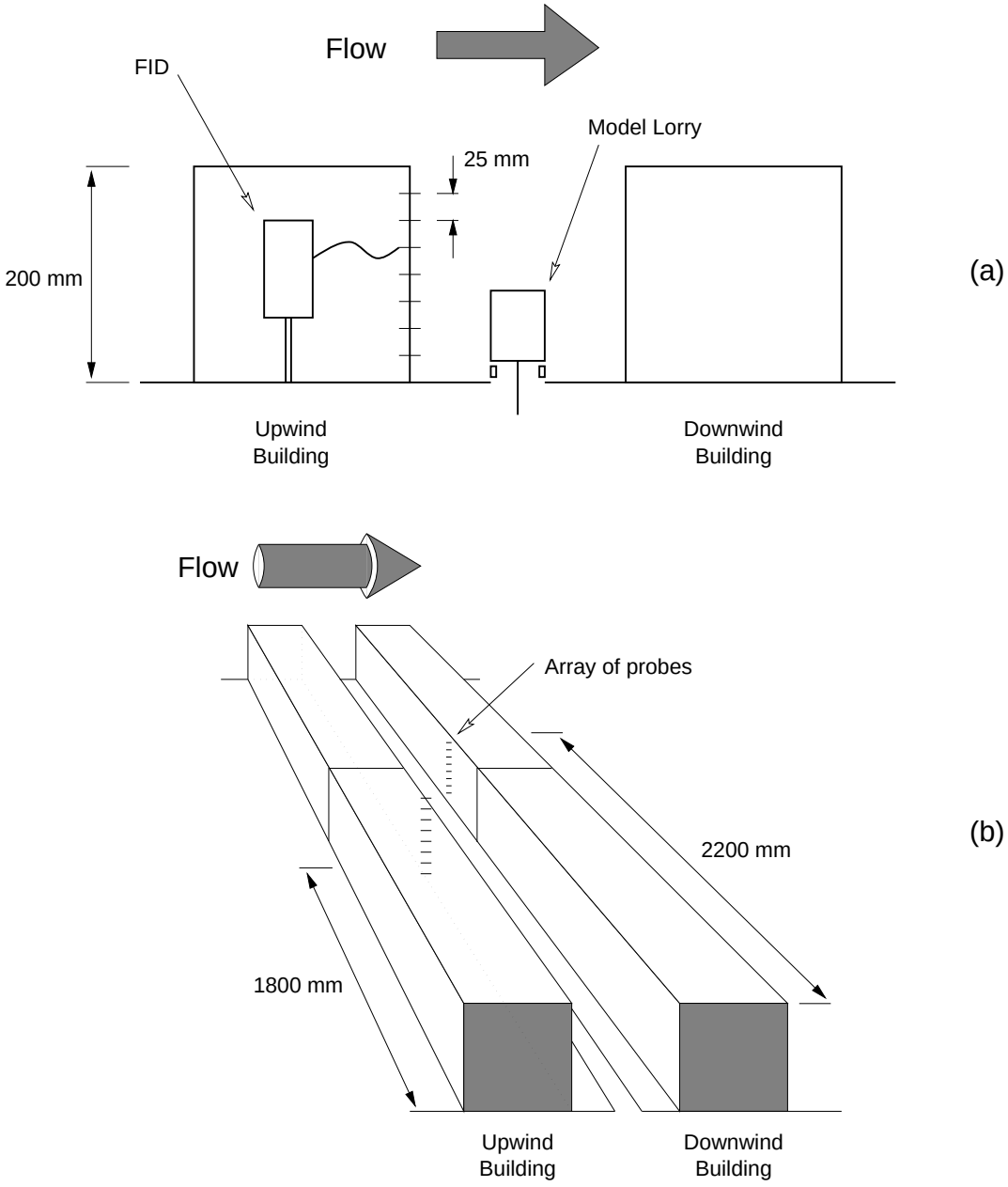


Figure 3.31: Street canyon configuration in the wind tunnel.

To get some feel for the time scales of the processes occurring in the canyon it is possible to perform a quick 'back-of-the-envelope' calculation[5] for the time it should take a massless particle to complete one revolution of the canyon. Using the parameters in this case and the fact that the speed of rotation of the vortex in the canyon is approximately $0.3u_{\text{ref}}$ (see Section 3.4.2), the non-dimensionless time of rotation, τ_P is ≈ 7.4. Those of the time series in Figure 3.32 which do display a double peak have the peak separated by something of the order of this period. While not conclusive evidence of the vortex, these results do tend to suggest that the pollutant is being swept round the canyon in the way observed by many other workers.

Variation of Concentration with Height

In this section, a series of plots showing how the ensemble averaged concentration time series vary with height on both the leeward and windward walls of the canyon for a number of aspect ratios. As the gathering of this data spanned several days (and therefore several FID calibrations), there may be problems with the absolute values of the concentrations presented here for reasons explained in Section 3.2.6. In all cases, only three positions on either wall were looked at. This was due to the time constraints placed on the experimental programme.

Figure 3.33 shows the variation in concentration on the leeward wall of a 1:1 aspect ratio canyon. A peak is seen at $z = H/2$ which is perhaps suggested by the analytical model (see Section 4.4.2). Figure 3.34 shows a similar plot with the aspect ratio increased to 2. Further evidence of the peak in concentration occuring at half-height in the canyon. One other interesting thing to note is the breakthrough times on the two plots. In both cases[6], the pollution arrives at $z = H/2$ first, with the foot of the canyon next to sense the gas. Intuitively, one would expect the sensor at the foot of the canyon to be first to register the presence of gas. Since this is not the case here, it would seem that there is either a dead region of flow in the lower corner of the canyon which in some way cuts off this region from the general vortex in the canyon or the wake of the vehicle throws the pollutant high in to the air.

There is little evidence for the latter effect, indeed there is literature to suggest that the

[5] Here, in brief, are the assumptions made in the calculation:

- The typical length of a complete circuit in the canyon is simply a square with side $0.8B$, which is $2 \times 0.1B$ smaller than the actual width of the canyon because its on that circuit that the FID was sampling.
- The speed of a massless particle along this circuit is $0.3 \times u_{\text{ref}}$.
- The time taken for a single circuit is then simply, length of circuit divided by the speed along the circuit. This time is then trivially converted to the non-dimensionalized form shown in Figure 3.32.

[6] A fault with the FID prevented the collection of similar data for the 1.5:1 aspect ratio canyon.

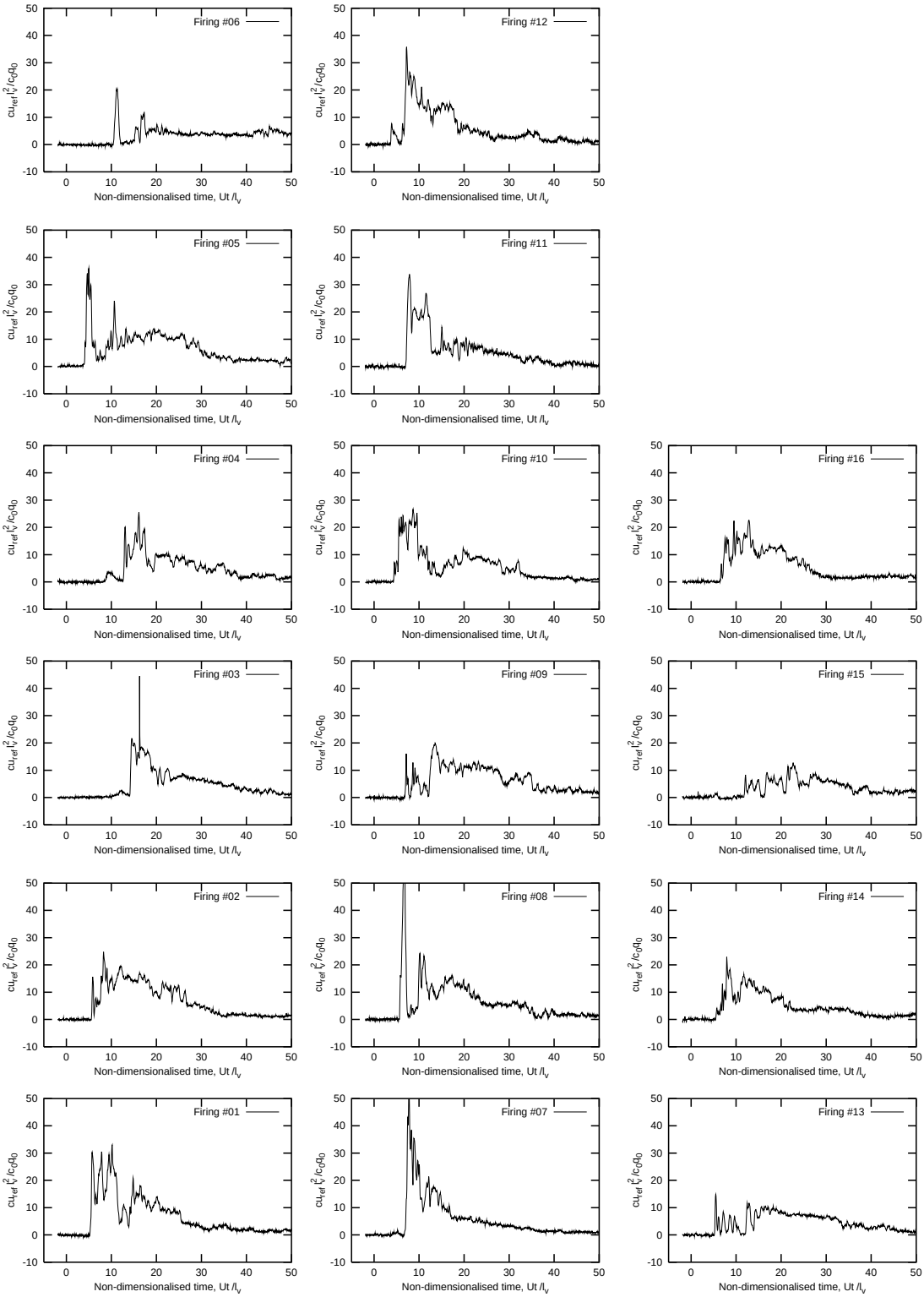


Figure 3.32: Sixteen individual concentration time series for $u_{\mathrm{ref}}/U = 1.0$ at $z = H/8$ on the leeward wall of a 1:1 aspect ratio canyon.

wake tends to concentrate the pollutant in the very near-field[7]. If this concentrating effect were occuring, and the pollutant remains in a small volume, then one would expect the sensor at half-height (which is on the same circumference in the vortex as the exhaust pipe) to sense the gas first.

Moving onto the windward wall now, Figures 3.35 and 3.36 show that there is little noticeable variation with height for both a 1:1 and 1.5:1 aspect ratio canyon. The absolute values, which suggest that the wider canyon has much lower concentrations are probably not reliable since these two sets of readings were taken on separate days. However, it may be noted that a wider canyon has a more open recirculation with a greater opportunity for the gas to escape. The lack of variation on the windward wall is in line with much of the field evidence.

Variation of Concentration with Aspect Ratio

Figure 3.37 shows the variation of the ensemble averaged concentrations at $z = H/2$ on the leeward wall with varying aspect ratio. Little can be discerned from this graph. Close attention to the three traces suggests the presence of a highly smeared second peak. The smearing is due to the ensemble averaging process.

Variation of Concentration with Wind Speed

Next the effect of changing the reference wind speed and hence the vortex speed in the canyon was investigated. Figures 3.38 and 3.39 show the effects for the leeward and windward building faces respectively. In this case, the vehicle speed, U, is used as the velocity scale when presenting the normalized concentrations.

Again, it is difficult to make any clear-cut observations from the first of these plots. The only obvious effect is that at the lower wind speeds, the curve is more spread out, although the magnitudes are by no means decreased. It could also be said that the peak occurs later as the wind speed decreases, if the minor peak for $u_{\text{ref}}/U = 0.25$ is ignored. The problems of ensemble averaging the data are yet again important.

What can be done, though, is to take advantage of the shape of the breakthrough curves and, in particular, the tail of each curve. Lee and Park [61], as mentioned briefly in Section 2.4.3, looked at the rate of decay of the average concentration in a whole range of urban canyon scenarios using a CFD model. Based on their approach, a curve of the form,

$$c' = c'_0 \exp\left(-\frac{t'}{\tau'}\right)$$

[7] Near-field in this context means the region of the wake very close to the vehicle, as opposed to the far-field regime extensively studied, for example, by Eskridge and Hunt.

where c' is the concentration, c'_0 is some initial concentration and τ' is the time constant, can be fitted to the tail of the curves in both Figures 3.38 and 3.39. The primes indicate that these are the non-dimensionalized values shown on the two figures. The decision as to where the tail begins is based on where the peak value (which may include one or more distinct peaks) is perceived to have been passed. Thus, for the two figures in question a value of 10 or 15 scaled time units would signal the start of the tail. The scale on the *y*-axis of the plots is not important when finding these time constants.

Once again using the curve fitting capabilities of GNUPLOT it was possible to find values of τ' for all three wind speeds on both walls of the canyon. Figure 3.40 shows the two sets of results which have been converted into absolute values of time and speed. There is a definite increase in the decay time constant as the wind speed is decreased which agrees with Lee and Park who found the relationship,

$$\tau = 9035\frac{V}{uL}\frac{(65+1.7\times10^{-5}P_e)}{R_e^{0.75}}A^{0.35}$$

where R_e is the Reynolds number ($= uL/\nu$), P_e is the Peclet number ($= uL/K$), A is the aspect ratio of the canyon, V is the cross-sectional area, K is the eddy diffusivity of air, u the above canyon wind speed and L is a reference height, some 10 m above the canyon. The fact the variation on the windward wall differs from that on the leeward wall indicates that there are regions of the canyon which lose the pollutant faster than others. Indeed, Lee and Park looked at the average concentration in the canyon and not its variation at specific points.

The fact that these time constants are much lower in value than those found by Lee and Park (which are typically $\sim$ 1000s) can be largely explained by the relative geometric scale of the two investigations. Most significantly perhaps is the parameter V, the cross-section area of the canyon which is 2500 times smaller in the wind tunnel and explains away much of the discrepancy between the time constants.

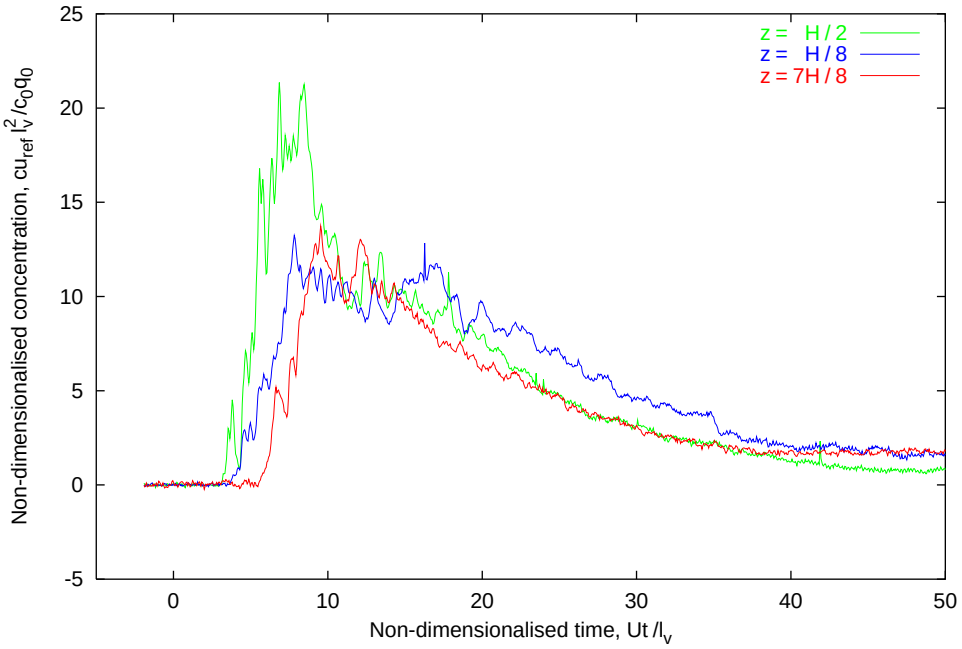


Figure 3.33: Variation of concentration with height on the leeward face of a 1:1 aspect ratio canyon.

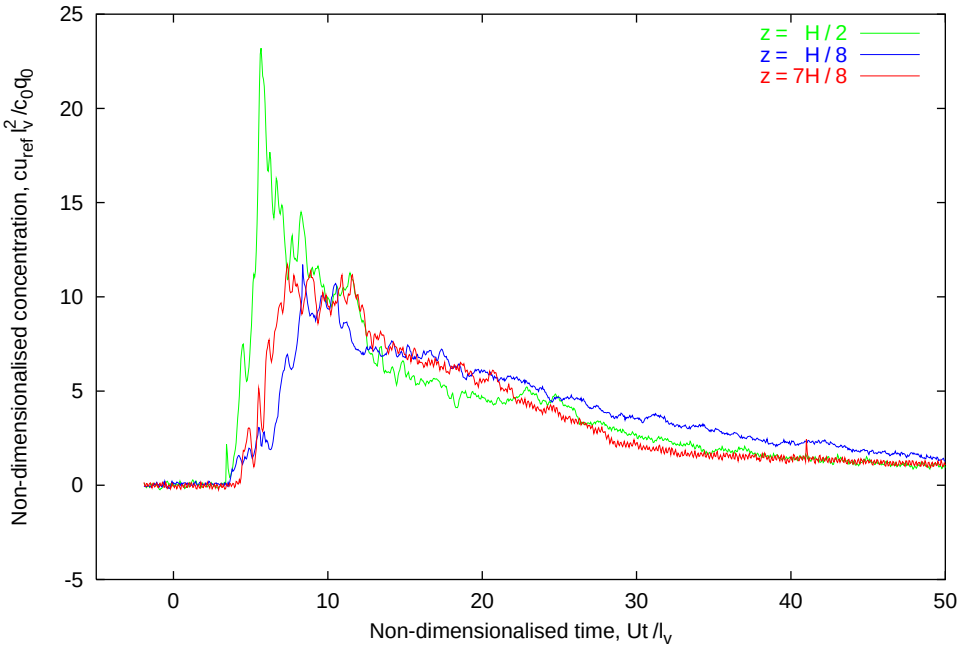


Figure 3.34: Variation of concentration with height on the leeward face of a 2:1 aspect ratio canyon.

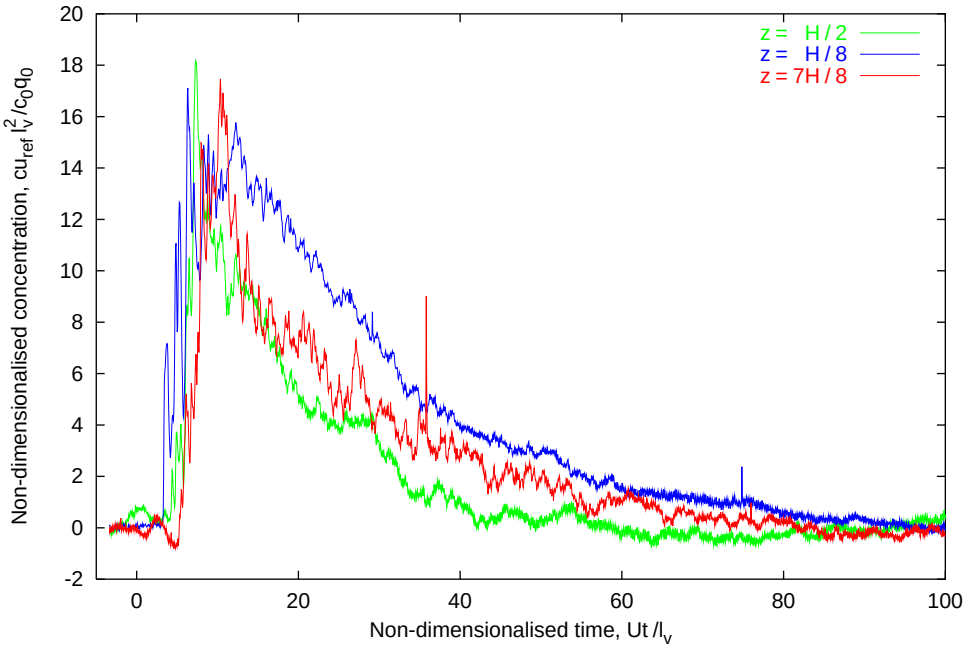


Figure 3.35: Variation of concentration with height on the windward face of a 1:1 aspect ratio canyon.

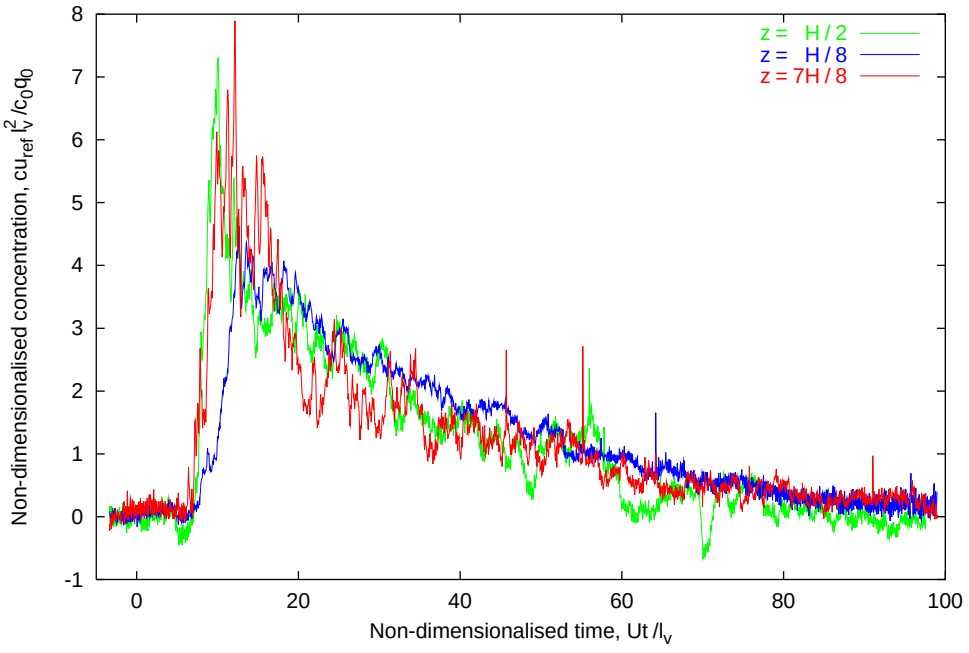


Figure 3.36: Variation of concentration with height on the windward face of a 1.5:1 aspect ratio canyon.

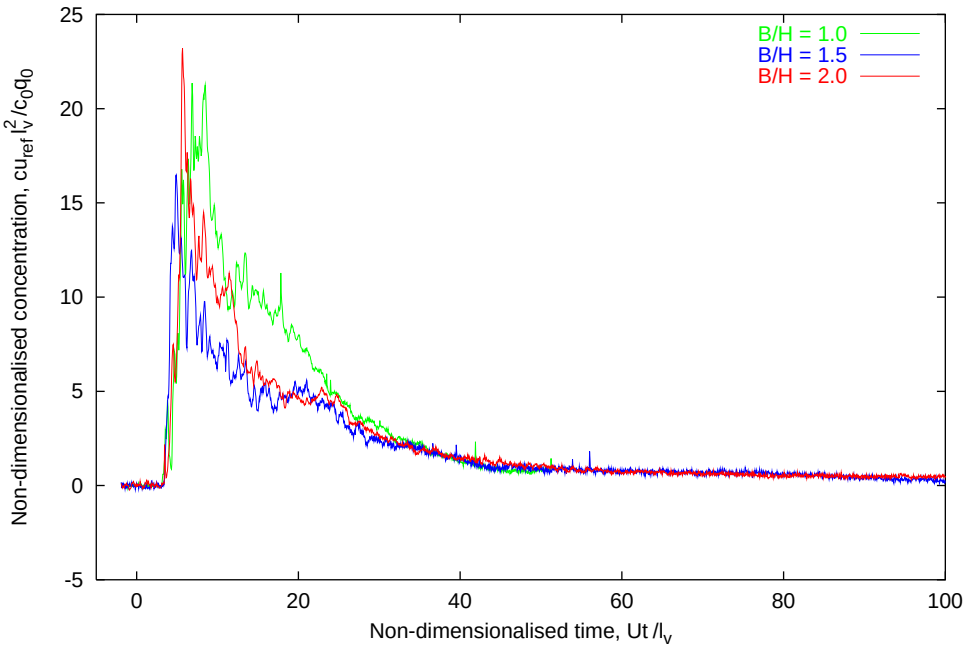


Figure 3.37: Variation of concentration with aspect ratio on the leeward face.

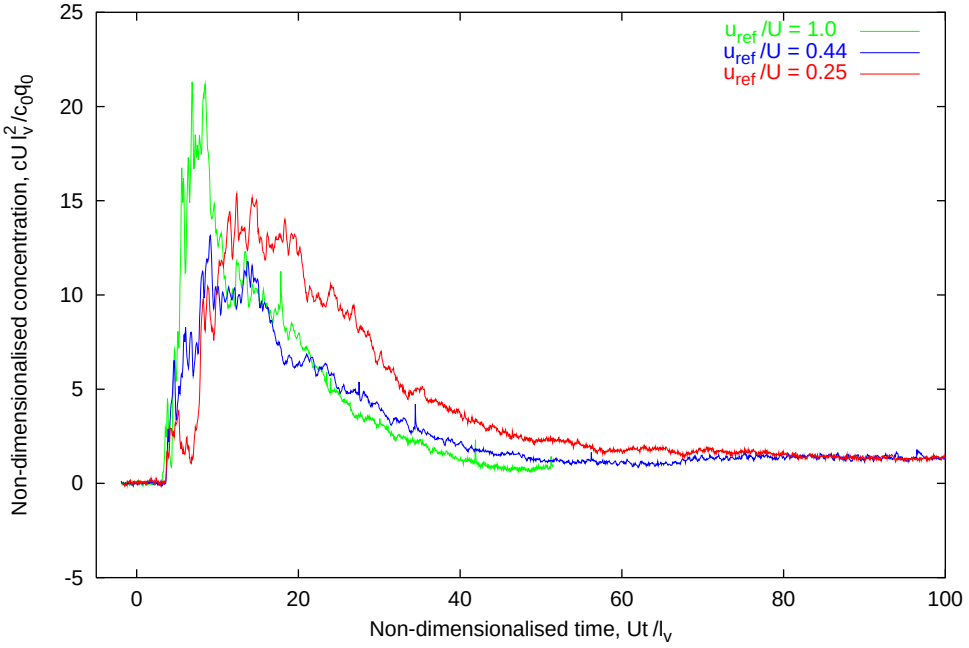


Figure 3.38: Variation of concentration with reference wind speed on the leeward face of a 1:1 aspect ratio canyon.

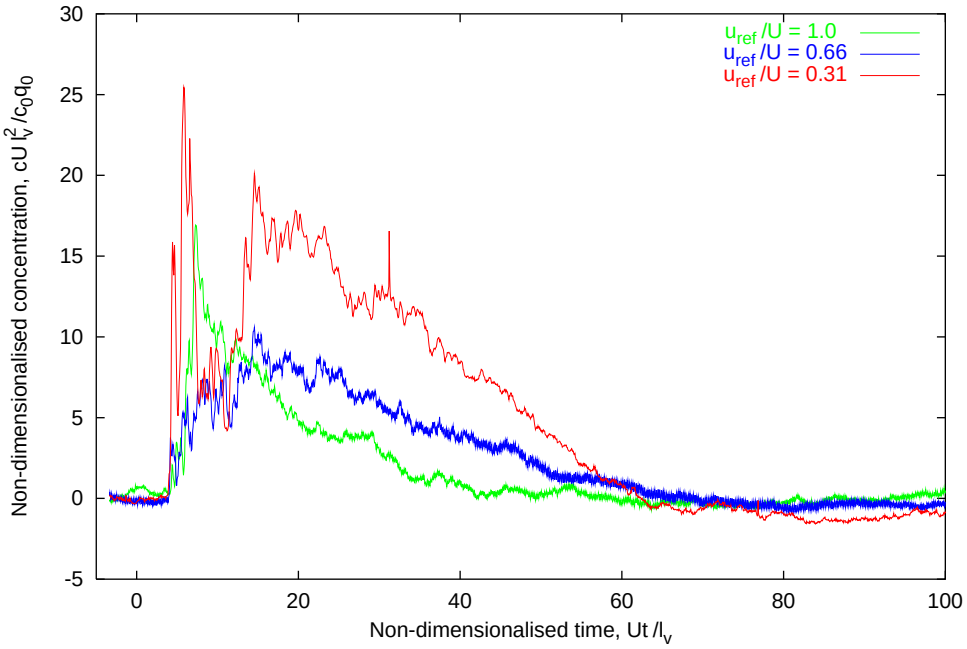


Figure 3.39: Variation of concentration with reference wind speed on the windward face of a 1:1 aspect ratio canyon.

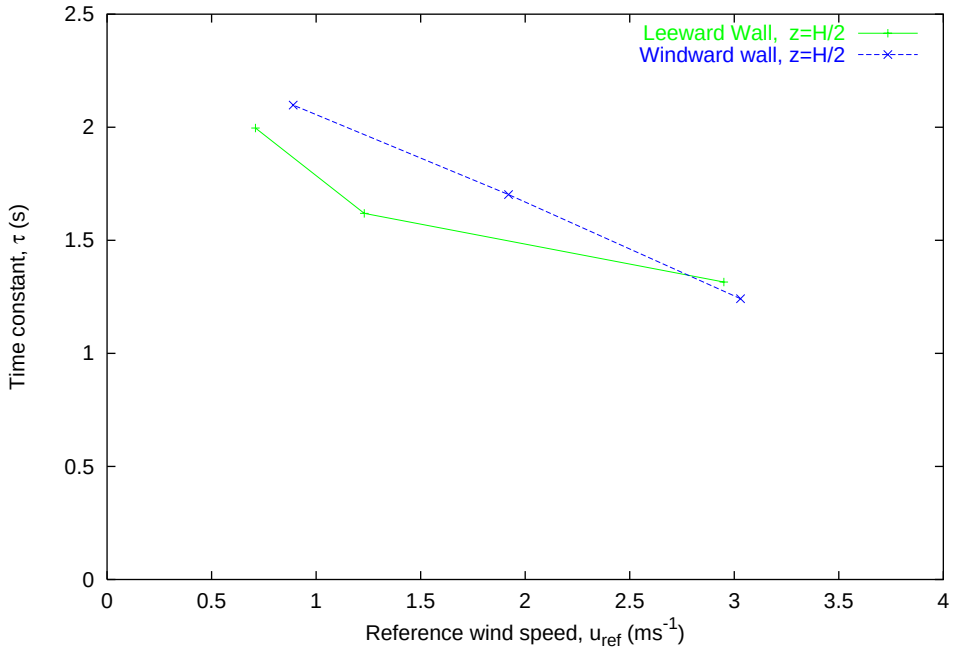


Figure 3.40: The effect of wind speed on the time constants for both the leeward and windward walls of a 1:1 aspect ratio canyon.

3.5 Conclusions

There are many interesting observations which can be made from these results - particularly in the rural case. It was shown that there was a distinct wake effect due to the passing vehicle in a cross-wind, a fact demonstrated most clearly by the perturbation in the *v*-component of flow in the wake. It was further possible to show that this 'velocity deficit' moved away from the vehicle at the speed of the ambient wind at that height.

The most encouraging result - and the most useful one from the point of view of validating the analytical model - was the variation of the wake concentration with distance downstream of the vehicle. A classic Gaussian dispersion process was revealed by this set of data. Indeed, the fact that we could be confident of the time dependency of these results was one of the more satisfying and interesting aspects of this whole study.

Moving on to the urban case, the situation becomes less clear. Here, it is more difficult to discern real dependencies or trends as various parameters were varied. It is here also that the lack of assurance with the absolute concentrations was of most concern. The introduction of a decay time constant is a useful tool in describing the efficiency of pollution removal after the vehicle has passed by. The calculation of the decay time constant depends solely on the shape of the ensemble average curves and thus is not affected by the FID calibration problem.

The time series for individual firings are also informative. In these plots, the true nature of the turbulent processes in the canyon is demonstrated. It is possible to see double (and sometimes triple) peaks which are tell-tale signs of the pollution being swept around the canyon by the resident vortex. What it is not so clear to discern from any of the data is the effect of the vehicle wake in the canyon. Perhaps the chaotic nature of the individual plots is due to the presence of the wake and with a simple moving source of pollutant things might be more obvious. Without a follow up study, this remains purely a conjecture.

Perhaps the last couple of points should be a negative ones. Despite the novel nature of the these tests, the problems with the calibration of the FID casts a dark shadow over everything we discuss here. In addition, the time pressures imposed on the experimental programme, due to the University's leasing arrangement with British Gas, means that the results presented are somewhat more limited than was hoped.

Chapter 4

Analytical Investigation

4.1 Introduction

In this Chapter, a full description of an analytical model of urban and rural vehicular pollution dispersion will be presented. A paper describing a previous version of the model has been presented at the Third International Colloquium on Bluff Body Aerodynamics and Applications (Hargreaves and Baker [38]), and the model has recently been referenced in a EEC publication (Schatzmann *et al* [80]). In addition, a statistical application of the model has been presented at the 20th Conference on Regional and Urban Statistics in Madrid (Baker and Hargreaves [9]).

The model was primarily developed in order to overcome the perceived drawbacks of existing urban canyon models such as those discussed in Section 2.4.3. During the development process it soon became clear, however, that the core of the model could be used to model the dispersion from vehicles in the open country case - an extension that would bring a certain symmetry to this research as a whole, bearing in mind the combined urban/rural nature of the experimental work.

As the chapter progresses, the theoretical basis of the model will be formulated in a series of sub-sections, each of which roughly describes the workings of a particular sub-model. An extensive parametric study then follows, the aim of which is to test the behaviour of the model under a variety of conditions. This chapter, however, avoids issues such as calibration and validation against wind tunnel data which will be held back until Chapter 5.

To round off the chapter, there will be a brief discussion of the ability of the model to produce statistical predictions of concentration levels - this is largely the content of the Madrid paper. This particular aspect of the model is perhaps the most exciting from the point of view of application to real world situations.

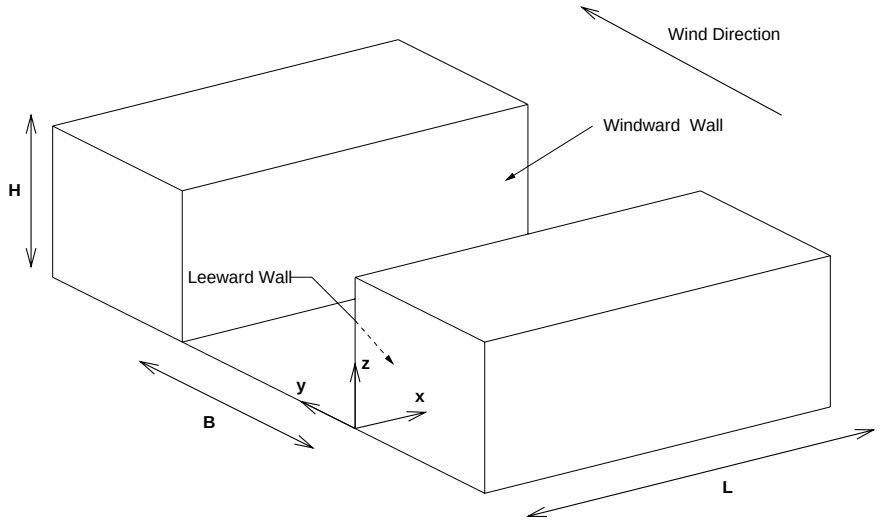


Figure 4.1: A section of the street canyon showing the origin of the coordinate system.

4.2 Theory

4.2.1 The Domain

The dual-purpose nature of the model (both rural and urban) presents us with two differing descriptions of the domain for the model. In the idealized street canyon, the domain can most simply be thought of as consisting of a section of street canyon of length, L, height, H, and width, B, as shown in Figure 4.1. The figure also shows the layout of the leeward and windward buildings.

In the rural environment a somewhat different approach is required. Here a purely conceptual box of length, L, height, H, and width, B, is used as the domain for the model. Although slightly less intuitive than the domain for the urban scenario, this definition does lend itself to the modelling approach used here.

4.2.2 Traffic Simulation Sub-model

Lanes of Traffic

In either domain, there exists a roadway which traverses the entire length of the domain, running parallel to the x-axis. This roadway consists of N_l lanes of traffic, each with an offset, y_{li}. The use of these offsets allows the modeller to construct a roadway anywhere in the domain. For instance, in the urban canyon, it would be typical if the roadway

ran down the centre of the canyon whereas it may be preferable in the rural situation to have the roadway skewed towards the upwind end of the domain so that pollution can be observed over a large area downwind.

Helly's Theory of Congestion

The model of traffic flow in each lane of traffic is based on the work of Helly [39] in which a mathematical model for a single lane of traffic is described. Using this model, it is possible to produce free flowing and congested traffic and all states in between.

In the following discussion, only one lane will be discussed. In this lane the traffic is assumed to travel in the positive x direction. The extension of the theory to a lane of traffic travelling in the opposite direction is trivial. In this formulation, a single vehicle, subsequently to be referred to as the *lead* vehicle, is introduced into the canyon at time, $t = 0$. It is given a velocity which can be controlled by the modeller by supplying suitable input data, the actual form of which will be discussed later.

Let successive vehicles in the canyon be labelled $1, 2, 3, \ldots, n-1, n$, with 1 being the lead vehicle. Helly assumes that the acceleration of the n^{th} vehicle is a function of its distance from and relative speed to the vehicle in front[1]. In other words,

$$\ddot{x}_n(t+\tau) \equiv (\ddot{x}_n)_{t+\tau} \quad = \quad f(x_n, x_{n-1}, \dot{x}_n, \dot{x}_{n-1}, t) \tag{4.1}$$

where x_n is the x coordinate of the n^{th} vehicle in the lane of traffic and τ is the driver's reaction delay time. The reaction time is introduced to indicate that the acceleration is not instantaneous but must occur after some time due to the finite reaction time of the driver.

So, the first rule which will govern a vehicle's acceleration is the driver's need to minimize the relative velocity between his own vehicle and the one in front. In other words,

$$(\ddot{x}_n)_{t+\tau} = \left[C_1(\dot{x}_{n-1} - \dot{x}_n)\right]_t \tag{4.2}$$

where C_1 is a velocity control parameter. The second such rule relies on the driver maintaining a desired headway between the vehicle in front and his own, the headway being defined as the distance between the front bumpers of successive vehicles. Thus,

$$(\ddot{x}_n)_{t+\tau} = \left[C_2(x_{n-1} - x_n - D)\right]_t \tag{4.3}$$

where C_2 is a headway control parameter. It can be seen that if the distance between the two vehicles $(x_{n-1} - x_n)$ is equal to the desired headway, D, then the n^{th} vehicle will not have to accelerate. Helly used an expression for the desired headway, D, from the then California Vehicle Code,

$$D = \alpha + \beta \dot{x}_n \tag{4.4}$$

[1] Helly also takes into account the braking of the vehicle in front and of different driver behaviour patterns. Both these effects are not of importance here.

where α is the minimum headway distance (usually the spacing of stationary traffic) and β is the headway calculation parameter. Therefore, in this simple description of the desired headway, the ideal (and safe) distance between vehicles increases proportionally with speed.

In the present formulation, only the controls embodied in Equations 4.2 and 4.3 are included: effects such as the braking of vehicles in front are ignored. Thus, if these two equations are combined, the following expression for the instantaneous acceleration of a vehicle in the canyon is found,

$$(\ddot{x}_n)_{t+\tau} = \left[C_1(\dot{x}_{n-1} - \dot{x}_n) + C_2(x_{n-1} - x_n - D)\right]_t \tag{4.5}$$

Further constraints such as a maximum rate of acceleration, a maximum rate of deceleration and a maximum velocity are imposed on the vehicles to keep the situation realistic.

The lead vehicle is not, however, subject to Equation 4.5. Instead, a modified form of Equation 4.2 is used with $\dot{x}_{n-1}$ replaced by $\dot{x}_0$ which is a speed supplied by the user. Thus, the lead vehicle will attempt to achieve the speed $(\dot{x}_0)_t$ by acceleration or deceleration.

The present model operates a simple time-stepping algorithm which divides the total run time into discrete time steps, each of length Δt. In order to accommodate Equation 4.5 into this scheme, the driver reaction delay time, τ, must be replaced by Δt. This contradicts Helly's assertion that...

> A driver does not operate in a frenzy of continuous revision on his acceleration program. Rather, he makes decisions at variable time intervals, as dictated by unforeseen changes in his environment.

Essentially it is assumed that drivers are perfect and, since Δt is typically smaller than τ, can react almost instantaneously to changes in driving conditions.

Within this time-stepping framework, the velocity and position of each vehicle are updated using the following standard relationships,

$$\dot{x}_i^{l+1} = \dot{x}_i^l + \ddot{x}_i^{l+1}\Delta t \tag{4.6}$$

$$x_i^{l+1} = x_i^l + \dot{x}_i^{l+1}\Delta t \tag{4.7}$$

where the superscript ^{l} refers to the current time level and $^{l+1}$ to the next.

The introduction of the lead vehicle is somewhat unique and occurs only at the start of the run, as shown in Figure 4.2(a). The rule governing the addition of further vehicles is more complicated. Once the distance between the last vehicle in the lane and the lane entrance exceeds the desired headway (see Equation 4.4), another vehicle is introduced at a position such that it is exactly a distance D behind the vehicle in front (Figure 4.2(b)).

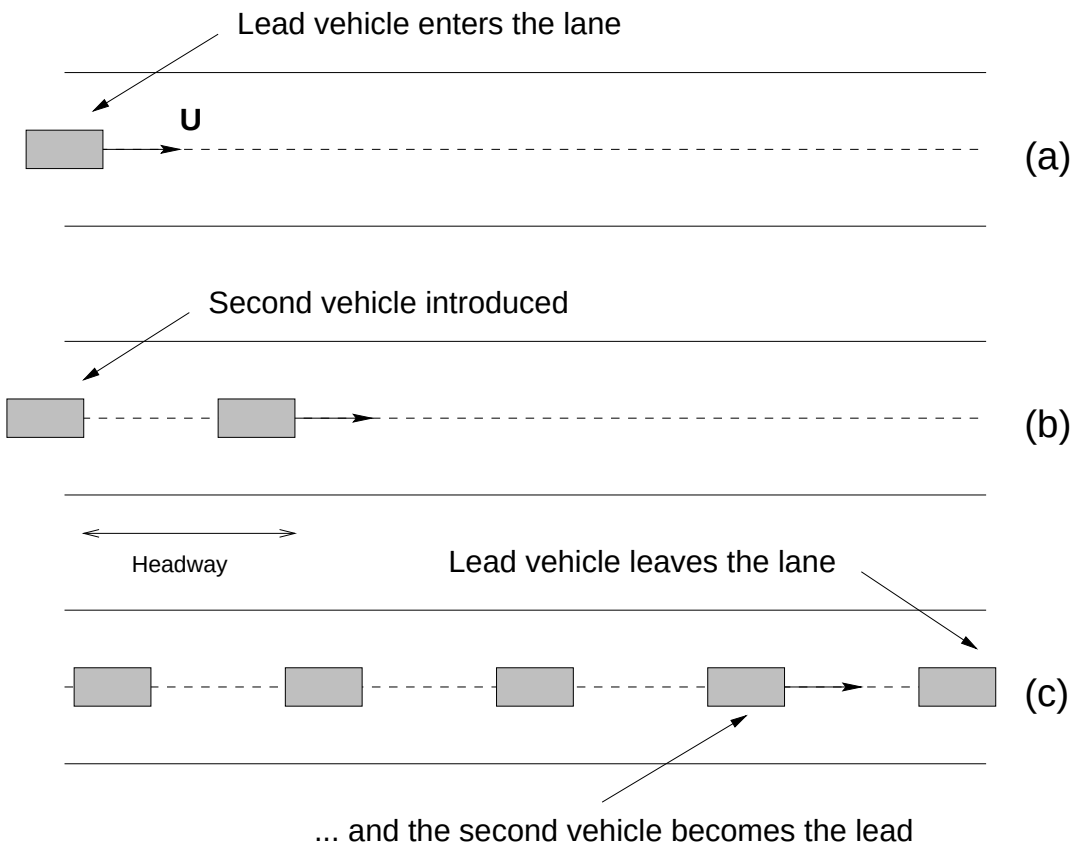


Figure 4.2: Schematic of several important features of the traffic model: (a) lead vehicle is introduced into the lane; (b) a second vehicle is introduced once the lead vehicle is more than one headway down the canyon; (c) the lead vehicle is removed from the canyon.

It is also afforded the same speed as the vehicle in front and replaces the vehicle in front as the last vehicle in the lane. Figure 4.2(c) shows that as the lead vehicle passes the lane exit it is immediately lost from the lane and the indices of the remaining vehicles are decreased by one. Thus the vehicles effectively 'shuffle' along.

Multiple Vehicle Types

There also exists within the model a method by which the heterogeneous nature of traffic can be modelled. A typical stream of traffic consists of many broad vehicle types: for example, cars; lorries; and buses. Each of these types has their own characteristics - different geometries, emission rates and accelerations.

In order to include these effects in the model, the concept of *vehicle type density,* ρ_i, is introduced. For example, if 80% of the vehicles are private cars, another 10% are

buses and the remainder are lorries, then the vehicle densities for the three vehicle types would be 0.8, 0.1 and 0.1 respectively. From this it is obvious that the sum of the vehicle densities is unity. This is purely a statistical construction - these values are only averages. At any particular instant in the canyon the actual numbers of each vehicle may vary quite significantly from these mean values.

The implementation of multiple vehicle types is achieved quite simply in the model. Whenever a new vehicle is to be introduced into the lane, an random number lying in the range 0.0 to 1.0 is generated. Then, depending on the value of this number, the relevant vehicle type is introduced into the lane. In the above example, if a random number of 0.823 were generated, a bus would be introduced - assuming the three types of vehicle were ordered in the manner just described.

Emission Rates

Helly's model of vehicle dynamics dictates that, in general, any vehicle may be accelerating, may be traveling at a constant speed, or may be stationary. In each of these states, the engine of the vehicle will be have different loads on it and consequently will produce varying amounts of pollution.

However, due to the diverse nature of driving conditions, driving behaviour and vehicle design, there is no simple relationship to link the instantaneous dynamic behaviour of a vehicle with its instantaneous emission rate. Much work has been carried out in this area but a lot depends on the driving cycle used and this varies from country to country and from continent to continent. Based on the observations of Hickman [44], it has been decided to split the problem into two parts. We assume that the flow rate of gas out of the exhaust, q_e and the concentration of pollutant therein, c_e, are linear functions of speed and acceleration thus,

$$q_e = q_i + q_s\dot{x} + q_a\ddot{x} \tag{4.8}$$

$$c_e = c_i + c_s\dot{x} + c_a\ddot{x} \tag{4.9}$$

and where q_i is the idling emission flow rate, and q_s and q_a are the coefficients for velocity- and acceleration-dependent flow rates, c_i is the idling exhaust concentration, and c_s and c_a are the coefficients for velocity- and acceleration-dependent concentrations. Using the product $q_e c_e$ it is possible to model emission signatures such as that observed by Hickman to some extent. Compare, for example, Figure 2.5 with Figure 4.3 which was generated using a somewhat arbitrary but nonetheless realistic set of values for c_i, q_i, etc.

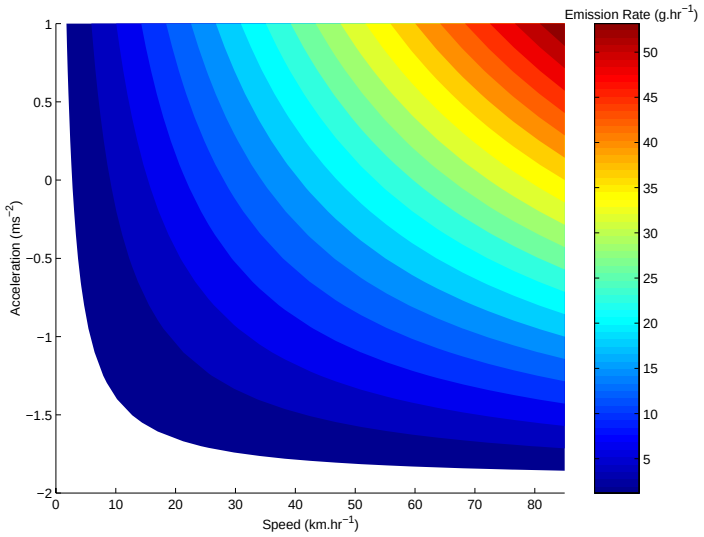


Figure 4.3: An example of emission rate variation that can be constructed using the emission sub-model.

4.2.3 Gaussian Puff Theory

The exhaust fumes are actually emitted as a series of puffs in this modelling approach which is commonly referred to as the Gaussian Puff Method. Similar approaches are adopted by Nishi and Cermak [67] for modelling airport pollution, by Rao *et al* [74] for modelling drainage flow in a valley, and by Hurley [54] - for more details see Section 2.5.

In this method, each puff diffuses, or expands, in a Gaussian manner about the centre of the puff. The rate of expansion is governed by the local levels of turbulence. At the same time the puff is moved bodily by the local flow field in which it finds itself. This combination of diffusive and convective terms is typical of all modelling of pollution transport.

At the start of every time step, each vehicle on the roadway emits a single puff which then moves and diffuses in a manner which will be discussed shortly. Each puff is free to move independently of all others - no consideration is made for puffs crossing each others path. Each puff initially has a mass $q_e c_e \Delta t$ which is simply the product of the emission rate, exhaust concentration and the length of the time step.

Throughout the domain there are distributed N_r receptors, each at a position (x_r, y_r, z_r). The concentration of pollutant at these positions is given by the expression,

$$c(x_r, y_r, z_r, t) = \sum_{p=1}^{N_p} \left(\frac{q_e c_e \Delta t}{(2\pi)^{\frac{3}{2}} (\sigma_x)_p (\sigma_y)_p (\sigma_z)_p} \right) \cdot X(x_r) \cdot Y(y_r) \cdot Z(z_r) \qquad r = 1, \ldots, N_r \tag{4.10}$$

where the subscript p refers to quantities associated with each puff and N_p is the number of currently active puffs and where,

$$X(x_r) = \exp\left\{-\frac{1}{2}\left(\frac{x_r - x_p}{(\sigma_x)_p}\right)^2\right\} \tag{4.11}$$

$$Y(y_r) = \exp\left\{-\frac{1}{2}\left(\frac{y_r - y_p}{(\sigma_y)_p}\right)^2\right\} + \exp\left\{-\frac{1}{2}\left(\frac{y_r + y_p}{(\sigma_y)_p}\right)^2\right\} + \exp\left\{-\frac{1}{2}\left(\frac{2B - y_r - y_p}{(\sigma_y)_p}\right)^2\right\} \tag{4.12}$$

$$Z(z_r) = \exp\left\{-\frac{1}{2}\left(\frac{z_r - z_p}{(\sigma_z)_p}\right)^2\right\} + \exp\left\{-\frac{1}{2}\left(\frac{z_r + z_p}{(\sigma_z)_p}\right)^2\right\} \tag{4.13}$$

where $(\sigma_x)_p$, $(\sigma_y)_p$ and $(\sigma_z)_p$ are the dispersion parameters (see Section 4.2.5).

The second and third terms in Equation 4.12 are due to the reflections from the walls of the canyon, if one is present, while the second term in Equation 4.13 accounts for the reflection of the pollutant in the roadway. It should be noted that Equation 4.11 may be modified when cyclical boundary conditions are employed. This will be discussed further in Section 4.2.7. Equations 4.10 to 4.13 are identical to those presented in Rao *et al* [74] for a Gaussian Puff Model of pollutant dispersal in a box-shaped valley.

4.2.4 Transport of the Puffs

It is assumed that there exists a velocity field which is generated by two quite separate processes: the movement of the vehicles and the ambient wind. The assumption is made at this stage that the air velocities due to these two effects can be treated separately and then superimposed to give a resultant velocity field.

The Wake

The dual-purpose nature of the model (both urban and rural scenarios) means that the treatment of the wake takes two quite distinct forms. Because it is the more general of the two, the wake of a vehicle in a cross wind (the rural case) will be discussed first with the specialization to the urban case following that.

In either case, the following assumption is made: any puff is influenced only by the wake of the vehicle directly in front[2]. This means that in any particular lane of traffic,

[2]Or behind the car in the driver's frame of reference. This distinction is made because of the bi-directional nature of the lanes of traffic.

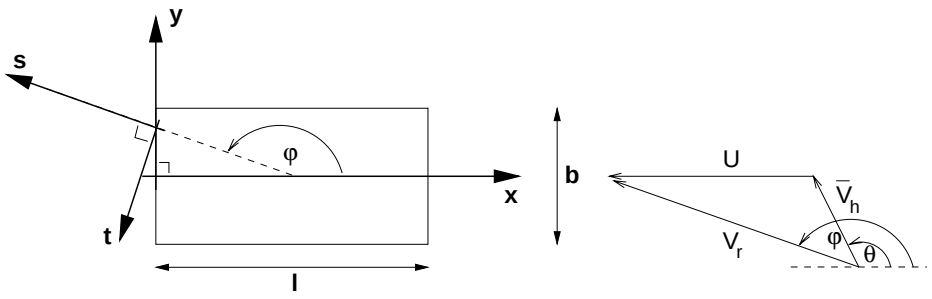


Figure 4.4: Wake coordinate system.

the region of influence of each vehicle wake extends only as far as the front bumper of the vehicle immediately behind it.

In general, the wind direction will not be in the same direction as the direction of travel in each lane of traffic. The reader is referred back to Figure 2.4 which shows the velocity vectors in this general case. The angle between the wind and the direction of travel is θ, and the resultant angle of incidence of the wind, the yaw angle, is ϕ.

Most of the theoretical approaches discussed in Chapter 2 dealt with wake effects in what we shall call the 'far field' - that is, many vehicle heights downstream. Unfortunately, in this model it is necessary to look at the wake effects close up behind the vehicles - the 'near field'. The assumption is made that the wake equations developed by the likes of Eskridge and Hunt hold in the near field, albeit with some modifications.

For instance, the yaw angle, ϕ, can vary between $-\pi$ and $+\pi$, depending of the relative wind speeds. In the present approach, the origin of the wake coordinate system, (s,t,z), is held to be on the shell of the vehicle, opposite the direction from which the wind is effectively coming. Figure 4.4 shows this more clearly. The (s,t,z) coordinate system is both rotated through an angle, ϕ, and translated with respect to the vehicle's coordinate system which is centred on the rear of the vehicle. The algorithm to find the offsets, x_0 and y_0, for this new coordinate system is complicated because the outline of the vehicle is not described by a simple algebraic expression.

The position of a puff at (x_p,y_p,z_p) with respect to the vehicle coordinate system is translated to a point in the wake coordinate system as follows,

$$\begin{aligned} s_p &= (x_p - x_0)\cos\phi + (y_p - y_0)\sin\phi \\ t_p &= -(x_p - x_0)\sin\phi + (y_p - y_0)\sin\phi \\ z_p &= z_p \end{aligned}$$

Based on the work of Baker [6] in which he modified the Eskridge and Hunt [30] wake equations by introducing a yaw angle dependency, the following equations are used to

calculate the wake deficit in the new coordinate system.

$$u_w = \begin{cases} U\xi^m\zeta \cdot \exp\left\{-[\eta^2+\zeta^2]/8\right\} \\ 0 \end{cases} \tag{4.14}$$

where $\xi = s_p/h$, $\eta = t_p/h_w(\xi)$ and $\zeta = z_p/h_w(\xi)$ with,

$$h_w(\xi) = h\xi^n \tag{4.15}$$

where $h_w(\xi)$ is the wake height at scaled distance, ξ down the wake centreline. The exponents n and m are yaw angle dependent and have already been discussed in Section 2.3.1 but are reproduced here for completeness,

$$m = -\frac{3}{4}\left(1+\frac{2\phi}{\pi}\right) \tag{4.16}$$

$$n = \frac{1}{4}\left(1+\frac{2\phi}{\pi}\right) \tag{4.17}$$

The use of angle-dependent exponents allows the model to cope with all situations between a high-speed vehicle in still air to a stationary vehicle in a strong cross-wind.

That covers the case for a general cross-wind. However, the situation in the street canyon is far less clear cut. When a spiral ambient wind (see next Section) exists in the canyon, it is not inconceivable that the wake of the vehicles will be swept around the canyon. The exact nature of this effect is not at all well understood and it is assumed in this model that the wakes are sufficiently robust in terms of momentum that they remain parallel to the direction of travel. This assumption simplifies matters greatly when calculating the wake velocity.

Canyon Wind Field

The Equations of Hotchkiss and Harlow [47] are used to model the cross canyon wind. The Equations are given in Section 2.4.3 and are repeated here for completeness,

$$v = \frac{v_H}{1-\beta}\left[\gamma(1+kz') - \beta(1-kz')/\gamma\right]\sin ky \tag{4.18}$$

$$w = -\frac{v_H kz'}{1-\beta}\left[\gamma - \beta/\gamma\right]\cos ky \tag{4.19}$$

where $k = \pi/B$, $\gamma = \exp(kz')$, $\beta = \exp(-2kH)$, $z' = z - H$ and v_H is the cross canyon wind speed at roof level.

The along canyon wind is in a form used by Yamartino and Wiegand [89] and which is a simple logarithmic profile,

$$u(z) = u_H \log\left[(z+z_0)/z_0\right]/\log\left[(H+z_0)/z_0\right] \tag{4.20}$$

where u_H is the along canyon wind speed at roof level and z_0 is the surface roughness. Yamartino and Wiegand found that z_0 was highly dependent on the approach flow direction, θ, where,

$$\tan\theta = u_H / v_H$$

from which the horizontal components of the above canyon wind speed are given by,

$$\begin{aligned} u_H &= V_H(t)\cos\theta \\ v_H &= V_H(t)\sin\theta \end{aligned}$$

where $V_H(t)$ is the reference wind speed at roof level and which can vary with time. A time series for discrete values of $(V_H)_k$ is generated by means of an Auto-Regressive Moving Average model of order (p,q) where successive terms are given by,

$$(V_H)_k + \sum_{i=1}^{p} a_i(p)(V_H)_{k-i} = e_k + \sum_{j=1}^{q} b_j(q) e_{k-j} \tag{4.21}$$

where $a_i(p), i = 1,\ldots,p$ are the autoregressive (AR) parameters, $b_j(q), j = 1,\ldots,q$ are the moving average (MA) parameters and e_k is white noise with zero mean and a variance of σ_e^2. The AR and MA coefficients are chosen such that the power spectral density of the generated wind field is a good fit to the von Kàrmàn spectrum. For full details of this approach, the reader is referred to Appendix C.1. The ARMA-generated time series is provided as an option in the model with a steady value for V_H being the default.

4.2.5 Dispersion Parameters

The dispersion parameters, σ_x, σ_y and σ_z, describe the degree to which the puff has expanded at any given time. The physical process which is responsible for this expansion is the small scale[3] turbulence in the canyon.

The initial dispersion parameters are set as follows. In a time Δt, a slug of exhaust gas is released. The length of this slug is Δl, which is given by,

$$\Delta l = \frac{4}{\pi}\frac{q_e}{d_e^2}\Delta t$$

where q_e is the flow rate from the exhaust pipe (Equation 4.8) and d_e is the diameter of the exhaust pipe. By approximating the slug to a puff, the initial dispersion parameters are set as,

$$\sigma_x^0 = \Delta l/2 \tag{4.22}$$
$$\sigma_y^0 = d_e/2 \tag{4.23}$$
$$\sigma_z^0 = d_e/2 \tag{4.24}$$

[3] "Small scale" here refers to gusts smaller than the size of the puff because really large gusts tend to move puffs bodily, rather than dispersing them.

where the superscripts ^{0} indicate that these are initial values. Notice that each value is divided by 2 because each σ represents only one side of the Gaussian distribution of pollution in the puff.

Thereafter the puffs expand due to the turbulence in the canyon. The method used in the present implementations is a variant on that presented in Peterson [72]. At each time step, the dispersion parameters are incremented as follows,

$$\sigma_x^{l+1} = \sigma_x^l + \overline{u'^2}^{\frac{1}{2}} \Delta t \tag{4.25}$$

$$\sigma_y^{l+1} = \sigma_y^l + \overline{v'^2}^{\frac{1}{2}} \Delta t \tag{4.26}$$

$$\sigma_z^{l+1} = \sigma_z^l + \overline{w'^2}^{\frac{1}{2}} \Delta t \tag{4.27}$$

where the superscript ^{l} refers to the previous time step, $^{l+1}$ to the current one, and u', v' and z' are the fluctuations in the mean air velocity due to turbulence as evaluated at the centre of the puff.

Estimating the Turbulence

Due to the nature of the turbulence in the canyon, the present model employs a very simplistic model of turbulence which, it is hoped, can be modified at a later date to fit empirical evidence. Indeed, the development of this model of turbulence relies on the empirical evidence available at the time of writing.

Quantitative evidence for turbulence in the canyon, such as DePaul and Sheih [26], suggests that the turbulence is largest in the region occupied by the vehicles and maintains a more constant value at heights above this. Mean values of turbulence in the range 0.1 to 0.4 ms^{-1} were observed in a typical street canyon. Indeed, these values are backed up by Hertel and Berkowvicz [42] who used values of turbulence in this range in their model of a canyon. They, however, related the turbulence levels to the resident velocity in the canyon, which makes a certain amount of sense. The higher the velocity, the higher the turbulence you might expect to observe. This implies that the turbulent intensity may remain at a roughly constant value across a large range of flow velocities.

Neither of the previous two sets of workers discuss the degree to which the turbulence is isotropic. Anisotropy of turbulence may be especially relevant in the vehicle wake. Indeed, Eskridge and Hunt [30] allowed for this in their model of turbulence in the wake of a single vehicle in a weak wind.

Therefore, based on these arguments, the following form of the turbulence in the canyon is proposed. It is based not on any analytical model but instead is in a form which allows for both the turbulent intensity and anisotropy of the turbulence to be varied by the numerical modeller. So at any point in the canyon, the *x*-component of turbulence,

u'^2 is given by,

$$u'^2 = \alpha_1 \left(\alpha_2 u^2 + (1-\alpha_2)\left[v^2 + w^2\right]\right)^{\frac{1}{2}} \tag{4.28}$$

where α_1 is the turbulence parameter which relates the level of turbulence to the local wind velocity, α_2 is the turbulence parameter which quantifies the anisotropy of the turbulence and u, v and w are the components of air velocity. It should be noted that the value of u^2 is, in fact, the sum of all the squares of the wake and ambient wind-induced velocities in the canyon. Similar expressions to Equation 4.28 can be found for the v and w components by cycling u, v and w.

4.2.6 Roof Level Puff Entrainment

Dabberdt and Hoydysh [22] used flow visualization techniques to look at trajectories within a scaled street canyon in an atmospheric wind tunnel. They observed that about half the trajectories left the canyon on the first rotation whenever a transverse vortex was present. Further, only about 1 in 10 of the trajectories survived to complete a second full rotation and no trajectories managed more than five rotations.

It would appear that this roof level entrainment needs to be incorporated into the present model. Instead of directly reducing the number of puffs in the canyon by some kind of stochastic method, a different approach is used here. One in which the mass associated with each puff is reduced in a consistent manner as it moves close to the roof level.

Consider a cross-section in the yz-plane of a single puff located, for no reason other than for clarity, very close to the roof level, as shown in Figure 4.5[4]. The puff is split into two parts: the lower part has travelled for a single time step of length Δt with a cross canyon component of velocity of v_p; the upper puff has travelled for the same time at the higher velocity of v_H, the above roof level wind velocity. The split is a very simplistic way of visualizing the process whereby the portion of the puff above $z = H$ is advected away from the main body of the puff by the higher ambient cross canyon wind velocity above the rooftops. It is proposed that this splitting is the main reason for the mass associated with the puff being decreased by an amount ΔM over the period of a time step.

Now, M is the total mass associated with the puff before the time step. This is given initially by $q_e c_e \Delta t$, where q_e is the release rate and c_e is the concentration of pollutant from the exhaust of the vehicle and where it has been assumed that the pollutant was released for a time Δt. Due to the shift of the top part of the puff to the right as shown in Figure 4.5, the mass of pollutant in the puff is reduced by an amount, ΔM, which is given by,

$$\Delta M = \frac{q_e c_e \Delta t}{(2\pi)^{\frac{3}{2}} \sigma_x \sigma_y \sigma_z} \cdot \int_{-\infty}^{\infty} \exp\left(-\frac{x'^2}{2\sigma_x^2}\right) dx' \cdot \int_{-\Delta y/2}^{\Delta y/2} \exp\left(-\frac{y'^2}{2\sigma_y^2}\right) dy'$$

[4]The solid boundary attributed to the puff is merely a schematic representation of the extent of the puff, based on the dispersion parameters, σ_y and σ_z.

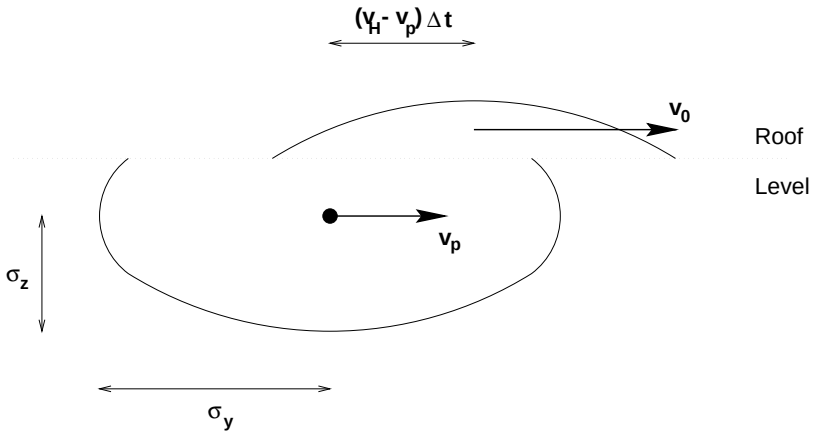


Figure 4.5: Schematic of the entrainment process for a single puff being sheared by the velocity differential at roof level.

$$\cdot \int_{H-z_p}^{\infty} \left[\exp\left(-\frac{z'^2}{2\sigma_z^2} \right) + \exp\left(-\frac{(z'+2z_p)^2}{2\sigma_z^2} \right) \right] dz' \tag{4.29}$$

where,

$$x' = x - x_p \, ; \qquad y' = y - y_p \, ; \qquad z' = z - z_p$$

which represents a translation to a coordinate system centred on the puff. The limits of the first integral indicate integration along the entire length of the canyon which is assumed to be endless and the limits of the third integration represent the portion of the plume above the plane $z = H$, including the image source of the puff in the canyon floor. The limits on the second integral require further clarification. Figure 4.6 shows the variation of concentration along a line parallel to the y axis in the upper portion of the puff before and after the shear takes place. It can be seen that the second Gaussian distribution is displaced to the right by a distance $\Delta y = (v_H - v_p)\Delta t$. The reduction in mass is represented by the cross-hatched region in the Figure. This area is given by the following expression,

$$\frac{1}{(2\pi)^{\frac{1}{2}}\sigma_y} \int_{-\Delta y/2}^{\Delta y/2} \exp\left(\frac{y'^2}{2\sigma_y^2} \right) dy' = \operatorname{erf}\left(\frac{\Delta y}{\sqrt{8}\sigma_y} \right) \tag{4.30}$$

where erf is the error function and where we have used the symmetry of the Gaussian distribution to simplify the integration. The properties of the error function are such that when $\Delta y = 0$, when there is no velocity differential between the puff and the roof level wind, then the mass loss will be zero.

Equation 4.29 can then be rewritten as,

$$\Delta M = \frac{1}{2} q_e c_e \Delta t \cdot \operatorname{erf}\left(\frac{\Delta y}{\sqrt{8}\sigma_y} \right) \cdot \left[\operatorname{erfc}\left(\frac{H - z_p}{\sqrt{2}\sigma_z} \right) + \operatorname{erfc}\left(\frac{H + z_p}{\sqrt{2}\sigma_z} \right) \right] \tag{4.31}$$

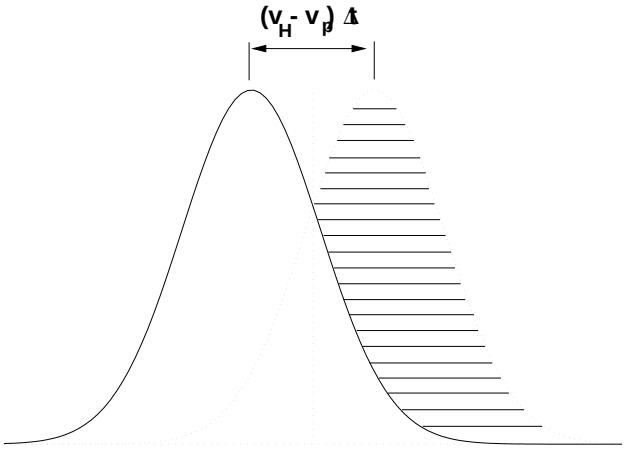


Figure 4.6: Displacement of the Gaussian distribution in the across canyon direction due to the velocity differential.

Thus, the mass associated with each puff can now be reduced in a consistent manner - but more control is required over this process than is afforded by the above. Two parameters, λ_f and λ_l, the puff reduction factor and the puff removal limit, are introduced at this stage. The former is simply a multiplier for Equation 4.31 which allows the modeller to manipulate the fraction of mass lost per revolution in the canyon. The latter, λ_l, defines the fraction of the initial mass of the puff below which the current mass must fall before the puff is systematically removed from the domain. Essentially, it is a computational aid - the fewer puffs there are in the domain, then the faster the model will run and when a puff is reduced to such a weak state its contribution to Equation 4.10 is deemed ineffectual.

4.2.7 End Entrainment and Cyclical Boundaries

Any puff which wanders beyond either end of the canyon (*ie* if $x_p < 0$ or $x_p > L$) can be treated in two quite distinct ways. It can either be removed from the model or it can be recycled to the other end of the canyon. It is assumed that puffs leaving the canyon by the first method are moved away from the canyon along other adjacent canyons or by the ambient wind.

The second approach requires some explanation. The recycling of puffs in this manner, very much akin to the recycling of vehicles as they drive up and down the canyon, is an attempt to lessen the effects of the canyon ends in any studies close to the centre of the canyon. Some modification of Equation 4.11 is required in this case. For puffs which

are more that a distance $L/2$ along the canyon from a receptor, Equation 4.11 becomes,

$$X(x_r) = \exp\left\{-\frac{1}{2}\left(\frac{|x_r - x_i| - L}{(\sigma_x)_i}\right)^2\right\}$$

which ensures that the contributions from puffs which are physically at the opposite end of the canyon to the receptor are correctly modelled.

4.3 Implementation on Computer

The model described in above has been coded up into a computer program called PUFFER. The program has been written in a combination of C and FORTRAN77 on the UNIX cluster at the Civil Engineering Department.

PUFFER is currently at version 5.3 - the development process has preceded in tandem with the development of the theoretical model. A comprehensive description of the source code, input and output requirements and usage of the program can all be found in Appendix B.

4.4 Sensitivity Study

With any mathematical model/computer code combination such as the one described above it is necessary to perform verification and validation[5] exercises.

As far as validation is concerned, the present study will be limited to the single vehicle case because the wind tunnel study was limited to the use of a single vehicle on the Moving Model Rig and this will be dealt with in Chapter 5.

This section is concerned with the verification of the model and will proceed as follows. Firstly, two sensitivity studies will be performed based around a multi-vehicular urban base case and a single vehicle rural case. Then the model will be compared with other models of similar capability, some of which were mentioned in Chapter 2.

4.4.1 The Urban Base Case

Definition

There follows a description of the base case which is used in the urban sensitivity study. By varying parameters around this base case, it is possible to test the way in which the model reacts to changes in vehicle density, canyon aspect ratio, wind speed, wind direction, etc. The multi-vehicle case has been chosen for the urban base case because of the possibilities of comparison between PUFFER and other models.

Consider a canyon with dimensions, $250 \times 20 \times 20$ m (length$\times$width$\times$height), which contains two lanes of traffic. Lane number 1 is 5 m from the leeward wall of the canyon and contains 10 vehicles travelling at 15 ms^{-1} in the positive x direction. Lane 2 is 5 m from the windward wall and also contains 10 vehicles again travelling at 15 ms^{-1} but this time in the opposite direction. Each of the 20 vehicles is 2.5 m long, 1.5 m high, 1.5 m wide and emits pollutant of concentration 1.0×10^{-3} kgm^{-3} at the rate of 1.0×10^{-3} $\mathrm{m}^3\mathrm{s}^{-1}$, the rate simply being determined by a combination of the idling value and a speed dependent factor in a ratio of 1:9. It should be noted that the vehicle numbers and emission rates represent the steady-state values: as will be seen shortly, there is a lead-in time before these numbers are reached.

The magnitude of the concentration used is almost irrelevant, it is the relative values produced by the model that are important since there is nothing in the theoretical model which depends on the absolute concentration. Thus, results will be presented in non-dimensionalized form. The roof level wind is perpendicular to the long axis of the

[5] There is often confusion about the precise definition of these two terms. In this instance, verification means checking that the code actually represents the mathematical model accurately and validation means checking the code against empirical results.

Parameter, symbol (units)	Value	Parameter, symbol (units)	Value
Canyon length, L (m)	250.0	Speed control parameter, C_1 (s^{-2})	1.0
Canyon width, B (m)	20.0	Headway control parameter, C_2 (s^{-1})	0.25
Canyon height, H (m)	20.0	Headway calculation parameter, β (s)	1.417
Vehicle length, l (m)	2.5	Idle emission rate, q_i (m^3s^{-1})	1.0×10^{-4}
Vehicle width, b (m)	1.5	Velocity emission factor, q_s (m^2)	6.0×10^{-5}
Vehicle height, h (m)	1.5	Idling concentration, c_i (kgm^{-3})	1.0×10^{-3}
Wind speed, u_H (ms^{-1})	4.0		
Surface roughness, z_0 (m)	1.0		
Turbulence parameter, α_1	0.25	Turbulence parameter, α_2	0.1
Puff reduction factor, λ_f	1.0	Puff removal limit, λ_l	1.0×10^{-12}
Time step, Δt (s)	0.05	No. of time steps	18000

Table 4.1: Values of parameters used in the urban base case.

canyon and has a mean velocity of 4 ms^{-1}. The two turbulence parameters, α_1 and α_2, are set to 0.25 and 0.1 respectively and the cyclical end boundaries are switched on. All other parameters for the base case are presented in Table 4.1.

Observations

There follow a number of observations made about the urban base case scenario, based on looking at the variation with respect to time of various properties of the model. The plots cover only the first 400 s of the base case run which actually extends for 900 s.

1. Figure 4.7(a) shows the variation of the *x*-component of the first puff in the list of puffs tracked by the computer program. Such is the nature of the program that as the first puff becomes too weak it is removed from this list and replaced, probably by the next one in the list. Such a discontinuity appears in the *x*-coordinate at roughly 175 s and manifests itself in plots (b) to (d) also. As the puff moves in the vortex from lane to lane it gets dragged first one way and then the other. Notice also the effect of the imposed cyclical boundary conditions - as the puff wanders out the end of the canyon it immediately reappears at the opposite end. This explains the presence of the vertical lines in the plot (a) which indicate the movement of the puff from one end of the canyon to the other.

2. Plot (b) in the Figure shows the variation of the *y*- and *z*-components of the puffs positions with time. Both trace paths according to the resident vortex in the canyon due to the cross-wind. It is noticeable that the centre of each puff is thrown outwards towards the walls in this particular vortex.

3. Plot (c) shows clearly the roof level entrainment process at work. The most violent reductions in the mass of the puff occur when the puff is close to the roof. This can be checked by a comparison with plot (b). Indeed as the mass is reduced below

the puff removal limit, the puff is deleted from the list of puffs because it no longer contributes significantly to the overall concentration.

4. Plot (d) shows the increase in the three dispersion parameters associated with the tracked puff. The most dramatic increase is seen in σ_x, the component aligned along the axis of the canyon. This occurs because the vehicle wakes are the most important source of turbulence in the canyon. Comparing plots (d) and (b), it is possible to see that the greatest rate of increase in σ_x occurs when the puff is near ground level (*ie* in the wake).

5. Plot (e) shows the overall mass balance. 'Storage' is the sum of the mass contained in the all the active puffs in the canyon at any one time. The 'In' value is found by keeping a running total of the initial mass of the puffs as they are released from the exhaust pipes of the vehicles. The 'Out' value is found by adding up the mass lost in the roof entrainment process, the residual mass in weak puffs as they are removed and, although not in the base case, the mass held in puffs lost at the ends of the canyon. From the plot it can be seen that after an initial settling period, in which vehicles are still being added to each lane of traffic, a quasi steady-state is reached. The storage remains within a definite range, while the gradients of the 'In' and 'Out' line tend to the same value.

6. The approach to a steady-state is further demonstrated in the sixth of the plots which shows, in absolute terms, the concentration variation with time at a receptor on the leeward wall at a height $H/10$ - approximately equal to that of an average person. The so-called 'steady-state' condition is by no means constant and displays a certain periodicity. This variation is due to the discrete passing of vehicles in both lanes of traffic, each of which contribute peaks to this trace.

4.4.2 Urban Sensitivity Study

The results in the following Sections are presented in the following format:

- All results are steady-state values. That means that they are time-averages of the concentrations produced by the program after the initial "settling down' period. Indeed, all the test cases are run for a period of 900 s, and the averaging process does not commence until 200 s have elapsed.
- Where appropriate, the following scaling is adopted,
  - Lengths are scaled with respect to the height of the street canyon, H.
  - Concentrations are scaled using the same method as Section 3.2.9 with the above canyon wind speed used as the reference wind speed in this case.

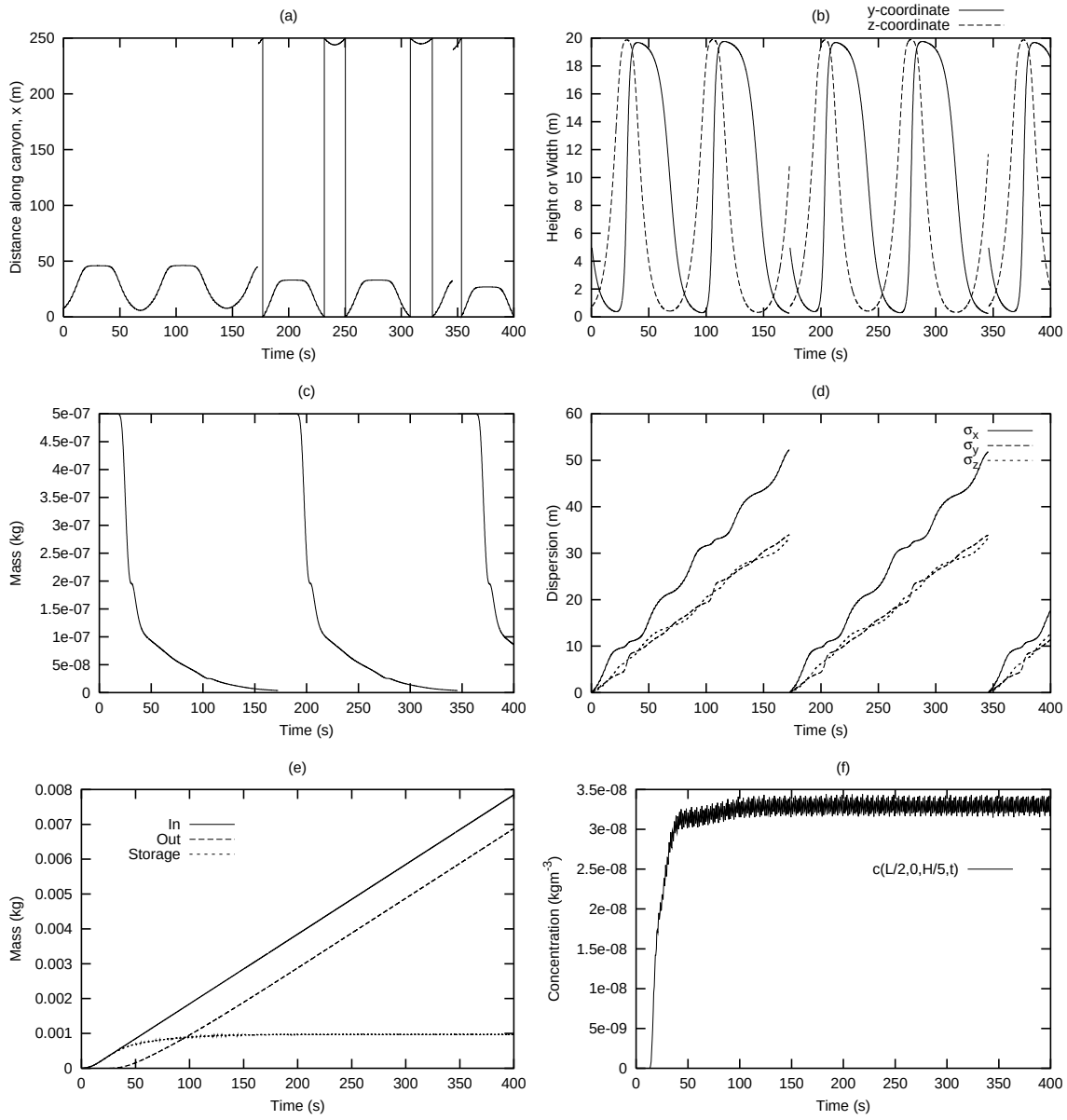


Figure 4.7: Characteristics of the urban base case.

- Shaded contour plots of concentration on the $x = L/2$ cross-section along the canyon will be presented (as far as possible from the ends of the canyon in order to minimize any boundary effects not negated by the cyclical boundary conditions). An array of 121 receptors were used to produced these plots, with the data being further interpolated onto a 21×21 grid to smooth the data. It was not possible on these plots to impose the same range of values for the contours and so each must be viewed with the proviso that the maximum contour value will inevitably vary between the base case and each sensitivity case.
- Profiles up the leeward wall of the canyon at $x = L/2$ will also be presented. The leeward wall was chosen because experience has shown that this is the region in which the highest concentrations generally occur.

Variation of Concentration with Wind Speed

By first reducing and then increasing the above canyon wind speed to half and then twice its base case value, it is possible to gain some understanding of how important a factor the wind speed is on the levels of concentration in the street canyon. Figure 4.8(b) is the base case distribution of concentration across the canyon, with (a) and (c) being for the halved and doubled wind speeds respectively. What initially becomes apparent from the three contour plots is that the degree of spread of pollutant is larger at the lower wind speeds. The aspect that requires some thought, however, it that the absolute concentrations at the lower wind speeds are much greater (the concentrations are scaled as $cu_{\mathrm{ref}}l^2/c_0q_0$) than at the higher speeds. Indeed, they are roughly three times higher at half the base case wind speed than the double wind speed case. This is broadly in line with many full-scale studies which found the concentrations approximately inversely proportional to the wind speed. Figure 4.8(d) shows the effect of the "eye" of high concentration as it moves onto the leeward wall at the higher wind speed. The peak in concentration moves from the foot of the wall to a height roughly equal to that of a person.

Variation of Concentration with Vehicle Speed

Figure 4.9 shows the effect of varying the vehicle speed on concentrations. Note that as the vehicle speed changes, the headway is maintained at its base case values in order to simplify the situation a little - this is not a realistic characteristic of traffic. Not only is the vehicle speed halved and doubled in this case, it must be remembered that the exhaust flow rate is roughly halved and doubled as well because of the significant speed-dependent component to the exhaust rate calculation. Thus, since q_0 forms a part of the concentration scaling factor, these results bear closer inspection than might at first be apparent.

From the contour plots it can be seen that the higher vehicle speeds, Figure 4.9(c), tend to mix the pollutant more as might be expected with the added turbulence. As for the absolute values of concentration, the higher vehicle speeds give rise to the expected higher concentrations since the exhaust rates are greater for the same density of vehicles in each lane. The profiles up the leeward wall confirm these observations with the exhaust height peak being smoothed when more turbulence is present.

Response to Changes in Puff Removal Limit

The puff removal limit, λ_l, is perhaps the least understood aspect of the computer model. This part of the sensitivity study aims to quantify the effect that this parameter can have on the behaviour of the model. The results are presented in the usual way in Figure 4.10 but with the base case occupying plot (a), instead of the normal (b) position. This is done because the puffer removal limit was increased from the base case, first by a factor of 1.0×10^3 in the case of plot (b) and then by a further factor of 1.0×10^3 for plot (c). Little perceivable difference can be seen at the first increment - although the difference is more marked on the profile plot (d). However, the final increase in λ_l yields a big drop in concentrations and a disappearance of the now familiar plume of contaminant up the leeward wall.

This indicates that there is a critical value of λ_l at which this change takes place. Keeping the value below this point is therefore an important aspect of the modelling process. It must be stressed, however, that the concentration values do vary with small changes in λ_l and so this parameter cannot be set with any kind of certainty until some calibration data has been run through the model.

Response to Changes in the Puff Reduction Factor

The effects of the puff reduction factor, λ_f, are also poorly understood. To recap, this parameter governs the rate at which the mass of the puffs is removed by the roof level entrainment process. Figure 4.20 shows the effect of first reducing λ_f by a factor of 10 and then by a factor of 100. From the contour plots, the is little change in the distribution but there is an increase nonetheless. This is only to be expected because by reducing the puff reduction factor the amount of pollutant in the canyon is being increase. From plot (d), it is noticeable that the profile is basically shifted by some offset rather than the whole profile being scaled. Thus, with less pollutant being lost at roof level, there is a disproportionate increase in that region. The fact that the further reduction of this parameter by a factor of 10 induces very little change indicates that there is a certain limiting effect taking place here. This is unexpected and may be explained by the dispersion of the puffs being responsible for their weakening.

Response to Changes in Dispersion Parameter, α_1

As expected, changes to the dispersion parameter, α_1, simply have the effect of increasing/decreasing the amount of turbulent mixing which occurs in the canyon. Figure 4.11(a) shows the concentration distribution for a doubling of the value of α_1 from its base case value shown in Figure 4.11(b). More dispersion occurs with the associated drop in peak values of concentration. The opposite effect is seen in Figure 4.11(c) with a value of α_1 only half that of the base case. It is interesting to note that for the high-valued case that there is significantly more pollutant around the windward lane of traffic. This is probably due to the fact that dispersive effects are, in this case only, dominating the advective effects.

Variation of Concentration with Wind Direction

In this case, the wind direction was varied and the cyclical boundary conditions were turned off. The latter had to be done because in the case where the wind is parallel to the longitudinal axis of the canyon, there would have been no roof level entrainment and the concentration in the canyon would simply have risen without bound.

With this in mind, Figures 4.12(a) to (c) show the concentration distributions at steady-state for a wind direction perpendicular to the street, at 45° and then parallel to the street.

For the 45° case, the magnitudes of the concentration are roughly the same as the base case but are more dispersed - very much like the reduced wind speed case of Figure 4.8(a). The parallel case, though, is somewhat unexpected with an asymmetrical concentration distribution being observed with peaks around the two lanes of traffic. This asymmetry is best explained by the fact that the leeward[6] lane goes with the flow of the wind, while the windward lane vehicles drive into the wind. This has implications for the wakes behind the vehicle which then explains the more dispersed distribution above the windward lane. In any case, the concentrations seen in this configuration are far greater than when there is a cross-canyon flow component.

Further investigation reveals that with the cyclical end boundary condition relaxed, there is a steady build-up of pollutant towards the exit of each lane. This is best illustrated by Figure 4.12(d) which shows a vertical cross-section along the length of the canyon, centred on the leeward lane of traffic. There is certainly a boundary effect at the exit which causes a drop in the concentration in that vicinity.

If any conclusion is to be drawn from this set of cases, then it is that the cross-canyon wind configuration is the most efficient at minimizing the maximum concentration to be found in the street canyon. However, up the leeward face, plot (e), the concentrations

[6] In the parallel case, 'leeward' and 'windward' have no real meaning but we use the convention of the previous test cases in order to distinguish between the two.

are roughly the same in all three cases.

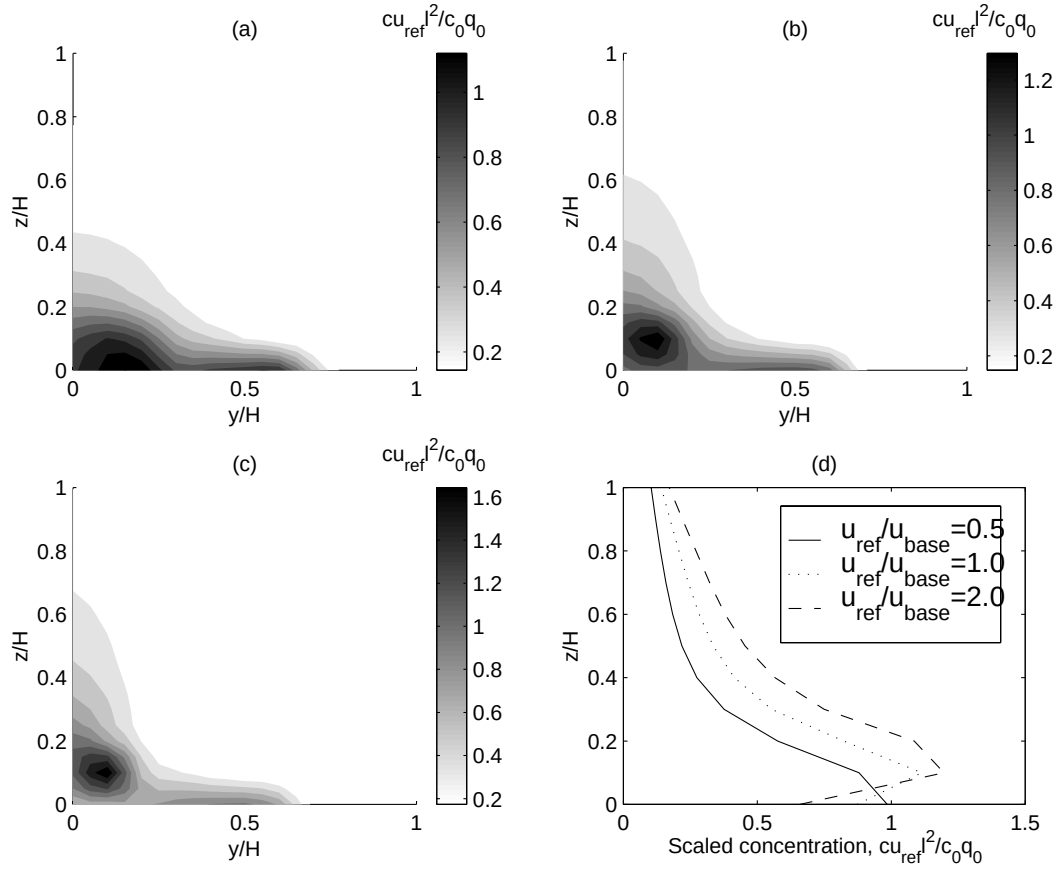


Figure 4.8: Variation of concentration with wind speed in a street canyon: (a), (b) and (c) are contour plots at $x = L/2$ for $u_{\text{ref}}/u_{\text{base}} = 0.5, 1.0$ and 2.0, (d) are profiles up the leeward wall.

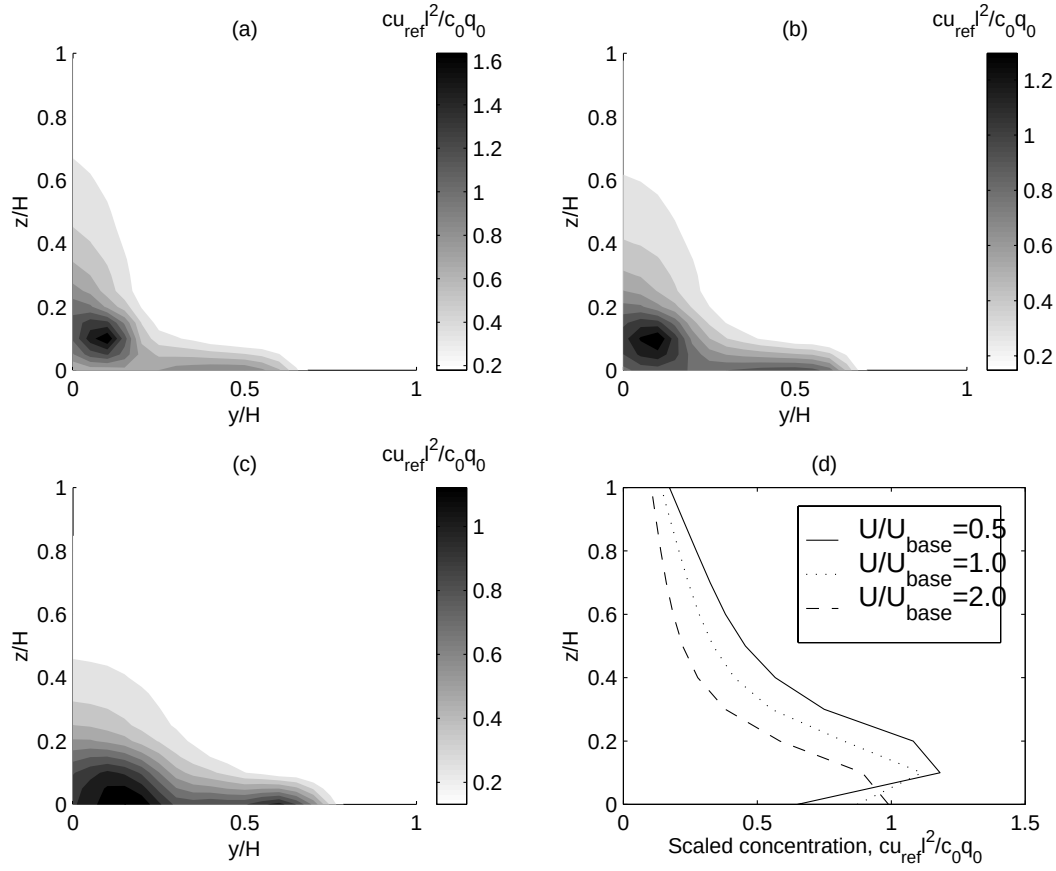


Figure 4.9: Variation of concentration with vehicle speed in a street canyon: (a), (b) and (c) are contour plots at $x = L/2$ for $U/U_{\text{base}} = 0.5, 1.0$ and 2.0, (d) are profiles up the leeward wall.

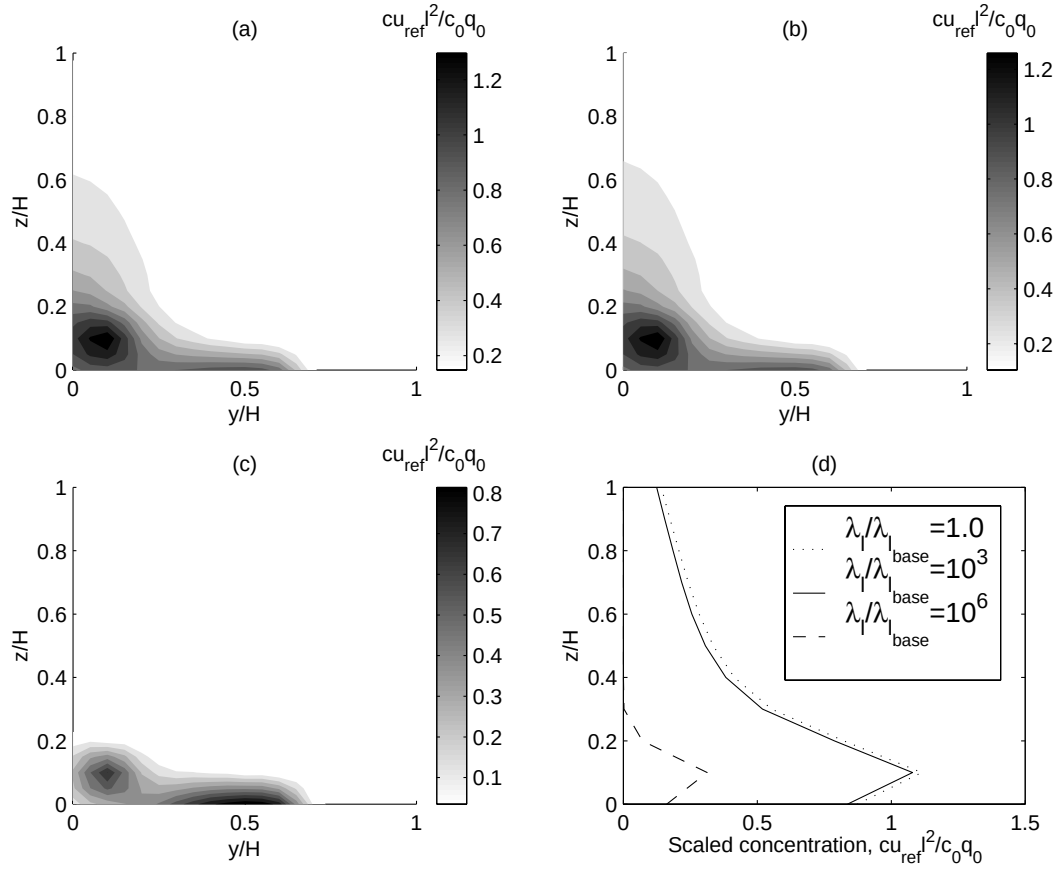


Figure 4.10: Response of the model to increases in the puff removal limit: (a), (b) and (c) are contour plots at $x = L/2$ for $\lambda_l/\lambda_{l_{\text{base}}} = 1.0,\ 1.0 \times 10^3$ and 1.0×10^6, (d) are profiles up the leeward wall.

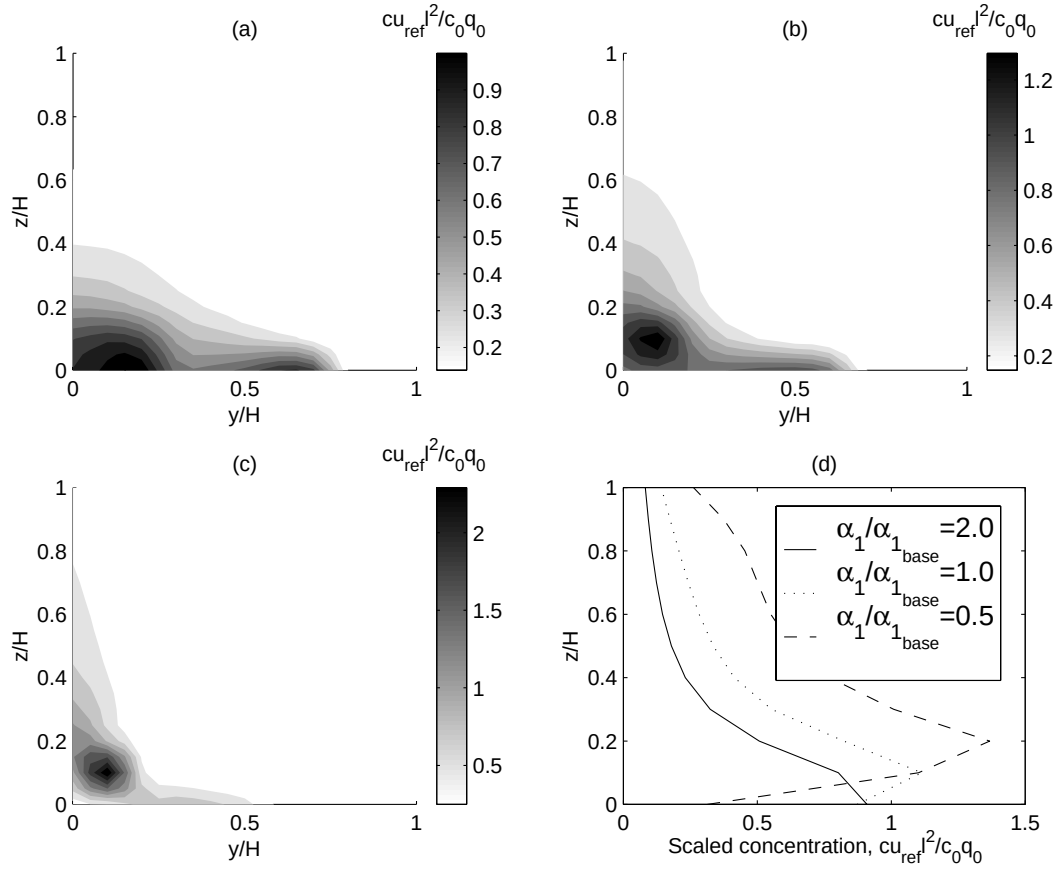


Figure 4.11: Response of the model to changes in the dispersion parameter, α_1: (a), (b) and (c) are contour plots at $x = L/2$ for $\alpha_1/\alpha_{1_{\text{base}}} = 2.0$, 1.0 and 0.5, (d) are profiles up the leeward wall.

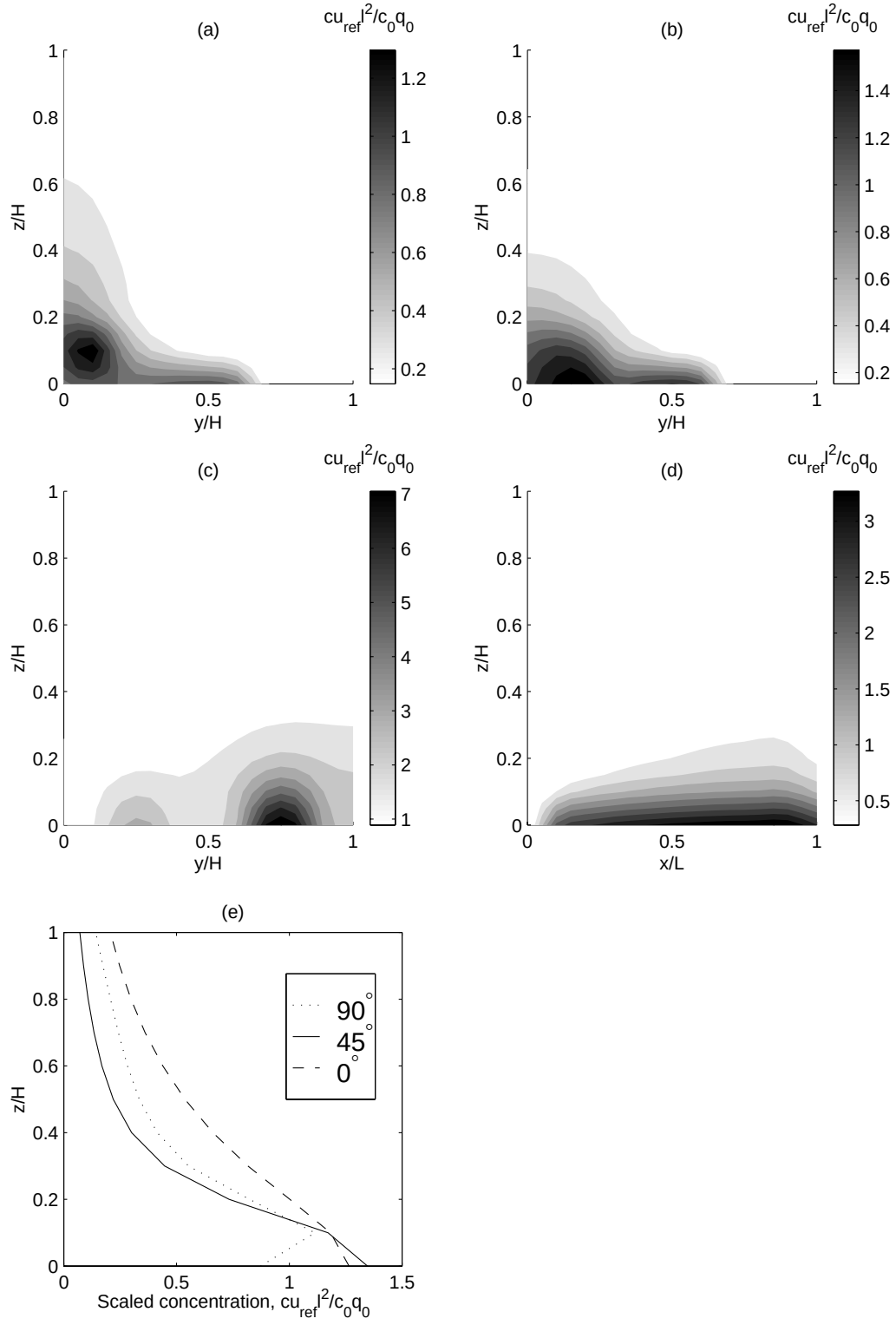


Figure 4.12: Variation of concentration with wind direction in a street canyon: (a), (b) and (c) are contour plots at $x = L/2$ for angles of 90°, 45°and 0°; (d) is an along-canyon plot at $y = B/2$; and (e) are profiles up the leeward wall.

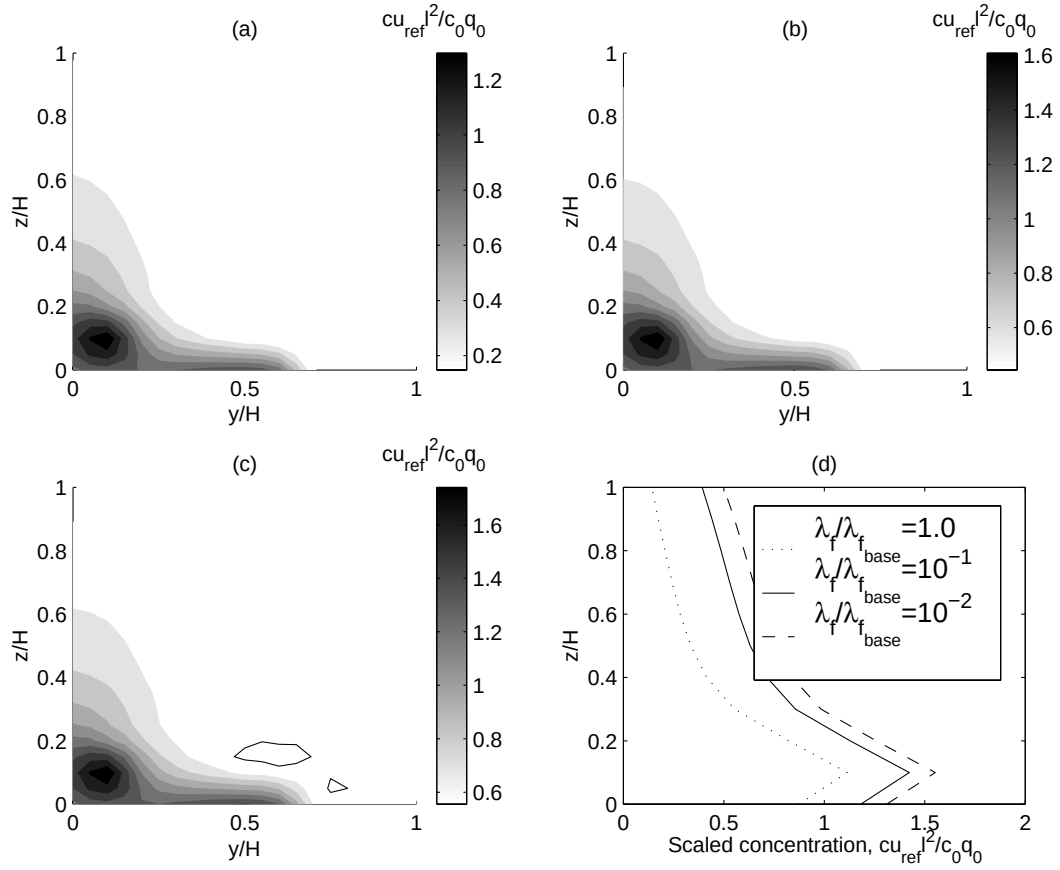


Figure 4.13: Response of the model to decreases in the puff removal limit: (a), (b) and (c) are contour plots at $x = L/2$ for $\lambda_f/\lambda_{f_{\text{base}}} = 1.0$, 1.0×10^{-1} and 1.0×10^{-2}, (d) are profiles up the leeward wall.

4.4.3 Rural Base Case

The rural base case differs markedly from the urban base case. Chief among the differences is that an open domain $250 \times 25 \times 3.0$ m is used with a single vehicle travelling along the x-axis at 15 ms^{-1}. The actual size of the domain is not an issue here as far as boundary effects are concerned as the domain is merely used as a volume in which to position the receptors - it has no bearing computationally. A side wind with a logarithmic profile is present, blowing in the negative y-direction with a speed of 4 ms^{-1} at a reference height of 10 m with a roughness length of 0.01 m. Also, the linear dependence of the exhaust flow rate on the vehicle speed is removed, to be replaced with a purely idling rate. Other than those changes, vehicle size and dispersion parameters are all the same as for the urban base case.

4.4.4 Rural Sensitivity Study

Before embarking on the presentation of the results of the sensitivity study it is necessary to make several observations about the format of the results.

- Most of the results will be presented as time histories of concentration at single receptors and will be scaled in the same way as described in Section 3.2.9. However, since we will be varying vehicle speed, it will become necessary to alter the velocity scaling occasionally. It will be made clear when this occurs.
- The other format used will be instantaneous profiles of concentration along various lines in the domain. Similar scaling arguments apply in these cases.
- The origin of the time axis of the plots will again coincide with the moment the front of the vehicle coincides with the x-coordinate of the receptor.

Variation of Concentration with Distance Downstream

Figure 4.14 shows the various breakthrough curves at five positions, $l/2$, l, $3l/2$, $2l$, $3l$ and $4l$, downstream of the roadway. The expected behaviour is shown with both the peak of the curves occuring later and the degree to which the curve is spread out increasing as distance from the roadway is increased. Indeed, it can be shown that the propagation speed of the peak is equal to the wind speed at $z = h/2$.

Variation of Concentration with Height

Figures 4.15 and 4.16 show a very interesting phenomenon. They both show the variation of concentration with time at a variety of heights, $z = 0,\ h/2,\ h,\ 3h/2$ and $2h$, but

Figure 4.15 is close to the vehicle at $y = l$, whereas the second is further downstream at $y = 4l$.

Close to the roadway, the vast majority of the pollutant is still concentrated around $z = h/2$, its release height. The slug of pollutant released every time step in the form of a puff does not have time to disperse much by this time. Quite some distance downstream, however, the situation is quite different. By this time, turbulent dispersion has had time to expand the puffs and the more expected decrease with height is observed. Indeed, these observations are reinforced by the plots in Figure 4.17 which shows several vertical profiles at a distance $4l$ downstream at various times after the vehicle has passed. Notice that the line for the first time, $\tau = Ut/l = 11$, uses the top scale whereas the remaining three all use the lower scale. From this figure, it can be seen that the largest concentration occurs around $\tau = 18$, which agrees with the peaks in Figure 4.16. An interesting effect is the initial kink in the profile with a peak at $z = h/2$, the height of the exhaust pipe.

Variation of Concentration with Wind Speed

When varying wind speed, it would be expected that the slower the wind, the later the pollution will arrive at a receptor downstream. This fact is confirmed by Figure 4.18 which shows the breakthrough curves for five differing wind speeds. Notice that the vehicle speed, U, is used for the concentration scaling. Further analysis predicts that there should be a reciprocal relation between the wind speed and the breakthrough time and such a relationship is found for this model. Notice, also, the fact that the lower wind speeds disperse the pollutant more than the higher wind speeds. This is due to the fact that the turbulent mixing process is not linearly related to the wind speed, but depends also on the vehicle-induced turbulence.

Variation of Concentration with Vehicle Speed

In Figure 4.19, an attempt is made to show the effect the vehicle speed has on the breakthrough curves observed at a distance $2l$ downstream of the roadway. Remember that the exhaust concentration and emission rate are not related to the vehicle speed in these tests in order to clarify matters. Also, the time axis is scaled with the reference wind speed rather than the more normal vehicle speed. From the figure it can be seen that as the vehicle speed increases, the concentrations decrease. This can be explained by the fact that the emission rate is not linked to speed and hence the more quickly the vehicle passes, then the less total pollution is emitted over the period of the run. This is, of course, unrealistic but serves to show that the model functions as expected. The pollutant does reach the receptor earlier at the higher vehicle speeds and this can be explained by the more vigorous mixing in the vehicle wake at these speeds. This shows that dispersion can be as effective a transport process as advection under the correct circumstances.

Sensitivity to Time Step, Dispersion Parameters and Exhaust Flow Rate

It is now necessary to test the response of the model to various parameters of a more esoteric nature. For instance, Figure 4.20 shows the effect of changing the time step size on the accuracy of the model under "base case conditions". There are two aspects of this plot which readily catch the eye. Firstly, as the time step size is increased (*ie* for $\delta t / \delta t_{\text{base}} = 10$) the lines on the graph become less continuous - due to the fact that there are now fewer time steps at which output is produced. Secondly, there is little discernible difference between the plots for the normal base case time step and for the time step size one order of magnitude smaller. This indicates that there is convergence towards a particular solution. Notice that the word "correct" is avoided at this point. Further, the time step size used for the base case seems more than acceptable given this evidence.

Figure 4.21 shows how first an increase by a factor of 2 and then a decrease by a factor of 2 in the base case value in the first dispersion parameter, α_1 (see Equation 4.28), effect the breakthrough curves. Increasing this dispersion factor is the same as increasing the turbulence and when this is done there is a increase in the spread of the breakthrough curve. A decrease brings about a similar but opposite effect. Again this is as expected.

A test was also conducted into the effect of increasing/decreasing the exhaust emission rate by an order of magnitude. Figure 4.22 shows that this has little or no effect in this case. The only thing that could happen is that the emission source is effectively offset behind the vehicle but this seems to make little difference when the scaling effects are taken into account.

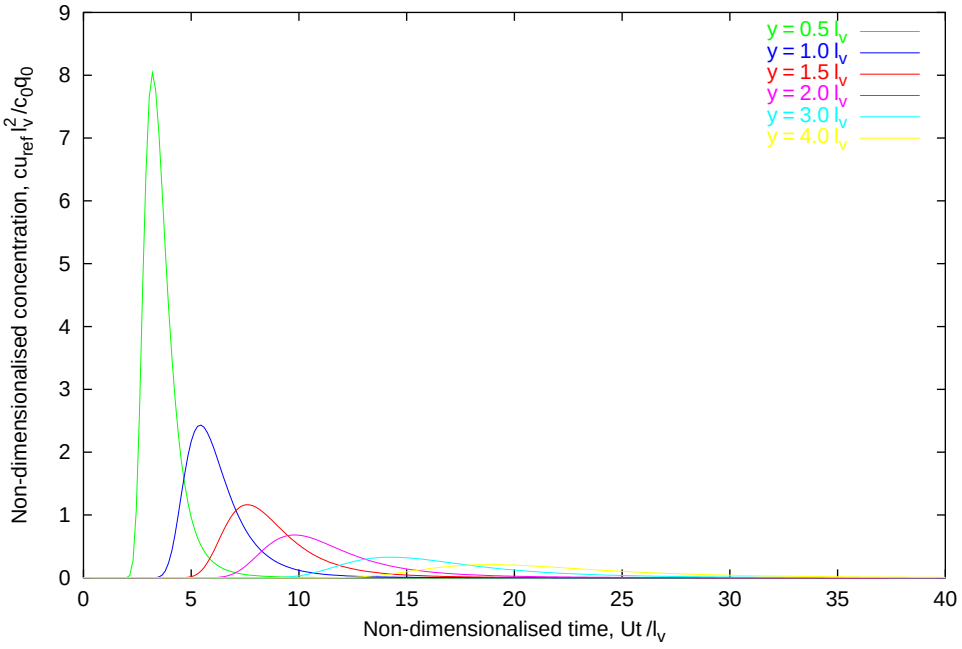


Figure 4.14: Variation of concentration with distance downstream of the roadway.

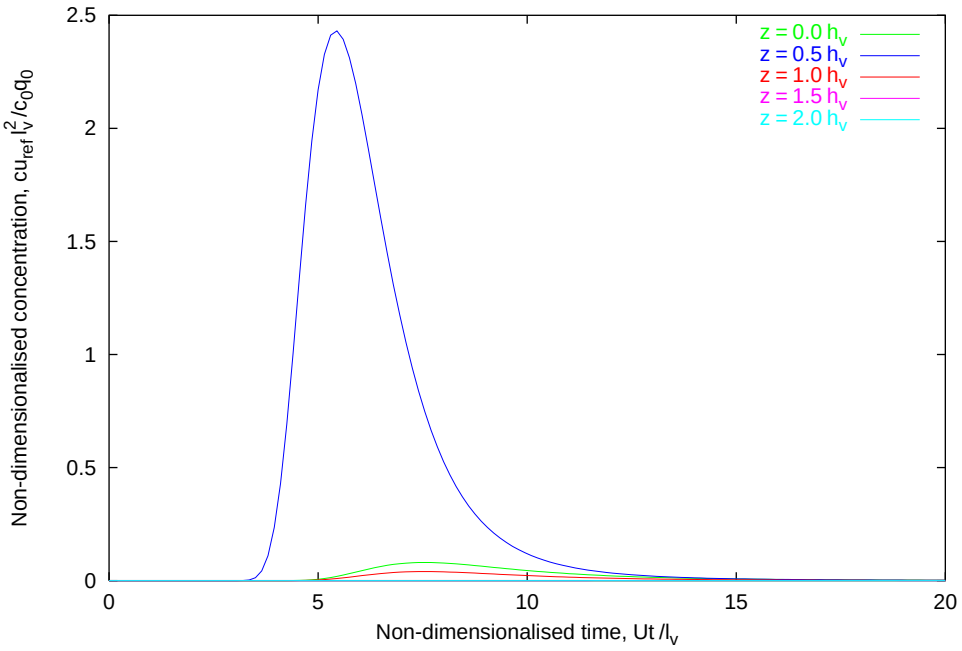


Figure 4.15: Variation of concentration with height at a distance l downstream of the roadway.

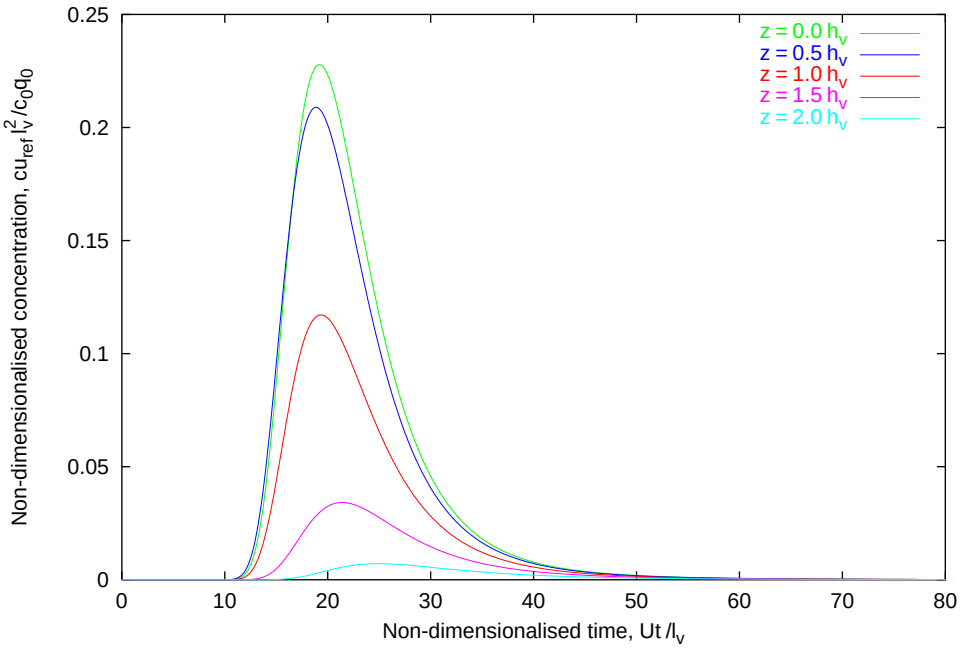


Figure 4.16: Variation of concentration with height at a distance 4*l* downstream of the roadway.

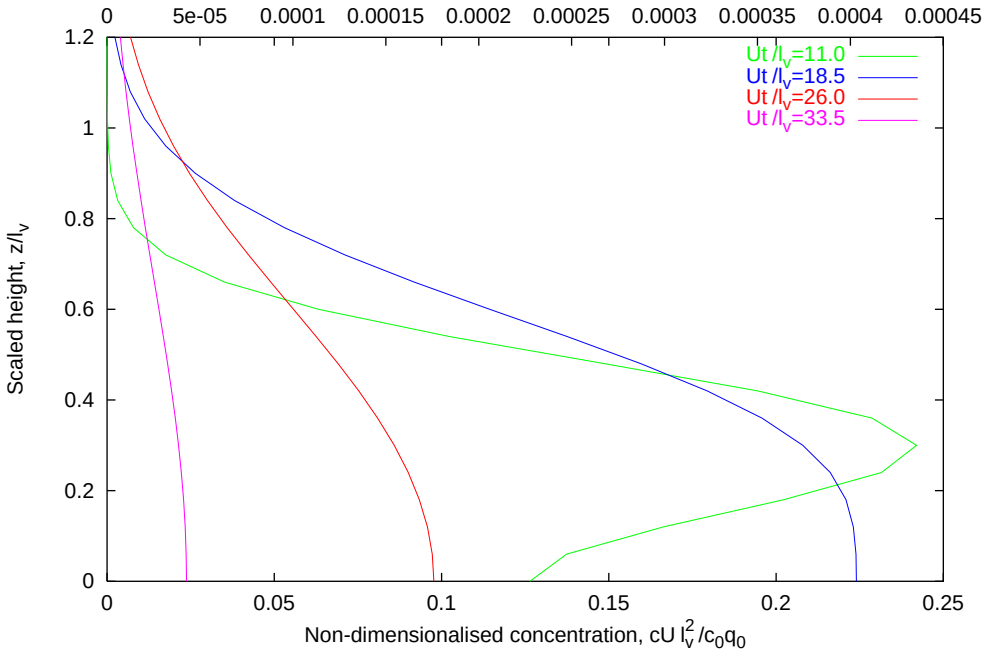


Figure 4.17: Vertical concentration profiles a distance 4*l* downstream of the roadway.

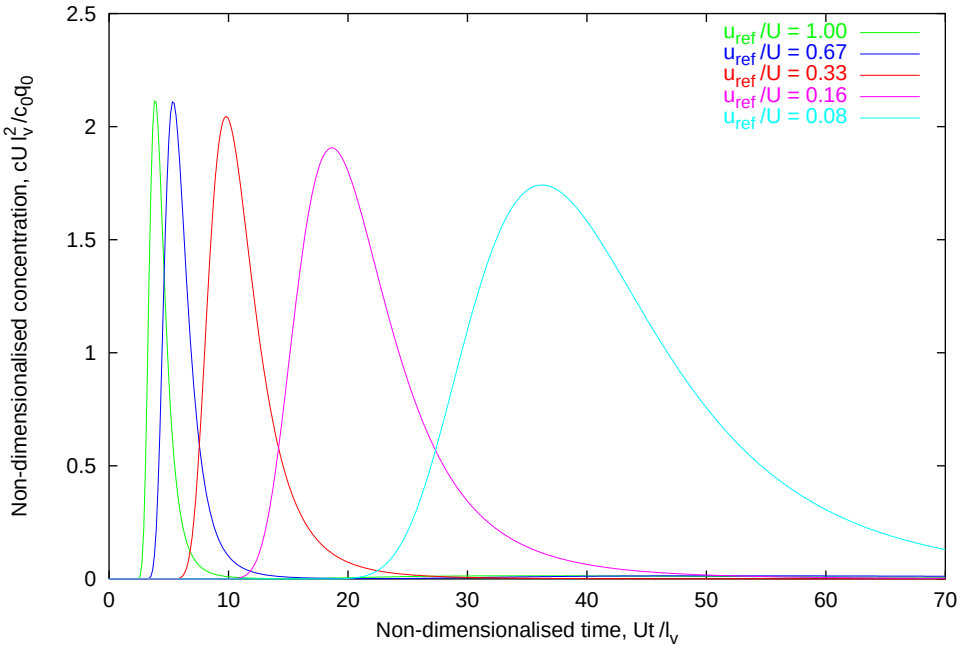


Figure 4.18: Variation of concentration with wind speed at a distance 2*l* downstream of the roadway.

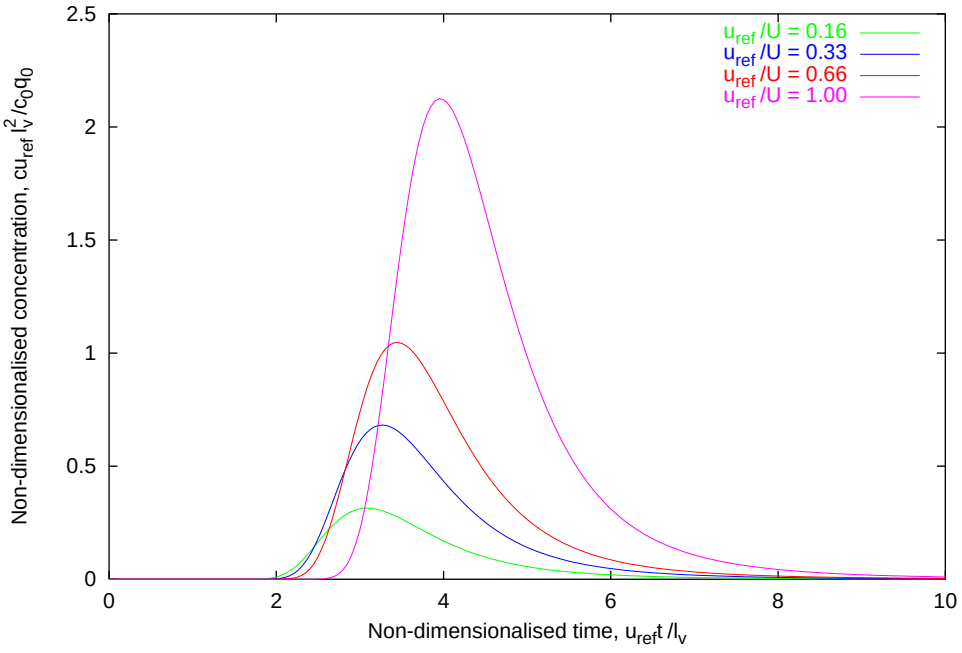


Figure 4.19: Variation of concentration with vehicle speed at a distance 2*l* downstream of the roadway.

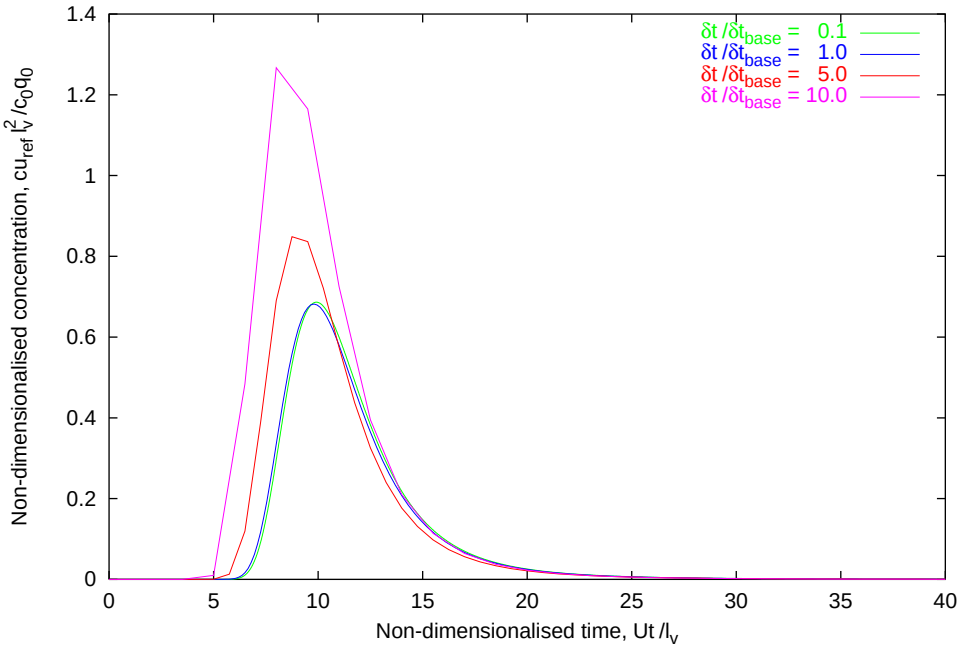


Figure 4.20: Variation of concentration with time step size.

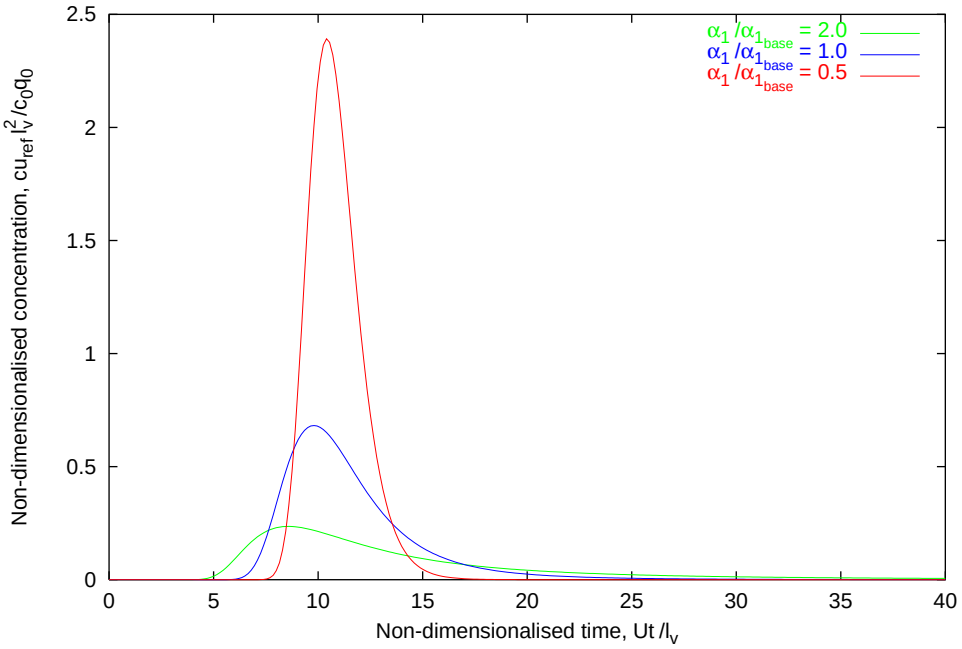


Figure 4.21: Variation of concentration with dispersion parameter, α_1.

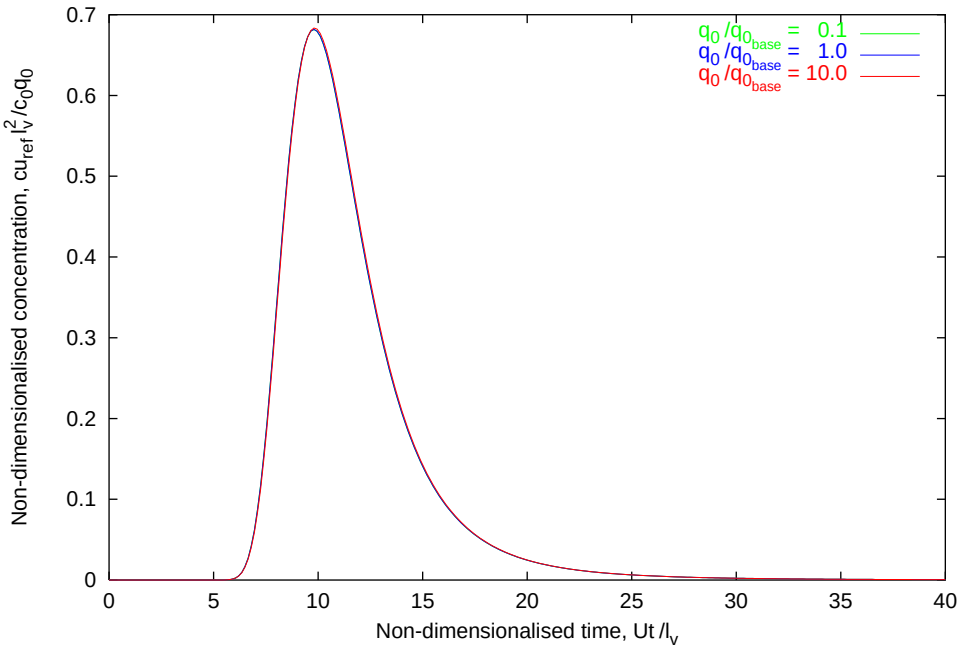


Figure 4.22: Variation of concentration with emission rate, q_0.

4.5 Inter-model Comparison

As part of the verification process, it is customary, when possible, to compare the model with other, similar programs/models. As mentioned in the literature review there are several such models in existence for he urban case. In this section, results from comparisons with the STREET and CPB3 models will be presented.

4.5.1 PUFFER versus STREET

The STREET model was described in some detail in Section 2.4.3 and, briefly, consists of two equations, one for each wall of the canyon, which attempt to predict the concentration profiles which would be seen there. Equation 2.20 and a modified version of Equation 2.21 which was suggested by Yamartino and Wiegand [89] to take into account the perceived variation on the windward face,

$$\Delta C_W = \frac{0.07N(H-z)}{B(v_H+0.5)} \tag{4.32}$$

were coded up in a short FORTRAN program. Using the experimentally determined parameters suggested by the STREET authors and values of H, B and v_H pertaining to the urban base case scenario it was possible to produce concentration profiles on each wall of the canyon for comparison with PUFFER's results.

The first attempt, with all the input data in PUFFER unchanged from the base case, over-predicted concentrations on the leeward wall by a factor of 3. A second attempt was made, this time with the dispersion parameter, α_1, increased by a factor of 3. This increase is justified on the grounds that α_1 is one of the less well understood parameters in the PUFFER model and changing it does not change the basic description of the base case scenario. A second alteration, decreasing the puff reduction factor, λ_f, by a factor of 10, was also made to decrease the very steep decrease in leeward wall concentrations with height.

Figure 4.23 shows the variation of both PUFFER and STREET concentrations on the two walls of the canyon. On the leeward wall, PUFFER still exhibits a much higher concentration gradient than STREET while on the windward wall, PUFFER predicts higher concentrations, but this time with a similar gradient to the modified STREET equation.

Considering the vastly differing approaches used in the two models, the level of agreement is gratifying. It should be remembered, however, that the agreement was only achieved after modification of two of the parameters in PUFFER.

4.5.2 PUFFER versus CPB3

CPB was described in some detail in Section 2.4.3 (Page 36) and in even more detail in the original paper (Yamartino and Wiegand [89]). A copy of the version 3 of the computer program, CPB3, was obtained from colleagues at the University of Nottingham with express permission from Dr. Wiegand, one of the original authors. The program was ported to a UNIX workstation and an attempt was made to run the program with a dataset as close as possible to the urban base case. As CPB3 considers effects such as building porosity and solar radiation, this was quite a difficult task. Nevertheless it was possible to produce concentration profiles up both the leeward and windward walls of the canyon and these are shown in comparison with the profiles from PUFFER in Figure 4.24. Note that none of the PUFFER parameters were altered from their base case values, except for a reduction of λ_f by a factor of 10.

The first thing to notice from this comparison is that PUFFER underestimates the windward wall concentrations by a factor of approximately 2. This implies that CPB3 has inherently more dispersion than PUFFER or that a lower proportion of pollutant is removed at roof level in CPB3. However, the shape of the windward curves is very encouraging. The leeward wall concentrations are of the same magnitude but display differing shapes. The PUFFER curve displays a greater vertical gradient than CPB3.

It can be concluded that PUFFER is operating broadly in line with its predecessors but that there are significant conceptual differences between PUFFER and both STREET and CPB3 which mean that anything other than the cursory comparison presented here should be treated with suspicion.

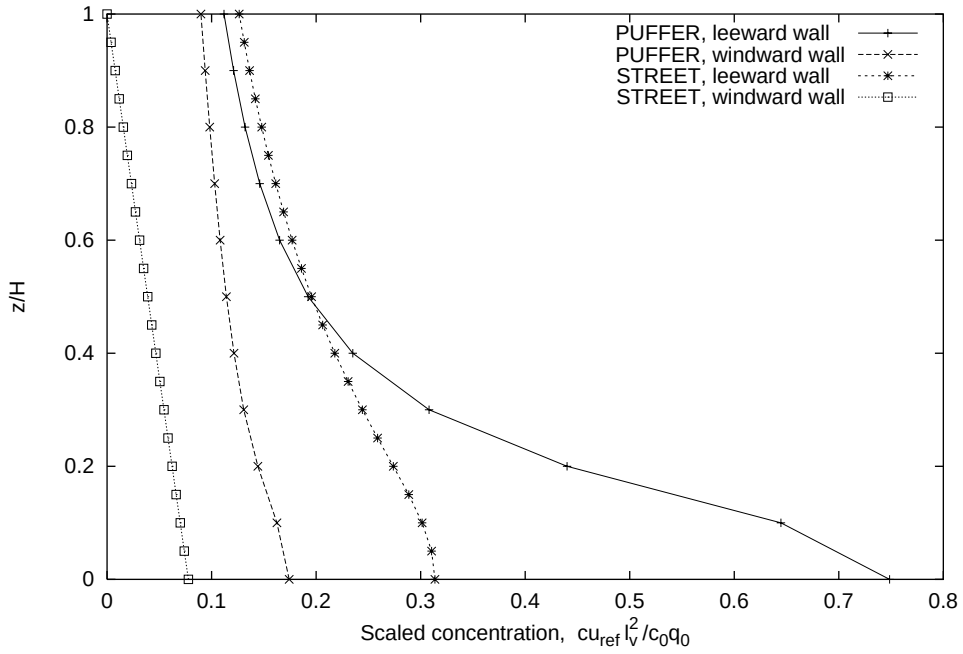


Figure 4.23: Comparison of results from the PUFFER and STREET models.

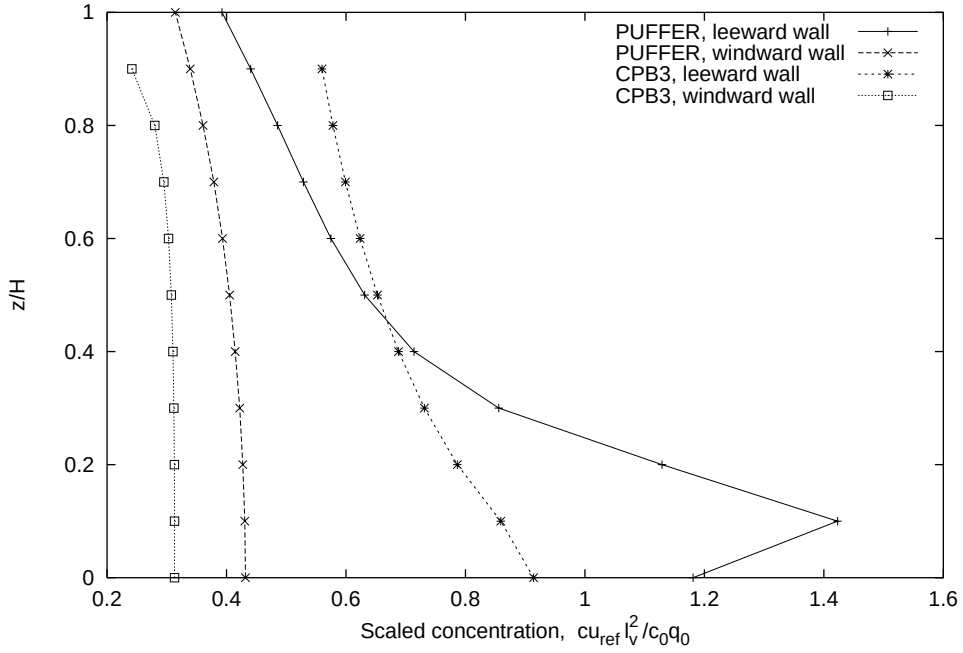


Figure 4.24: Comparison of results from the PUFFER and CPB3 models.

4.6 Statistical Application of the Model

It became apparent during the development of the model that it would be a useful exercise to look in more depth at the time series of concentrations at single receptors in the street canyon. For instance, Figure 4.7(f) shows the variation of concentration at a single receptor on the leeward wall of the canyon for the base case. Once the trace reaches steady-state, there is still a great deal of variation about the mean. This can largely be explained by the non-continuous passing of vehicle wakes.

It was decided to see whether or not this variability in concentration levels produced by the model (and associated probability density) was related in any way to that observed in the real world by workers such as Bell and Reynolds [10]. At the time of writing they are involved in an investigation which is attempting to find some rationale behind the relationship between measured roadside pollution levels and various flow parameters. Figures 4.25(a) and 4.25(b) show time series of carbon monoxide concentration and traffic flow for an urban street canyon in one of the cities being monitored (either Nottingham or Leicester). The associated probability distribution for the CO concentration is shown in Figure 4.25(c). It is highly skewed in appearance.

Much of the following discussion is taken from Baker and Hargreaves [9] but is reproduced here because it represents an exciting and interesting area of potential application for the model.

The present model, as it was described in Section 4.2, can readily be seen to capable of producing very random fluctuations in the predicted receptor concentrations. Those aspects of the model which could be responsible are listed here:

- The ARMA generated above canyon wind speed.
- The random introduction of various vehicle types each with differing geometric, dynamic and polluting characteristics.
- The ability to control the speed of the lead vehicle in each lane of traffic in a random or cyclical manner.

In the first instance it was decided to look at each of the above effects in isolation in order to gain some insight into the magnitude of each effect. Using the base case for the sensitivity study of Section 4.4 as the starting point, the effect of imposing a non-uniform wind speed was investigated. For all the times series and concentration distributions presented here, the receptor in question was at pedestrian level $(z = H/10)$ on the leeward wall of the canyon. Also, the same width for the bins in the concentration distribution plots is used throughout, enabling more sensible comparisons to be made.

An ARMA model of order $(3,3)$ was used to generate a time series with a mean speed of 4 ms^{-1}, a turbulence intensity of 30% and characteristic length scale, ${}^{x}L_u$ of 40 m. In-

Figure 4.25: Full scale experiments of Reynolds and Bell [10] - (a) Time series of Carbon Monoxide concentration; (b) Time series of traffic flow; (c) Concentration probability distribution.

stead of the fixed wind speed of the base case, this variable wind speed was used and the resultant change in the concentration time series can be seen if Figures 4.7(f) and 4.26 are compared. There is a pronounced increase in the the spread of the time series in the modified case. Also note that there is a significant spread in the concentration distribution (Figure 4.27) and that this is skewed towards the lower end, much the same as the full-scale data was.

Next, the effect of imposing a variable speed on the lead vehicle was investigated. This was done in such a way as to mimic the presence of a traffic signal at each end of the canyon. The period of the signal was 150 s with the lead vehicle being taken from its constant speed of 54 km/hr (15 ms^{-1}) to rest and then back to 54 km/hr in each cycle. Thus, six cycles could be fitted into the 15 minutes (900 s) for which the model was run. In this scenario, the positions of the vehicles were monitored and indeed queueing was observed at both ends of the canyon much as was expected. It should be noted that the emission rates of all the vehicles in the canyon are functions of their speed only. The time series and concentration distributions are again shown for this case in Figures 4.28 and 4.29. An obviously cyclical trend is noted in the time series which is only to be expected because the only perturbation is itself cyclical. It should be noted that the receptor is positioned halfway along the canyon and thus may both receive the full effect of the traffic lights which are some 125 m distance at each end of the canyon. The probability distribution is double peaked which is hard to explain. The time series is also 'two-peaked' which can be explained by one peak being due to the presence of larger numbers of vehicles when queueing, the other being due to less vehicles moving at higher speeds with the associated increase in emission rates.

The base case was then perturbed by adding a second type of vehicle into the canyon. The second type of vehicle can best be described as an approximation to a bus since it was considerably larger and more sluggish than the cars of the base case. The mean ratio of the cars to buses was 4:1. With reference to Section 4.2.2, it should be remembered that the vehicles are introduced randomly into the canyon, only on average will there be 80% cars and 20% buses in the canyon at any one time. The introduction of buses in this manner results in a high frequency fluctuation in the time series as shown in Figure 4.30. The probability distribution (Figure 4.31) in this case is skewed in the opposite direction to the previous ones. This may be due to the buses having double the constant speed emission rate than the cars but this is not at all clear.

Taken in isolation, these three effects are explained in terms of the (relatively) predictable nature of the model. However, the real interest lies in the combination of the three effects. The results for the three-fold perturbation to the base case are presented in the usual form in Figures 4.32 and 4.33. As might be expected the time series appears not to be just the superposition of all three effects but a non-linear combination of them. This is reflected in the distribution which is greatly skewed and has a greater spread.

The last investigation carried out in this particular study was an attempt to take into account the gross variations in a daily traffic cycle. To do this, the model was run with

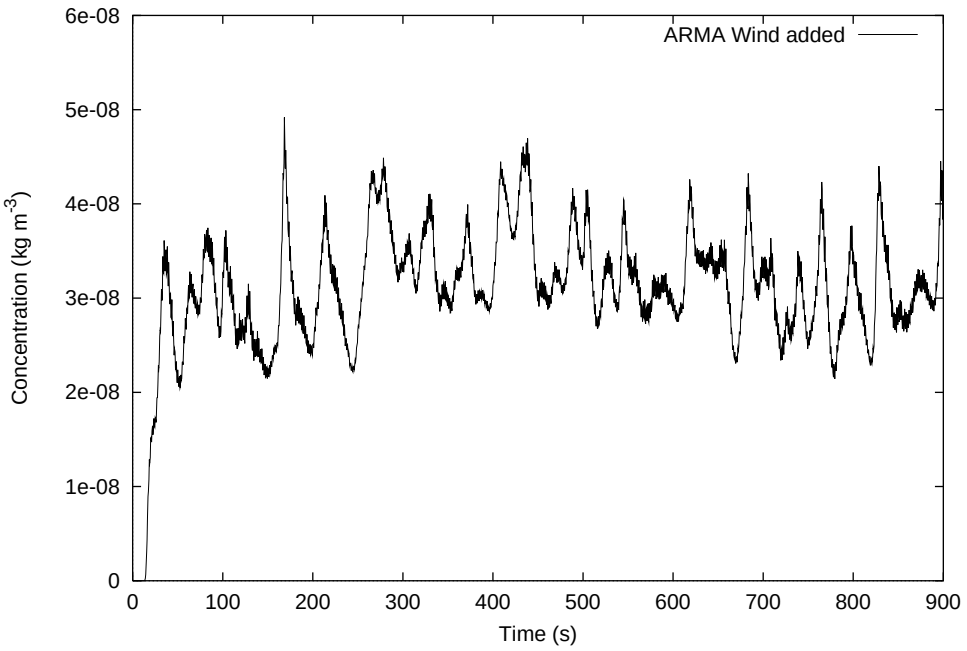


Figure 4.26: Concentration time series for base case with simulated wind speed fluctuations.

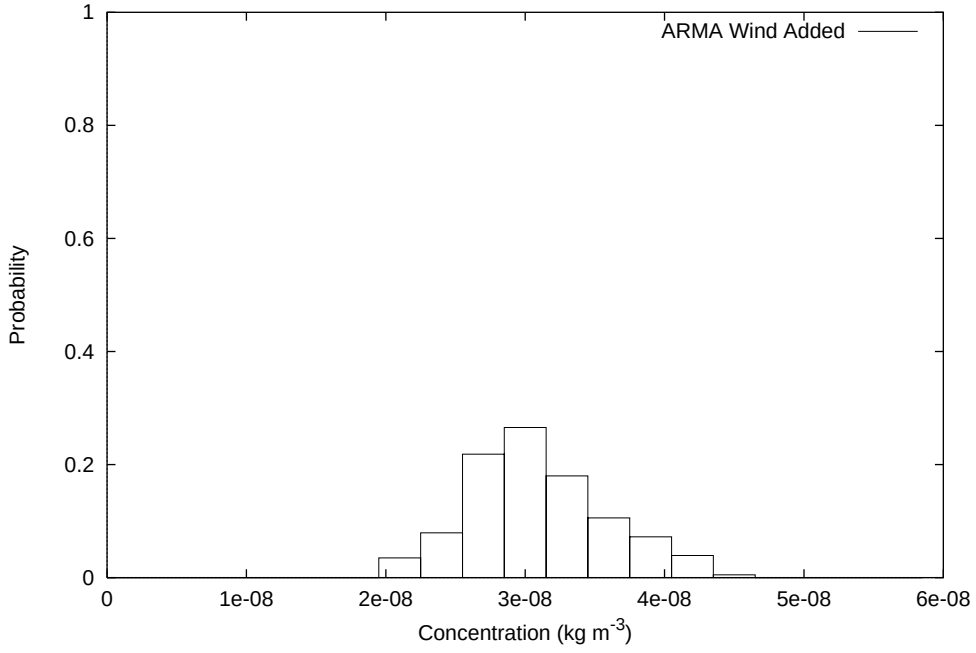


Figure 4.27: Concentration probability distribution for base case with simulated wind speed fluctuations.

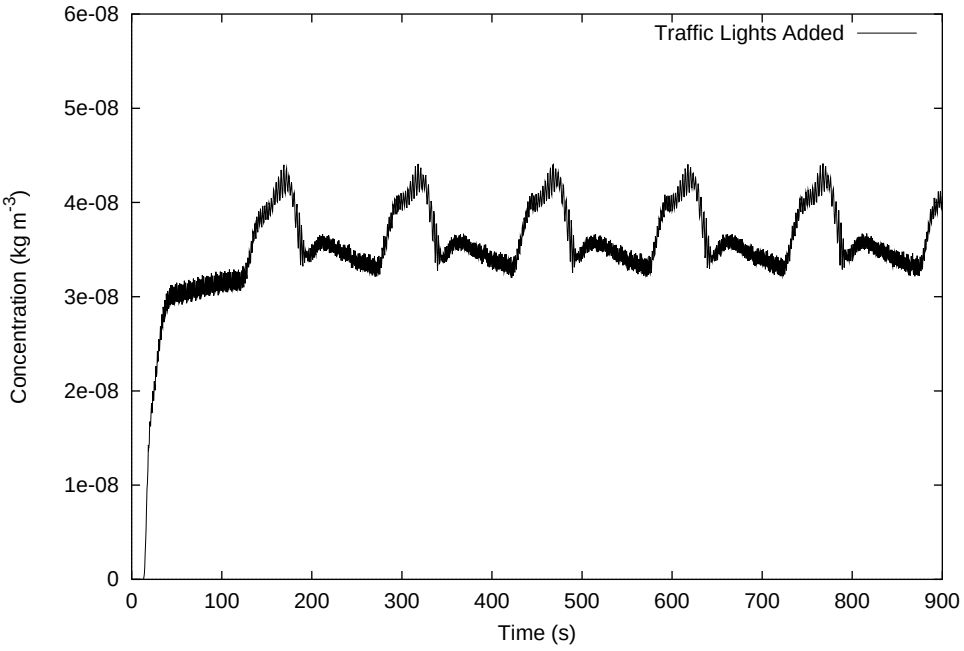


Figure 4.28: Concentration time series for base case with traffic signal control.

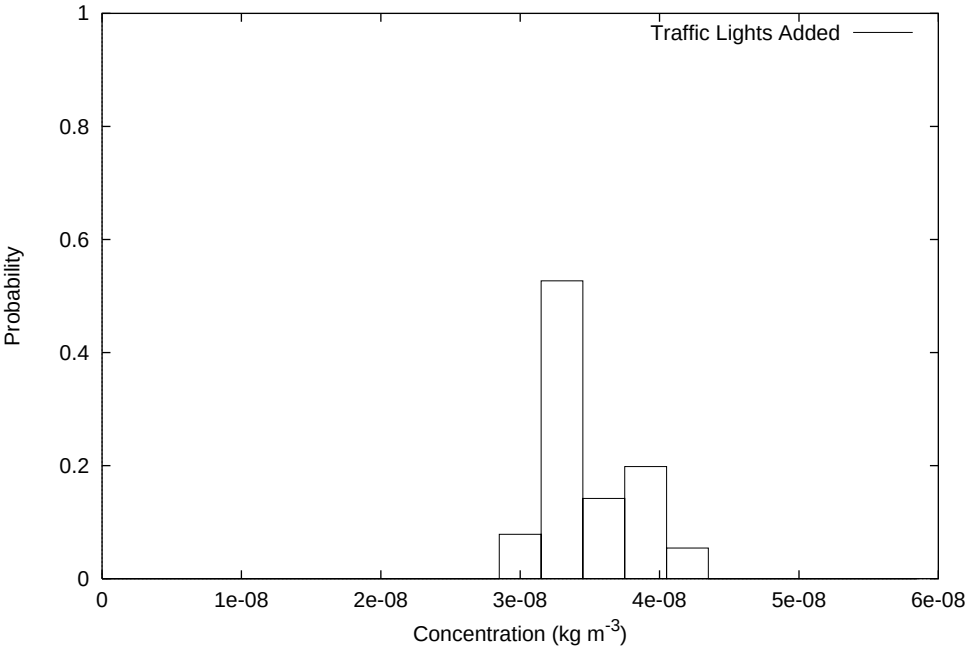


Figure 4.29: Concentration probability distribution for base case with traffic signal control.

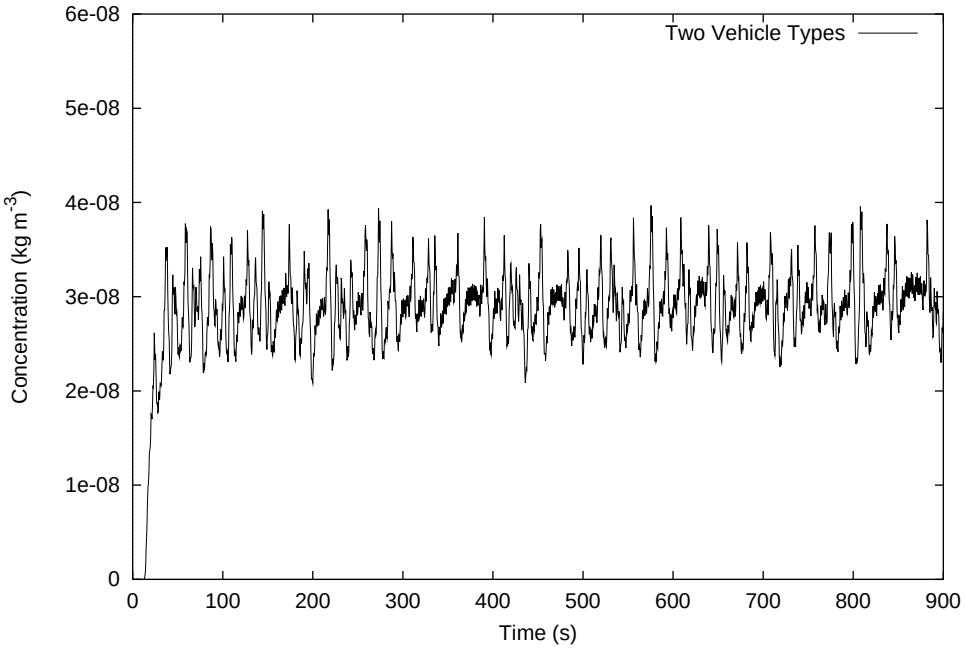


Figure 4.30: Concentration time series for base case with two vehicles types.

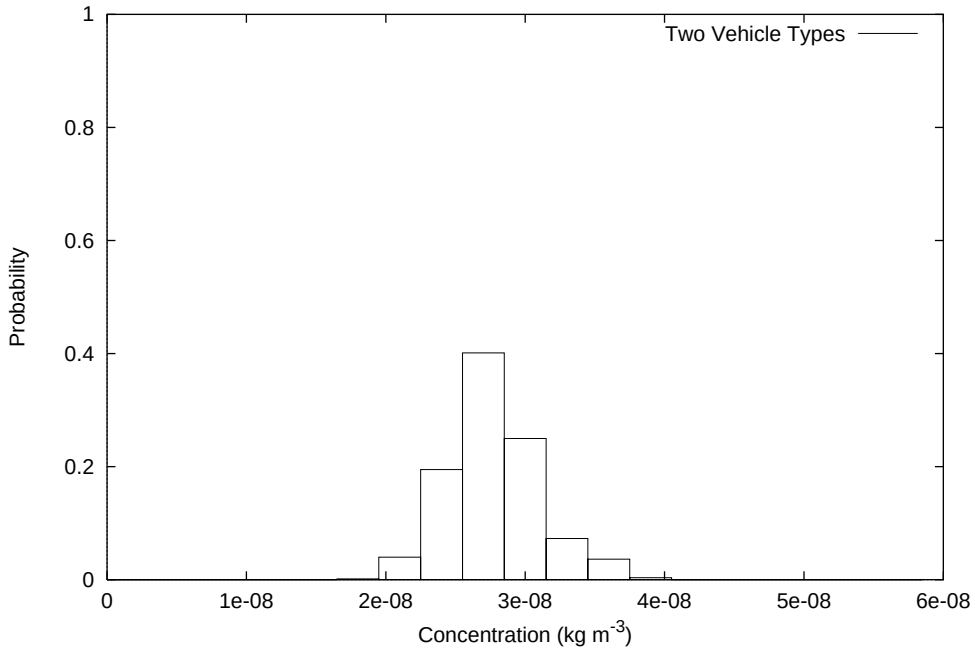


Figure 4.31: Concentration probability distribution for base case with two vehicle types.

all three effects turned on for a further two scenarios: one with traffic levels decreased to 75% of the base case levels, to simulate the build up to and fall away from rush hour levels; and one with levels decreased further to 50%, to simulate off-peak levels levels. The base case traffic levels would then form the peak hour values. The results from the three levels of traffic were combined in a ratio of 4:1:1. For a 12 hour period there are two peaks corresponding to the evening an morning rush hours. The probability distribution in this case is even more smeared.

To conclude this section, using this statistical approach it has been possible to gain an appreciation of the relative importance of meteorological and traffic conditions to the pollutant concentration in a street canyon. The evidence of Figures 4.26 to 4.31 suggests that the greatest effect is due to the variable wind speed. Also, the combination of all the effects results in a distribution which, qualitatively at least, resembles the real data of Figure 4.25.

4.7 Conclusions

In this Chapter a new model for the prediction of pollution levels in a street canyon has been presented. In terms of being an improvement on previous models, the present model has two distinct advantages. First, it is transient in nature and can thus model time dependent effects such as changing wind speed, congestion and traffic signal control. Second, the vehicles, for the first time, are introduced as turbulence-generating entities in their own right which has to be a step forward.

As has been shown, the model behaves largely as expected in the two scenarios in which is was designed to perform - the urban street canyon and the open country case. The two comprehensive sensitivity studies have proven its predictive capabilities whilst drawing attention to inadequacies such as the uncertainties in the use of the roof entrainment parameter.

Finally, the application of the model to the prediction of concentration distributions in an urban street canyon points to a very positive ’real world’ use for the model.

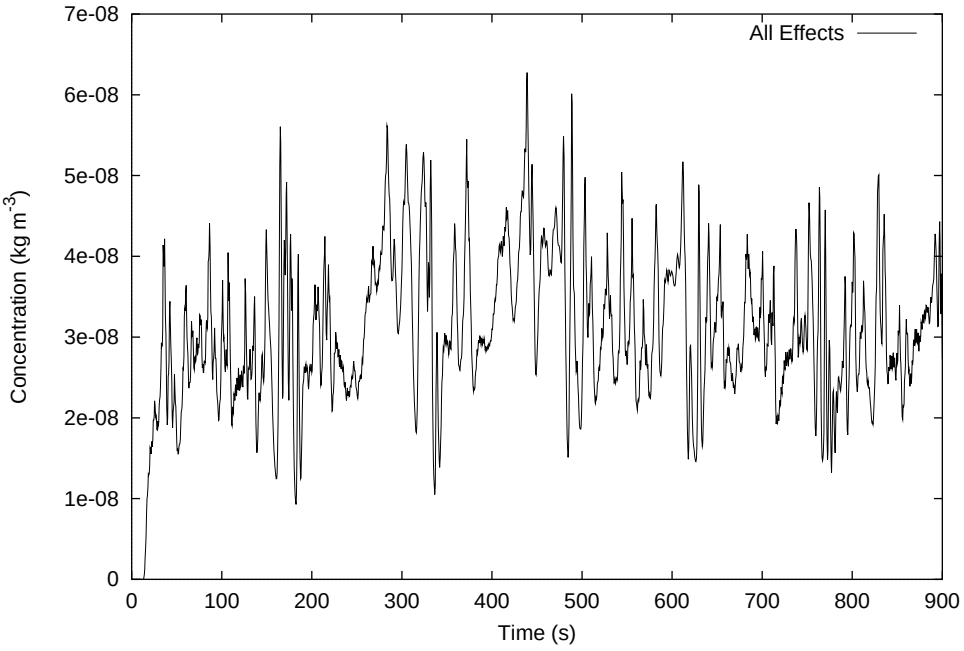


Figure 4.32: Concentration time series for base case with all effects combined.

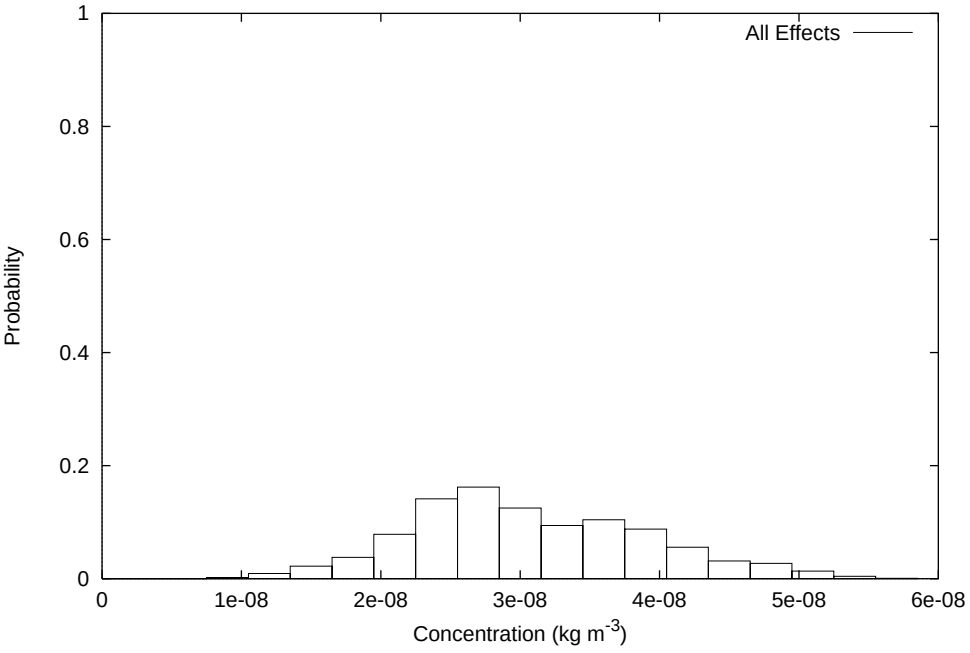


Figure 4.33: Concentration probability distribution for base case with all effects combined.

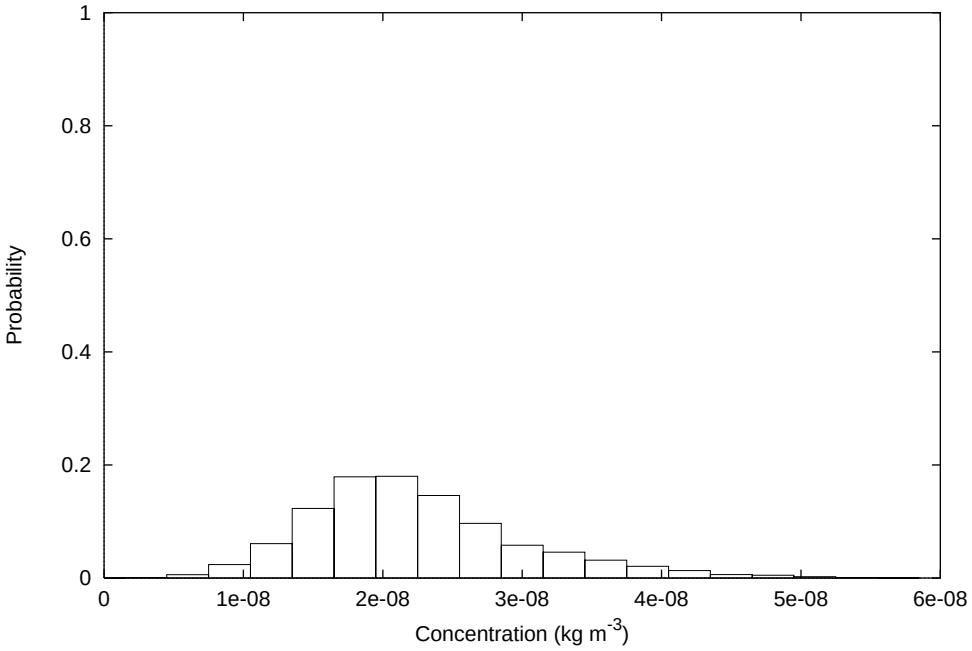


Figure 4.34: Concentration probability distribution for daily traffic simulation.

Chapter 5

Reconciling the Investigations

5.1 Introduction

In this Chapter, an attempt will be made to draw together the two aspects of the research, namely the experimental and the analytical investigations. In many ways, this phase of the work amounts to a validation of the computer program, PUFFER, inasmuch as the theory is being compared with a 'real' situation, albeit a wind tunnel. Ideally, the validation would be against full-scale data but the wind tunnel data nonetheless provides a very useful comparative tool.

This comparison is limited in several ways. Firstly, the multiple vehicle case was not studied in the wind tunnel mainly for historical reasons. The initial brief for this research was to look at wake effects of a single vehicle and the multiple vehicle canyon case was merely a useful spin-off from the main thrust of the research. Thus, for both the open country and urban canyon cases, we are limited by the scope of the experimental investigation. Secondly and crucially, the absolute values of concentration were not measured correctly in the wind tunnel for reasons discussed in detail in Appendix C.6. This imposes a severe limitation on the validation process, although it does not prevent a comparison completely. Due to the transient nature of the wake passing event, there is still a great deal of information that can be gleaned from the breakthrough curves such as time of arrival and the actual shape of the curves. Respectively, these two properties of the curves reveal much about the transport and dispersion of the pollutant. In light of this, all concentrations will be normalized with respect to their peak value and so will lie between 0.0 and 1.0. This will serve to emphasize the relative shapes of the breakthrough curves.

The spiky individual traces shown in, for example, Figure 3.19 could not be modelled by PUFFER, the reason being that PUFFER, although capable of modelling transient effects, uses a series of assumptions which effectively time-average the data. There is

no way to model the spread of breakthrough curves observed in the wind tunnel where turbulence dictated that every single firing was highly individual in nature. Thus, for the majority of the comparisons the ensemble averaged results which have already been presented in Chapter 3 will again be used. As will be shown it is possible to introduce some of the spread in individual breakthrough curves by using several runs of PUFFER with different ARMA generated wind series, more of this in the next section.

With these provisos, the chapter will progress as follows. In line with the previous chapters, the rural case will be addressed first, followed by the urban scenario. The decision has been made to feed PUFFER input data commensurate with the actual wind tunnel model. In other words, the full-scale equivalent of the wind tunnel model will not be modelled. The reason for this decision was that PUFFER is scale-independent without Reynolds or Froude scaling effects included. Further, although the $1/50^{\text{th}}$ scale wind tunnel is not a real situation, it is one which still obeys the laws of physics and hence can be modelled in its own right. It will not be possible, from the results and arguments presented in this chapter, to discern this fact because the geometric and dynamic scalings of the previous two chapters will be used.

5.2 The Rural Case

5.2.1 Constructing the PUFFER input data

Since the experimental data was fixed at the time of this comparison, the main difficulties arose in the writing an appropriate input deck for PUFFER. Vehicle and domain geometries were trivial with the dimensions of the working section being used for the latter. Since the emission rate from the model lorry and the concentration of the propane-in-air mixture were fixed and had no velocity or acceleration dependency, only q_i and c_i, the idling emission rate and idling concentration were non-zero in Equations 4.8 and 4.9 in Chapter 4.

The wind speed and reference height proved more troublesome. It was decided that the important area was close to the floor of the tunnel, around about $z = h/2$, with h being the vehicle height, and so the value of the reference height was chosen so that the wind speeds observed in the tunnel at this height were correctly modelled. In addition, an appropriate ARMA wind series is generated during the run. This was the only way to introduce some randomness into the proceedings. Using the ARMA model with a different random seed for a series of, say, 10 runs, a number of slightly different breakthrough curves were generated as shown in Figure 5.1. Thus individual curves can be equated to the individual firings of the MMR but they do not exhibit anything like the variation of the data obtained in the wind tunnel for individual runs. Nevertheless the ensemble average of these breakthrough curves provides a more realistic approach than a single

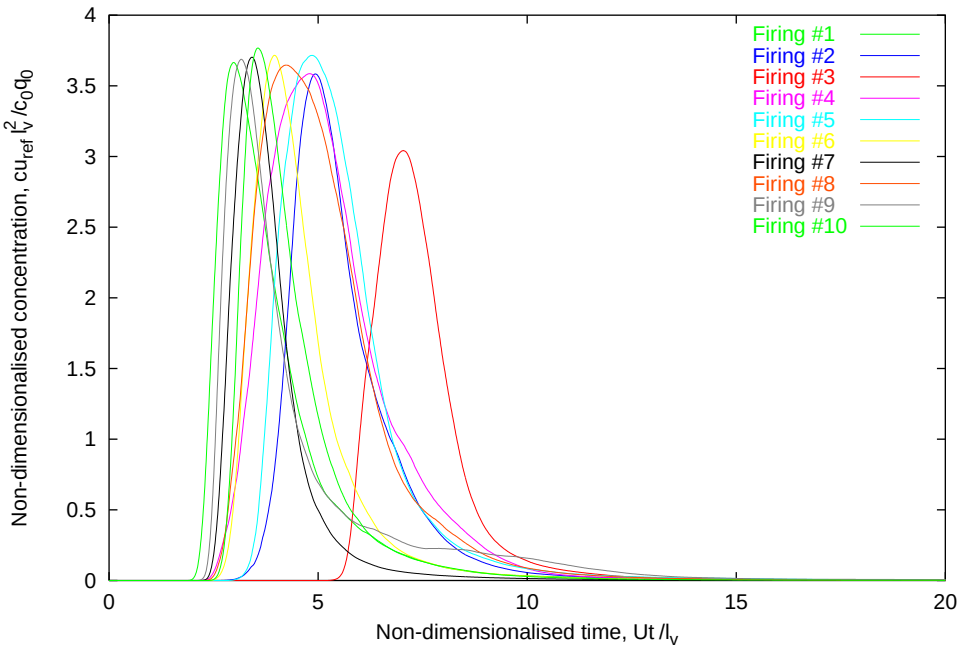


Figure 5.1: Individual breakthrough curves obtained using PUFFER with an ARMA-generated wind speed in rural mode.

run with a constant wind speed[1].

Again with reference to Figure 5.1, a single outlier (Firing #8) is distinguishable from the main group of curves. This is due to an lull in the wind as the lorry passed during this firing. Although relatively uncommon, the existence of these outliers is confirmed experimentally by, for instance, Figure 3.19. In particular, the readers attention is brought to Firing #13 of that figure whose time of arrival is some 20% later than the rest. There is also some evidence, as shown by Firing #9 in Figure 5.1, of a slight second peak which is seen most notably in Firing #8 in Figure 3.19.

Inevitably, problems would occur with the turbulence levels in the region of the ground. Values of 0.30 and 0.1 for the turbulence parameters α_1 and α_2 were used throughout in order to simulate the turbulence intensities of 30% found in the tunnel at $z = h/2$ - see Figure 3.13.

[1]This was proved by a process of trial and error, the results for the single, constant wind speed case, however, are not presented here for reasons of clarity.

5.2.2 Variation of Concentration with Distance Downstream

Figure 5.2 shows the comparison between the actual and predicted results for the rural situation as the receptor/FID is moved downstream. The arrival times (defined as the point at which the sharp rise from zero is encountered) become more consistent as the receptor is moved downstream. This backs up the suggestion that the modified Eskridge and Hunt theory holds only in the far wake region. At $y = l/2$ the arrival time in the wind tunnel was 50% later than that predicted by PUFFER. This suggests a vortex behind the model lorry which perhaps traps the pollutant and delays its passage in the wind. As the receptor position is moved further away this delays becomes proportionally smaller and indeed appears to diminish completely. Again, this may be due to the short term, along-wind speed-up effect seen in Figure 3.18. Ideally these measurements could have been extended further downstream.

As far as the shapes of the curves are concerned, there is more agreement close to the lorry. With all the experimental curves, there is a more symmetrical shape which may be due to the ensemble averaging process. Reference back to Figure 3.19 shows that for individual firings the breakthrough curves exhibit more of a skewed form in general. Indeed the perceivable second peak in plots (a) and (b) in Figure 5.2 can be attributed to the averaging process. It is unlikely that a double "emission" of pollutant in which a fraction of the exhaust gas is held in the wake is actually taking place. Rather, it is more likely that as the wind speed varied quite considerably over periods greater than the period of a firing, the later times of arrival for a significant proportion of the firings would create this false double peak.

5.2.3 Variation of Concentration with Wind Speed

Figure 5.3 shows the comparison between model and wind tunnel for varying wind speed at half a vehicle length downstream of the lorry. The curves are similar to those presented in Figure 5.2 inasmuch as the experimental breakthrough curve arrives after the time predicted by PUFFER. For the low wind speed case, there is a large spread in the experimental data which is not predicted by PUFFER. This may indicate that the vehicle-induced turbulence is more suitable at mixing the pollutant than the wind-induced turbulence. Hence at the low wind speed we see proportionally more mixing taking place.

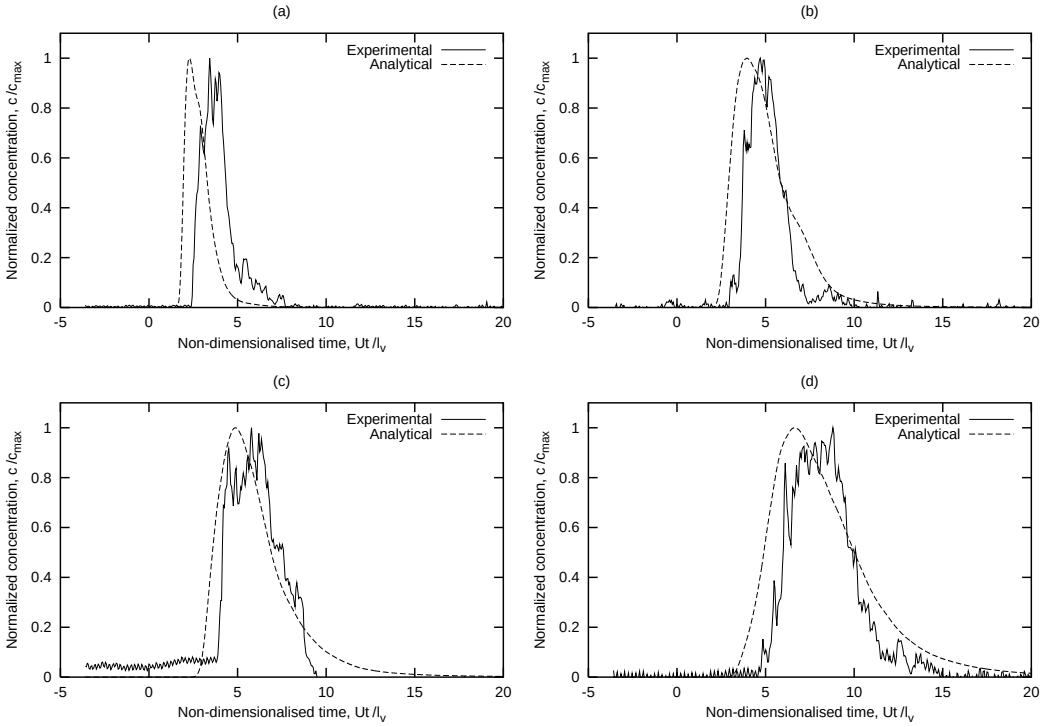


Figure 5.2: Comparison between experimental and analytical predictions for the variation of concentration with distance downstream, rural case at (a) $y = l/2$, (b) $y = l$, (c) $y = 3l/2$ and (d) $y = 2l$.

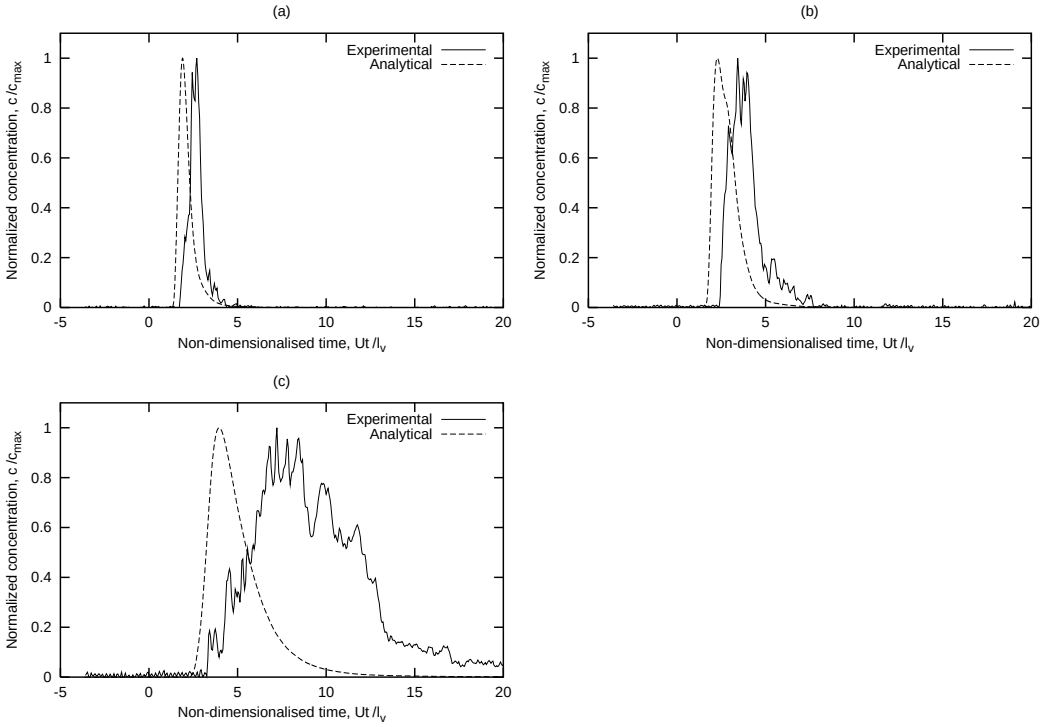


Figure 5.3: Comparison between experimental and analytical predictions for the variation of concentration with wind speed, rural case for (a) $u_{\text{ref}}/U = 0.98$, (b) $u_{\text{ref}}/U = 0.54$, and (c) $u_{\text{ref}}/U = 0.25$.

5.3 The Urban Case

5.3.1 Constructing the PUFFER input data

The situation is slightly more complex in the urban canyon case than in the open country case. Extra parameters need to be discussed. In particular the puff removal limit, λ_l, and puff reduction factor, λ_f, which are important in the roof entrainment model. From both the experimental individual and ensemble average plots (e.g. Figures 3.32 and 3.33), it is clear that there is a significant retention of pollutant over time scales several times the time taken for a single rotation of the in-canyon vortex. This indicates a weak removal process at roof level. It follows that a reduced value for λ_f would simulate this effect most closely. Thus, a value of 0.1 was used throughout these comparisons. This was found to provide a good response.

Again, an ARMA generated wind was used over a series of 10 "firings" which were then ensemble averaged to facilitate the experimental/analytical comparison. Figure 5.4 shows the 10 traces. There is an outlier on Firing #4, again probably due to exceptionally low wind speed during this "firing". The reference wind speed used in these comparisons was not that measured at the pitot-static tube but a log-law modified version at roof height. This was done so that the in-canyon air flow modelled in PUFFER would be similar to that found in the wind tunnel. The Hotchkiss-Harlow model used in PUFFER to model the in-canyon vortex needs different boundary conditions to produce the flow field seen in the wind tunnel.

Only two cases will be discussed here. First breakthrough curves at three positions on the leeward wall will be compared, followed by a look at the effect of changing the wind speed.

5.3.2 Variation of Concentration with Height on the Leeward Wall

Figure 5.5 shows the comparison at three heights on the leeward wall. Using the ensemble average of several "firings" of the PUFFER model was the only way of recreating the huge spread of pollutant seen in the wind tunnel. In addition, the low value of the puff reduction factor allowed the modelling of the persistent tail of pollutant seen in all three plots. This experimental lingering of pollutant was not expected and required the introduction of the puff reduction factor into the roof entrainment sub-model.

As far as arrival times are concerned, the only plot to exhibit a close agreement in plot (b) at $z = H/2$. At the foot of the wall PUFFER predicts the first wave of pollutant arriving too early, while at the top it arrives too late. This is difficult to explain. Perhaps at the foot of the wall there is a region of 'dead air' which has been mentioned in the literature on several occasions. This may prevent the direct advection of the pollutant

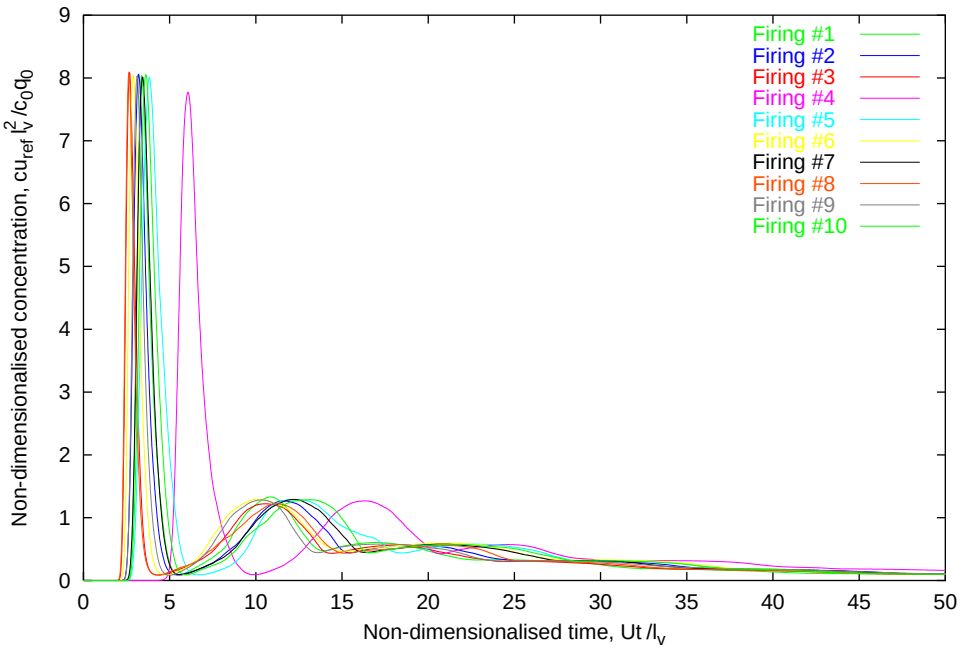


Figure 5.4: Individual breakthrough curves obtained using PUFFER with an ARMA-generated wind speed in urban mode.

which occurs in the PUFFER model. Also there is perhaps more vertical mixing of pollutant actually occuring due to the wake of the vehicle than presently incorporated in the PUFFER model - this may well explain the shorter arrival time of the pollutant at the top of the wall.

Although not shown in these plots, in both the experimental and analytical approaches, the peak values of concentration are seen close to mid-height on the wall. This observation can be made because the three sets of experimental curves were taken for the same FID calibration.

5.3.3 Variation of Concentration with Wind Speed

Perhaps surprisingly, the two sets of results in Figure 5.6 exhibit similar arrival times. However, the shapes of the curves are not that similar with the lowest wind speed showing a distinct second peak in PUFFER results while the experimental results merely show the characteristic decay over the same period.

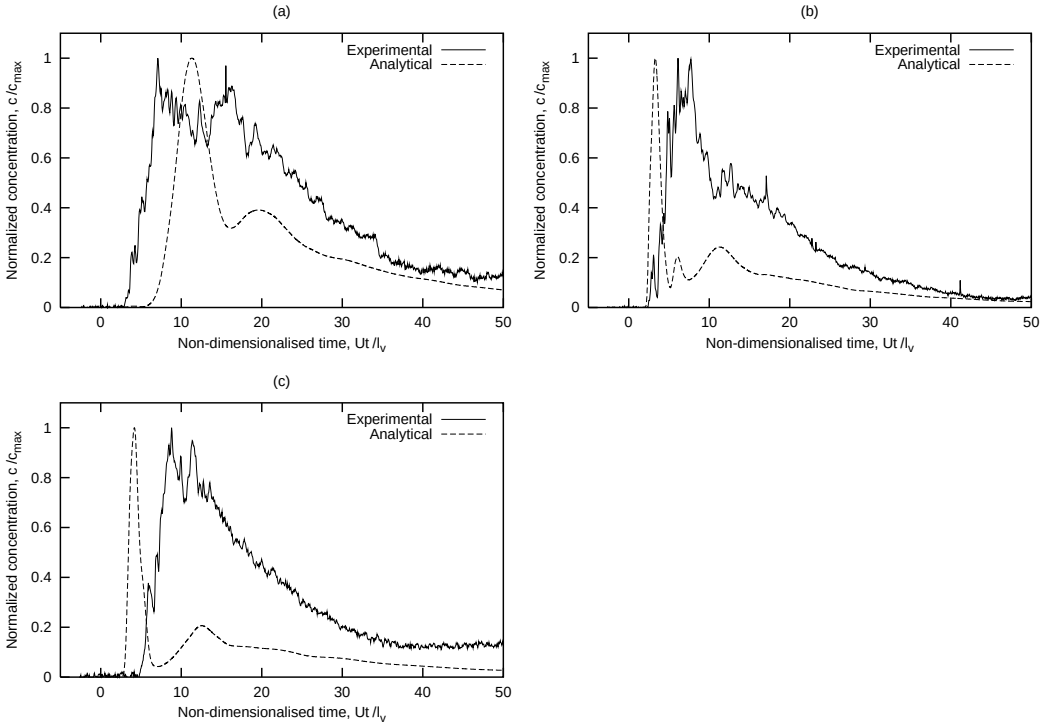


Figure 5.5: Comparison between experimental and analytical predictions for the variation of concentration with height on the leeward wall at (a) $z = H/8$, (b) $z = H/2$, and (c) $z = 7H/8$.

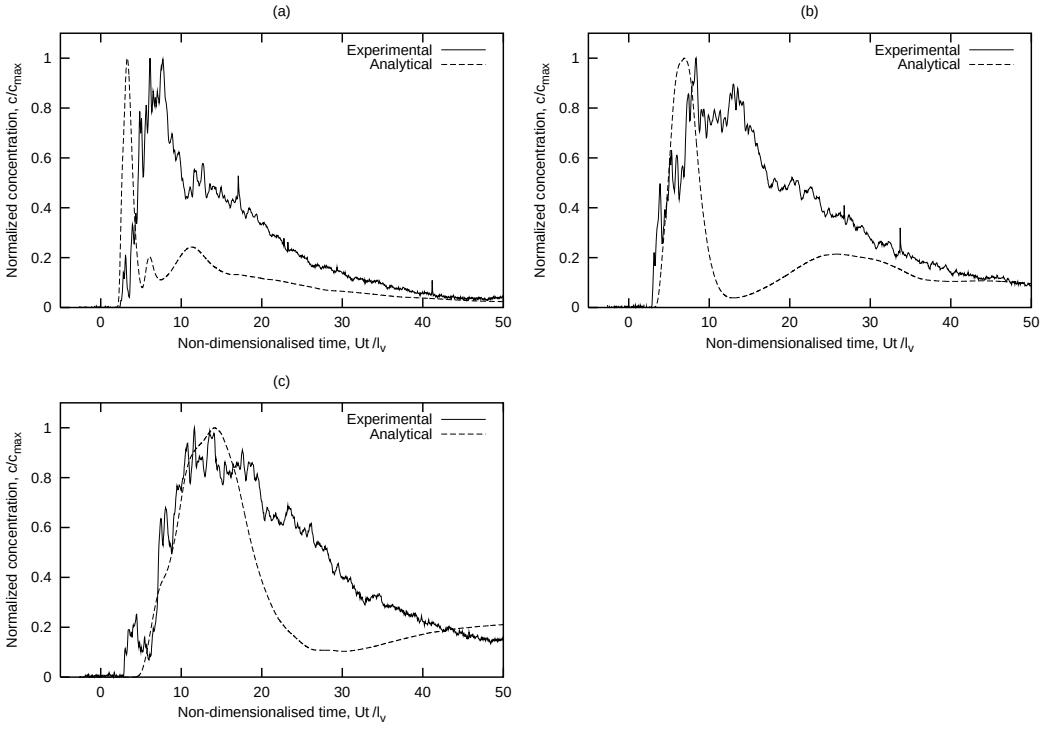


Figure 5.6: Comparison between experimental and analytical predictions for the variation of concentration with wind speed on the leeward wall for (a) $u_{\text{ref}}/U = 1.0$, (b) $u_{\text{ref}}/U = 0.44$, and (c) $u_{\text{ref}}/U = 0.25$.

5.4 Conclusions

On the whole, this exercise has been very worthwhile. It has, in the opinion of the author, vindicated the analytical model in many ways. While the entire discussion has been overshadowed by the FID calibration problem, some very encouraging agreements have been found.

In summary, the following positive comments can be made,

- Even with the uncertainties in the FID calibration, the differences in the magnitudes of the concentrations cannot be more than an order of magnitude.
- The use of multiple ARMA-generated "firings" has proved not only to be a useful way of mimicking the actual behaviour in the wind tunnel but may also point to the way forward in any possible future development of the model. Many of the aspects of the model which now rely on time-averaging effects could be replaced by quasi-random processes. The method of averaging many runs with randomly varying wind speeds, vehicle speeds, turbulent mixing parameters, etc. may well prove to be the way forward.

The following negative conclusions can be drawn,

- The comparison was made with wind tunnel data. The attendant scaling issues mean that this comparison is not a validation in the real sense of the word. No real data was used in this comparison. Indeed, all that has been proved is that PUFFER can predict, to some degree, the behaviour of a small lorry model in a wind tunnel.
- The inability to reproduce the exact breakthrough curves, especially in the near wake of the vehicle is something of a concern, although the theoretical model of the vehicle wake was known to be deficient in this area.

Chapter 6

Conclusions and Suggested Future Work

6.1 Introduction

In this chapter a number of conclusions are drawn from the work described in this thesis. They will be presented in a list and will be followed in Section 6.3 by a another list, this time of suggestions for future work in this area.

6.2 Conclusions

The following major conclusions can be drawn from the experimental work:

1. The use of a vehicle moving a right angles to the flow provided a unique opportunity to study the behaviour of vehicle exhaust gases in a cross wind.
2. The gas delivery system which was mounted below the moving vehicle allowed a moving point source to be modelled rather than the more conventional, and contrived, fixed line source.
3. In the rural case, for a strong side wind, the experiments revealed a distinct increase in the along-wind component of flow just prior to the arrival of the vehicle. This is akin to the familiar speed-up around a stationary body in an air flow. Indeed, the increase from the mean wind speed was approximately the same magnitude as the decrease seen in the lee of the vehicle as it passed. The magnitude of this peak-to-peak variation coupled with the short time over which it occured could have implications for cyclists. It is possible that the presence of a side wind serves to exacerbate the problems associated with being overtaken by a lorry.

4. There was a noticeable perturbation observed in the component of flow in the vehicle's direction of travel. As the vehicle passed, a small volume of air was dragged behind it. This manifested itself as a short peak in the trace of speed versus time. The disturbance was propagated downstream at the ambient wind speed and as it did so it became less pronounced. This confirms the presence of a wake and agrees qualitatively with the work of Eskridge and Hunt in which the wake velocity deficit reduces with distance behind the vehicle. It should be noted that the present tests were conducted close to the vehicle in a region not covered by Eskridge and Hunt's theoretical model.

5. Some interesting questions were raised by the nature of the experiments. With a number of discrete firings of the Moving Model Rig and the turbulent nature of both the ambient wind and the lorry wake, each firing (even under the same conditions) produced different breakthrough curves. For the flow measurements in the wake in particular, very little could be discerned from an individual firing. Any trend or gross effect could only be seen by the ensemble averaging of 10 or more firings. That was not to say that the time histories for the individual firings were not in themselves informative. They served to reinforce the view that the situation was a highly unpredictable one.

6. The rural experiments demonstrated that the dispersion process, while being extremely unpredictable for a single firing, conformed, when ensemble averaged, to an approximately Gaussian model. This was most clearly shown by the series of breakthrough curves obtained as the FID was moved downstream. In this set of curves, the peak occured later as the FID was moved away from the vehicle and the peak itself became smaller and more spread out - very much in agreement with the Gaussian model.

7. It was observed, however, that very close to the vehicle (*ie* half a vehicle length away) that the gas arrived slightly later than would have been expected from a simple transport process in which a tracer gas would move with the flow. It is hypothesized that this is due to various near-wake effects which retain the pollution behind the vehicle for a short time. The horseshoe vortices often seen in the wakes of bluff bodies may well be responsible for "folding" the gas plume back into the wake.

8. The set of experiments conducted in the urban street canyon were less revealing. The smoke visualization tests showed that a stable vortex existed in the canyon - this was nothing new but did show that the urban boundary layer was having the desired effect.

9. Further evidence for the vortex was obtained using the hot-wires but, due to their lack of directionality, these results were far inferior to other work in this area. Laser Doppler Anemometry was tried but could not be operated correctly.

10. The ensemble averaging of the street canyon breakthrough curves, if anything, tended to obscure any patterns which may have emerged. Far more revealing were

the individual traces which showed two or more peaks which can be equated to the multiple rotation of the pollutant in the resident vortex. Calculations confirmed that the time between the first and second peaks was of the order of the time taken a massless particle to complete one rotation of the canyon in the vortex.

11. One aspect of all the ensemble averaged breakthrough curves in the urban case was a sharp increase in concentration just after the vehicle passed, followed by a long decay time. The decay was faster at higher roof level wind speeds which is broadly in line with other researchers. For example, Lee and Park [61] used a time constant which was defined as the time required by the pollutant concentration in the canyon to fall by a factor of e. By fitting exponential decay curves to the tail of the ensemble averages, it was possible to quantify the decay rate which was found to scale roughly as expected from the full-scale measurements of Lee and Park.

12. The mistake during the calibration of the FID was significant in the urban case. With the rural case, there was sufficient information in the shape of the breakthrough curves to warrant the drawing of several conclusions. However, the urban case relied significantly on the absolute values and without them we can really count this part of the experiment a failure.

The following observations can be made from the development and use of the analytical model:

1. The inherently transient nature of the model enables both the steady-state modelling of pollution dispersion in street canyon through time averaging and the modelling of time dependent effects such as varying wind speed, congestion and traffic signal control to be modelled.

2. The model introduces vehicles as both individual turbulence and pollutant sources. This more realistic approach supersedes previous methods which treated the vehicles as line source of pollutant and a diffuse source of turbulence in the lower reaches of the canyon.

3. The range of application of the model is wide with either the rural roadways or urban street canyons being able to be modelled with very little modification to the input data.

4. The model performed well under the extensive sensitivity study described. None of its behaviour was inexplicable and much of it was intuitively in line with expectations.

5. The statistical use of the model in predicting concentration distributions by the road side was particular encouraging. Such is the nature of the situation being modelled, that this approach where there is not single answer but a range, points to the future of this kind of modelling and is probably the best that can be hoped to be achieved.

6. The new model compared favourable with other existing models, although the agreement was by no means exact.

7. When the analytical model was validated against the experimental results, it was found that the best agreement was produced by ensemble averaging several sets of breakthrough curves from individual runs of the computer program each with a different ARMA generated wind time series. In many ways, this was a mirroring of the averaging of the individual firings of the Moving Model Rig in the wind tunnel and shows there is a certain symmetry between the two approaches.

6.3 Suggestions for Future Work

1. The experimental method, in the author's opinion, was not flawed to any great degree. The whole operation was blighted by the FID calibration problem. It is therefore suggested that a more extensive set of experiments, with those presented here as their basis, could be carried out but this time with a reliable calibration procedure for the FID.

2. As part of this more extensive study, the rural investigation could be extended further downwind of the model into the territory in which Eskridge and Hunt's wake theory is valid.

3. It would be very interesting to use Laser Doppler Anemometry to look at the flow field in an urban canyon as the lorry passed by. The extent to which the resident vortex were disturbed would be most revealing. Indeed, it would be useful to find out if the wake was swept around the canyon.

4. As a final suggestion for the experimental work, the following somewhat outlandish, money-no-object idea is put forward. Instead of using the complex, difficult to maintain, mechanical Moving Model Rig, replace it with a linear motor of the type pioneered by Professor Eric Laithwaite. The advantages of this approach are manifold. First, the ride quality would be near perfect which would be a boon, not for these experiments perhaps, but for measurements of forces of moving vehicles. Second, the need for a return mechanism would be nullified because a simple reversal of the current would bring the model back. Lastly, the control of acceleration and speed achievable with such motors would allow the modelling of a wide range of velocities.

5. The analytical model requires further validation. The proposed enhancements and repetition of the experimental program would fulfil this need to a large extent. However, the validation program needs extending on two scores. Firstly, full-scale data is required if the model is to be used in real applications. Secondly, this data must include the multiple vehicle case which is not easy to simulate in the wind tunnel but is commonplace in the real world. Indeed, there exist many full

scale studies, including those mentioned in Chapter 2 such as the General Motors experiments, against which this model could be tested.

6. The model could be extended to cope with more than one urban canyon, aligned on a grid with intersections. The preliminary theory for this extension has been developed. The main difficulties arise in disregarding contributions from puffs which are not in the "line of sight" of a receptor. This problem has been surmounted but the method used will consume large amounts of computational time and needs to be made more efficient.

7. Another possible route the development process could take is the modelling of particulates. The inclusion of particulates in a puff model is not clear at this stage but it may be possible to handle particulate deposition in a similar manner to the roof entrainment process. In other words, a fraction of the mass of pollutant in the puff could entrain from the puff based on the mass of the particulates and the local flow field. The particulates would, in this approach, adhere to the walls and floor of the canyon thus allowing a concentration distribution to build up with time.

8. Although PUFFER was intended as a model which would reduce the number of so-called "fudge factors" which were commonplace in previous models, the omission of a coefficient to modify the strength of the wake velocity deficit would seem to be an oversight. Indeed, Eskridge and Hunt use such a coefficient in some of their work and its introduction into the present model would be trivial but useful.

9. In Chapter 5, the ensemble averaging of several runs of the program with different seeds for the generation of the wind time series was seen to produce better agreement with the experimental results than a single run with a constant wind speed. Producing these results was quite a laborious task and is one which could easily be automated in a future version of the model.

Bibliography

[1] Abbott, M.B. and Basco, D.R. *Computational Fluid Dynamics: An Introduction for Engineers*. Longman Scientific & Technical, 1989.

[2] Ahmed, S.R., Ramm, G., and Faltin, G. Some salient features of the time-averaged ground vehicle wake. *SAE Special Publications*, (840300):1–31, 1984.

[3] Bächlin, W., Theurer, W., and Plate, E.J. Dispersion of gases released near the ground in built up areas: experimental results compared to simple numerical modelling. *Journal of Wind Engineering and Industrial Aerodynamics*, 41–44:2721–2732, 1992.

[4] Baker, C.J. Train aerodynamic forces and moments from moving model experiments. *Journal of Wind Engineering and Industrial Aerodynamics*, 24:227–251, 1986.

[5] Baker, C.J. Ground vehicles in high cross winds. Part I: Steady aerodynamic forces. *Journal of Fluids and Structures*, 5:69–90, 1991.

[6] Baker, C.J. Outline of a novel method for the prediction of atmospheric pollution dispersion from road vehicles. Technical Report FR93021, Nottingham University, Department of Civil Engineering, 1993.

[7] Baker, C.J. Outline of a novel method for the prediction of atmospheric pollution dispersion from road vehicles. In *East European Wind Engineering Conference, Warsaw*, 1994. also accepted for publication in the Journal of Wind Engineering and Industrial Aerodynamics.

[8] Baker, C.J. Module H2CH06 Wind Engineering. Lecture Notes, Department of Civil Engineering, University of Nottingham, 1995.

[9] Baker, C.J. and Hargreaves, D.M. Urban air pollution from road traffic - statistical and deterministic approaches. In *20th Conference on Regional and Urban Statistics*, Madrid, Spain, October 1996. Standing Committee on Regional and Urban Statistics.

[10] Bell, M.C. and Reynolds, S. ITEMMS - Integration of traffic and environmental monitoring and management systems. Paper presented at Universities Transport Studies Group Conference, Cranfield University, January 1995.

[11] Berkowicz, R., Hertel, O., Sϕrenson, N.N., and Michelson, J.A. Modelling air pollution from traffic in urban areas. Draft, Danish National Environmental Research Institute, 1994.

[12] BMT Fluid Mechanics Ltd., Teddington, England. *High Sensitivity Hydrocarbon Gas Detector*, 1993. USER MANUAL.

[13] Box, G.E.P. and Jenkins, G.M. *Time Series Analysis, Forecasting and Control*. Holden-Day, Oakland, California, 1969.

[14] Builtjes, P.J.H. Determination of the flow field in a street canyon by means of wind tunnel experiments. Technical Report 83-09553, TNO, 1983. Progress Report.

[15] Ca, V.T., Asaeda, T., Ito, M., and Armfield, S. Characteristics of wind field in a street canyons. *Journal of Wind Engineering and Industrial Aerodynamics*, 57(1):63–80, June 1995.

[16] Chadwick, A.J and Morfett, J.C. *Hydraulics in Civil and Environmental Engineering*. Chapman & Hall, London, 2nd edition, 1993.

[17] Chock, D.P. The GM sulfate dispersion experiment: An overview of the wind, temperature and cocnentration fields. *Atmospheric Environment*, 11:553–559, 1977.

[18] Coleman, S.A. *The Aerodynamics of Ground Vehicles in Cross Winds*. Ph.D. Thesis, Department of Civil Engineering, University of Nottingham, University Park, Nottingham, NG7 2RD, October 1990.

[19] Coleman, S.A. and Baker, C.J. The reduction of accident risk for high sided road vehicles in cross winds. *Journal of Wind Engineering and Industrial Aerodynamics*, 41–44:2685–2695, 1992.

[20] Cook, N.J. *The Designers Guide to Wind Loading on Building Structures, Part 1*. Butterworths, London, 1985.

[21] Counihan, J., Hunt, J.C.R., and Jackson, P.S. Wakes behind two-dimensional surface mounted obstacles in turbulent boundary layers. *J. Fluid Mech.*, 64:529–563, 1974.

[22] Dabberdt, W.F. and Hoydysh, W.G. Street canyon dispersion: sensitivity to block shape and entrainment. *Atmospheric Environment*, 25A(7):1143–1153, 1991.

[23] Dabberdt, W.F., Ludwig, F.L., and Johnson, W.B. Validation and applications of an urban diffusion model for vehicular emissions. *Atmospheric Environment*, 7:603–618, 1973.

[24] Deaves, D.M. and Harris, R.I. A mathematical model of the structure of strong winds. Technical Report CIRIA Report 76, Construction Industry Research and Information Association, 1978.

[25] DePaul, F.T. and Sheih, C.M. A tracer study of dispersion in an urban street canyon. *Atmospheric Environment*, 19(4):555–559, 1985.

[26] DePaul, F.T. and Sheih, C.M. Measurements of wind velocities in a street canyon. *Atmospheric Environment*, 20(3):455–459, 1986.

[27] ESDU. Characteristics of Atmospheric Turbulence Near the Ground. Part II: Single Point Data for Strong Winds (Neutral Atmosphere). Technical Report 74031, Engineering Sciences Data Unit, 251–259, Regent Street, London, W1R 7AD, 1974.

[28] ESDU. Characteristics of atmospheric turbulence near the ground. Technical Report 85020, Engineering Sciences Data Unit, 251–259, Regent Street, London, W1R 7AD, 1985.

[29] Eskridge, R.E., Binkowski, F.S., Hunt, J.C.R., Clark, T.L., and Demerjian, K.L. Highway Modeling. Part II: Advection and Diffusion of SF_6 Tracer Gas. *Journal of Applied Meteorology*, 18(4):401–412, 1979.

[30] Eskridge, R.E. and Hunt, J.C.R. Highway Modeling. Part I: Prediction of Velocity and Turbulence Fields in the Wake of Vehicles. *Journal of Applied Meteorology*, 18(4):387–400, 1979.

[31] Eskridge, R.E. and Rao, S.T. Turbulent diffusion behind vehicles: experimentally determined turbulence mixing parameters. *Atmospheric Environment*, 20(5):851–860, 1986.

[32] Eskridge, R.E. and Thompson, R.S. Experimental and theoretical study of the wake of a block-shaped vehicle in shear-free boundary flow. *Atmospheric Environment*, 16(12):2821–2836, 1982.

[33] Ruff, R.E. *et al* Design Manual for a SO_2 Emission Limitation Program at the Kingston Steam Plant, Vol.1. Final Report 75 K-3-66322, Stanford Research Institute, Menlo Park, CA, 1976.

[34] Georgii, H.W., Busch, E., and Weber, E. Investigation of the temporal and spatial distribution of the emission concentration of Carbon Monoxide in Frankfurt/Main. Technical Report 11, Institute for Meteorology and Geography of the University of Frankfurt/Main, 1967.

[35] B.D. Greenshields. A study of traffic capacity. *Proc. Highw. Res. Bd*, 14:448–474, 1934.

[36] Hargreaves, D.M. Measurement of the flow patterns and pollution in the wake of a moving vehicle. Safety/Operating Procedures NU/F/10, Department of Civil Engineering, University of Nottingham, December 1996.

[37] Hargreaves, D.M. Proposed design of the Moving Model Rig at Fauld. Technical Report FR 96014, Department of Civil Engineering, University of Nottingham, 1996.

[38] Hargreaves, D.M. and Baker, C.J. Gaussian puff model of an urban street canyon. Paper presented at BBAA3 in Blacksburg, VA, July, 1996 (also accepted for publication in the Journal of Wind Engineering and Industrial Aerodynamics).

[39] Helly, W. Simulation of bottlenecks in single-lane traffic flow. In Herman, R., editor, *Proceedings of the Symposium on the Theory of Traffic Flow, held at the General Motors Research Laboratories, Warren Michigan, U.S.A.* Elsevier Publishing Company, 1961.

[40] Hertel, O., Berkowicz, R., and Larrsen, S. The Operational Street Pollution Model (OSPM). In van Dop, H. and Steyn, D.G., editors, *Air Pollution Modelling and Its Applications*, volume VIII, pages 741–749. Plenum Press, New York, 1991.

[41] Hertel, O. and Berkowitz, R. Modelling NO_2 concentrations in a street canyon. Technical Report DMU LUFT-A131, National Environmental Research Institute, Frederiksborgvej 399, DK-4000 Roskilde, October 1989.

[42] Hertel, O. and Berkowitz, R. Modelling pollution from traffic in a street canyon. evaluation of data and model development. Technical Report DMU LUFT-A129, National Environmental Research Institute, Frederiksborgvej 399, DK-4000 Roskilde, May 1989.

[43] Hertel, O. and Berkowitz, R. Operational Street Pollution Model (OSPM). Evaluation of the model on data from St. Olavs Street in Oslo. Technical Report DMU LUFT-A135, National Environmental Research Institute, Frederiksborgvej 399, DK-4000 Roskilde, November 1989.

[44] Hickman, J. Vehicle operation and emissions. Article in Issue No. 23, Building and Civil Engineering Research Focus, October 1995. Published by the ICE.

[45] Hider, Z., Hibberd, S., and Baker, C. Modelling particulate dispersion in the wake of a vehicle. In *Computational Wind Engineering Conference, Colorado*, 1996. also accepted for publication in the Journal of Wind Engineering and Industrial Aerodynamics.

[46] HMSO. *National Road Traffic Forecasts (GB) 1989*. Number ISBN 0-11-550919-4. Her Majesty's Stationary Office, 1989.

[47] Hotchkiss, R.S. and Harlow, F.H. Air pollution transport in street canyons. Technical Report EPA-R4-73-029, NTIS PB-233 252, Prepared by Los Alamos National Laboratory for U.S. Environmental Protection Agency, 1973.

[48] Hoydysh, W.G. and Chiu, H.H. An experimental and theoretical investigation of the dispersion of carbon monoxide in the urban complex. In *Urban Technology*

Conference, New York City, U.S.A., number 71-523. American Institute of Aeronautics and Astronautics, May 1971.

[49] Hoydysh, W.G. and Dabberdt, W.F. Kinematics and dispersion characteristics of flows in assymmetric street canyons. *Atmospheric Environment*, 22:2677–2689, 1988.

[50] Hoydysh, W.G. and Dabberdt, W.F. Concentration fields at urban intersections: Fluid modelling studies. *Atmospheric Environment*, 28(11):1849–1860, 1994.

[51] Hoydysh, W.G., Ogawa, Y., and Griffiths, R.A. A scale model study of dispersion of pollution in street canyons. In *67th Annual Meeting of the Air Pollution Control Association, Denver, Colarado*, number 74-157, June 1973.

[52] Hunt, J.C.R. A theory for the laminar wake of a two-dimensional body in a boundary layer. *J. Fluid Mech.*, 49:159–178, 1971.

[53] Hunter, L.J., Johnson, G.T., and Watson, I.D. An investigation of three-dimensional characteristics of flow regimes within the urban canyon. *Atmospheric Environment*, 26B(4):425–432, 1992.

[54] Hurley, P. PARTPUFF – A Lagrangian particle–puff approach for plume dispersion modeling applications. *J. Appl. Meteorology*, 33:285–294, 1994.

[55] Jenkins, G.M. and Watts, D.G. *Spectral Analysis and its Applications*. Holden-Day, 1968.

[56] Johnson, G.T. and Hunter, L.J. A numerical study of dispersion of passive scalars in city canyons. *Boundary-Layer Meteorology*, 75:235–262, 1995.

[57] Johnson, W.B., Ludwig, F.L., Dabberdt, W.F., and Allen, R.J. An urban diffusion simulation model for Carbon Monoxide. *Journal of the Air Pollution Control Association*, 23(6):490–498, 1973.

[58] Karim, M.M. and Matsui, H. A stochastic model of emission expansion for an urban road. In *Vehicle Navigation and Information Systems Conference Proceedings*, pages 363–368, Yokohama, Japan, 1994.

[59] Kennedy, I.M. and Kent, J.H. Wind tunnel modelling of carbon monoxide dispersal in city streets. *Atmospheric Environment*, 11:541–547, 1977.

[60] Lanzani, G. and Tamponi, M. A microscale Lagrangian particle model for the dispersion of primary pollutants in a street canyon. Sensitivity analysis and first validation trials. *Atmospheric Environment*, 29(23):3465–3475, 1995.

[61] Lee, I.Y. and Park, H.M. Parameterization of the pollutant transport and dispersion in the urban street canyons. *Atmospheric Environment*, 28(14):2343–2349, 1994.

[62] Leitl, B. and Meroney, R.N. Car exhaust dispersion in a street canyon - numerical critique of a wind tunnel experiment.

[63] Ludwig, F.L., Gasiorek, L.S., and Ruff, R.E. Simplification of a gaussian puff model for real-time minicomputer use. *Atmospheric Environment*, 11:431–436, 1977.

[64] Maeda, J. and Makino, M. Charactersitics of gusty winds simulated by an A.R.M.A. model. *Journal of Wind Engineering and Industrial Aerodynamics*, 41-44:427–436, 1992.

[65] Meroney, R.N., Pavageau, M., Rafailidis, S., and Schatzmann, M. Study of line source characteristics for 2-D physical modelling of pollutant dispersion in street canyons. *Journal of Wind Engineering and Industrial Aerodynamics*, 62:37–56, 1996.

[66] Moriguchi, Y. and Uehara, K. Numerical and experimental simulation of vehicle exhaust gas dispersion for complex urban roadways and their surroundings. *Journal of Wind Engineering and Industrial Aerodynamics*, 46–47:689–696, 1993.

[67] Nishi, A. and Cermak, J.E. Modeling of pollutant dispersion from a moving source - Application to airport pollution. In *Wind Engineering - Proceedings of the 5th International Conference, Fort Collins, Colarado*, volume 2, July 1979.

[68] The Numerical Algortithms Group Ltd., Oxford, UK. *NAG FORTRAN 77 Library*.

[69] Oke, T.R. *Boundary Layer Climates*. Methuen, London and New York, 1987.

[70] Pearce, W. A review of wind tunnel tests of the flow and gaseous dispersion in an urban environment. Technical Report FR93015, Department of Civil Engineering, University of Nottingham, 1993.

[71] Pearce, W. and Baker, C.J. Wind tunnel tests on the influence of vehicular motion on pollutant dispersion in an urban street canyon. Paper presented at BBAA3 in Blacksburg, VA, July, 1996.

[72] Peterson, W.B. A demonstration of INPUFF with the MATS Data Base. *Atmospheric Environment*, 20(7):1341–1346, 1986.

[73] Press, W.H., Flannery, B.P., Teukolsky, S.A., and Vetterling, W.T. *Numerical Recipes (FORTRAN Version)*. Cambridge University Press, 1989.

[74] Rao, K.S., Eckman, R.M., and Hosker, R.P., Jnr. Simulation of tracer concentration data in the Brush Creek Drainage flow using an integrated puff model. *Journal of Applied Meteorology*, 28:609–616, 1989.

[75] Rao, S.T. and Keenan, M. Suggestions for the improvement of the EPA-HIWAY model. *J. Air Pollution Control Assoc.*, 30:247–256, 1980.

[76] Rao, S.T., Sedefian, L., and Czapski, U.H. Characteristics of turbulence and dispersion of pollutants near major highways. *Journal of Applied Meteorlogy*, 18(3):283–293, March 1979.

[77] Read, C., editor. *How vehicle pollution affects our health*, 9, Red Lion Court, London, EC4A 3EB, 1994. The Ashden Trust. Summary of papers presented at a symposium in London on 20th May 1994.

[78] Rotach, M.W. Turbulence close to a rough urban surface. Part I: Reynolds Stress. *Boundary-Layer Meteorology*, 65(1-2):1–28, 1993.

[79] Salter, R.J. *Highway Traffic Analysis and Design*. MacMillan, 1989. Second Edition.

[80] Schatzmann, M., Rafailidias, S., Britter, R., and Arend, M. Database, monitoring and modelling of urban air pollution: Inventory of models and data sets. Technical report, European Commission, 1996. European cooperation in the field of scientific and technical research.

[81] Scibor-Rylski, A.J. *Road Vehicle Aerodynamics*. Pentech Press, 2nd edition, 1984. Second Edition revised by Sykes, D.M.

[82] Shale, G.A. The simulation of atmospheric boundary layer profiles in the British Gas Fauld wind tunnel. Technical Report MRS I 5641, British Gas plc, Research and Technology Division, Midlands Research Station, 1991.

[83] Simmon, P.B., Patterson, R.M., Ludwing, F.L., and Jones, L.B. The APRAC-Mobil emission and diffussion modelling package. Technical Report EPA-909/9-81-002, Environmental Protection Agency, 1981.

[84] Sini, J-F., Anquetin, S., and Mestayer, P.G. Pollutant dispersion and thermal effects in urban street canyons. *Atmospheric Environment*, 30(15):2659–2677, 1996.

[85] Stone, R. *Motor Vehicle Fuel Economy*. MacMillan, 1989.

[86] Swaid, H. The Role of Radiative-Convective interaction in creating the microclimate of urban street canyons. *Boundary-Layer Meteorlogy*, 64(3):231–259, April 1993.

[87] Tangirala, R.S., Rao, K.S., and Hosker, R.P., Jnr. A puff model simulation of tracer concentrations in the nocturnal drainage flow in a deep canyon. *Atmospheric Environment*, 26A(2):299–309, 1992.

[88] Verver, G.H.L. and De Leeuw, F.A.A.M. An operational puff dispersion model. *Atmospheric Environment*, 26A(17):3179–3193, 1992.

[89] Yamartino, R.J. and Wiegand, G. Development and evaluation of simple models for the flow, turbulence and pollutant concentration fields within an urban street canyon. *Atmospheric Environment*, 20(11):2137–2156, 1986.

[90] Zannetti, P. A new mixed segment-puff approach for dispersion modelling. *Atmospheric Environment*, 20(6):1121–1130, 1986.

[91] Zimmerman, J.R. and Thompson, R.S. User's guide for HIWAY, a highway air pollution model. Technical Report EPA-650/4-74-008, Environmental Protection Agency, 1975.

Appendix A

Installing the Moving Model Rig

A.1 Introduction

Over a number of weeks in the latter half of 1996, the Moving Model Rig was moved from its home in the environmental wind tunnel at Nottingham University to the wind tunnel at the British Gas Test Site at Fauld in Staffordshire. While involved throughout the design and installation process, the author was instrumental in the early design and fabrication of much of the steel substructure on which the MMR would eventually sit. This appendix describes the design of the steel substructure and the thinking behind using this particular design. At the end of the appendix, there is a section which describes some of the later problems which had to be overcome in the installation.

This appendix is written largely in the future tense because it is in part a reproduction of a report submitted to British Gas early in 1996. The actual report (Hargreaves [37]) is not included verbatim because much of its content has already been discussed in Chapter 3. Peppered around the appendix, where they are thought to be useful, are footnotes which describe subsequent changes to the original design.

Many of the drawings which were used in the initial fabrication of the MMR are reproduced here. They are, however, reduced to 75% of their original size. Thus, the scales on the drawings are inaccurate but the drawings are still of use in demonstrating the thinking behind the design.

The overall installation process was fraught with difficulties - not least because of the complex geometry beneath the wind tunnel. In addition, numerous ducts, wires and pipes were standing in the way of the proposed path of the MMR. Some of these difficulties are demonstrated in Drawing MMR/001 (Figure A.3) which shows the existing structural configuration of the tunnel in cross-section, just downwind of the proposed position of the MMR.

For a more schematic representation of the actual location of the MMR in its new environment, Figures A.1 and A.2 show where the new MMR is to be situated.

A.2 Design of the New Sub-structure

It was decided at an early stage that the concrete blocks used in the Nottingham University wind tunnel (see Figure 3.2) could not be used in the Fauld wind tunnel, the reasons being:

1. The complex geometry of the control room and working section at Fauld would not house the blocks.
2. The blocks were probably "over-engineered" for the purpose. In other words, the reduction in mechanical noise afforded by the blocks was not sufficient to justify their use in the new location.
3. The cost of moving the blocks and installing them at Fauld would be prohibitive.
4. One of the stipulations made by British Gas was that the control room could be easily cleared of the MMR when it was not in use. Obviously, with the blocks in place this could not be achieved easily.

Thus a replacement for the concrete blocks was required - namely a steel sub-frame consisting of three sections:

Main section which would lie under the working section of the tunnel. This was the section where ride quality was of the utmost importance and thus required the most stable sub-frame.

Launch section which would be housed in the control room of the wind tunnel for the duration of any experiments which require the use of the MMR. This section could then be removed thus satisfying the requirements laid down by British Gas. As this is the length of the track over which the vehicle is accelerating, ride quality was not such a factor here.

End section extends beyond the working section into the gap between the tunnel and the external wall of the tunnel building (B501). Over this section the trolley will be rapidly decelerated using a combination of bungy ropes and sprung metal plates.

Drawing MMR/002 shows how the three sections fit together to form the new sub-structure of the MMR.

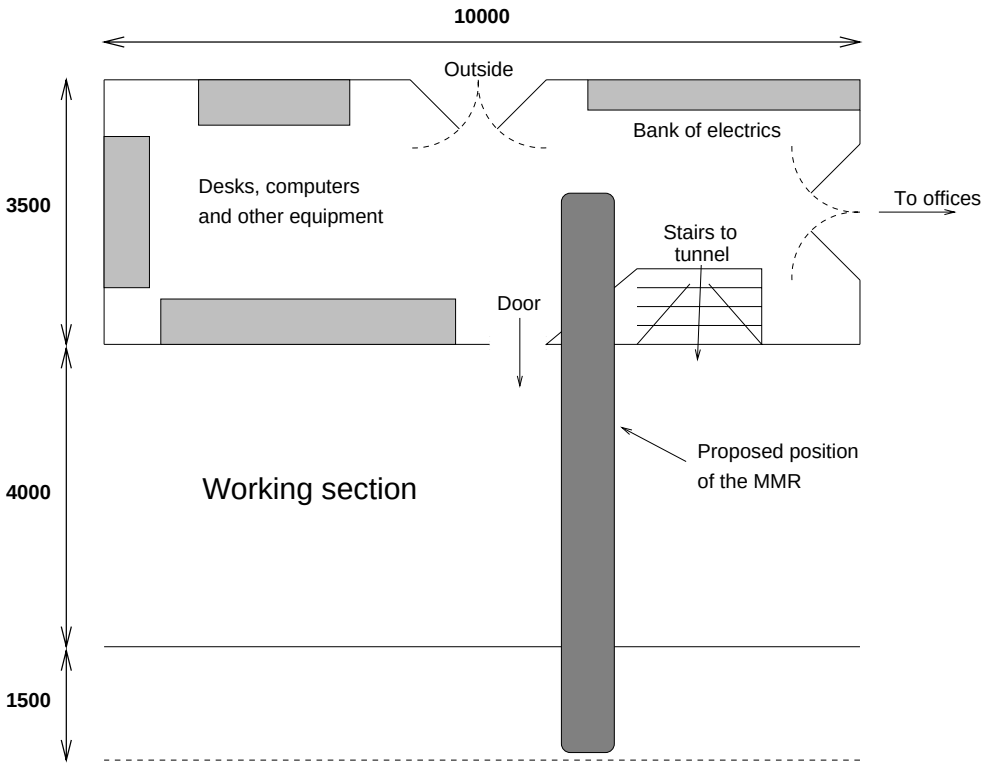


Figure A.1: Schematic plan view of the British Gas Environmental Wind Tunnel at Fauld, Staffordshire, showing the proposed position of the Moving Model Rig.

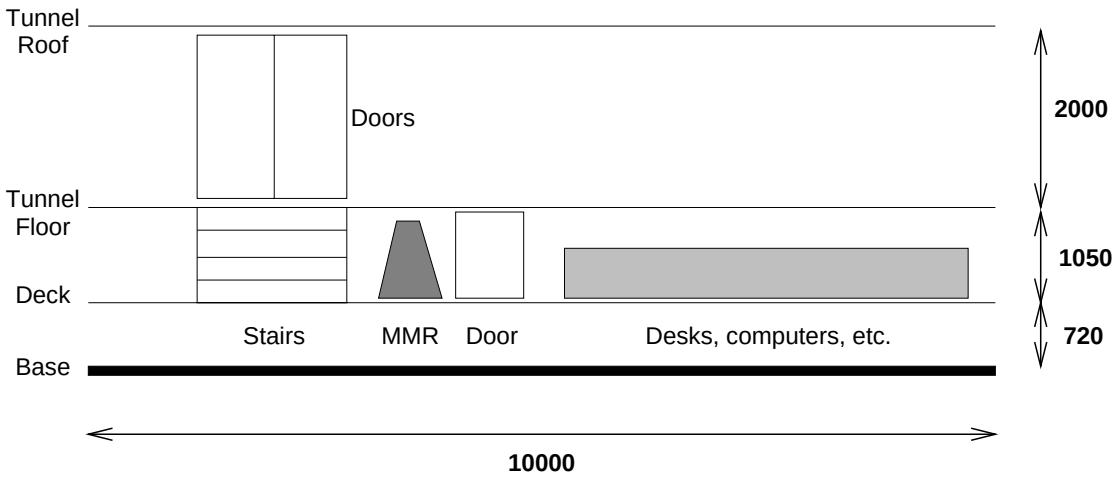


Figure A.2: Schematic side elevation of the British Gas Environmental Wind Tunnel at Fauld, Staffordshire, showing the proposed position of the Moving Model Rig.

A.2.1 Design of the Main Section

The main section of the MMR consists of four steel H-columns (MS-H1 to MS-H4) supporting a beam with taper flanges (the support beam or MS-B1). The track beam (here the one attached to the Hepco track) lies above the support beam. The inter-column gap[1] for these four columns will be 800 mm.

Drawings MMR/003 and MMR/004 (Figures A.5 and A.6) show the side and end elevations of the H-columns and their method of connection to the track of the MMR. Onto each end of the H-columns, an 8mm thick steel plate will be welded. At the top of the column, MS-B1 will be bolted through the plate which will secure the support beam to the column. At the foot of each column, the plate will sit over four rawl plugs which will be grouted into the floor of the tunnel building and will be secured using bolts, as shown in Drawing MMR/005..

This method of connection at the top and bottom of each column is repeated for the launch and end sections, as the next two sections demonstrate.

A.2.2 Design of the Launch Section

The launch section will be of essentially the same design as the main section with different lengths for the two H-columns (LS-H1 and LS-H2) and the support beam (LS-B1). The launch section will be removable so the connections to the floor and main section need to be temporary. Bolts will be used in both cases with a beam splice connecting the beams MS-B1 and LS-B1 - see Drawing MMR/010.

The motor which drives the return mechanism will be floor-mounted, just beyond the base of LS-H1. A fan-belt will connect the motor to the pulley on the return mechanism. The motor requires a power supply and since it also is a temporary fixture, it would seem sensible to pass the wiring from under the wind tunnel and along LS-B1, instead of from the closer bank of electrics in the control room[2] (see Figure A.1).

A.2.3 Design of the End Section

The end section will protrude under the existing wooden floor on the far side of the wind tunnel. Again the design of choice is a beam, ES-B1, supported by two columns, ES-H1 and ES-H2.

[1] Defined as the space between successive columns, and not, for instance, the distance between the mid-points of the columns.

[2] As it turned out, the bank of electrics was used to supply the power to the motor, via a cable which lay across the floor under protective matting.

ES-B1 will be connected to MS-B1 by means of a beam splice, as shown in Drawing MMR/007. The track support beam is currently in several sections of varying length. Thus, it has not been possible to show the exact position of the join in the track support beam - it is highly unlikely that it will coincide with the join in the lower beams. However, it is not envisaged that the strength of the structure will suffer because of this.

A.2.4 Configuration of the Support Plates

Between the track beam and the support beam in each section, there will be the support plate. Each plate (one for each of the launch, main and end sections) will be an 8 mm thick, 200 mm wide, steel plate with regularly spaced holes, the configuration of which is shown in Drawing MMR/011. The outer holes are 11 mm diameter holes, drilled straight through the plate and will be used to support the return mechanism. The inner holes again pass through the plate but this time are threaded to take the bolts which secure the track holders in place - see, for instance, Drawing MMR/003. There is not enough room on the inside of the support beam flange to accommodate nuts for these bolts.

A.2.5 Configuration of the Beam Splices

In order to provide some kind of connection between the three sections of the new subframe, beam splices will be used. Drawings MMR/007 and MMR/010 show the location of the beam splices. Obviously, there is a plate on both sides of the support beams in order to provide the maximum strength in the joint. Another reason for using beams splices with bolts and not welds or rivets is the temporary nature of the launch section.

A.3 Alterations to the Wind Tunnel

A.3.1 Working Section

In order to allow models to be fired across the wind tunnel, obviously a slot needs to be cut in the floor of the wind tunnel, at right angles to the wind direction. A metal tunnel presents its own set of problems in this respect. However, since the steel plates are no more than about 8 mm thick, it should be possible to cut through the shell of the tunnel with the appropriate equipment.

It is proposed to cut a slot 50 mm wide across the floor of the tunnel, as shown in Drawing MMR/008. A plasma cutter, owned by the University, will be used to cut the slot. Grinders will then be used to produce the required finish on the exposed steel plate.

When the MMR is in operation, plates can be fitted to the gap in order to bring the gap down to the required width and then brushes will be used to minimize suction through the gap and to allow un-retarded passage of the models. When not in operation, the slot will be sealed using three lengths of 8 mm thick steel plate[3].

When cutting the slot in the floor of the tunnel, there will be the four stiffeners to negotiate. These will have to have slots cut in them at least as wide as the main slot across the tunnel. And, because they extend quite a distance below the tunnel floor, they may well need to be further modified to accommodate the track and/or trolley. One such proposal is shown in Drawing MMR/008.

At each end of the slot a larger hole will be cut in the side of the tunnel to allow passage of the model. In the first instance a square hole of side 200 mm will be sufficient[4]. Again when the tunnel is not in use it will be necessary to block the holes up - this time using the hinged hole covers. When the MMR is in use the hole covers will be lifted into the up position, with a magnetic clasp or similar holding the cover in place[5]. During periods when the MMR is out of service, the covers can be lowered into place, again being secured using magnetic fitments in much the same way as the existing covers for the door handle access holes are. Rubber seals will also be fitted around the holes in order to prevent leakage when the tunnel is in operation.

The breaching of the tunnel floor and its stiffeners will weaken the floor of the tunnel beyond its limits, especially when bearing the weight of a person. In order to combat this effect, an angle will be welded across the tunnel, perpendicular to the wind direction, on both sides of the slot. Drawing MMR/008 shows these angles more clearly. These will provide the necessary stiffness in the cross-tunnel direction. The box design of the tunnel will prevent any sagging in the along-tunnel direction[6].

The angles will have holes tapped into them at 160 mm intervals to allow the sealing plate to be screwed or bolted into place. In addition, the already beveled edge of the angle may need to be made larger to accommodate the fillet weld on the sealing plate.

A.3.2 Control Room

Next to the access door to the underneath of the tunnel, a large hole will need to be cut to allow the bungees, track, support beams and return mechanism to pass below the tunnel.

[3]Notice that in MMR/008 the plates are screwed in from below - this proved to be impractical and the plates now drop in from above. The slot in the tunnel floor had to widened to accommodate this new design.

[4]This hole was subsequently extended upwards because of some work which involved a train passing over an embankment.

[5]These covers are now removed completely during use.

[6]To our cost, this was not the case. An additional two H-columns had to be placed under the tunnel upstream of the MMR in order to reduce the considerable sagging which had occured when the slot was cut.

The size of this hole is unknown at the time of writing and can be cut to the size of the existing access door without compromising the strength of the tunnel.

A.3.3 Far/Laser Side

In the terminology of the wind tunnel building, the area on the opposite side of the wind tunnel from the control is known as the far side or laser side, the latter because laser equipment is sometimes housed there. The end section of the MMR will lie below the wooden deck which leads into the laser room. Again, a slot will need to be cut into this platform but, because it is fabricated from wood, this should be significantly easier than cutting through the wind tunnel itself. Also the width of the slot is not critical because there will be no suction effects to contend with outside the wind tunnel. Indeed, the wooden deck is lower than the floor of the wind tunnel and so a large gap may be required in the deck to allow the Hepco track or model to protrude through.

Drawing MMR/007 shows a side elevation of the end section in its proposed position.

A.4 Further Work

On the whole, the steel work was built to the specifications of the preceding sections. Problems were encountered due to the concrete floor under to the tunnel not being flat. Indeed, it was initially assumed (quite rightly) that all four of the main section columns would be in compression. Because of the floor only the central two are with the end being in tension. This is not thought to be a problem - if anything it will add to the rigidity of the structure.

Once the steel work and track had been fixed in place and leveled, it was soon realized that air was going to be sucked through the slot and end holes and would invalidate any reading taken. In order to prevent this happening a large airtight box was built to permanently enclose the end and main sections (access doors were provided) with a temporary one to enclose the launch section. Preliminary flow visualization tests show that this box is performing the required function. The box was fabricated out of Medium Density Fibre (MDF) board with any holes sealed with a combination of silicone sealant and expanding foam.

The original return mechanism used while the MMR was at Nottingham was replaced by a much modified design. In particular, the cables were replaced by a bicycle chain mainly because the cables had become irreversibly twisted. Also, because the space limitations were much more acute at Fauld, the launch mechanism had to redesigned to reflect this. As a result, the distance over which the bungy ropes can be tensioned has reduced dramatically with the possible implication of reducing the maximum trolley

velocity. Luckily for the experiments described in this thesis, the trolley speeds used were well within the capabilities of the much-modified MMR.

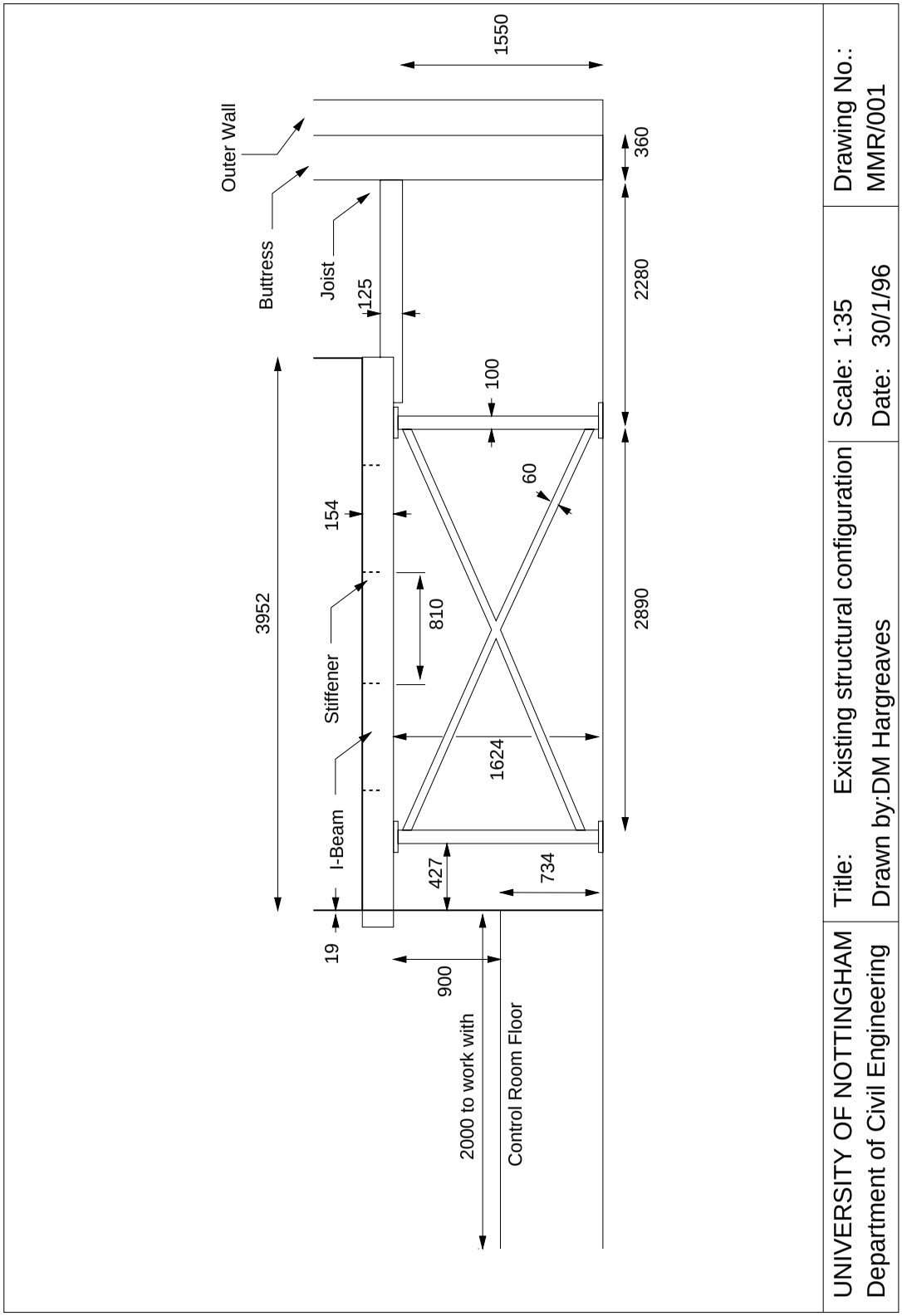


Figure A.3: Reproduction of Drawing MMR/001.

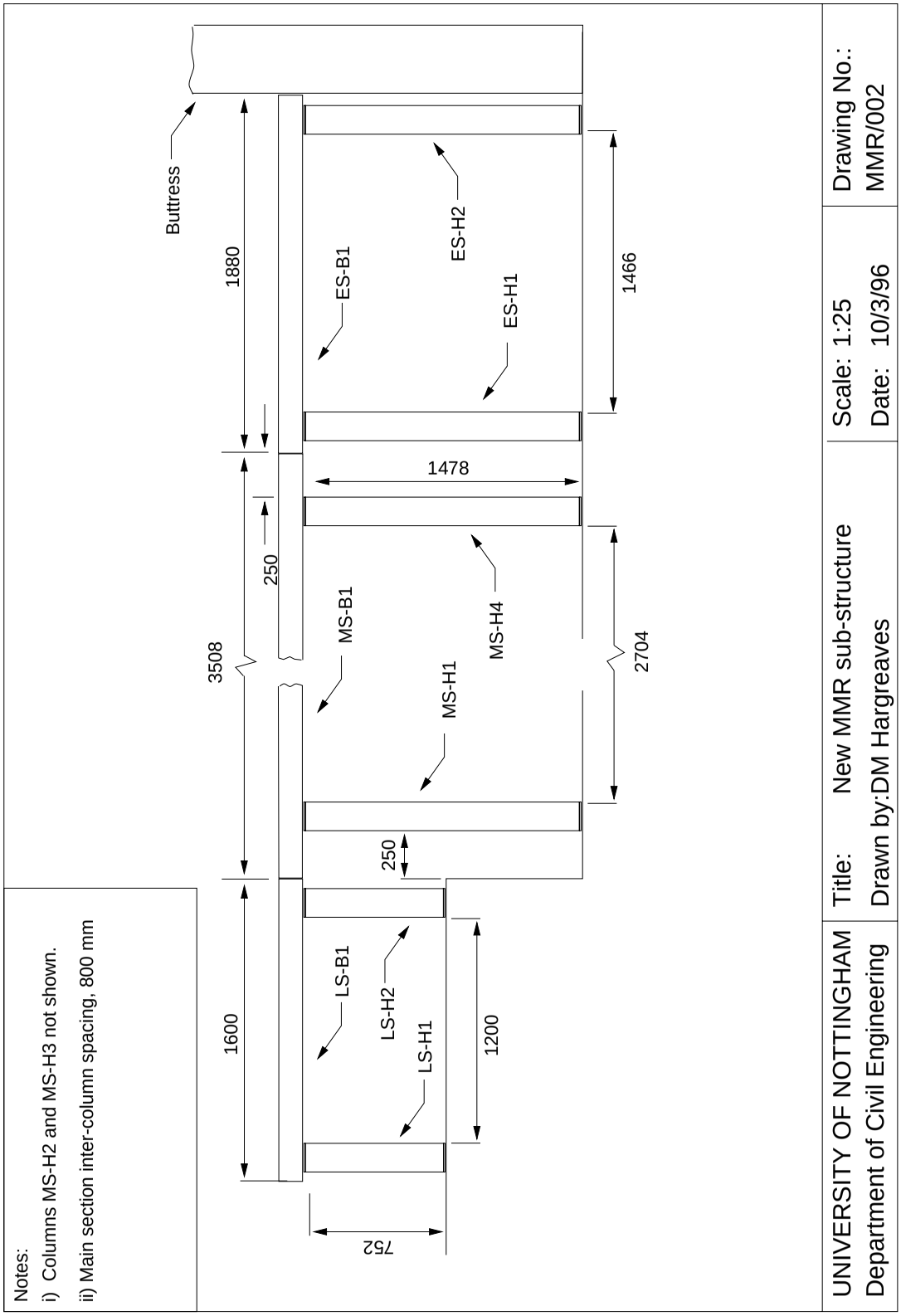


Figure A.4: Reproduction of Drawing MMR/002.

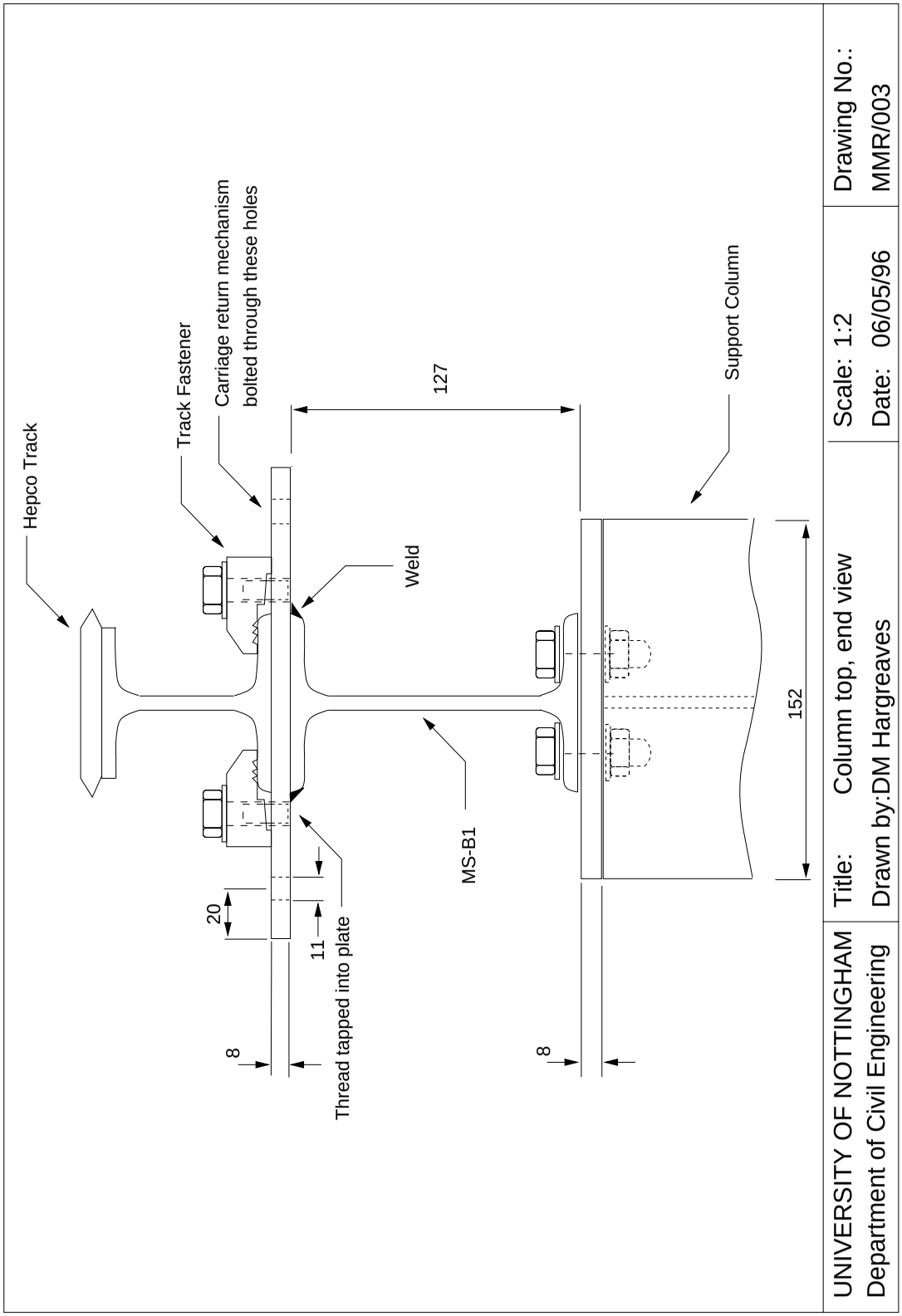


Figure A.5: Reproduction of Drawing MMR/003.

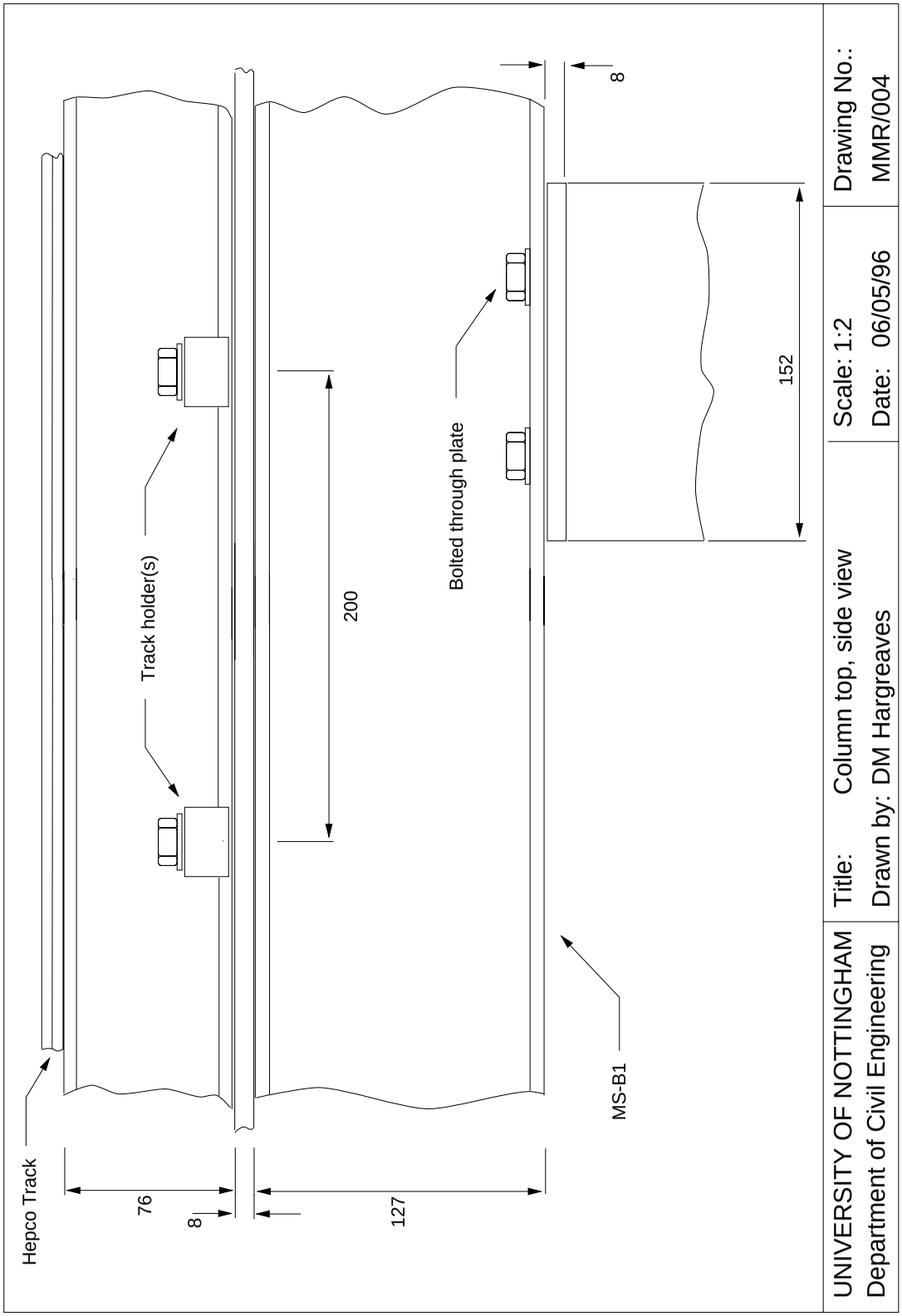


Figure A.6: Reproduction of Drawing MMR/004.

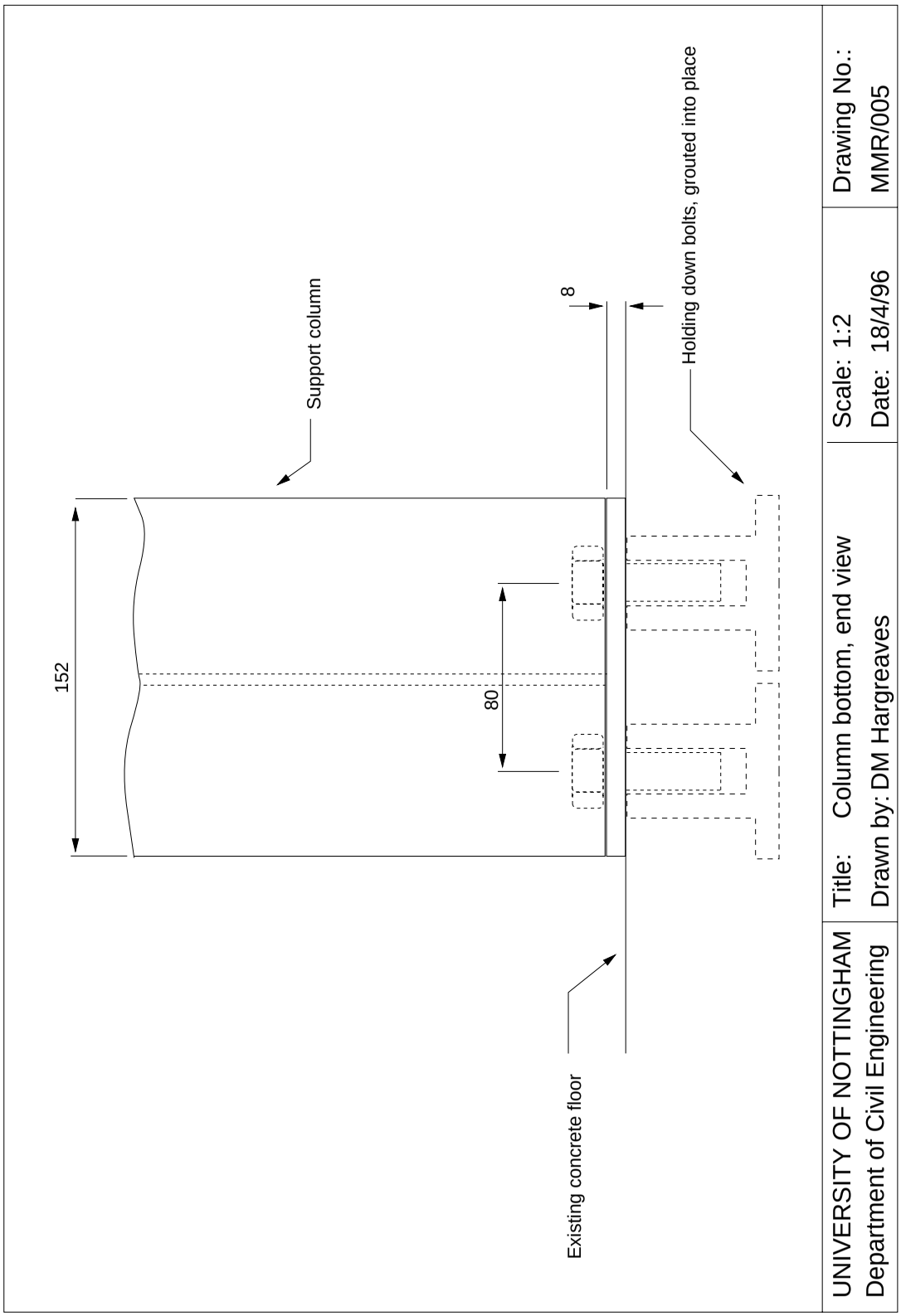


Figure A.7: Reproduction of Drawing MMR/005.

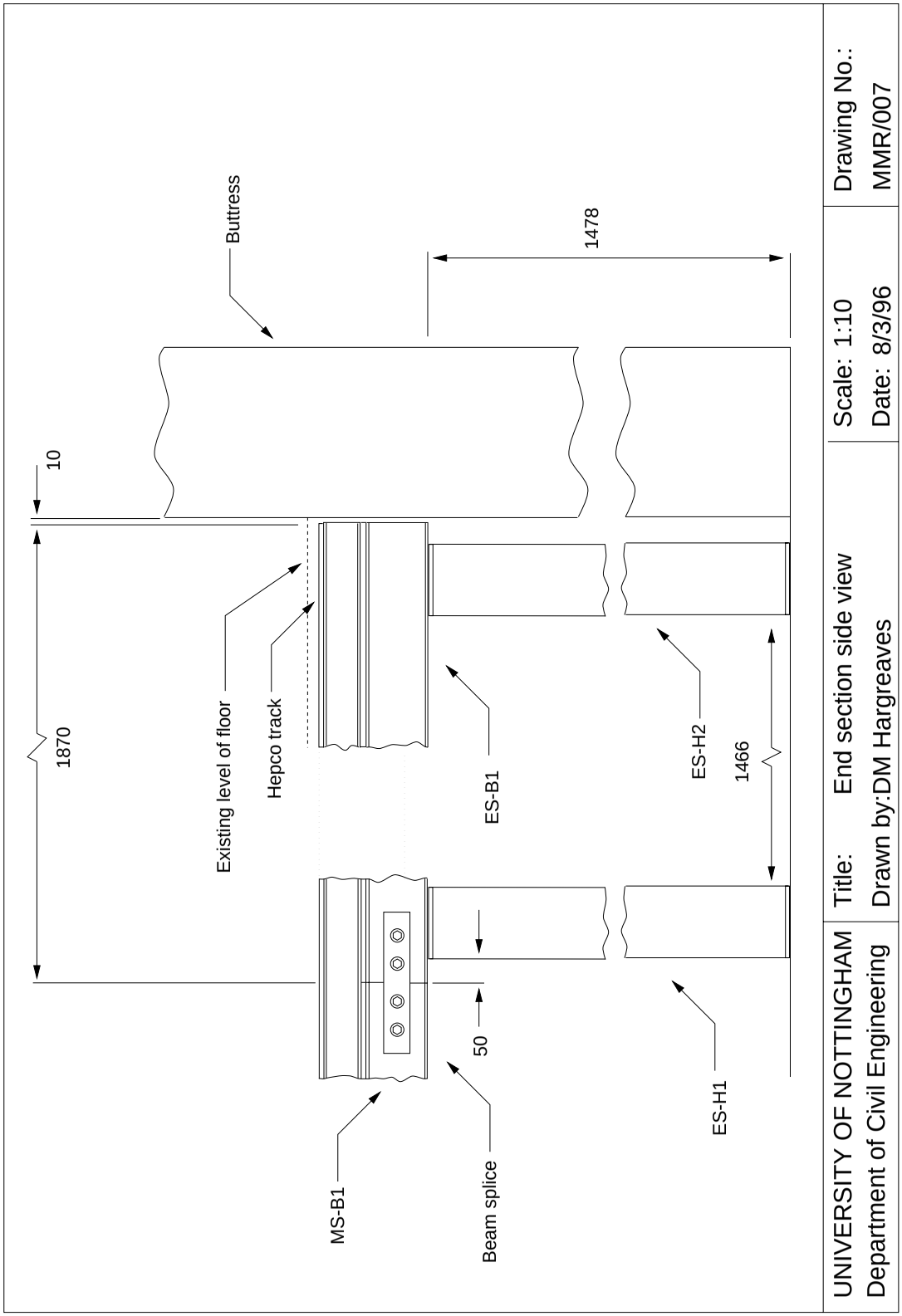


Figure A.8: Reproduction of Drawing MMR/007.

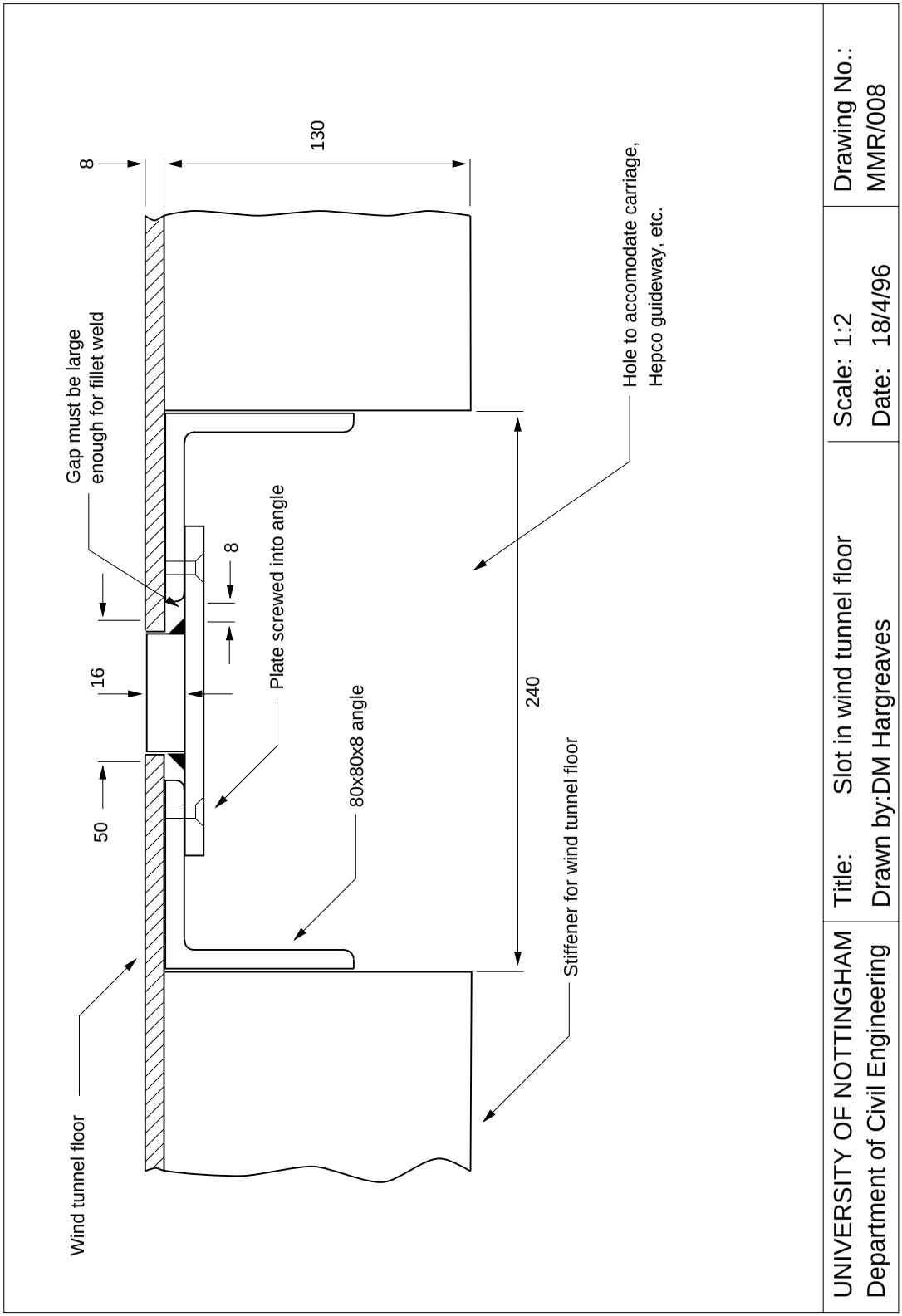


Figure A.9: Reproduction of Drawing MMR/008.

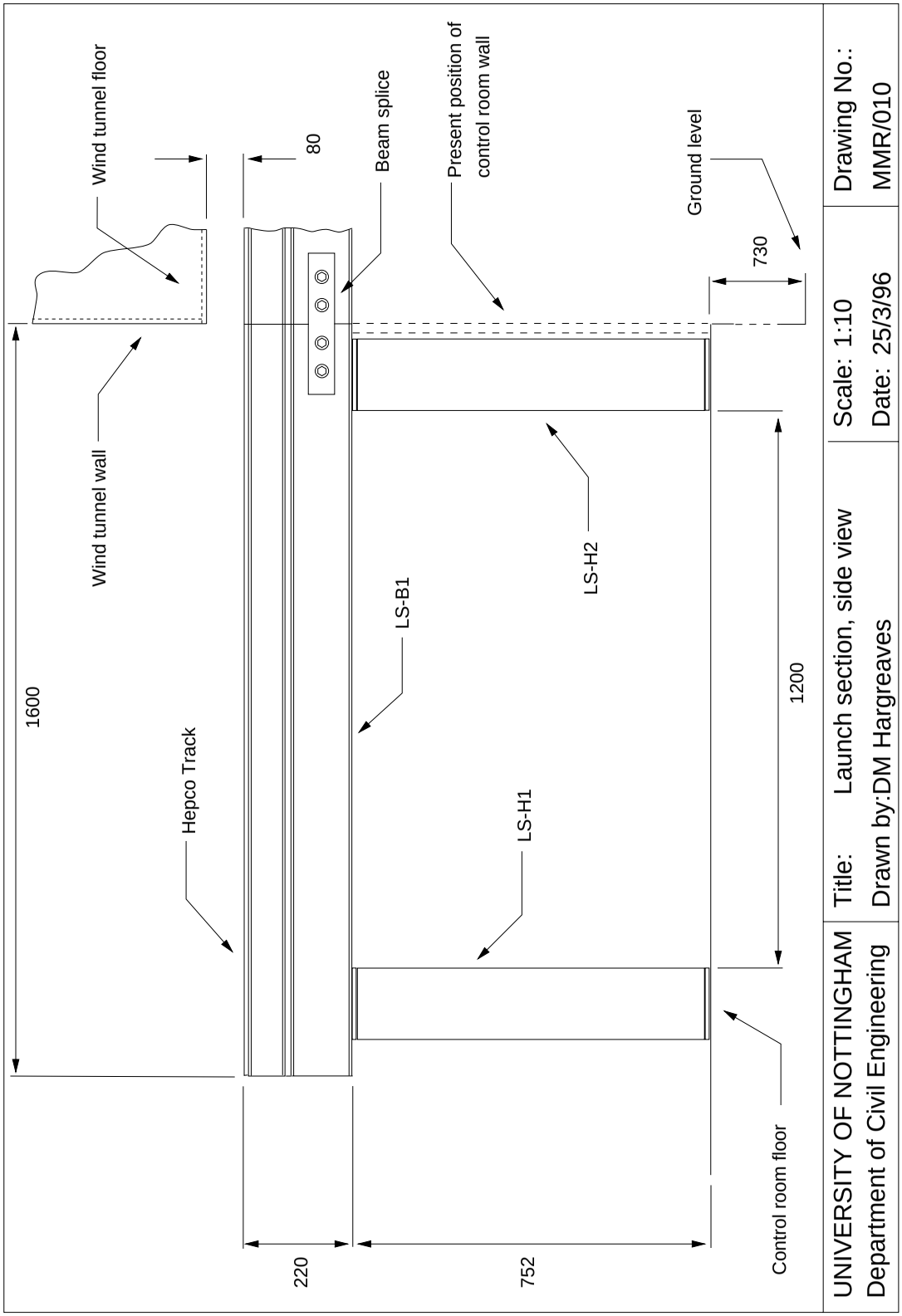


Figure A.10: Reproduction of Drawing MMR/010.

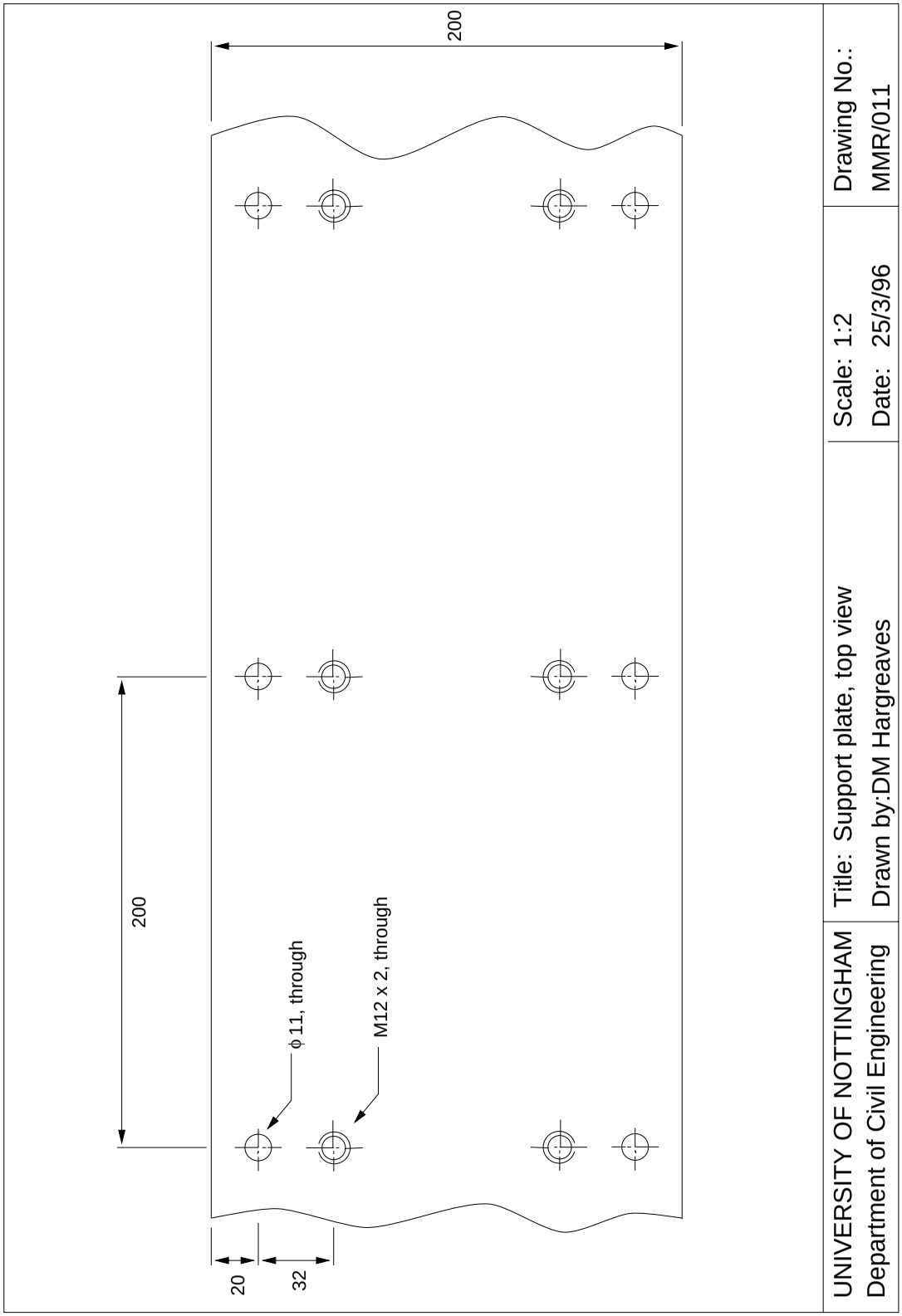


Figure A.11: Reproduction of Drawing MMR/011.

Appendix B

Documentation of PUFFER

B.1 PUFFER Data Files

The overall file handling for the PUFFER program is shown schematically in Figure B.1.

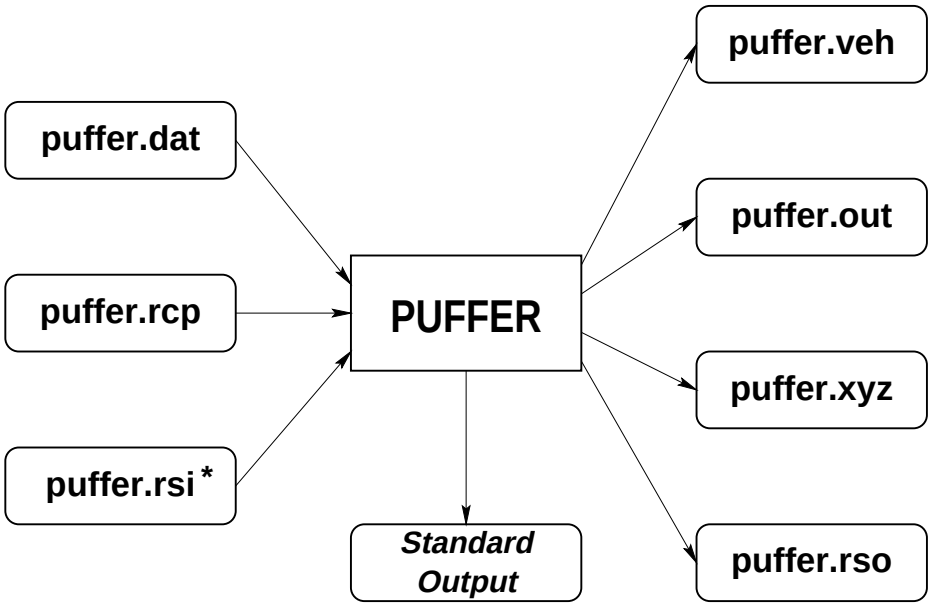


Figure B.1: Diagram of the input and output files for the PUFFER program.

B.1.1 Main Input File, `puffer.dat`

This file contains most of the input data required for the running of PUFFER. Notice the importance of distinguishing between integers (`int`) and reals (`double`).

Variable	Type	Units	Description
Line 1			
–	`int`	–	Restart option flag; 0 is off, 1 is on
–	`int`	–	Cyclic canyon ends; 0 is off, 1 is on
–	`int`	–	Single pass for vehicles; 0 is off, 1 is on
–	`int`	–	Vehicle wake effects; 0 is on, 1 is off
Line 2			
–	`int`	–	Rural option flag; 0 is off, 1 is on
–	`int`	–	Variable wind angle flag; 0 is off, 1 is on
–	`int`	–	ARMA wind flag; 0 is off, 1 is on
–	`int`	–	Not required
Line 3			
–	`int`	–	Concentration data; 0 is off, 1 is on
–	`int`	–	Not used
–	`int`	–	Not used
–	`int`	–	Not used
Line 4			
L	`double`	m	Length of the domain (along x-axis)
B	`double`	m	Width of the canyon (along y-axis)
H	`double`	m	Height of the canyon (along z-axis)
Line 5			
U_H	`double`	ms^{-1}	Reference wind speed
h_{ref}	`double`	m	Reference height
θ	`double`	–	Angle between wind and canyon axis
σ_θ	`double`	–	Standard deviation in wind angle
z_0	`double`	m	Roughness length for along canyon wind
Next line required only if ARMA wind option is on.			
Line 6			
${}^{x}L_u$	`double`	m	Characteristic length scale of wind spectra
I	`double`	–	Turbulence intensity of wind (percentage)

Variable	Type	Units	Description
Line 7			
N_v	`int`	–	No. of vehicle types
Repeat the next 6 lines for each i of the N_v vehicle types.			
Line 7.1			
ρ_i	`double`	–	Normalized vehicle type density
Line 7.2			
l_i	`double`	m	Length of the vehicles
b_i	`double`	m	Width of the vehicles
h_i	`double`	m	Height of the vehicles
Line 7.3			
$(C_1)_i$	`double`	s^{-1}	Velocity control parameter
$(C_2)_i$	`double`	s^{-2}	Headway control parameter
β_i	`double`	s	Headway calculation parameter
Line 7.4			
$(q_i)_i$	`double`	m^3s^{-1}	Idling emission rate
$(q_s)_i$	`double`	m^2	Speed-dependent emission coefficient
$(q_a)_i$	`double`	m^2s^{-1}	Acceleration-dependent emission coefficient
Line 7.5			
$(c_i)_i$	`double`	kgm^{-3}	Idling exhaust concentration
$(c_s)_i$	`double`	$kgsm^{-4}$	Speed-dependent concentration coefficient
$(c_a)_i$	`double`	kgs^2m^{-4}	Acceleration-dependent concentration coefficient
Line 7.6			
$(d_e)_i$	`double`	m	Exhaust pipe diameter
Line 8			
N_l	`int`	–	No. of lanes of traffic
Repeat the next line for each i of the N_l lanes of traffic.			
Line 8.1			
$(y_l)_i$	`double`	–	Offset of lane *i*
–	`int`	–	Direction of lane *i*; +1 for positive *x*
$(N_p)_i$	`int`	–	No. of time points for lanes *i*
Repeat the next line for each j of the N_{pi} time points.			
Line 8.1.1			
–	`double`	s	Time
–	`double`	$m.s^{-1}$	Speed

Variable	Type	Units	Description
Line 9			
N_t	`int`	–	No. of time steps
Δt	`double`	s	Time step length
f_p	`int`	–	Frequency of puff generation
f_o	`int`	–	Frequency of main output generation
f_t	`int`	–	Frequency of tracking output generation
Line 10			
α_1	`double`	–	Turbulence intensity parameter
α_2	`double`	–	Turbulence anisotropy parameter
Line 11			
λ_l	`double`	–	Puff removal limit
λ_f	`double`	–	Puff reduction factor
The next 3 lines are required only if in post-processing mode			
Line 12			
–	`int`	–	Format type: 0 is time variation at a single receptor; 1 is a time-averaged profile along a line; 2 is a cross-section; 3 is a probability density; 4 is for AVS UCD output; 5 is an instantaneous profile along a line
–	`int`	–	Scaling type: 0 is for absolute values; 1 is for non-dimensionalised values
–	`int`	–	Line plot axis: 0 is *x*-axis; 1 is *y*-axis; 2 is *z*-axis
–	`int`	–	Cross-section plane; 0 is *xy*; 1 is *yz*; 2 is *zx*
–	`int`	–	Velocity scaling: 0 is wind-wind; 1 is wind-vehicle; 2 is vehicle-wind; 3 is vehicle-vehicle
Line 13			
–	`double`	–	*x*-offset
–	`double`	–	*y*-offset
–	`double`	–	*z*-offset
Line 14			
–	`int`	–	Time step for start of averaging or the exact time for an instantaneous profile along a line
–	`int`	–	No. of bins for frequency distribution
–	`double`	$\mathrm{kg.m^{-3}}$	Lower limit for frequency bins
–	`double`	$\mathrm{kg.m^{-3}}$	Upper limit for frequency bins

B.1.2 Receptor Position File, `puffer.rcp`

Contains a line with the number, N_r, of receptors, followed by N_r lines of the normalized coordinates (x_r, y_r, z_r) of the receptors. The values of each coordinate should lie between 0 and 1 - *ie* $0 \leq x_r \leq 1$, etc.

B.1.3 Restart Input File, `puffer.rsi`

Contains the restart data for a restarted run. The format of this file is not important since it is created by renaming a restart output file.

B.1.4 Main Output File, `puffer.out`

Contains the concentration at each receptor for every output time step. This file is a binary file and as such the contents cannot be viewed but can, however, be read by PUFFER when run in post-processing mode with the `-p` flag - see Section B.2.

B.1.5 Tracking File, `puffer.xyz`

Contains the position, mass and dispersion data for the first puff[1]. This file also contains information about the current number of vehicles of each type in the first lane and also mass balance data, including the total pollutant flow into and out of the model and that currently in storage[2].

B.1.6 Restart Output file, `puffer.rso`

Contains data about the time, the positions of the vehicles and the current status of all the active puffs in the model. It is produced so that a restart using this data can be performed.

B.1.7 Vehicle Position File, `puffer.veh`

Contains time versus position data for all the vehicles in the first lane of traffic only. Used mainly to verify that the traffic sub-model was functioning correctly.

B.1.8 Echo File on Standard Output

All error messages and data echoes are written by PUFFER to the standard output (with FORTRAN that would be unit 6). The shell script which controls the execution of

[1] If the first puff is lost from the model, then it is replaced by the next one in the list.

[2] Storage is a term borrowed from groundwater flow meaning the total mass of pollutant contained within the domain.

PUFFER under the UNIX environment redirects this output to the file `name.ech` where `name` is the stem of the input file - see Section B.2.

B.2 Running the PUFFER program

The current implementation of PUFFER is available only on the DEC Alpha cluster in the Department of Civil Engineering at Nottingham University. These are powerful machines which run the UNIX operating system. PUFFER can be invoked on any of these machines by means of a standard shell script. The syntax of the command to run PUFFER is as follows,

```
puffer [-v VER] [-D|O] [-?] [-k] name

        -v      followed by the version number (default is 5.3)
        -D      debugging mode
        -O      optimized run
        -p      post-processing mode
        -?      to display this message
        -k      kill an existing run
        name    is the stem of the input file
```

which needs some clarification.

`puffer` is the command name.

`-v` is the version number of the program which is to be run. If this argument is omitted then the default (and usually the latest), in this case 5.3, is run.

`-D` runs the debuggable version of the executable through the standard UNIX debugger, `dbx`.

`-O` runs the optimized version of the executable. Since this is the fastest version, this is the one which gets run by default if either of the options -D or -O are omitted.

`-?` prints out the message above.

`-k` can be used to kill an existing run whose stem is `name`. The run is killed by removing the file `puffer.run` which the program looks for at the start of each time step - if it is not there then the program terminates cleanly.

The usual method of running puffer is to create the relevant input files (see Section B.1) and to type the above command. So, suppose an input file `test.dat` and receptor position file `test.rcp` exist. Typing,

```
puffer -v5.2 test &
```

would run version 5.2 of puffer as a background task with the added protection given by `nohup` which allows the program to continue even after the user logs out. To kill the current run you would type,

```
puffer -k test
```

Notice that the version is not required and this task has not been back-grounded.

When running, the shell script creates a sub-directory `test` which holds all temporary files. On completion, this directory is removed with all relevant files being moved back into the starting directory.

B.3 Description of the Source Code

There follows a detailed description of each of the separate sub-programs which form the PUFFER program. Files ending in `.f` contain FORTRAN source code and files ending in `.c`, which form the majority of the program, contain C source code. C header files end in `.h` and can be found along with the source code in the directory

```
/home/evxdmh/codes/puffer/src
```

on the University of Nottingham's UNIX workstation cluster. They are stored as a special kind of file called an RCS file which holds incremental versions of the source code for each sub-program.

Figures B.2 and B.3 show the overall structure of the program, broken down into functional blocks. The initialization phase and time stepping loop have been separated to clarify the structure.

B.3.1 File `pdefines.h`, version 1.8

This file contains a number of frequently used parameters which are declared using the `#define` command. Some are used to define the size of arrays - although this is rarely done because C is capable of dynamically allocating array space. The remainder of these definitions are used to make the coding in other functions more readable. For instance the statement

```
if ( ! options[RURAL_OPTION] ) {
```

is more descriptive than

```
if ( ! options[4] ) {
```

which could have been the result had use of `define`s not been made. Finally there are a couple of macros which are needed because C does not have intrinsic maximum and minimum functions.

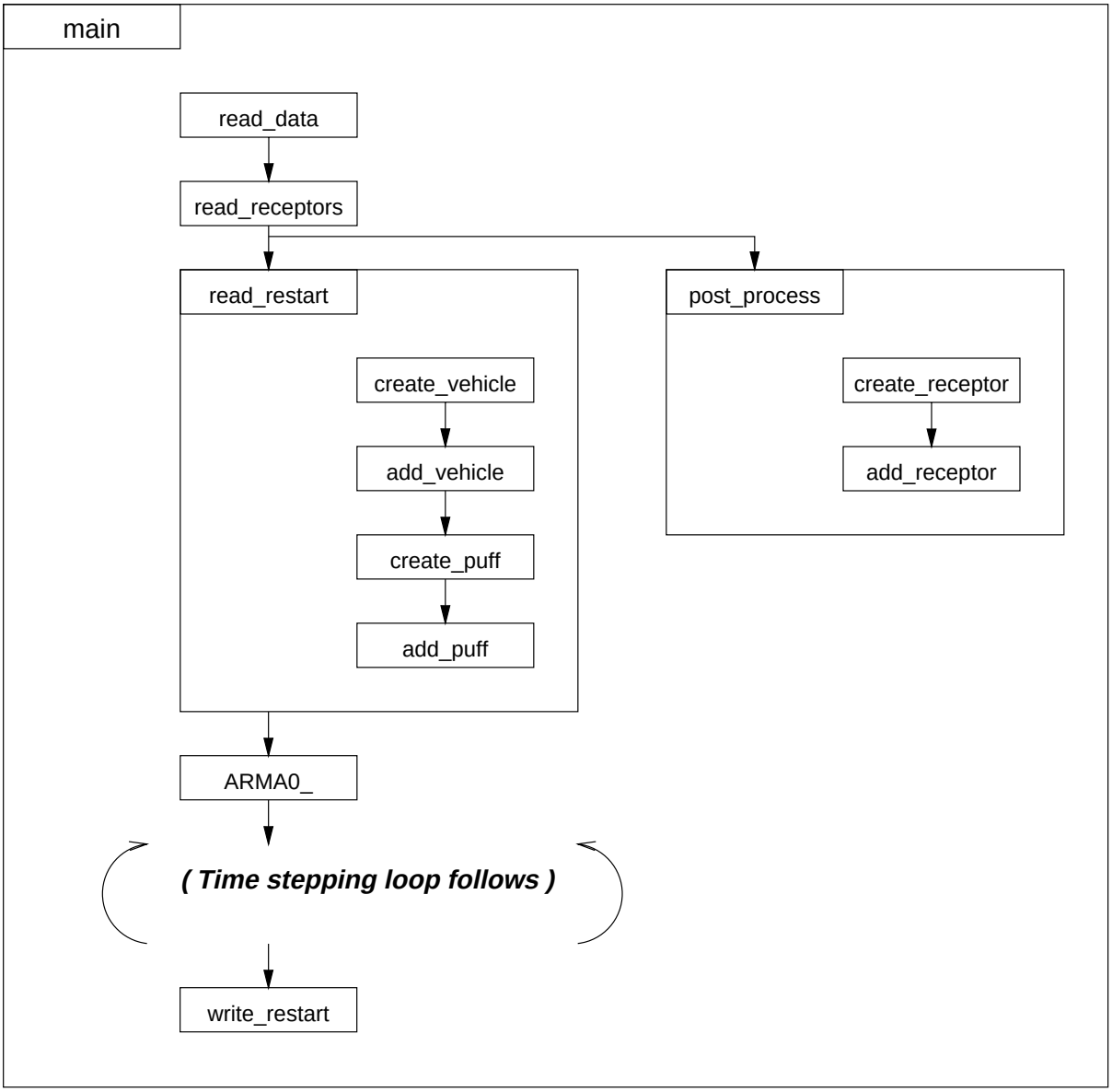


Figure B.2: Initialization phase of the PUFFER program.

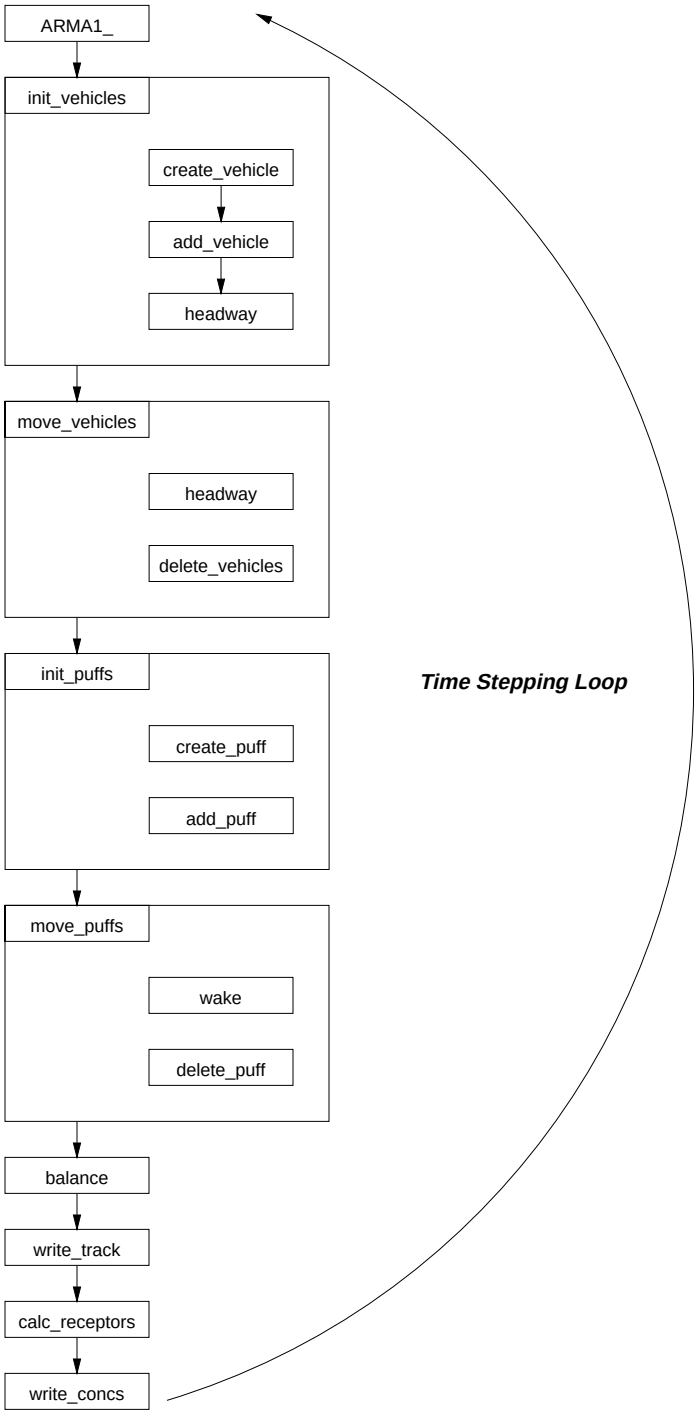


Figure B.3: Time stepping loop of the PUFFER program.

- Maximum size definitions...

  `MAX_OPT` – maximum number of run-time options available.

  `MAX_OUT` – maximum number of output data types - only one is used at present.

  `MAX_FORMAT` – maximum number of output formats - used in post-processing mode.

  `MAX_SCAL` – maximum number of data scalings - there are only two: scaled or absolute values.

- Option numbers...(used in conjunction with array `options`)

  `RESTART_OPTION` – data is read from the restart file in this mode.

  `CYCLIC_OPTION` – puffs are re-cycled from one end of the lane to the other in this mode.

  `ONE_PASS_OPTION` – vehicles are only allowed one pass along the lanes of traffic in this mode.

  `WAKE_OPTION` – mainly a debugging feature which allows the user to 'turn off' the wakes behind vehicles.

  `RURAL_OPTION` – converts the model to a rural one - turns off reflections in canyon walls and invokes a more complex wake model.

  `RANDOM_ANGLE_OPTION` – invokes a random wind angle which causes the incidence angle of the wind to vary about the mean with a given standard deviation.

  `ARMA_WIND_OPTION` – turns on the simulation of a realistic time series of the wind using ARMA modelling.

  `POST_PROCESSING_OPTION` – is self-explanatory - the program runs in post-processing mode - this is now set internally automatically.

- Output numbers...(used in conjunction with array `outputs`)

  `CONC_OUTPUT` – turns on output of concentration at all receptors.

  `others` – are not used in the present version of the code.

- Scaling numbers...

  `ABSOL` – absolute values are output.

  `NODIM` – non-dimensionalised values are output.

- Combinations of velocity scaling...

  `WINDWIND` – wind speed/wind speed scaling.

  `WINDVEHS` – wind speed/vehicle speed scaling.

`VEHSWIND` – vehicle speed/wind speed scaling.

`VEHSVEHS` – vehicle speed/vehicle speed scaling.

- Output types...

  `POINT` – time evolution at a single receptor.

  `LINE_MEAN` – time-averaged profile along a line of receptors.

  `PLANE` – time-averaged values on a plane of receptors.

  `PROBABILITY` – probability distribution at a single receptor.

  `AVS` – unstructured cell data is produced for the AVS package.

  `LINE_INST` – instantaneous profile along a line of receptors.

- Plane numbers...

  `XY` – the *xy* plane.

  `YZ` – the *yz* plane.

  `ZX` – the *zx* plane.

- Line numbers...

  `X` – a line parallel to the *x* axis.

  `Y` – a line parallel to the *y* axis.

  `Z` – a line parallel to the *z* axis.

- Miscellaneous...

  `MAX_AVS_STEPS` – the maximum number of time steps allowed for AVS output.

  `MAX_ACCELERATION` – vehicles cannot exceed this acceleration.

  `MAX_DECELERATION` – vehicles cannot exceed this deceleration - notice it is greater than the acceleration.

  `MIN_SPEED` – used to prevent the vehicles reversing.

  `PI` – hmmm...

  `PIPI32` – obviously this is equal to $2\pi^{3/2}$.

  `DEG_2_RAD` – factor for converting from degrees to radians.

  `LIMIT1` – a small number which probably is not used at present.

  `LIMIT2` – a very, very small number required to keep certain values within the two-digit exponent fields for output.

  `ROOT2` – the square root of one less than three.

  `ROOT8` – $2\sqrt{2}$ or the square root of 8.

`TRUE` – sometimes it is necessary to explicitly give `TRUE` and `FALSE` values. Here the convention of zero being false and true being non-zero (1 will do) is used.

`FALSE` – see above.

`BIGGY` – a big number.

- Macros...

`MAX( a, b )` – finds the maximum of two numbers.

`MIN( a, b )` – finds the minimum of two numbers.

B.3.2 File `ptypes.h`, version 1.8

This file contains the type definitions for the PUFFER code. All are new structures, defined using the `typedef struct` method. They are used variously to group similar variables together, such as the accountancy structure, or in the more traditional sense to describe all the properties of a single entity, such as a puff.

`struct DOMAIN_DATA` – holds the values associated with the domain (either a canyon or a conceptual box for the rural case), including things like wind speed:

`double length, width, height` – dimensions of the domain.

`double speed` – mean wind speed at the reference height.

`double ref_height` – reference height.

`double theta, theta_sd` – angle between the wind and the *x*-axis and the standard deviation thereof.

`double intensity` – turbulence intensity of the above canyon wind (used in the ARMA wind generation calculations).

`double z_0` – surface roughness length, used in generating wind speed profiles.

`double xlu` – characteristic length scale for the wind turbulence, used in the ARMA wind generation calculations.

`double turb1, turb2` – turbulence intensity and isotropy parameters.

`double puff_removal_limit` – puff removal limit - the reduction in the concentration at the centre of the puff which must occur for the puff to be removed from the model.

`double puff_reduction_factor` – puff reduction factor - governs the rate at which the mass of the puff is reduced by the roof level entrainment process.

`double k_vortex, b_vortex` – holding values for in-canyon vortex wind speed calculations.

`struct VEHICLE_TYPE` – contains data for each type of vehicle as opposed to individual vehicles:

`double density` – normalized density for the vehicle type - the sum of all these densities must be unity.

`double length, width, height` – dimensions of the vehicle.

`double alpha` – aspect angle of the vehicle, used when determining the origin of the wake of the vehicle.

`double speed_control` – speed control parameter which determines the rate at which the vehicle tries to gain parity with the speed of the vehicle in front.

`double headway_control` – headway control parameter which determines the rate at which the vehicle tries to reach the ideal distance behind the vehicle in front.

`double headway_calc` – parameter used to calculate the ideal headway, given the speed of the vehicle.

`double q_idle` – idling emission rate.

`double q_speed` – speed-related emission coefficient.

`double q_accel` – acceleration-related emission coefficient.

`double c_idle` – idling concentration.

`double c_speed` – speed-related concentration coefficient.

`double c_accel` – acceleration-relation concentration coefficient.

`double d_e` – exhaust pipe diameter.

`struct TIME_STEP` – time step and output data:

`double delta_t` – length of time step.

`long number` – number of time steps.

`long puff_gen` – puff generation frequency, (*ie* puffs are only generated every `puff_gen` time steps).

`long spatial_gen` – spatial output data generation frequency, (*ie* output is only generated every `spatial_gen` time steps).

`long tracking_gen` – tracking output data generation frequency, (*ie* data is only generated every `tracking_gen` time steps).

`int lead_puff_removed` – is a flag which indicates that the lead puff has been removed from the linked list of puffs. When set to one, the function `write_tracking` outputs a blank line to the tracking data file so that the discontinuity can be picked up by the plotting package used.

`struct PUFF puff_struct` – puff structure:

- `double x, y, z` – coordinates of the puff.
- `double mass` – mass of pollutant contained within the puff.
- `double c0` – the initial concentration of pollutant at the centre of the puff, used in calculation of puff depletion.
- `double sigma_x, sigma_y, sigma_z` – dispersion parameters.
- `struct puff_struct *next` – pointer to the next puff structure in the linked list.
- `struct puff_struct *previous` – pointer to the previous puff structure in the linked list.

`struct VEHICLE vehicle_struct` – contains data for individual vehicles:

- `double x` – *x* coordinate of the rear bumper of the vehicle.
- `double u` – *x* component of velocity of the vehicle.
- `double a` – *x* component of acceleration of the vehicle.
- `double emit` – instantaneous emission rate of the vehicle.
- `double conc` – instantaneous concentration of exhaust gas.
- `int type` – vehicle type (see the `VEHICLE_TYPE` structure).
- `struct vehicle_struct *next` – pointer to the next vehicle in the linked list.
- `struct vehicle_struct *previous` – pointer to the previous vehicle in the linked list.

`struct TPOINT` – structure which holds single points in the lead vehicle speed versus time curves for each lane of traffic:

- `double time` – time value.
- `double value` – speed.

`struct LANE` – holds the data associated with lanes of traffic:

- `int direction` – indicates the direction of the traffic in the lane (+1 indicates flow in the positive *x* direction, while any other value, usually -1, indicates flow in the opposite direction).
- `int single_pass` – indicates that the vehicles in this lane should not be recycled.
- `int time_points` – number of points in the curve which describes the variation of the speed of the lead vehicle in the lane with time.
- `long number_vehicles` – counter which keeps track of the number of vehicles in the lane at any instant. Used as output data in the tracking file.

`TPOINT *points` – pointer to the list of time points (see previous structure).

`VEHICLE *vehicles` – pointer to the first vehicle in the lane of traffic (the lead vehicle).

`double y_offset` – the non-dimensional *y* offset of the lane of the traffic. (*ie* if `y_offset` were 0.5 then the lane would lie down the centreline of the domain).

`struct RECEPTOR` – holds receptor data such as position and concentration:

`double x, y, z` – coordinates of the receptor.

`double c` – concentration at the receptor.

`double mean` – mean concentration at the receptor, only used when the model has reached some kind of equilibrium.

`struct ACCOUNT` – the accountancy data structure:

`double mass_in` – total mass of pollutant emitted by the vehicles into the domain.

`double mass_out` – total mass of pollutant lost from the canyon via roof entrainment, end entrainment or puff depletion.

`double mass_store` – total mass in the canyon at any instant, formed by summing over the mass in all the active puffs.

`long lanes` – number of lanes of traffic.

`long receptors` – number of receptors.

`long vehicles` – number of types of vehicles.

`long active_puffs` – number of active puffs in the canyon.

`long weak_puffs` – number of puffs lost because they become too weak to contribute to the total.

`long end_puffs` – number of puffs lost at the ends of the canyon when cyclical boundary condition are not in effect.

`struct POST` – contains post-processing data:

`double x0, y0, z0` – coordinates which can define the position of a) a single receptor, b) a line aligned parallel to one the major axis, or c) a plane.

`int format` – type of output format: 0 is a time trace at a single receptor; 1 is a time-averaged concentration profile along a line; 2 is a time-averaged concentration probability distribution on a plane; 3 is a concentration distribution at a single receptor; 4 is UCD output; and 5 is for an instantaneous profile along a line.

`int scaling` – scaling of output: 0 causes the absolute value to be output, 1 causes the non-dimensionalised form to be written.

`int line` – axis along which the profile should be aligned: 0 is the *x* axis, 1 is the *y* axis, and 2 is the *z* axis.

`int plane` – plane on which the distribution should be found: 0 is the *xy* plane, 1 is the *yz* plane, and 2 is the *zx* plane.

`int vscale` – defines the velocity scale.

`long start` – time step at which the various averaging processes should begin.

`long bins` – number of bins for the probability plot.

`double clower` – lower limit of concentration for the bins in the probability plot.

`double cupper` – upper limit of concentration for the bins in the probability plot.

`double *bin` – pointer to the array of bin counts - a `double` is used because a renormalisation takes place so that the sum of the values in all the bins comes to unity.

`struct RLIST rlist_item` – contains a linked list of the receptors which make up the line or plane for post-processing plots.

`long index` – receptor index.

`struct rlist_item *next` – pointer to the next receptor in the linked list.

B.3.3 File `puffer.c`, version 1.7

`void main`

This is the main executive sub-program for the PUFFER program and has been written with the minimum of calculations in order to clearly show the overall structure of the program.

The source code starts with all the necessary `#include` statements, including the two include files specific to the PUFFER code: `ptypes.h` and `pdefines.h`. Then come the function allusions which define the types of all the the functions called by the `main` function and their respective arguments (if any). Notice that an allusion is required for the FORTRAN functions `arma0_`, `arma1_` and the NAG routine `g05ddf_` in order to ensure the correct transfer of data between the C calling function and the called FORTRAN function. The arguments are all pointers because FORTRAN operates on a call-by-reference basis. These three allusions are only included at compile time if the `NAG` macro has been defined.

There are two major modes of operation of the program: normal and post-processing. Which one is chosen depends on whether the file `puffer.out` exists in the working

directory. If it does then is data is available for a post-processing run, otherwise it is created as empty for a normal run. This is all achieved by the two calls to `fopen` which first tries to open `puffer.out` in read binary mode (`rb`) mode for post-processing. Failing this, it attempts to open it in append binary (`ab+`) mode for a normal run. Which mode is chosen is echoed to standard output and the relevant entry in the `options` array is set.

A call is then made to the function `read_data` which reads and echoes much of the data concerned with the operation of the program. For instance, the run time options are read in `read_data`, one of which determines whether or not a restart is required. The remaining input data, which is just the number and positions of receptors is read in via a call to sub-program `read_receptors`.

The inclusion of some post-processing capabilities into the code requires two approaches to the opening of the remaining output files in PUFFER. In normal mode, the tracking file, `puffer.xyz`, and the vehicle position file `puffer.veh` (both ascii mode) are opened. Then, if the program is in restart mode, the function `read_restart` is called in order to set up the data for a restarted run. However, when post-processing is on, there is no need for the tracking, vehicle and restart files to be opened or read - the only file that needs opening is the previously generated output file, `puffer.out`. Once opened, the file structure `iout` is passed to the function `post_process` which, as its name suggests, performs the operation necessary to produce the required data.

After setting the end timestep number `t_end`, the last initialization function, `arma0_` is called, but only if the ARMA wind generation option is on. As mentioned above, `arma0_` is, in fact, a FORTRAN subroutine which goes some way to explain the underscore appended to the name of this function. This is an idiosyncratic method used to identify the function as being non-C in nature. Again, only if the `NAG` macro has been defined, does the possibility of a call to function `ARMA0` exist, otherwise an error trap is compiled into the code.

After the initialization of the program has been completed, the main time stepping loop of the program is entered. Notice that the counter `tstep` runs from `t_start` to `t_end` so that non-zero initial time step numbers can be used from a restart. The elapsed time `elapsed_time` is immediately incremented by `tdata.delta_t`, the time step size.

If the random wind angle option has been set by the user, then this angle is generated by means of call to a NAG routine, `g05ddf_`, based on the mean and standard deviations of the wind angle. Otherwise, the variable `theta` is set to the mean value stored in the `domain` structure. `theta` has local scope and is later passed to `move_puffs` so that the various components of the wind field may be calculated. Use of compile time definitions prevents the call to `g05ddf_` if it is not available on the host machine.

Similarly, the next portion of code contains the same compile time checks, but this time is used to conditionally prevent the inclusion of a call to the function `arma1_`. If the ARMA wind option is on, a new value of the wind speed is generated by a call to

the FORTRAN subroutine `arma1_` which returns a modified `speed_ref`. Otherwise, `speed_ref`, which again has local scope, is set to the mean value of wind speed at the reference height set by the user.

There then follow a series of calls to a number of self-contained functions which perform the bulk of the operations. The first of these, `init_vehicles` checks the current positions of the vehicles in each lane of traffic and can introduce new vehicles or remove the lead vehicle, depending on the current state of things. Another function, `move_vehicles` then updates the positions of the vehicles using the simple 'follow-the-leader' model employed in PUFFER.

Once the vehicles have been moved, the other main set of entities in PUFFER, the puffs, are initialized by means of a call to the function `init_puffs`. This function, however, is called only every `tdata.puff_gen` time steps. The reason for this being that it is then possible for the user to limit the number of puffs (and hence the run-time) without compromising the accuracy of the time stepping scheme (which relies on a small time step). For this very reason, the puffs are moved every time step in the function `move_puffs`. In addition to the positions of the puffs being changed, the dispersion parameters and mass of the puffs are updated and, if necessary, some of the puffs can be entrained at roof level or at the ends of the canyon.

`balance` is an anomalous function - it calculates the total mass of pollutant in the canyon at that particular time. The other parts of the mass balance calculations, mass in and mass out are calculated in `init_puffs` and `move_puffs` respectively.

Tracking data is only written to file every `tdata.tracking_gen` time steps. This again is an attempt to limit the reams of data that can be produced by the program when using very short time steps. Next comes potentially the most computationally intensive stage of the whole program. The calculation of the concentrations at receptors is dealt with in the function `calc_receptors`. This time spent in this function is almost exactly linearly related to the product of the number of puffs and receptors. Thus, it is wise only to call this function when required and so the `spatial_gen` entry in the `tdata` structure is provided to reduce the number of times these expensive calls are made. Once the concentrations at each receptor are known, they can be written to the main binary output file via the function `write_concs`.

For any number of reasons it is often necessary to kill or interrupt a run of PUFFER in mid-flow. The existence of the file '`puffer.run`' is checked every time step. If the file is not present then this fact is indicated on standard output and the program exits the time loop. Thus, a controlling shell script or batch file can remove `puffer.run` at any time during the run of PUFFER in order to facilitate a clean exit.

All the data required for a restart such as time step information, vehicle positions and puff properties are written to the restart file `puffer.rso` in binary mode. By simply renaming this file to `puffer.rsi`, a restart can be performed with the appropriate flag set in the input deck.

All extraneous files are then closed and the program exits.

B.3.4 File `puffs.c`, version 1.10

`init_puffs`

This function initializes the position, dispersion parameters and mass of each puff released by a vehicle. This function is called from the `main` function only every `tdata.puff_gen` time steps for reasons explained in the documentation of that function. After the various declarations, the main body of the function is entered and two nested loops are encountered: the outer loop steps through the lanes while the inner one steps over the vehicles within each lane.

The dispersion parameters are first calculated, following Equations 4.22 to 4.24. This is done because σ_x^0 defines the distance between the centre of the puff and the rear of the vehicle. The proposed x coordinate of the puff is then stored in the variable `new_x`. This new position depends largely on the direction of the traffic in the lane.

If cyclical boundaries are in place, the position of the puff is checked to see if it lies beyond either end of the lane. If it does then it is reflected back at the other end of the lane (see Section 4.2.7 for more details).

Regardless of whether the cyclical boundaries are on or not, if the puff still lies within the domain, it is added to the linked list of puffs by means of calls to the functions `create_puff`, which allocates memory for the puff, and `add_puff` which actually places the puff in the list. However, it should be noted that each puff (and its associated properties) are described by a structure of type `PUFF`, the members of which can be found described in Section B.3.2.

Some of those members are then set. The member `x` is set equal to the, possibly modified, value of `new_x`, `y` is set equal to the y-coordinate of the lane of traffic and `z` is set equal to half the vehicle height and the three initial dispersion parameters are then set as well .

Using the product of the current exhaust flow rate, the current exhaust concentration, the time step and the puff generation frequency, the mass of pollutant in the puff is then set. The initial concentration is then stored in the puff structure for use later when it is used to test the strength of the puff.

The `active_puffs` member of the `number` structure is then incremented because we have just introduced another puff. Control is then passed back to the calling function, `main`.

`move_puffs`

This function controls the movement, dispersion and depletion of the puffs. After the various declarations, if the `puff1` structure is `NULL` then the function is immediately exited because this signals that there are no puffs to move.

The *u* and *v* components of the wind velocity at the reference height are calculated, along with a couple of useful constants which are not dependent on the position of the puff.

The main loop in this function is then entered. The loop is controlled by a `while` construct which checks whether the condition of the puff structure `p` not being `NULL` is satisfied. This indicates that the last puff in the linked list has not yet been encountered.

Depending on whether the rural option has been chosen, the components of the wind at the puff centre are calculated. The calculations are based on Equations 4.18 and 4.19, when there is a canyon present, and 4.20 regardless of there being a canyon or not. Notice that in the rural case, the *w* component is zero.

The function `wake` is then called which calculates the contributions to the *u* and *v* components of the wake velocity from all lanes of traffic. The function returns, by means of pointers, these wake components which are then added to the existing values of `u` and `v`.

The position of the puff is then updated by a simple differencing scheme. The new positions are checked to see if they are valid. For instance, in the cross-canyon plane, the puffs are moved back onto the walls if they go through the walls. For puffs which stray beyond the ends of the lanes, two quite distinct fates await them. With cyclical boundaries, the puff simply appears at the opposite end of the lane. With end entrainment boundaries, the puff is lost from the domain completely. When this happens the `mass_out` member of the structure `number` is incremented by the mass of the puff at the time it strayed from the canyon. The actual deletion of the puff is somewhat complicated with copying of pointers to and fro, but essentially the function `delete_puff` removes any trace of the puff from the linked list.

Once the new position of the puff has been calculated, the turbulence at the puffs centre is calculated from Equations 4.25 to 4.27. And based on the new position and dispersion parameters, the mass reduction due to roof entrainment is calculated (from Equation 4.31), regardless of the position of the puff within the canyon - this calculation is not necessary in rural mode. The `mass_out` variable is incremented in accordance with the reduction in the puff's mass. If concentration at the centre of the puff has fallen below some predefined fraction of its initial value, the puff is again deleted from the linked list. This ensures that really weak puffs are excluded from the very time consuming calculations described above.

Finally, the loop counter `p` is set equal to the pointer to the next puff in the linked list. It is for this reason that there is a slight complication when deleting a puff because if the

puff were to have gone then `p` would be `NULL` and the loop would quit too soon.

`wake`

This function calculates the contribution to the flow field in which the puff finds itself due to the wake of the vehicle(s) in front of it. Notice that it can be vehicle**s** because when there are two or more lanes of traffic, the puff is affected by a vehicle from each lane. To this end a loop over in `i` over the number of lanes is entered.

If there are no vehicles in the lane (which may only happen when the single pass option is in effect), the `continue` statement takes us to the next lane of traffic. A nested loop is then entered which searches for the vehicle in front of the puff. If none can be found and cyclical boundary conditions are in effect, it is possible that the vehicle at the opposite end of the lane can be used instead. In the event of no vehicle being found (*ie* the puff must be in front of the lead vehicle with no cyclical boundary conditions), then the next lane is investigated.

If a vehicle can be found, the variable `xd_min` will contain the actual distance between the rear of the vehicle and the centre of the puff.

For the rural case, the theory of Section 4.2.4 is developed into an algorithm to find the offsets x_0 and y_0 of the new, wake-based coordinate system. Four cases are considered - one for each side of the vehicle. Which one is used depends on the effective yaw angle and the aspect angle of the vehicle. The coordinates of the puff centre in the new (s,n,z) coordinate system are then calculated, as are the exponential factors *n* and *m* of Equations 4.16 and 4.17.

For the urban canyon mode, things are trivial. It is assumed in this situation that the wake is aligned with the direction of travel, along the *x* axis. As such the (s,n,z) coordinate system is aligned with the (x,y,z) system and exponent values of 0.25 and -0.75 are used in this case.

For both cases, the local wake coordinates (ξ,η,ζ) are then calculated in line with Equation 4.14. This 'along-wake' component, stored in `q`, must then be rotated back into global Cartesians for the rural case. The matter is trivial for the urban case. Regardless of scenario, the *u* and *v* components of the wake velocity at the puff centre are stored in the variables `u_wake` and `v_wake` which are returned, using pointers, to the calling function, `move_puffs`. Notice that they have to be multiplied by the direction of the lane before they are returned.

`create_puff`

`add_puff`

`delete_puff`

This trio of sub-programs deal, respectively, with the allocation of memory for, the addition to and deletion from the linked list of puff structures.

B.3.5 File `read_data.c`, version 1.7

`read_data`

The purpose of this function is to read in the run-time data which is contained in the file `puffer.dat`. Indeed, this file is opened on immediately on entry to the function. The file must be present: if it is not then an error message is printed and the program terminates. When the file is present, this fact is written to standard output and the data is read.

Preceeding the opening of `puffer.dat`, a number of local character arrays are initialised with information which may be used when echoing the information read in this function. For example, `char *option_names` holds the names of the various options available to the user.

The first dataset is the run time options which consists of a number of 0s and 1s. Generally, the option is assumed to be on if a value of 1 is read, and is off for all other values - but this is not a strict rule. These values of 0 and 1 are read into the array `options` and for all options, the name of the option (held in the array `options_names`) is written to standard output along with the word “on” or “off” as appropriate. In much the same way, the output options are read in and those which have been chosen are echoed to standard output. In both cases, the actual numbers of the options or output variables are specified in the file `pdefines.h`.

The dimensions of the canyon and wind speed and direction then follow. A series of calculations, based on this data, are then carried out for use later in the program. The majority of these values are stored in the structure `domain` which holds the canyon-related data. Notice that if the ARMA wind generation option has been set, then the input deck must contain extra information relating to the characteristics of the wind.

One of the new capabilities of PUFFER is the ability to model multiple vehicle types. In order to handle this, the next item of data specifies the number of vehicle types present in the canyon. Based on this data, memory is allocated for a number of `vdata` structures

and for the vehicle type counter array, which is pointed to by `nvt`. For each vehicle type, the density, dimensions, dynamic emission and pollutant concentration data are then read in and echoed to standard output. The density corresponds to the relative mean proportion of that type of vehicle in the canyon. Ideally, the total of all the densities should come to 1, but in case this is not so, the densities are normalised before the next set of data is read in.

The number of lanes of traffic is then read and sufficient memory for this number of lane structures is allocated using the `calloc` library function. For each lane of traffic, the scaled offset, direction of traffic flow and the number of points in the time curve is then read in. The scaled offset specifies the position of the lane in the canyon in scaled coordinates. The direction can be +1, for vehicles travelling in the positive x direction and -1 for vehicles travelling in the opposite sense. The time points specify the velocity of the lead vehicle in each lane at any one time. Using them, the behaviour of all the vehicles in a lane can be controlled. Because there can be any number of these time points, memory has to be allocated dynamically for them and the next few lines of code take care of this operation, again with a call to `calloc`.

The dataset for the time stepping, puff generation and output frequencies is then read. The next dataset holds turbulence parameters which are not checked. Neither are the puff removal and reduction parameters checked after they are read.

New to this version of the function is the inclusion of post-processing capabilities into the code. This allows the user to pick out various types of data from the main output file generated by a previous run of PUFFER. So, if the post-processing option is chosen, a number of parameters are read in which specify the type of data to be generated, whether it be the variation of concentration at a single recptor with time or a concentration distribution at some other receptor.

The pointer to the `lanes` structure is returned by this function.

B.3.6 File `receptors.c`, version 1.6

`read_receptors`

This function is required to read in the scaled receptors positions within the domain. It does this by first opening, or at least attempting to, the receptor position file. If the file is not present then an error is indicated on standard output and the program exits. Then the number of receptors in the file is read into the `number` structure - this determines the amount of memory required to hold all the coordinates. The memory is allocated by means of a call to the function `calloc`, with the first location in the block referenced by the pointer `receptors` to a structure of type `RECEPTOR` (see the documentation of `ptypes.h`). If there is a problem with the memory allocation then this is signaled

on standard output and the program terminates.

Because the receptor file is potentially very long, there is an output option available to the user to prevent the receptor positions from being echoed to the standard output. So, the text header is only written to standard output if this option is on - signaled by a value of 1 (or true). A `for` loop is then entered with index `i` which steps through the receptors, reading the normalized coordinates of the receptors as it goes. Any coordinates outside the range 0.0 to 1.0 throws up a warning on standard output but is not potentially fatal enough to terminate the program.

The coordinates of the $\texttt{i}^{\text{th}}$ receptor are then scaled into actual coordinates by multiplying them by the dimensions of the domain. Again, if the output option is on, these new values are the ones which get written to standard output.

Once the loop over `i` has completed, the receptor file is closed and the pointer `receptors` is returned from the function to the calling routine.

`calc_receptors`

This function calculates the concentration at every receptor in the domain. The core of this function is based on the coded form of Equations 4.10 and 4.11, 4.12 and 4.13.

Since Equation 4.10 demands that two summations are to be performed, then all the concentration members of the receptor structure are initialized to zero. Somewhat belatedly, the pointer to the first puff, `puff1`, is compared with the `NULL` pointer and, if the same, then there are no puffs currently in the domain. In this case the function returns control to the calling function.

Since the summation requires that we step through both receptors and puffs then it is possible to have either nested inside the other without any theoretical difference in the final results. However, it is computationally desirable to have the loop over the puffs as the outer loop. Once inside the outer loop, some variables which relate only to the puff pointer, `p`, are calculated. These are basically combinations of the three dispersion parameters which describe the extent to which the puff has expanded.

The inner loop over the receptors is then entered. Again in an attempt to reduce the number of floating point operations to a minimum, the various contributions to Equation 4.10 are calculated only when there is a change in the particular receptor coordinate. Thus, the $X(x)$ contribution is only calculated for the first receptor and thereafter only when the x coordinate changes from that of the previous receptor. It is therefore computationally advantageous to order the receptor file in such a way that the receptors are ordered along the axes as much as possible. The `exp` is a very slow function and is essentially the major limiting factor in the speed of operation of the program.

Notice that `fx`, `fy` and `fz` have various numbers of terms which depend to some extent on the options supplied by the user. `fx` is modified when cyclical boundary conditions are in place. It only does this when the distance, `d1`, between the puff and receptors is greater than half the domain length. In this case, the contribution is determined by wrapping round the distance between the puff and receptor. This inevitably means that `d1` is reduced in such cases. `fy`, by default, has three terms - the last two account for reflections in the canyon walls. In rural mode, only the first term is necessary. `fz` always has two terms - one for the direct contribution and one for the reflection in the floor.

With all the three factors calculated, the concentration member is incremented by their product with `a`, one of the puff-specific parameters calculated inside the outer loop.

When both loops have completed, a final loop over the receptors is performed to reset any very small values of concentration (*ie* less that 1.0×10^{-99}) to zero to prevent field corruptions in the output data.

`write_concs`

With the receptors concentrations calculated, its is necessary to output them to file. The file `puffer.out` is used to store this so-called *spatial* output. Binary mode is used because it is most the most efficient method of storage.

`write_concs` is called only when spatial output is required. a short header is written to file which contains the time step number, the elapsed time and the output type which is always 0 for concentrations.

Then a loop over the receptors is entered and the concentrations are written to file.

The library function `fwrite` is used to write the data to file. It is a very efficient function which writes bytes of data rather than actual integers or floating point numbers to file.

B.3.7 File `vehicles.c`, version 1.8

`init_vehicles`

This function checks each lane of traffic and, depending on the situation, adds a new vehicle to the lane.

The loop with index `i` steps over the number of lanes of traffic. The first section of code deals with the determination of the type of vehicle to be added. This is done only if the `next_type` variable is set to -1 which indicates that a decision was not made on the

previous call to the function[3]. Alternatively, there is the case where there are no vehicles in the lane which should, typically, only occur at the start of the run.

If a new vehicle type is to be added, a pseudo-random number is generated using the generic function `drand48` which lies in the range 0.0 to 1.0. Associated with each type of vehicle, as defined in the input deck by the user, there is a entry `density` in the `vdata` structure. This is a normalized number between 0.0 and 1.0 such that, for instance, if there are 80% of cars in the roadway, then `density` will be 0.8. The loop with index `j` steps through each of the ranges, until it finds the type of vehicle to which `rtype` corresponds. Thus, if we continue the example above and assume the remaining 20% of vehicles are lorries, then a value of 0.82 for `rtype` would lie outside the car range and thus we would be adding a lorry. That assumes the car vehicle type was defined before the lorry type in the input deck.

The are two situations in which a vehicle is added to a lane of traffic. The first occurs generally at the start of a run when there are no vehicles in the lane. The only other time it could be envisaged that this could happen is when the headway exceeds the length of the lane which is unlikely. In this situation, there is a special circumstance which occurs when the single pass option is on. This option was introduced so that comparisons with the wind tunnel experiments described elsewhere in this thesis could be modelled. In this mode the flag `single_pass` in the `lanes` structure is set to one to indicate that no further vehicles are required. Otherwise, the following steps are taken when introducing a new vehicle:

- The counter `number_vehicles` in the `lanes` structure is incremented.
- The function `create_vehicle` is called to reserve space for a new vehicle in the vehicle linked list for this lane of traffic - there is one linked list for each lane of traffic. The memory put aside for the new vehicle is pointer to by `v`.
- The vehicle is added to the linked list by means of a call to function `add_vehicle` and the pointer `vehicles` in the `lanes` structure is used to point to the memory location held in `v`.
- For this first vehicle, the speed is set equal to the first speed found in the list supplied by the user for this lane.
- The *x* coordinate of the rear of the vehicle is set to zero - there is no need to set the *y* and *z* coordinates because they are implicit in the *y* offset of the lane and the height of the vehicle.
- The local `static` variable `next_type` is then used to set the type of the new vehicle.

[3]Note that the `static` variable `next_type` is used to remember from one call of the function to the next, whether or not another vehicle type is to be generated.

- The array `nvt`, which hold the current number of each type of vehicle is incremented for that particular type of vehicle.
- `next_type` is then set back to -1 to indicate that a new vehicle type should be generated on the next call to the function.

The much more frequently used part of the function adds a new vehicle based on how far from the entrance to the lane the rear vehicle is. So the first thing this part of the code does is to search through the linked list to find the rear vehicle. Notice that the loop stops short of the last vehicle by checking that the next but one vehicle does not exist (*ie* is a `NULL` pointer). The variable `overshoot` represents the distance between the rear of a vehicle at a single headway distance behind the rear vehicle and the lane entrance. If this value is greater than 0.0 then a new vehicle is required. Using steps similar to those described previously, the new vehicle is added. The main differences being that the speed of the vehicle is set equal to that of the one in front and the x coordinate is set equal to the overshoot. Obviously, the more refined the time step, the smaller the size of the `overshoot` will be.

`move_vehicles`

This function is responsible for the movement of vehicles in the lanes of traffic. It is based on the theory outlined in Section 4.2.2 of a follow-the-leader based algorithm and assumes that all lanes of traffic flow in the positive x-direction. Their actual direction is only needed in the functions `move_puffs` and `wake`.

Most of the code is contained within a loop over `i` of the lanes of traffic. Once inside the loop, if the pointer to the first vehicle in the lane is `NULL` then this lane of traffic is skipped. Otherwise, the speed versus time curve for this lane is scanned to find the current speed of the lead vehicle in the lane. Based on this ideal speed, the acceleration of the lead vehicle is then calculated - it is not always possible for the lead vehicle to attain the new speed in a single time step. Sensible maximum acceleration and deceleration rates are defined in `pdefines.h` which limit the value just calculated. At present the same maximums are applied to all vehicle types but this may change eventually because cars generally out-perform lorries when accelerating. The previous values of velocity and positions (x coordinate) are stored for use later and the new velocity and position of the lead vehicle are calculated using simple first order time differences.

The remainder of the vehicles are then moved. Their movement is performed in a similar way to that described above for the lead vehicle, except that their acceleration is calculated from Equation 4.5 which related acceleration to both the relative speeds of the vehicle and the one in front and their separation. Again, limits are imposed on the magnitude of this acceleration before it is used to calculate first the new velocity of the vehicle and then, based on the velocity, the new position. A check is performed to prevent the vehicle from moving backwards in the lane.

It is a distinct possibility that the lead vehicle in the lane may well overshoot the lane exit. In this case, the lead vehicle is removed from the linked list by means of a call to `delete_vehicle`. The two counters which hold the number of vehicles in the lane and the number of vehicles of the lead vehicle's type are both decremented. The vehicle which was previously second in the lane now becomes the new lead vehicle.

Finally, based on the new speeds and acceleration of the vehicles, the emission rates and exhaust concentrations for all the vehicles are calculated based on Equations 4.8 and 4.9. Mainly intended as a debugging aid, the positions of all the vehicles in the first lane alone are written to the file `puffer.veh`.

`headway`

This function returns the value of the ideal headway for a given speed, vehicle length and headway calculation parameter. The calculation is the direct equivalent of Equation 4.4. In this implementation, the α in Equation 4.4 is set equal to 1.5 times the length of the vehicle - this means that, at rest, each vehicle will be have a gap of half a vehicle length between it and the car ahead.

`create_vehicle`

`add_vehicle`

`delete_vehicle`

This trio of sub-programs deal, respectively, with the allocation of memory for, the addition to and deletion from the linked list of vehicle structures.

B.3.8 File `write_track.c`, version 1.3

`write_track`

This function is called from `main` every `number.tracking_gen` timesteps and is designed to output transient data to the tracking file `puffer.xyz`. This function relies on there being at least one puff present, so if the pointer to the first puff in the linked list, `*p`, is `NULL` then the function exits, handing program control back to the calling function.

If there is a puff present, the decision is made whether or not to output a header to the

file. The function of these headers is purely aesthetic - they help the user to distinguish between the 15 or 16 columns of data in the file. A header is written at the first call to the function and thereafter every 20 calls. This achieved using a `static` variable `static_write` to keeping a running total of the number of calls to the function. The header contains brief descriptions of each of the columns of data. They appear in the same order and the data which is now discussed.

One further point, if the lead puff has been replaced since the last call to the function, a blank line is written to file because the plotting package used to look at this data requires a blank line when dealing with discontinuities.

Column 1 contains the elapsed time.

Columns 2 to 4 contain the x, y and z coordinates of the first puff in the linked list. On occasions when this puff is removed from the domain and replaced by the next one in the list, these coordinates will probably jump dramatically.

Column 5 contains the mass of pollutant contained in the tracked puff.

Columns 6 to 8 contain the values of the three dispersion parameters for the tracked puff, σ_x, σ_y and σ_z.

Columns 9 to 11 contain respectively the number of active puffs, the number of puffs lost because they were too weak and the number of puffs lost from the end of the domain or canyon.

Next N_v columns contain the number of each of the N_v vehicles types currently in all lanes of traffic.

Next 3 columns contain the mass balance information: the mass which has entered the domain (from exhausts); the mass which has left the model (from depleted puffs and roof entrainment); and the storage (the mass of pollutant currently in the domain).

Last column is optional and is only printed when the ARMA wind options has been chosen. It contains the current wind speed at the reference height.

Finally a newline character `\n` is written to file and control is returned to the calling routine.

B.3.9 File `restart.c`, version 1.4

`write_restart`

`read_restart`

These two functions respectively write and read the restart file. The restart file is a binary file which contains sufficient data to restart a previous run in the same state as it ended.

As these two functions are so similar, except for the direction the data is travelling, it has been decided to describe both simultaneously.

In both functions, the restart file is opened, if possible. Notice that in write mode the extension `.rso` is used, while in read mode, the extension `.rsi` is used. This differentiation is required because it is conceivable that during a restarted run, both the restart file from the previous run and the one produced for a possible third run will both be present.

All file access uses the two functions `fwrite` and `fread` which write/read bytes to/from the file.

The restart file contains the following information:

- The initial/final time step number.
- The initial/final elapsed time.
- Data related to all the vehicles in all the lanes of traffic such as position, emission rates and speed.
- Data related to the number of each vehicle type in the lanes.
- Data related to all the puffs such as position, dispersion coefficient, etc. - in fact everything held in the `PUFF` structure for each puff.

For the read function, various messages are written to file to indicate restart time offsets, etc.

Finally, both functions close the restart file and exit.

B.3.10 File `arma0.f`, version 1.5

`ARMA0`

This FORTRAN subroutine is called only when the ARMA wind generation option has been chosen by the user. Its function is to initialize an array `R` which holds the auto-regressive and moving average coefficients required to create a time series which displays all the characteristics of a real wind. Much of the theory used in the coding of this subroutine can be found in Appendix C.1 but there follows a brief description of the code which attempts to link it to the theoretical basis. Once the array `R` has been generated, a second sub-routine `ARMA1` is called within the time stepping loop of the `main` program to generate the individual wind speeds.

The first thing to do is to set the seed for the generation of the white noise in the ARMA series. A call to the NAG routine `G05CCF` is used which bases the seed on the current time and therefore should produce a different time series every time the program is run.

Next, `NP+NQ+1` autocorrelation coefficients are calculated in accordance with Equation C.2. Note the use of a `COMPLEX` number `Z` and the NAG routine `S18DCF` which was used to calculate the modified Bessel functions needed. The autocorrelation coefficients are stored in the array `C`.

The Yule-Walker equations (Equation C.4) are then generated, with the matrix Y_{ij} being stored in array `YWA` and the right hand side of Equation C.4 being stored in array `YWB`. This system of equations is then solved using a standard LU-decomposition method, embodied in the NAG routine `F04ATF`.

The solution vector, `A`, represents a first guess at the autoregressive parameters. However, the zeroth element of this array must be set to -1 for reasons not quite understood by the author. Having done that a triplet of nested `DO` loops over `J`, `I` and `K` are performed to mimic Equation C.5.

The four-step algorithm in Section C.1.2 is then performed. Essentially there is an initialization of the array `TAU`, followed by an Newton-Raphson iteration which is allowed to converge. On convergence the values in `TAU` can be used to evaluate the Moving Average (MA) coefficients which are then stored in array `B`.

A call to the NAG routine `G05EGF` concludes the exercise by filling the vector `R` with the appropriate values needed later in `ARMA1` to generate successive terms in the time series.

B.3.11 File `arma1.f`, version 1.2

`ARMA1`

This subroutine returns the next wind speed in the ARMA-generated time series which was initialized in subroutine `ARMA0`. This piece of FORTRAN is essentially a wrapper for the NAG routine `G05EWF` which returns the next term in an ARMA time series, given the array `R`. The `COMMON` block `ARMA` is shared between only `ARMA0` and `ARMA1` so as to facilitate the passing of the array `R`.

B.3.12 File `post.c`, version 1.2

`post_process`

This somewhat messy function is called only when the PUFFER program is operating in post processing mode. It is unusual to include the post processing code in the body of the solver program. Normally the two are quite separate. However, the decision was made to combine the two because of the large amount of shared data structures. In essence, the function reads the binary output file produced by a previous run of PUFFER and extracts and manipulates the data and outputs it in a variety of forms.

Now for the detail. With the binary output file `puffer.out` already having been opened in the `main` function, it is now necessary to open the output file. In the array of pointers to character strings `names` there are held the names of the various output files which correspond to the various output formats available. The element `format` of the `post_data` structure contains the format type number - see the description of the input deck for more details (see Section B.1.1. So, depending on the format number, the output file is opened in ascii write mode.

The next significant section of code deals with the selection of the scaling to be used. A couple of nested `switch` constructs are used to this end. The outer one has two cases: the absolute case in which the various scaling variables are set to one or zero depending on whether they are multiplicative or additive; the non-dimensional case in which the scaling variables are set according to the discussion of Section 3.2.9. Notice the elaborate choice of velocity scaling for the x and y axes of the plots - any one of four combinations of vehicle or wind speed are available.

Once scaling has been dealt with, the next part of the code determines which of the list of receptors are required for output. For the various types of output either a single receptor or a series of receptors on a line or plane are searched for. They are stored in a linked list whose first entry is `receptor0`.

The next bit of code is called on when AVS unstructured cell data is required as output. A call to the function `write_ucd_grid` is called first to write a finite difference grid to the output file. Then memory is allocated to store the output data for use later.

A loop is then entered which reads the output data from the binary file. A brief header, containing details of time and output types is read before the data at all the receptors is read for the current time step. Then another series of choices is made, depending on whether the data is to be immediately written to file or added to some time-average.

Once all the data has been read, those format types which are concerned with the output of time-averaged data or probability distributions are then dealt with. Notice there are difference cases which depend on which axis a line lies parallel to or on which plane a series of receptors lie.

For the AVS data a call is made to `write_ucd_data` which appends the output data to the end of the grid data which was written previously.

`create_receptor`

`add_receptor`

Respectively allocate memory for and add a receptor to the linked list of output receptors.

B.3.13 File `write_ucd.c`, version 1.5

`write_ucd_grid`

Writes an AVS unstructured cell data grid to file. It relies on the list of receptors forming a $21 \times 11 \times 11$ regularly spaced array. Anything else and this rather rudimentary function will not work and will probably crash.

The required header is written first to the output file and contains information such as the number of nodes, number of cells and details concerning how much field data will be written to the file. Then the nodal position data is written to file, each of which corresponds to a receptor location. In other words, a finite difference grid, equivalent to the 3D array of receptors, is being written to file.

Next comes the tricky bit, writing the cell connectivity data. Each cell has 8 vertices or nodes and this section of code writes the node numbers which form each cell. The function then returns control to `post_process` from whence it was called.

`write_ucd_data`

Appends the concentration data to the AVS UCD file by first writing some header information which really serves to inform AVS that there are 100 items of data - one for each time step. A name for each component is then written to file.

The data for all time steps at all nodes is held in a block of memory pointed to by `*AVS_data`. Two nested loops write the data to file. The data is retrieved from the block of memory by means of explicitly calculating the offset from the base pointer, `*AVS_data`.

Appendix C

Miscellaneous

The contents of this chapter are somewhat diverse. All those methodologies, techniques and algorithms which would have interrupted the flow of the main thesis but which are nonetheless important are included here.

C.1 Simulation of time series of gusty winds

Maeda and Makino [64] presented a method by which the longitudinal and lateral components of a von Karman wind could be simulated using a mixed Auto-Regressive Moving Average (ARMA) model. Their method, with certain enhancements taken from Box and Jenkins [13], has been implemented with the aid of NAG routines [68] and is described in this Appendix.

C.1.1 Characteristics of the von Karman Spectra

Considering only the *u* component of the wind at present, the single-side power spectral density function is written as,

$$\frac{nS_{uu}(n)}{\sigma_u^2} = \frac{4\tilde{n}_u}{(1+70.8\tilde{n}_u^2)^{-5/6}} \tag{C.1}$$

where $\tilde{n}_u = {}^xL_u n/\bar{u}$, n is the frequency, S_{uu} is the spectral density, $\bar{u}$ is the mean wind speed, σ_u^2 is the variance and ${}^xL_u$ is the longitudinal length scale of turbulence. The mathematically deduced autocorrelation coefficient for this spectra is taken from ESDU [27] and is given by,

$$\rho_u(\tau_u) = \alpha(\beta\tau_u)^{1/3}K_{1/3}(\beta\tau_u) \tag{C.2}$$

where $\tau_u = \bar{u}\tau/^x L_u$ is a non-dimensional time lag and $K_\mu(z)$ is the modified Bessel function of the second order. The other values are $\alpha = 0.593$ and $\beta = 0.747$. The NAG routine S18DCF is used to calculate the value of the modified Bessel function.

C.1.2 Simulation

The aim of this simulation is to produce a time series of measurements of the u-component of wind velocity, u_k, $k = 1,\ldots,L$ which correspond to the signal $u(t)$ at intervals of Δ. An ARMA model of order (p,q) which represents this series is written as,

$$u_k + \sum_{i=1}^{p} a_i(p) u_{k-i} = e_k + \sum_{j=1}^{q} b_j(q) e_{k-j} \tag{C.3}$$

where $a_i(p), i = 1,\ldots,p$ are the autoregressive (AR) parameters, $b_j(q), j = 1,\ldots,q$ are the moving average (MA) parameters and e_k is white noise with zero mean and a variance of σ_e^2.

The autoregressive parameters are estimated from the set of linear equations but only if $p > 0$,

$$Y.a = x \tag{C.4}$$

where,

$$\begin{aligned} Y_{ij} &= \rho_{|q+i-j|} \\ x_i &= \rho_{q+i} \\ i,j &= 1,2,\ldots,p \end{aligned}$$

where the matrix Y represents the coefficients of the so-called Yule-Walker equations and $\rho_i \equiv \rho(i\Delta)$. This system of equations is solved for a_i using the NAG routine F04ATF which is a general purpose LU decomposition solver. Using these estimate of the autoregressive parameters, the following modified autocorrelation sequence ρ'_j is calculated,

$$\rho'_j = \begin{cases} \displaystyle\sum_{i=0}^{p}\sum_{k=0}^{p} a_i a_k \rho_{|j+i-k|}, & p > 0 \\ \rho_j, & p = 0 \end{cases} \tag{C.5}$$

where $j = 0,1,\ldots,q$. For the purposes of generating this new series it should be noted that the coefficient, $a_0(p)$, which was not calculated in Equation C.4, is set to -1.

A Newton-Raphson iteration loop is entered which precedes as follows:

1. Set up the vector $\tau = (\tau_0,\tau_1,\ldots,\tau_q)$ with values, $\tau_0 = \sqrt{\rho'_0}, \tau_1 = \tau_2 = \cdots = \tau_q = 0$.

2. Calculate the vector h from the solution of,

$$T^i h = f^i$$

where,

$$f_j = \sum_{i=0}^{q-j} \tau_i \tau_{i+j} - \rho'_j, \qquad j = 0, \ldots, q$$

and,

$$T = \begin{bmatrix} \tau_0 & \tau_1 & \cdots & \tau_q \\ \tau_1 & \cdots & \tau_q & 0 \\ \vdots & \vdots & \vdots & \vdots \\ \tau_q & \cdots & 0 & 0 \end{bmatrix} + \begin{bmatrix} \tau_0 & \tau_1 & \ldots & \tau_q \\ 0 & \tau_0 & \ldots & \tau_{q-1} \\ \vdots & \vdots & \vdots & \vdots \\ 0 & \cdots & 0 & \tau_0 \end{bmatrix}$$

3. Update the vector τ using the incremental relationship,

$$\tau^{i+1} = \tau^i - h$$

where τ^{i+1} is the value at the $(i+1)^{\text{th}}$ iteration.

4. Repeat Steps 2 and 3 until $|f_j| < \varepsilon, j = 1, \ldots, q$ for some prescribed value ε, when the process is said to have converged.

Once convergence has taken place, the values of the MA parameters can be calculated from,

$$\theta_j = -\tau_j / \tau_0, \qquad j = 1, 2, \ldots, q$$

where τ_j are the final values from the iteration. The variance of the white noise σ_e^2 is given by,

$$\sigma_e^2 = \begin{cases} \tau_0^2, & q > 0 \\ \rho_0 - \sum_{i=1}^{p} \phi_i \rho_i & q = 0 \end{cases}$$

Two NAG routines are then used to generate the time series: a call to G05EGF initializes a reference vector which is then used by G05EWF to generate successive terms in the series. As input, G05EGF requires two arrays A and B which contain the autoregressive and moving average parameters of the ARMA model. There is a slight difference in terminology between the array B and the MA parameters. Indeed, in order to allow us to use G05EGF, B must contain,

$$\begin{aligned} \mathtt{B(1)} &= \sigma_e . \sigma_u \\ \mathtt{B(I+1)} &= -\theta_i \sigma_e = \theta_i \mathtt{B(1)}, \qquad i = 1, \ldots, q \end{aligned}$$

where σ_u is the standard deviation of the time series, as required by the user. It should be noted that the length of B is one greater than q. It is also possible to pass the mean of the time series to G05EGF so that the mean wind speed $\bar{u}$ can be incorporated into the time series easily.

C.1.3 An ARMA-generated time series

In order to test the validity of the above approach, attempts were made to generate a typical time series of wind speed. The first column in the table below lists the properties of the chosen wind, while the second lists the actual recorded values produced from the analysis of the generated time series. As can be seen the agreement is acceptable.

	Predicted	**Observed**
Mean wind speed, $\bar{u}$ (ms^{-1})	4.00	4.09
Turbulence intensity (%)	10.00	10.82
Characteristic length scale, ${}^{x}L_u$ (m)	40.0	35.9

C.2 Calculation of Spectra

The calculation of spectra in this report is achieved using a FORTRAN subroutine from the NAG [68] suite of programs. By choosing this route, rather than creating a spectral analysis package from scratch, we gain all the benefits associated with using a product with several decades of development behind it.

The NAG routine used is G13CAF which, formally,

> ... calculates the smoothed sample spectrum of a univariate time series using one of four lag windows - rectangular, Bartlett, Tukey or Parzen window.

Given a series of measurements x_t, $t = 1,\ldots,L$ which correspond to the value of the signal $x(t)$ at intervals of Δ, it is generally accepted (see, for instance Jenkins and Watts [55]) that the smoothed sample spectrum, $\hat{f}(\omega)$, is given by,

$$\hat{f}(\omega) = 2\Delta\left\{C_0 + 2\sum_{k=1}^{M-1} w_k C_k \cos(\omega k\Delta)\right\}, \qquad 0 \le \omega \le \frac{\pi}{\Delta} \tag{C.6}$$

which is calculated for the discrete frequency values,

$$\omega_i = \frac{2\pi i}{\Delta L}, \qquad i = 0,1,\ldots,\left[\frac{L}{2}\right] \tag{C.7}$$

where [] denotes the integer part, w_k is the lag window of size, M, and C_k are the autocovariances of the time series.

The NAG routine G13CAF is able to take a time series as an argument, produce the autocovariances and calculate a sample spectrum which has some important differences to the above:

- The NAG routine assumes that $\Delta = 1$, which means that frequency scaling is required.
- Instead of the factor 2Δ in Equation C.6, the NAG routine returns spectral estimates multiplied by a factor of $1/2\pi$. (This is chiefly because of the assumption that Δ is unity.) Thus, when using the NAG routine to calculate spectra for analysis in this reports, it has been necessary to multiply the returned values from the NAG routine by a factor of $4\pi\Delta$.

The versatility of the NAG routine enables us to choose the size and type of the lag window for smoothing the spectra. The smoothing function is defined as,

$$w_k = W\left(\frac{k}{M}\right), \qquad k \leq M-1 \tag{C.8}$$

where W for the Parzen window, which is used for all the spectra in this report, is given by,

$$W(\alpha) = \begin{cases} 1-6\alpha^2+6\alpha^3, & 0 \leq \alpha \leq \frac{1}{2} \\ 2(1-\alpha)^3, & \frac{1}{2} < \alpha < 1 \end{cases} \tag{C.9}$$

In addition, the standard relationship, $f = 2\pi/\omega$ is used to convert from rad.s^{-1} to the more useful Hz.

C.3 Method for the Determining ${}^xL_u$

It is stated in ESDU 74031 [27] that there are three distinct methods by which values of ${}^xL_u$ can be obtained from the measured data. The first involves the integration of the autocorrelation function with respect to the time lag, the second is to obtain the value of $n = \hat{n}$ at which the value of $nS_i i(n)/\sigma^2$ when plotted against $\log n/\overline{u}$ is a maximum. The third method, and the one which is discussed in this Appendix, relies on obtaining the best overall fit to measured data with the appropriate spectral equation.

For the u-component of wind speed, the generally accepted spectral equation is Equation C.1. Assuming that $N/2$ spectral estimates, S_i can be obtained at the frequencies, $n_i = 0, \ldots, \frac{2i\pi}{N}, \ldots, \frac{\pi}{2}$, it is possible to find the best approximation for ${}^xL_u$ as follows.

The sum of the squares of the residuals can be written as,

$$R = \sum_{i=1}^{N/2} \left(\frac{n_i S_i}{\sigma_u^2} - \frac{4\tilde{n}_{u_i}}{(1+70.8\tilde{n}_{u_i}^2)^{5/6}} \right)^2 \tag{C.10}$$

where $\tilde{n}_{u_i} = {}^x L_u n_i/\overline{u}$. To obtain the best fit of the measured data against the theoretical predictions, it is necessary to find the minimum of R with respect to ${}^xL_u$. This can be

done using searching algorithms similar to those described in Press *et al* [73, pages 280–282].

Thus, it is possible to find values for ${}^{x}L_u$ to a high degree of precision.

C.4 Calibration of a Hot-wire Anemometer

One of the most common techniques for measuring air velocities is by use of a hot-wire. In this technique, a small metallic wire is placed in the airflow and is heated by an electrical current. Under these conditions, the temperature of the wire will drop as the air cools it. The heat loss is a function of the speed of the stream and so the temperature of the wire is a measure of the airspeed at the wire's location.

The constant temperature hot-wire anemometer works on the principle that when the temperature of the hot-wire is fixed the electrical power supplied to the metal is a function of the air velocity. A simplified circuit diagram for the constant temperature anemometer is shown in Figure C.1. The central element is a Wheatstone Bridge in which the hot-wire is integrated into one of the branches. The imbalance of the bridge is amplified and fed back into the bridge by means of an operational amplifier. As a result of the feedback, the current through the wire and hence its temperature and resistance is controlled. The output voltage, E of the anemometer is a measure of the air velocity. The wire only reacts to the normal component of the flow (see Section C.5 on cross-wires).

In mathematical terms, the heat transfer from the heated element and the cooling due to the fluid flow can be related thus,

$$I^2 R_w = (a + bV^n)(T_w - T_f) \tag{C.11}$$

where I is the current; R_w is the resistance of the heated wire; a and b are constants which are related to the size of the sensor, and on properties of the fluid such as thermal conductivity, viscosity and specific heat; V is the velocity of the fluid; n is some power; and T_w and T_f are the temperatures of the wire and fluid respectively.

Using Ohm's law, $E = IR_w$, and some manipulation, the following equation can be derived,

$$E^2 = E_0^2 + BV^n \tag{C.12}$$

where E_0 is the output voltage when $V = 0$, B is some constant and n is a power.

Thus, in order to calibrate a hot-wire it is necessary to find the output voltage for a number of known wind speeds[1]. A 'wind-off' measurement must also be taken to determine E_0, the so-called 'wind-off' voltage. Then, a plot of $\ln(E^2 - E_0^2)$ versus $\ln V$ should

[1] Various methods can be used to measure the wind speed such as pitot-static tubes attached to differential pressure devices.

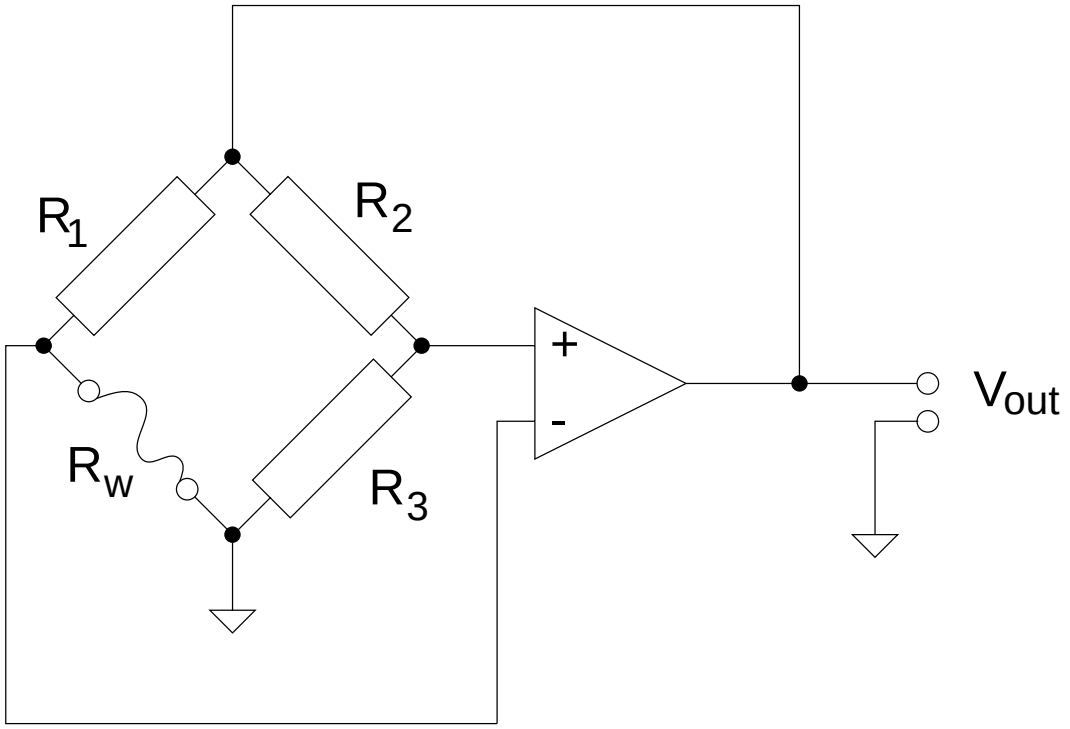


Figure C.1: Circuit diagram for a constant-temperature anemometer.

produce a straight line of gradient n and intercept $\ln B$. Having found these values, the airspeed at the hot-wire can easily be calculated from the output voltage,

$$V = \left(\frac{E^2 - E_0^2}{B} \right)^{\frac{1}{n}} \tag{C.13}$$

C.5 Calibration of Cross-wire Anemometers

Consider a flow with the three velocity components as shown in Figure C.2b. The primed quantities refer to the turbulent components of the flow. The resultant velocity U_R is given by,

$$U_R = \left[(U + u')^2 + v'^2 + w'^2 \right]^{\frac{1}{2}} \tag{C.14}$$

Next consider a standard cross-wire configuration with the two sets of prongs in parallel planes and with one wire at 90° to the other - both wires lie at 45° to the probe axis (see Figure C.2a).

If the turbulence is low, it can be assumed that the resultant, U_R, lies in the plane of the probe (the xy-plane). The component of the airflow which cools wire 1 (see Figure C.2c)

will be,

$$\begin{aligned} U_{\text{eff}_1} &= U_R \cos(45-\theta) \\ &= \frac{U_R}{\sqrt{2}}(\cos\theta + \sin\theta) \end{aligned} \tag{C.15}$$

A similar expression can be written for wire 2,

$$\begin{aligned} U_{\text{eff}_2} &= U_R \cos(45+\theta) \\ &= \frac{U_R}{\sqrt{2}}(\cos\theta - \sin\theta) \end{aligned} \tag{C.16}$$

Adding the two responses from the two wires gives,

$$U_{\text{eff}_1} + U_{\text{eff}_2} = \sqrt{2} U_R \cos\theta \tag{C.17}$$

and subtracting gives,

$$U_{\text{eff}_1} - U_{\text{eff}_2} = \sqrt{2} U_R \sin\theta \tag{C.18}$$

If turbulence is low and the effect of the w' component is small then it can be seen from Figure C.2b that,

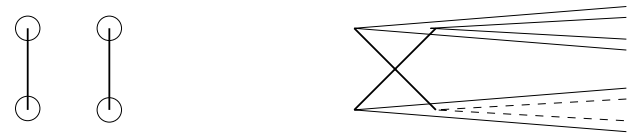
$$\left.\begin{array}{l} U_R\cos\theta \simeq (U+u') \\ U_R\sin\theta \simeq v' \end{array}\right\} \Rightarrow \begin{array}{l} U_{\text{eff}_1} + U_{\text{eff}_2} \simeq \sqrt{2}(U+u') \\ U_{\text{eff}_1} - U_{\text{eff}_2} \simeq \sqrt{2}v' \end{array} \tag{C.19}$$

In conclusion, if the cross-wire is set up such that the wires are inclined at 45° to the mean flow and it is assumed the response to pitch is cosine, then the calibration is straightforward. The procedure described in Appendix C.4 can be done simultaneously for each wire, bearing in mind that the effective velocity is reduced by a factor of $\sqrt{2}$ for each wire. Once calibrated, the along-wind component is proportional to the summed output and the difference in output is proportional to the horizontal cross-wind component.

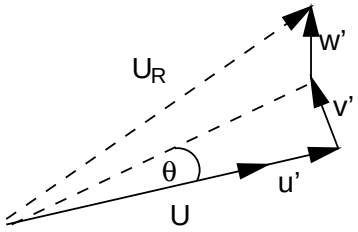
C.6 Calibration of the FID

In order to calibrate the Flame Ionisation Detector correctly, a gas mixer was employed. As was mentioned in the main text, the inlet pressures used throughout the calibration process were too low which meant that the gas mixer was not functioning in its optimum region.

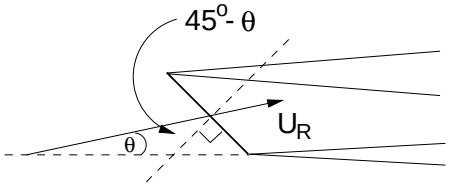
Equal pressures were to be fed into the mixer. This much was known before testing began. No manual was available at that time and a decision was taken to have both the propane/air and compressed air lines at 1 bar - mainly in order not to waste the precious



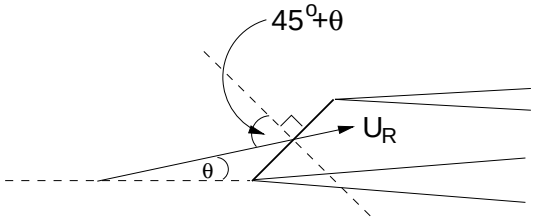
End View Side View (a)



(b)



(c)



(d)

Figure C.2: Schematic of cross-wire configuration and geometry.

gas inside the lecture bottle. As it transpired, conversations with the manufacturers of the mixer revealed that 1 bar was far to low for the mixer to function consistently. It was reported that a higher pressure (in excess of 3 bar) was required for the predictable behaviour of the mixer.

This was obviously a major problem. It meant that all the readings taken using the FID would be incorrect, at least in absolute terms. A whole series of further calibrations using the mixer for various inlet pressures were then conducted in order to get some feel for the magnitude of the problem. It should be noted that even at 1 bar the mixer functioned well enough to give a linear response which is why such a low inlet pressure was not questioned earlier.

Figure C.3 shows the results of 4 calibration 'Passes'. Each pass consisted of five calibrations at each of 1.00, 1.25, 1.50, 1.75 and 2.00 bar[2]. The output voltage from the FID (at a gain of 1) was recorded at gas mixes of 0.0%, 3.0%, 4.5% and 6.0% and each of the four plots in Figure C.3 show the variation at each of these mixes. Since the mixer is effectively by-passed for the 0.0% mix then it would be expected that the FID would respond in the same way at each inlet pressure, but the plot is included to show that the notorious drift of the FID was not significant over the period of the four passes.

The other three plots show that there is a convergence of the mixer behaviour as the pressure is increased. Disturbingly, however, at 1 bar there is a wide spread in the mixers behaviour - due, so the manufacturer will have it, to unpredictable pressure losses in the tubing and the uncertainty in the pressures indicated on the regulators[3]. Note that Pass 3, in particular, differs greatly from the other three which can only be assumed to be the norm rather than some outlying result. On the 6.0% Mixture plot it should be noted that the amplifier on the FID saturated on all Passes except the third one - the saturated state is indicated by a 9 volt output value and may, in actuality, have been much higher than this.

Figure C.4 shows more clearly this convergence at the higher inlet pressures, but this time shows the FID response in percentage concentration per volt. This figure was calculated at each of the 5 pressures by fitting a straight line through all the data points at that pressure. The FID response is simply the gradient of that line. The error bars[4] show in Figure C.4 re-enforce the perception that at the lower inlet pressures the mixer behaves anomalously.

However, if the mixer is assumed to behave in this manner in a repeatable fashion, then it could be assumed that the factor of roughly 3.2 between the converged FID response and the 1 bar FID response could be applied to all the results obtained using the FID. In this case, the measurements taken using the FID may again be correct in absolute terms but with an associated error somewhere in the region of 10%.

[2]The regulator attached to the lecture bottle could go no higher than 2 bar.

[3]Regulators are not a very good way of setting pressures accurately.

[4]Produced by the line fit software.

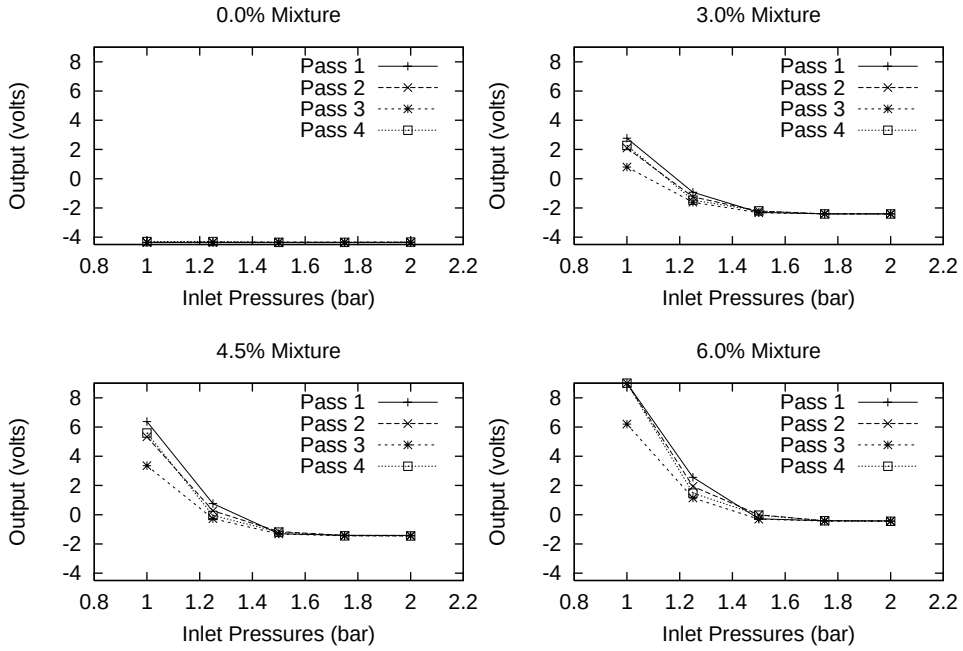


Figure C.3: Behaviour of the mixer at various inlet pressures.

However, closer inspection of the FID calibration factors from day-to-day reveal a wildly varying value. Thus, the decision was made to use this final, correct calibration throughout the experiments, based on the assumption that any changes in the day-to-day FID setup were smaller than the errors associated with the incorrect FID calibration.

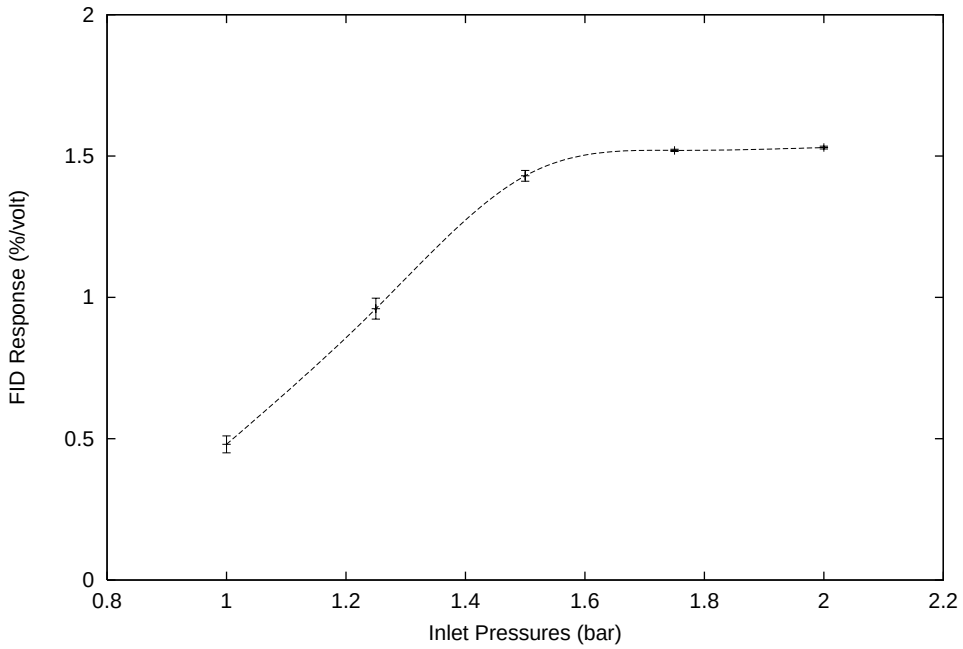


Figure C.4: FID response values for various mixer inlet pressures